Network topology and robustness of coexistence in the antisymmetric Lotka-Volterra equation

Philipp Moritz Geiger

Herrsching 2022

Network topology and robustness of coexistence in the antisymmetric Lotka-Volterra equation

Philipp Moritz Geiger

Dissertation
der Fakultät für Physik
der Ludwig-Maximilians-Universität
München

vorgelegt von
Philipp Moritz Geiger
aus Moers

Herrsching, den 01.02.2021

Erstgutachter: Prof. Dr. Erwin Frey
Zweitgutachter: Prof. Dr. Ulrich Schollwöck
Tag der mündlichen Prüfung: 11.03.2021

Zusammenfassung

Robustheit ist die Fähigkeit eines Systems die Charakteristik seiner Dynamik gegen äußere Einflüsse zu bewahren. Im Kontext biologischer Systeme kann das Verständnis der Ursachen von Robustheit dazu beitragen ein System zu kontrollieren, seine Funktionalität zu beeinflussen, und Einsichten in Entstehung und Evolution geben. Wie die Robustheit eines Systems von dessen Interaktionsnetwerk beeinflusst wird ist ein vielfältiges Forschungsgebiet.
In dieser Dissertation untersuche ich am Beispiel der antisymmetrischen Lotka Volterra Gleichung wie die Robustheit eines dynamischen Systems von der Topologie seiner Interaktionen beeinflusst wird. In der antisymmetrischen Lotka Volterra Gleichung, der Replikator-Gleichung für Nullsummenspiele im Bereich der evolutionären Spieltheorie, ist die Intensität paarweiser Interaktionen von Strategien durch eine antisymmetrische Matrix festgelegt. Typischerweise sterben einige Spezies aus, während bei den verbleibenden Spezies komplexe Schwingungen zu beobachten sind. Koexistenz von allen Spezies tritt auf wenn die Interaktionsmatrix einen strikt positiven Kernvektor hat. Kernvektoren können mithilfe der pfaffschen Determinante berechnet werden, einer für antisymmetrische Matrizen definierte Funktion ähnlich der Determinante. Die Repräsentation antisymmetrischer Matrizen durch gewichtete Netzwerke ermöglicht eine graph-theoretische Charakterisierung der pfaffschen Determinante und damit der Kernvektoren. Dadurch ist es möglich, den Zusammenhang von Koexistenz aller Spezies und der Topologie des Interaktionsnetzwerkes zu untersuchen.
In dieser Arbeit diskutiere ich *Koexistenznetzwerke*, Netzwerktopologien in denen Koexistenz von allen Spezies robust ist gegen beliebige Störungen der Interaktionsstärke. Mithilfe der pfaffschen Determinante werden einfache graph-theoretische Regeln hergeleitet die die Identifikation und Konstruktion von Koexistenznetzwerken beliebiger Größe ermöglichen. Für Koexistenznetwerke ist das qualitative Verhalten der Dynamik, robuste Koexistenz aller Spezies, eine Konsequenz der Netzwerktopologie. Meine Arbeit zu Koexistenznetzwerken kann möglicherweise dazu beitragen robuste Netzwerkmotive in Ökosystemen zu identifizieren.
Die einem Koexistenznetzerk entsprechende antisymmetrische Matrix hat einen strikt positiven Kernvektor der die mittlere Massenverteilung im System beschreibt, sodass auch quantitative Eigenschaften der antisymmetrischen Lotka-Volterra Gleichung und ihre Robustheit untersucht werden können. In der Analyse eines großen Koexistenznetwerks, bestehend aus zusammengefügten Netzwerkmotiven wie dem Schein-Schere-Papier-Zyklus,

finde ich einen *topologischen* Phasenübergang der quantitativen Dynamik. Topologische Zustände werden als Polarisation der Masse sichtbar, und es kann gezeigt werden dass das System in der Symmetrieklasse D der Klassifizierung topologischer Supraleiter ist. Diese Polarisierung ist robust gegen Störungen der Interaktionsstärke und bleibt sogar bestehen wen die Netzwerktopologie verändert wird. Die Beschreibung von topologischen Phasen in Lotka-Volterra Gleichungen weitet das Forschungsgebiet der topologischen Phasenübergänge auf nichtlineare dynamische Systeme mit biologischen Anwendungen aus. Die Ergebnisse dieser Dissertation zeigen, dass in der Dynamik der antisymmetrischen Lotka-Volterra Gleichung robuste Koexistenz und robuste Polarisierung aufgrund von Netzwerktopologie möglich ist. Netzwerktopologie kann also sowohl das qualitative als auch das quantitative Verhalten eines nichtlinearen dynamischen Systems mitbestimmen.

Abstract

Robustness is a systems ability to preserve the characteristics of its dynamics against external influences. In the context of biological systems, understanding sources of robustness can help to either guide, manipulate or secure a systems function, or give insight into its evolutionary origins. The interplay between robustness of a system and the interaction network of its variables is a focus of ongoing research.
In this thesis, I investigate how robustness of a dynamical system is influenced by the coupling topology of its interaction network using the example of the antisymmetric Lotka Volterra equation, the replicator equation of zero-sum games in evolutionary game theory. The antisymmetric Lotka Volterra equation is a nonlinear dynamical system, in which the strengths of pairwise interactions between species are defined by an antisymmetric matrix. In the mass-conserving dynamics typically some species go extinct over time, while the other species survive and perform complex oscillations. However, when the antisymmetric interaction matrix has a strictly positive kernel vector, all species coexist for all times. Exploiting the equivalence of antisymmetric matrices and directed networks, the kernel vector of an antisymmetric matrix can be characterized by network topological properties through the Pfaffian, a determinant like function for antisymmetric matrices. This allows for a discussion of coexistence of all species in terms of network topology.
I find *coexistence networks*, that is, interaction network topologies in which survival of all species is robust against arbitrary perturbations of the interaction strengths and initial conditions. With help of the connection between kernel vectors and the Pfaffian, simple graph-theoretical rules are derived by which coexistence networks of arbitrary size can be identified and constructed. For coexistence networks, the qualitative behavior, namely robust coexistence of all species, is a consequence of the network topology. The work on coexistence networks may help to identify robust network motifs arising, for example, in ecology.
The antisymmetric matrices corresponding to coexistence networks have strictly positive kernel vectors which characterize the average mass distribution in the system, such that also the quantitative behavior of the antisymmetric Lotka Volterra equation dynamics and its robustness can be discussed. In an analysis of large coexistence networks obtained by concatenation of simple network motifs such as rock-paper-scissors cycles, I find a *topological phase transition* of the quantitative dynamics. The topological states become manifest as polarization of the average mass, and it can be shown that the system lies in the symmetry class D within the 'ten-fold way' classification of 1D superconductors. The polarization

is robust against perturbations of the interaction strength and can even withstand changes in the network topology. The analysis of topological phases in Lotka-Volterra systems extends the study of topological phases to nonlinear dynamical systems in biological context. In total, the results of this thesis show that in the dynamics of the antisymmetric Lotka Volterra equation, network topology can lead to robust coexistence of all species, and can give rise to robust polarization as known from topological phase transitions. Hence, topology of the interaction network can influence both the qualitative and the quantitative behavior of a nonlinear dynamical system.

Structure of this thesis

In this thesis we present a comprehensive study of the role of network topology for the long-time dynamics of the antisymmetric Lotka Volterra equation. After a general introduction and mathematical background information, this thesis contains three chapters with the main results. Although the chapters are successively based on each other, they can be read independently. Therefore, each chapter contains an appendix with further details that are specific to the chapter.

1 Introduction: Robustness of coexistence in the antisymmetric Lotka Volterra equation

The first chapter introduces the main theme of this thesis, robustness and its connection to network topology, and the dynamical system that we explore, the antisymmetric Lotka Volterra equation (ALVE). We provide a non-technical introduction to the ALVE and motivate its derivation from the evolutionary game theory of zero sum games such as the rock-paper-scissors game. Additionally, we present a survey of other branches of physics where the ALVE has relevance.

2 Mathematical properties of the ALVE

Here we define the ALVE and derive its mathematical properties. We show that condensates can be identified from properties of the antisymmetric interaction matrix. When the interaction matrix has a strictly positive kernel vector, no states become extinct (coexistence of all states). Furthermore, in case the strictly positive kernel vector is unique, its entries contain key information about the non-equilibrium steady state of the ALVE. The main results in this chapter are reproduced from the work of *Johannes Knebel*, *Markus F. Weber*, *Torben Krüger* and *Erwin Frey* [1, 2], which served as inspiration and starting point for the original work presented in the later chapters.

3 Networks and real antisymmetric matrices

This chapter contains an overview of basic properties of antisymmetric matrices, and how each antisymmetric matrix can be represented by a weighted network. We introduce concepts from graph theory and show how they can be used to characterize the kernel of antisymmetric matrices.

4 Topologically robust coexistence and coexistence networks
with Johannes Knebel and Erwin Frey [49]

In this chapter we identify and characterize coexistence networks, that is, antisymmetric matrices for which the position of positive and zero values secures a strictly positive kernel vector. As such matrices can be represented by directed networks, this property is a direct consequence of the network topology. We define coexistence networks, present network characteristics to identify and construct coexistence networks of arbitrary size and discuss in length possible interpretations and applications. For the ALVE, coexistence networks are relevant as for these networks no extinction takes place: all states are part of the dynamics for all times. In addition, the strictly positive kernel vector characterizes the complex dynamics in these coexistence networks. Apart from the ALVE, coexistence networks have interesting implications for game theory as topologically robust zero sum games, and they are a generalization of Pfaffian orientation.

5 Topological phase transition in coupled rock-paper-scissors cycles
with Johannes Knebel and Erwin Frey [50]

Here we analyze the dynamics and mass distribution of the ALVE on a specific coexistence network that can be interpreted as a one-dimensional chain of rock-paper-scissors cycles. Dependent on one control parameter, a ratio of two rates which we call 'skewness', robust polarization is observed that bears all characteristics of a topological phase transition as known from condensed matter. We show that the antisymmetric interaction matrix indeed undergoes a topological transition that translates to the ALVE dynamics through the strictly positive kernel vector. This chapter discusses topological phase transitions in the context of linear algebra, and its effects for a system from population dynamics.

6 Topological phases beyond rock-paper-scissors

The results from the previous chapter are generalized to more complex one-dimensional chains. We show that the topological phase transition of the rock-paper-scissors chain is robust against changes of the network topology. The topological invariant and with it the topological phase transition is easily identified using the methods from the previous chapter. Polarization strength is determined as the asymptotics of linear recursive sequences that arise from graph-theoretical properties of the chains. As a new feature, extinction is observed in the topologically non trivial phase. Finally, for one dimensional chains at the point of the topological transition, we derive differential difference equations which admit solitary waves.

7 Conclusion, discussion and outlook

The final chapter contains a discussion of the results of this thesis and their significance. We comment on the limitations of the model, possible augmentations and potential paths for future research.

Contents

Chapter 1

Introduction

In the natural sciences, networks are a common and convenient way to visualize and analyze complex systems [3, 4, 5]. The nodes and edges of a complex network can have various meanings: Ecosystems consist of different species (nodes) preying on or cooperating with each other (edges) [6, 7], in the brain neurons (nodes) are interconnected (edges) [8]. The complex workings in a cells can be represented as genes (nodes) that activate or inhibit each other (edges) [9, 10], chemical reactants (nodes) can react and transform (edges) [11]. In all of these examples the complex system is be represented by its network topology: a collection of nodes that are connected by edges. Network topology often is either a byproduct of elaborate analysis or (relatively) simple obtainable, inviting the following questions:
What is the role of the network topology for the properties or dynamics of the system? Does the network topology constrain, support, secure its function?
These questions have inspired a wide array of fascinating research, studying drastically simplified yet still functional models that strongly rely on network topology [12, 13, 14], the influence of interaction network topology on attractors [15, 16] to elaborate graph theoretical conditions for robustness of chemical networks [11, 17, 18].

In this thesis, we investigate the role of network topology for robustness of complex dynamics in the context of the antisymmetric Lotka Volterra equation, a dynamical system that models the population dynamics of networks of competing species [19, 20]. Generally, in this population dynamics some species die out, other species become isolated and some groups of species survive and interact indefinitely [1]. The guiding question of this thesis is if and to what extend the set of surviving species is robust against perturbations of the interaction strength. Here, we show that for the antisymmetric Lotka Volterra equation there are network topologies which predetermine robustness of coexisting species their distribution. We introduce network theoretical criteria that secure coexistence of all species, and show how robust population structure can emerge on the basis of network topology.

We start this thesis by introducing the antisymmetric Lotka Volterra equation as the replicator equation of zero sum games, illustrating its phenomenology and discussing its relevance beyond population dynamics.

1.1 The antisymmetric Lotka Volterra equation (ALVE): Replicator equation for zero sum games

In game theory, a game is called zero sum if in each round the gain of the winner equals the loss of the loser. Pictorially speaking, the loser gives some amount of money to the winner, such that the total amount of money in the game is unchanged, hence the name zero sum game.

1.1.1 The rock-paper-scissors (RPS) game

The most famous zero sum game is the rock-paper-scissors game (RPS), a game that is widely known in various versions all around the world [21]. In this game there are three strategies, rock (R), paper (P), and scissors (P). Each strategy wins against one of the others and is beaten by the third strategy: rock blunts scissors (win) and is wrapped by paper (loss), paper wraps rock (win) and is cut by scissors (loss), scissors cuts paper (win) and is blunted by rock (loss). It is convenient to formalize this list of interactions in the so-called payoff-matrix: The own strategy corresponds to the rows of the matrix, the opponents strategy to the columns. For example, when A chooses rock and B plays paper, player A looses, receiving a payoff of $a_{RP} = a_{12} = -1$. Reversing the roles, in the same encounter player B wins $a_{PR} = a_{21} = +1$. In case of a draw both players receive a payoff of 0, translating to $a_{RR} = a_{11} = 0$, and so on. For this zero sum game, the win equals the loss[1], such that the payoff matrix is antisymmetric. The payoff matrix A_{RPS} is

$$A_{RPS} = \begin{array}{c} \begin{array}{ccc} \text{R} & \text{P} & \text{S} \end{array} \\ \begin{pmatrix} 0 & -1 & 1 \\ 1 & 0 & -1 \\ -1 & 1 & 0 \end{pmatrix} \end{array} \begin{array}{c} \text{R} \\ \text{P} \\ \text{S} \end{array} , \tag{1.1}$$

which is visually presented as a directed cycle in Figure 1.1.
In this matrix notation, the above example yields the payoff of A playing rock (written as the strategy vector $\boldsymbol{s}_A^T = \begin{pmatrix} 1 & 0 & 0 \end{pmatrix}$) against B's paper (that is $\boldsymbol{s}_B^T = \begin{pmatrix} 0 & 1 & 0 \end{pmatrix}$) as

$$\boldsymbol{s}_A^T A_{RPS} \boldsymbol{s}_B = \begin{pmatrix} 1 & 0 & 0 \end{pmatrix} A_{RPS} \begin{pmatrix} 0 \\ 1 \\ 0 \end{pmatrix} = -1 = -\boldsymbol{s}_B^T A_{RPS} \boldsymbol{s}_A \ .$$

A major goal of game theory is to find a strategy that maximizes one players outcome in a series of repeated games. Assuming logical players, a predictable strategy (e.g., always choose 'rock') will always loose as the opponent can tailor his replies accordingly (e.g., always reply with 'paper'), making a random, stochastic strategy necessary. With the probability $p_{A,R}$ of player A choosing strategy 'rock', and so on, the stochastic strategy of player A is expressed as $\boldsymbol{p}_A = (p_{A,R}, p_{A,P}, p_{A,S})^T$. The average payoff for player A against

[1] Of course the payoff can deviate from 1.

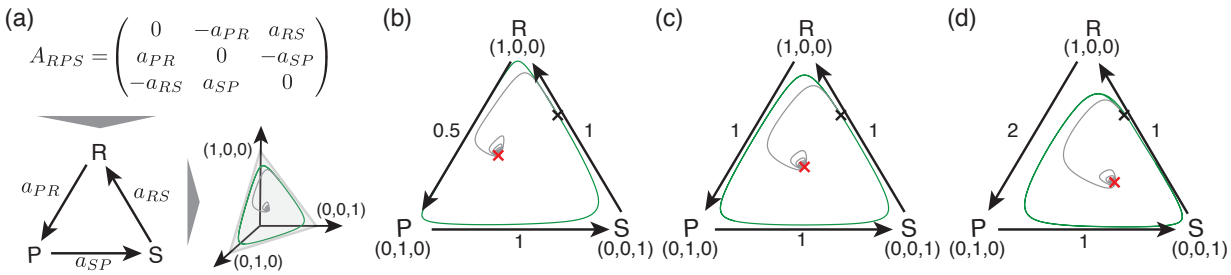

Figure 1.1: Examples for the evolutionary dynamics of the RPS cycle. The matrix A_{RPS} can be represented as a directed cycle topologically robust zero sum games (a). Both the trajectory $\boldsymbol{x}(t)$ (green) and its temporal average $\langle \boldsymbol{x} \rangle_t$ (grey) are shown for different choices of the interaction rate a_{PR} (b)-(d). The trajectory $\boldsymbol{x}(t)$ lies on a limit cycle (green) which is fixed by the initial condition (black cross), while the temporal average $\langle x_\alpha \rangle_T$ (grey) approaches the systems fixed point (red cross), the Nash equilibrium. Depending on the rates, the trajectory in the system is skewed towards the boundaries of the simplex. Nonetheless, for all choices of weights that preserve the network topology no species goes extinct.

the mixed strategy of player B, $\boldsymbol{p}_B$, is then $\boldsymbol{p}_A^T A_{RPS} \boldsymbol{p}_B$. Each player can always force the opponents payoff to zero simply by copying her strategy, $\boldsymbol{p}^T A_{RPS} \boldsymbol{p} = 0$. The optimal strategy for A, the Nash equilibrium, is the strategy that performs best against every choice of the opponent, $\boldsymbol{p}_B$ (or, equivalently, the strategy that minimizes the earnings of player B [22]). Since an average gain is not possible, the Nash equilibrium is the kernel vector of A_{RPS}, the vector $A_{RPS}\boldsymbol{r} = \boldsymbol{r}^T A_{RPS} = 0$. When one player chooses this strategy, the average gain is always $\boldsymbol{r}^T A_{RPS} \boldsymbol{p}_B = 0$ for every choice of the opponents strategy $\boldsymbol{p}_B$.

1.1.2 Evolutionary game theory of zero sum games

At the heart of evolutionary game theory stands the idea that interactions between different phenotypes or behavioral programs are encoded in a game between species in a population. Instead of single agents that choose (probabilistic) strategies, we assume that all individuals of the population 'play' a pure strategy that identifies them as a member of a species. If an individual adopts another strategy, it also changes the species[2]. The game acts as a stand-in for complex biological and ecological interactions, struggles and competitions. Examples are outperformance by agility or fertility, advantage due to resistance against environmental factors, or direct competition due to predation. All interactions are condensed into the game matrix that describes the fitness advantages between different species [23, 24, 25, 20, 26].

For zero sum games, such as the rock-paper-scissors game, one assumes that the advantage of one species is another species disadvantage, for example one species is consumed by the other. This is captured by the antisymmetry of the payoff matrix $A_{RPS} = -A_{RPS}^T$. Of course it is highly unlikely that all interaction strengths are equal, such that the entries

[2]Note that this behavioral species must not coincide with the biological species

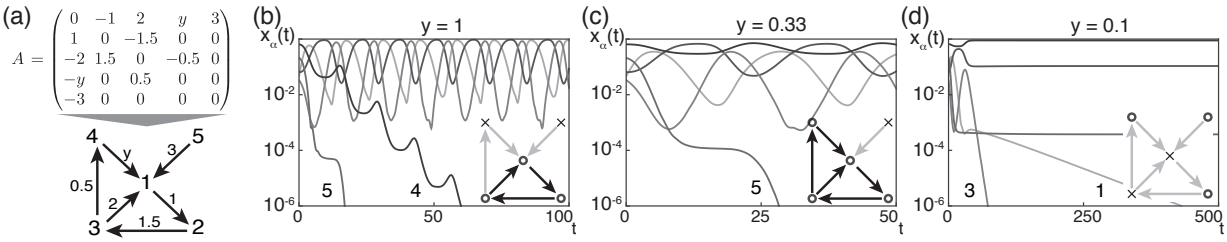

Figure 1.2: Survivors and extinct states depend on both the network topology and the rates. The position of positive and zero entries define the network topology (a). Varying one rate, $4 \xrightarrow{y} 1$ can change the outcome drastically. Depending on the value of y, either three interacting (b), four interacting (c) oder three non-interacting species (d) survive. When the surviving species interact and form a network of coexisting species, complex oscillations are observed (b)-(c).

of the game matrix differ from $+1$ and -1 as in equation (1.1).

Due to the differing fitnesses of the species, the composition of the population, $\boldsymbol{x} = (x_R, x_P, x_S), x_R + x_P + x_S = 1$ changes, creating a dynamics of the population. Each species grows relative to its abundance, $(\partial_t x_\alpha)/x_\alpha$, with a growth rate according to its fitness advantage over the rest of the population. The fitness of species α is determined by $(A_{RPS}\boldsymbol{x})_\alpha$ and thus depends on the rest of the population. A species that is less fit than the rest of the population is outperformed and decreases, while a fitness advantage results in growth. For the RPS game, the populations average fitness is $\boldsymbol{x} \cdot A_{RPS}\boldsymbol{x} = 0$ (as $A_{RPS} = -A_{RPS}^T$), resulting in the following example of the antisymmetric Lotka Volterra equation (ALVE) [25],

$$\frac{\mathrm{d}}{\mathrm{d}t} x_\alpha(t) = x_\alpha(t)(A_{RPS}\boldsymbol{x})_\alpha \ . \tag{1.2}$$

The interaction matrix A_{RPS} defines number $S = 3$ of dynamic variables x_α and the topology and rates of their interactions, see Figure 1.1.

The ALVE for the RPS game is a popular model for population dynamics with cyclic dominance. There is not one strongest species, and success is only temporary, leading to oscillations as shown in Figure 1.1. Starting from some initial configuration (black cross), the composition of the population oscillates, leading to a majority of rock followed by paper followed by scissors, followed by rock and so on in a circular fashion (green line). The shape of this limit cycle depends on the values of the transition rates, but the qualitative dynamic behavior, coexistence of all states despite competition, remains unchanged. For large times T, the temporal average $\langle x_\alpha \rangle_T \coloneqq 1/T \int_0^T \mathrm{d}t \ x_\alpha$ approaches the fixed point of the dynamics (grey line and red cross) that coincides with the Nash equilibrium of the game.

1.1.3 Characteristics of the ALVE dynamics

In this thesis, we are interested in the role of network topology for the ALVE dynamics. For this purpose the interaction matrix A_{RPS} in equation (1.1) is replaced with an

arbitrary antisymmetric matrix A, resulting in a differential equation for S states. Each antisymmetric matrix can be represented as a weighted network by interpreting a positive entry $a_{\alpha\beta} = -a_{\beta\alpha} > 0$ as an edge $\beta \to \alpha$ with weight $|a_{\alpha\beta}|$, as discussed in detail in Chapter 3. We consider weighted networks of different size S, where in addition to links with arbitrary weight also neutral interactions are possible, that is, a species is not necessarily in competition with all other species.

Numerical analysis of the ALVE dynamics on general networks shows condensation [1, 2]: Starting from an initial condition where all states are present, the mass in the system retracts into a subset of all states. Which strategies survive and which die out generally depends on both on the network topology and the interaction rates, but is independent from the initial conditions.
This behavior is exemplified in Figure 1.3: For a fixed network topology with $S = 5$ species (a), by varying one interaction strength, $4 \xrightarrow{y} 1$, we achieve drastically different outcomes (b)-(d). While for (b) and (c), the surviving states interact with each other, yielding a dynamical behavior for all times, in (d) the extinction of intermediary states leaves the survivors disconnected. Notably, in (d) also the purely dominated state 5 survives since its dominator goes extinct fast enough. The mathematical details of this example are presented in Section 2.2.2.

In summary, in the ALVE dynamics, species either survive or die out. Which states survive is independent from the initial condition and a consequence of both network topology and transition rates. The surviving states can either be isolated or in contact with other survivors. In this latter case, survivors form a network in which all coexisting states interact dynamically despite their competition for all times. The goal of this thesis is to work out the role of network topology for such networks of condensates.

1.2 Overview of this thesis

The above introduction of the basic concepts for the ALVE allows for an overview of the results presented in this thesis:
Comparing the two examples of the ALVE dynamics on networks, we find that in Figure 1.3 different states die out dependent on the rates, while for the RPS cycle in Figure 1.1 all three states survive for every choice of interaction strengths. This property of *topological robustness* of the RPS cycle, that is survival of all states for every choice of interaction strength, is discussed in Chapter 4. There, we identify simple graph-theoretical rules by which networks that are topologically robust can be identified and constructed.
For the RPS system presented in Figure 1.1 the temporal average $\langle x_\alpha \rangle_T$ approaches the kernel vector of A_{RPS} for large times T. This is the case for all topologically robust networks constructed with the methods that we introduce in Chapter 4. Hence, we can study how the long-time behavior of the ALVE is influenced by variation of rates. In Chapter 5, we show that a one dimensional chain constructed from RPS cycles undergoes a topological phase transition: the temporal average mass shows robust polarization. Finally, Chapter 6 discusses the robustness of the topological phase transition in the RPS chain

against changes in the network topology. Changing the network topology can also break topological robustness such that extinction occurs, as in Figure 1.3. Before introducing the necessary mathematical concepts needed to make the results outlined above, we discuss applications of the ALVE.

1.3 Relevance of the ALVE

This thesis focuses on mathematical properties of the ALVE, such as coexistence of all states and stability of long-time behavior. In particular, we do not aim to describe or model the behavior of a specific biological system. Nonetheless, we hope that the properties of ALVE dynamics discussed in this thesis are robust enough to carry over to less restricted systems, or inspire and stimulate studies on robustness in different biophysical contexts.
In the following, we give an overview of the areas in physics where the ALVE has interpretations and applications. and discuss its relevance there.

1.3.1 Population dynamics

The ALVE can be viewed as a special case of two prominent and closely related models in population dynamics. The generalized Lotka-Volterra equation (gLVE) is defined as [25]

$$\frac{\mathrm{d}x_\alpha}{\mathrm{d}t} = x_\alpha(\boldsymbol{r} + M\boldsymbol{x})_\alpha \ . \tag{1.3}$$

Each species α duplicates or dies as described by the growth rate r_α, and interacts with the other species through the interaction matrix M as $\sum_\beta (M)_{\alpha\beta} x_\beta$. The dynamics of the gLVE can be varied from fixation to heteroclinic orbits [25]. The total mass in the system, $\sum_\alpha x_\alpha$, is not fixed. By a change of variables to $x_\alpha/(\sum_\alpha x_\alpha)$ one obtains a set of differential equations for the composition of the population, which has the form of a replicator equation [25].

In the replicator equation one assumes that every fraction of the population replicates according to its fitness advantage over the rest of the population. It has the form [25]

$$\frac{\mathrm{d}x_\alpha}{\mathrm{d}t} = x_\alpha \left((M\boldsymbol{x})_\alpha - \boldsymbol{x}^T M \boldsymbol{x} \right) \ , \tag{1.4}$$

where x_α is the fraction of species α in the population. As for the rock-paper-scissors dynamics above, the relative growth of species α, $\partial_t x_\alpha / x_\alpha$, is decided by its fitness advantage over the rest of the population. The relative fitness in comparison to other species is defined with the so-called community matrix M. As the replicator describes the dynamics of the composition of a population the overall mass is conserved, $\sum_\alpha \partial_t x_\alpha = 0$. Also, each replicator equation can be mapped onto a gLVE 1.3 with the variables x_α/x_S [25].

The ALVE is a special case of both of this dynamics [27, 28, 2, 29, 30]: The ALVE is the restriction of the gLVE to the case where species only interact by predation on each

other: the win of one species is the other species loss (zero sum game, $M = -M^T$). There is no additional dynamics such as birth or death ($\boldsymbol{r} = 0$). Alternatively, the ALVE is the most simple example of the replicator equation, as the interaction matrix alone ensures that the average fitness is zero, $\boldsymbol{x}^T A \boldsymbol{x} = 0$.

Although being a special case of already simplified models for ecosystems, the ALVE is a suitable toy model to explore the population dynamics of competing species. It shows a rich phenomenology resembling features known from ecosystems, such as extinction and coexistence of competing species, and complex oscillations [28, 2]. Due to its simplicity, an analysis of the ALVE over the limitations of linearization around fixed points is possible, allowing an investigation of mechanisms of stability in competitive systems.

1.3.2 Chemical systems, stochastic population dynamics

In contrast to the heuristic models introduced above, the ALVE can also be derived from microscopic reactions, either in the context of population dynamics, where interactions of individual agents are phrased as reactions [2], or in the context of chemical reactions [31, 32, 33].
Consider reactions of the kind

$$\alpha + \beta \xrightarrow{r_{\alpha\beta}} \beta + \beta \ , \tag{1.5}$$

where $r_{\alpha\beta}$ is the reaction rate. In the population dynamics context, such a reaction describes an encounter between two individuals of different species α and β (i.e., different evolutionary strategies). The defeated agent is replaced by a copy of the winning agent [2]. In the context of chemistry, this is an autocatalytic reaction scheme [32].
In a well-mixed setting, this reaction scheme can be used to derive the ALVE. For this process, the master equation [34] describing the dynamics of the probability distribution of a configuration $\boldsymbol{N}$, $P(\boldsymbol{N}, t)$, is

$$\frac{\mathrm{d}x_\alpha}{\mathrm{d}t} P(\boldsymbol{N}, t) = \sum_{\alpha,\beta=1}^{S} \left(r_{\alpha\beta}(N_\alpha + 1)(N_\beta - 1) P(\boldsymbol{N} - \boldsymbol{e}_\alpha + \boldsymbol{e}_\beta, t) - r_{\alpha\beta} N_\alpha N_\beta P(\boldsymbol{N}, t) \right) \ . \tag{1.6}$$

In the limit of a large population $N \gg 1$ the ALVE arises as the deterministic dynamics for $x_\alpha = N_\alpha / N$. Allowing also mutation-like reactions

$$\alpha \xrightarrow{s_{\alpha\beta}} \beta \ ,$$

the resulting deterministic equation reads [2]

$$\frac{\mathrm{d}}{\mathrm{d}t} x_\alpha = x_\alpha \sum_{\beta=1}^{S} (r_{\alpha\beta} - r_{\beta\alpha}) x_\beta + \frac{1}{N} \left(\sum_{\beta=1}^{S} s_{\alpha\beta} x_\beta - s_{\beta\alpha} x_\alpha \right) \ .$$

Note that the second term is suppressed by a factor of $1/N$, such that it would play a minor role in a large population. Therefore, the ALVE is the leading order dynamics for

reactions of the kind (1.5) above.
In the context of evolutionary game theory, cyclically dominated reaction schemes built from the motif (1.5) are often analyzed and simulated as spatially extended systems. For example, one assumes that the system consists of well-mixed compartments in which ALVE dynamics takes place. Additionally, agents can diffuse between neighboring compartments, adding a spatial component to the system. In such a setting, cyclic dominance can lead to pattern formation and traveling waves of species [20, 35, 36]. This spatially extended case is not considered in this thesis.

1.3.3 Coarse grained dynamics of driven-dissipative bosons

Also in the context of quantum physics, the ALVE has relevance. When a gas of non-interacting bosons is weakly coupled to a heat bath, applying a time-periodic driving force leads to a behavior of the particles that can be described by a classical stochastic process [37, 38]. The dynamical equation of this system can be achieved by eliminating the heat bath's degrees of freedom (Born-Markov approximation), and applying Floquet's theorem [39]. Off-diagonal matrix elements of the density operator decay to zero, such that on a coarse grained time scale only incoherent, 'classical', dynamics remains.
The transitions of particles can be described by a classical master equation with transition rates $\Gamma_{\alpha\leftarrow\beta}(N_\alpha, N_\beta) = r_{\alpha\beta}(1 + N_\alpha)N_\beta$. The factor $(1 + N_\alpha)$ arises from the commutation relation for bosons that results effectively in an attractivity between particles. As the transitions can be interpreted as reactions of the kind introduced above ($s_{ij} = r_{ij}$), the deterministic behavior of the stochastic process of bosons is described by the ALVE.
In the context of quantum physics, the ALVE is interesting for two reasons: first, on a coarse grained time scale, the quantum particles behave as classical particles, their quantum property only enters in the transition rates; and second, the process shows condensation into multiple states, opposed to a single ground state [38, 40].

1.3.4 Discrete nonlinear wave equations and integrable systems

The ALVE on specific lattices appears as a model system in the context of integrable systems [41]. When the interaction topology is a directed cycle, the ALVE becomes the so-called Volterra lattice (e.g. with periodic boundary conditions $\alpha = \alpha + S$),

$$\frac{\mathrm{d}}{\mathrm{d}t}x_\alpha = x_\alpha(x_{\alpha+1} - x_{\alpha-1}) \,. \tag{1.7}$$

Despite its nonlinearity the Volterra lattice is an integrable system: when considered as an infinite system it has an infinite number of conserved quantities. Analytical solutions in the form of solitary waves can be found using the inverse scattering method [42, 43]. The Volterra lattice is of main interest in mathematical physics for the algebraical properties of its solutions [44, 41], and its interpretation as a discretization of the Korteweg-de Vries equation (KdV) [45, 43], a famously exactly solvable nonlinear partial differential equation [46]. The relation between the Volterra lattice and the KdV equation is of interest

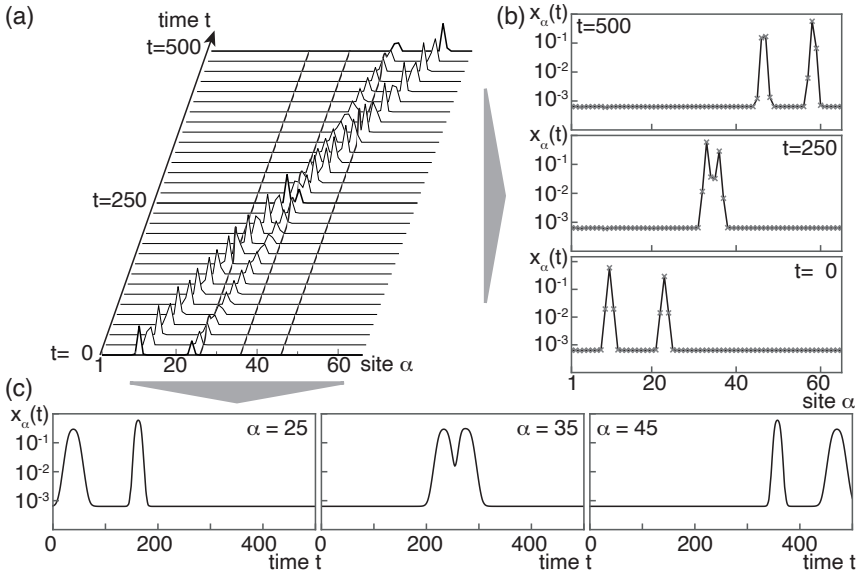

Figure 1.3: Solitons in the Volterra lattice. (a) Two suitably initialized peaks of mass travel with uniform velocity through the periodic Volterra lattice. Their shape is preserved after a collision. The velocity increases with the mass in the peak, as can be seen from $\boldsymbol{x}(t)$ specific time points (b). Each state goes through the same temporal evolution with a shift that depends on the states' index α (c).

when studying if and how exact solutions of nonlinear systems can be recovered in discretized systems. This so-called *integrable discretization* is a relevant theoretical question as numerical simulations include discretization schemes [41]. Although the Volterra lattice is mainly of interest for mathematical physics, it can be derived as an approximation of the interaction of jets in Langmuir oscillations of plasma [47, 42], or as the dynamics of a chain of exponentially coupled beads [45]. Next to the Volterra lattice there are other differential difference equations that can be read as the ALVE on specific lattices, for example the relativistic Toda lattice [48].

Chapter 2

Mathematical properties of the ALVE

This chapter contains definitions and mathematical properties of the ALVE that serve as background information for the main results presented in the second half of this thesis. The methods used in the later work on coexistence networks in Chapter 4 and topological phase transitions in one dimensional chains in Chapters 5 and 6 partially overlap, such that we collected and organized the relevant information of our publications [49, 50] here. In addition, we reproduce the relevant results from the publications [1, 2] and [49] which were direct predecessors and inspiration for the original work of this thesis.

2.1 Definition of the ALVE

The antisymmetric Lotka-Volterra equation is defined for a system of S dynamical variables, which we refer to as states α (or strategies in the context of evolutionary game theory). The concentration or mass in state α is denoted as x_α and the vector of state concentrations is denoted as $\boldsymbol{x}(t) = (x_1(t), \ldots, x_S(t))$. These masses evolve through a system of nonlinearly coupled ordinary differential equations of first order in time:

$$\frac{\mathrm{d}}{\mathrm{d}t} x_\alpha(t) = x_\alpha(t) \sum_{\beta=1}^{S} a_{\alpha\beta} x_\beta(t) \ , \tag{2.1}$$

for all $\alpha = 1, \ldots, S$. The matrix $\{A\}_{\alpha,\beta} = \{a_{\alpha\beta}\} \in \mathbb{R}^{S\times S}$ is *antisymmetric* (or skew-symmetric), that is $a_{\alpha\beta} = -a_{\beta\alpha}$. The vector of initial masses is assumed to be strictly positive and normalized, such that $\boldsymbol{x}(t=0) =: \boldsymbol{x}_0$ lies in the open $(S-1)$-simplex Δ_{S-1} ($x_{0,\alpha} > 0$ for all $\alpha = 1, \ldots, S$ and $\sum_{\alpha=1}^{S} x_{0,\alpha} = 1$). A state with $x_{0,\alpha} = 0$ has zero occupation for all times and thus does not take part in the dynamics. As this has the same effect as deleting the state from the system, and thus changing the network topology, this case is excluded when discussing a the ALVE dynamics on a network topology. For brevity, the time variable t is omitted in most of the following derivations.

The entries $a_{\alpha\beta}$ of the antisymmetric matrix A define the set of control parameters of the ALVE (and define the zero-sum game). They specify how mass is exchanged between the S

states through pairwise interactions. Mass in state α changes through interaction with state β as $a_{\alpha\beta}x_\alpha x_\beta$. A negative matrix entry $a_{\alpha\beta} < 0$ means that mass is transported from state α to β, mass in state x_α is reduced. At the same time β gains this mass through $-a_{\alpha\beta}x_\beta x_\alpha = a_{\beta\alpha}x_\beta x_\alpha$ and $a_{\beta\alpha} > 0$. A vanishing off-diagonal entry $a_{\alpha\beta} = a_{\beta\alpha} = 0$ implies that no mass can be exchanged between states α and β. As mass moves directionally between states, it is convenient to represent the antisymmetric matrix as a directed network. This is achieved by interpreting every positive matrix entry $a_{\alpha\beta} > 0$ as a directed link between the states $\beta \to \alpha$. The direction of the edge is chosen to be aligned with mass flow in the ALVE dynamics. Examples are shown in Figures 1.1 and 1.3. Details of the equivalence between antisymmetric matrices and weighted networks are presented in Section 3.1. Since no interaction besides directed mass transport is defined by the ALVE (2.1), the total mass is conserved over time ($\frac{\mathrm{d}}{\mathrm{d}t}\sum_{\alpha=1}^{S} x_\alpha = 0$). Consequently, the ALVE defines a trajectory bound to the open simplex, that is, $\boldsymbol{x}(t) \in \Delta_{S-1}$ for all times [25]. If the dynamics are initialized on the boundary of the simplex, $\boldsymbol{x}_0 \in \partial\Delta_{S-1} = \overline{\Delta}_{S-1}\backslash\Delta_{S-1}$, they will remain restricted to the boundary.

The natural question about the long-time behavior of a state concentration x_α is whether it remains bounded away from 0, whether it approaches 0, or whether it expresses any other qualitatively different behavior (such as, for example, a heteroclinic orbit). Numerical integrations of the ALVE show that, dependent on the weights of the interaction network, a state concentration either vanishes for long times ($x_\alpha(t) \to 0$ as $t \to \infty$), in which case α is referred to as a *depleted state* ("depletion" or "extinction"), or it remains bounded away from zero for all times ($x_\alpha(t) \geq Const > 0$ for all times t), in which case α is called a *condensate* ("condensation" or "survival") [2]. Examples for both cases are presented in Figures 1.1 and 1.3. In the next Section we prove that the ALVE dynamics shows condensation and extinction by means of a Lyapunov function and the so-called condensate vector, an algebraical property of the antisymmetric matrix A [2].

2.2 The condensate vector and a Lyapunov function for the ALVE

Given an antisymmetric matrix A with real entries, there exist specific vectors $\boldsymbol{c}$, which we refer to as *condensate vectors*, that fulfill the following properties for an unique index set $I \subseteq \{1, \ldots, S\}$:

$$c_\alpha > 0 \text{ and } (A\boldsymbol{c})_\alpha = 0 \,, \quad \text{for all } \alpha \in I \tag{2.2}$$

$$c_\alpha = 0 \text{ and } (A\boldsymbol{c})_\alpha < 0 \,, \quad \text{for all } \alpha \in \bar{I} = \{1, ..., S\}\backslash I. \tag{2.3}$$

A proof of this algebraic property of antisymmetric matrices can be found in the book on linear programming theory by Kuhn and Tucker [51]. Most importantly, although for an antisymmetric matrix A there may be several condensate vectors, the index set of positive entries I is unique for each matrix A, as shown in Section 2.A.

Closely following [2], a connection between the condensate vectors with the long-time dynamics of the ALVE is possible through a Lyapunov function is defined. The Lyapunov has

the form of the Kullback-Leibler divergence (or relative entropy [52]) $D(\boldsymbol{c}||\boldsymbol{x})$ of an arbitrarily chosen condensate vector $\boldsymbol{c}$ of A (fulfilling properties (2.2) and (2.3) and normalized to the simplex, $\sum_\alpha c_\alpha = 1$) to the state concentrations $\boldsymbol{x}(t)$:

$$D(\boldsymbol{c}||\boldsymbol{x}(t)) = \sum_{\substack{\alpha=1 \\ (c_\alpha \neq 0)}}^{S} c_\alpha \log\left(\frac{c_\alpha}{x_\alpha(t)}\right) = \sum_{\alpha\in I} c_\alpha \log\left(\frac{c_\alpha}{x_\alpha(t)}\right) \ . \tag{2.4}$$

The value of $D(\boldsymbol{c}||\boldsymbol{x})$ decreases over time as one computes directly,

$$\frac{\mathrm{d}}{\mathrm{d}t} D(\boldsymbol{c}||\boldsymbol{x}) = \sum_{\alpha\in\bar{I}} (A\boldsymbol{c})_\alpha x_\alpha < 0 \ , \tag{2.5}$$

where it was used that $(A\boldsymbol{c})_\alpha < 0$ for $\alpha \in \bar{I}$ (2.3). As $D(\boldsymbol{c}||\boldsymbol{x})$ has the functional form of a relative entropy, it is positive and bounded [52], such that we can write

$$0 \leq D(\boldsymbol{c}||\boldsymbol{x})(t) = D(\boldsymbol{c}||\boldsymbol{x})(0) + \int_0^t \mathrm{d}s \sum_{\alpha\in\bar{I}} (A\boldsymbol{c})_\alpha x_\alpha(s) \leq D(\boldsymbol{c}||\boldsymbol{x})(0) \ < \infty \ . \tag{2.6}$$

One concludes that all states with index $\alpha \in I$ remain bounded away from 0 for all times, that is, $x_\alpha(t) \geq Const > 0$ for all $\alpha \in I$ and for all t (otherwise, D would diverge in contradiction to the boundedness of D). These states are called *condensates* [2].
For the states that are not condensates, $\alpha \in \bar{I}$, equation 2.6 implies for all t

$$-\int_0^t \mathrm{d}s (A\boldsymbol{c})_\alpha x_\alpha(s) \leq -\int_0^t \mathrm{d}s \sum_{\alpha\in\bar{I}} (A\boldsymbol{c})_\alpha x_\alpha(s) \leq D(\boldsymbol{c}||\boldsymbol{x})(0) \ . \tag{2.7}$$

Especially, this means that the integral over all times is bounded for non-condensate states $\alpha \in \bar{I}$,

$$0 < \int_0^\infty \mathrm{d}s \ x_\alpha(s) \leq \frac{D(\boldsymbol{c}||\boldsymbol{x})(0)}{-(A\boldsymbol{c})_\alpha} \ . \tag{2.8}$$

As additionally the time derivative for all states is bounded ($|\partial_t x_\alpha| = |x_\alpha (A\boldsymbol{x})_\alpha| < \sum_{\alpha\beta} |a_{\alpha\beta}| < \infty$), it follows that all states $\alpha \in \bar{I}$ become depleted, $x_\alpha \to 0$ for $t \to \infty$. We call these states *depleted states* [2].
In total, condensation and depletion in the ALVE (2.1) are determined by an algebraic property of the antisymmetric matrix. The set of condensates I is given by the antisymmetric matrix alone through its condensate vectors. All states with index $\alpha \in I$ become condensates, all states with index $\alpha \in \bar{I}$ become depleted for $t \to \infty$; no other cases can occur for long times. Whether a state is a condensate or becomes depleted is independent of the initial conditions $\boldsymbol{x}_0$ and depends only on the antisymmetric matrix A. However, the Lyapunov function gives no details of the dynamics within the surviving condensate states.

2.2.1 Interpretation of the condensate vector

In the context of the ALVE and its Lyapunov function $D(\boldsymbol{c}||\boldsymbol{x})$ (2.4), the two defining properties (2.2) and (2.3) of the condensate vector can be interpreted as follows: We reorder the rows and columns of A such that $I = \{1, ..., k\}$ and $\bar{I} = \{k+1, ..., S\}$. In this form, the product of the condensate vector with the antisymmetric matrix A is

$$\begin{pmatrix} A_I & A_{I\leftarrow\bar{I}} \\ -A_{I\leftarrow\bar{I}}^T & A_{\bar{I}} \end{pmatrix} \begin{pmatrix} \boldsymbol{c}_I \\ \boldsymbol{c}_{\bar{I}} \end{pmatrix} = \begin{pmatrix} A_I & A_{I\leftarrow\bar{I}} \\ -A_{I\leftarrow\bar{I}}^T & A_{\bar{I}} \end{pmatrix} \begin{pmatrix} \boldsymbol{c}_I \\ 0 \end{pmatrix} = \begin{pmatrix} A_I \boldsymbol{c}_I \\ -A_{I\leftarrow\bar{I}}^T \boldsymbol{c}_I \end{pmatrix} = \begin{pmatrix} 0 \\ -A_{I\leftarrow\bar{I}}^T \boldsymbol{c}_I \end{pmatrix} . \quad (2.9)$$

Here, A_I ($A_{\bar{I}}$) is the submatrix of the index set I ($\bar{I}$), respectively. The matrix $A_{I\leftarrow\bar{I}}$ defines the interactions between condensates I and depleted states $\bar{I}$. In this form, one sees that condition (2.2) implies that the submatrix A_I has a strictly positive kernel vector, $\boldsymbol{c}_I > 0$ with $A_I \boldsymbol{c}_I = 0$. As this condition only influences the set of condensates, I, we call it the *condensate condition*. Condition (2.3) appears in this notation as $\boldsymbol{c}_{\bar{I}} = 0$ and $-A_{I\leftarrow\bar{I}}^T \boldsymbol{c}_I < 0$. This expression ensures that the Lyapunov function decreases over time (2.5), hence we call this condition the *attractivity condition*. As a consequence of the attractivity condition, mass flows from the subsystem of extinct states into the condensate states.
The condensate vector can be identified either by solving a linear programming problem [2], or by finding subsystems with a strictly positive kernel vectors, and check for the attractivity condition. There may exist linearly independent condensate vectors for a given antisymmetric matrix A if the kernel of A_I is high-dimensional. A trivial example for this case occurs when the submatrix A_I is the zero matrix. In this case, all condensates are unconnected and every strictly positive vector is a kernel vector of A_I.

2.2.2 Example: Calculation of the condensate vector for different rates

In order to show how network and rates work together to determine coexistence and extinction in the ALVE dynamics, we present here the mathematical details of the example shown in Figure 1.3 in the Introduction 1.1.
The interaction matrix shown in Figure 1.3 (a) is

$$A_{\text{example}} = \begin{pmatrix} 0 & -1 & 2 & y & 3 \\ 1 & 0 & -1.5 & 0 & 0 \\ -2 & 1.5 & 0 & -0.5 & 0 \\ -y & 0 & 0.5 & 0 & 0 \\ -3 & 0 & 0 & 0 & 0 \end{pmatrix} \quad (2.10)$$

The condensates of the systems in Figure 1.3 are identified by calculating the condensate vector as follows: The numerical integrations predict three different sets of condensates I. For each of these sets I, we can first search for strictly positive kernel vectors of A_I to determine if the condensate condition can be met. If this is the case, checking additionally for the attractivity condition reveals if and for which value of y the condensate set I is assumed by the ALVE dynamics (for simplicity, the condensate vectors are not normalized):

- $I = \{1, 2, 3\}$: For this condensate set, the attractivity condition is fulfilled when $0 > 0.5 - 1.5y$:

$$A_{\text{example}} \cdot \boldsymbol{c}^{(i)} = \begin{pmatrix} 0 & -1 & 2 & y & 3 \\ 1 & 0 & -1.5 & 0 & 0 \\ -2 & 1.5 & 0 & -0.5 & 0 \\ -y & 0 & 0.5 & 0 & 0 \\ -3 & 0 & 0 & 0 & 0 \end{pmatrix} \begin{pmatrix} 1.5 \\ 2 \\ 1 \\ 0 \\ 0 \end{pmatrix} = \begin{pmatrix} 0 \\ 0 \\ 0 \\ 0.5{-}1.5y \\ -1.5{\cdot}3 \end{pmatrix}. \tag{2.11}$$

  Note that as the subsystem $\{1, 2, 3\}$ always has a unique strictly positive kernel vector, the condensate condition is always fulfilled. However, the value y restricts when the attractivity condition applies. The vector $\boldsymbol{c}^{(i)}$ is only a condensate vector for $A_{example}$ when $0 > 0.5 - 1.5y$.

- $I = \{1, 2, 3, 4\}$: The submatrix A_I of this condensate set only fulfills the condensate condition when $1.5y - 0.5 = 0$:

$$A_{\text{example}} \cdot \boldsymbol{c}^{(ii)} = \begin{pmatrix} 0 & -1 & 2 & y & 3 \\ 1 & 0 & -1.5 & 0 & 0 \\ -2 & 1.5 & 0 & -0.5 & 0 \\ -y & 0 & 0.5 & 0 & 0 \\ -3 & 0 & 0 & 0 & 0 \end{pmatrix} \begin{pmatrix} 0.5 \\ 0.5a_1 \\ y \\ 1.5a_1{-}2 \\ 0 \end{pmatrix} = \begin{pmatrix} a_1(1.5y{-}0.5) \\ 0.5{-}1.5y \\ 0 \\ 0 \\ -1.5 \end{pmatrix}. \tag{2.12}$$

  The attractivity condition is always fulfilled for $\boldsymbol{c}^{(ii)}$. However, the condensate condition requires that A_I has a strictly positive kernel vector. In the above form, this is the case when $1.5y - 0.5 = 0$ (A_I has a kernel vector) and $1.5a_1 - 2 > 0$ (the kernel vector is strictly positive). As a_1 can be chose freely, this restriction can always be met, and the condensate vector is not unique.

- $I = \{2, 4, 5\}$: For this set of condensates, the submatrix of condensates is the zero matrix, $A_I = 0$. As every strictly positive vector is a kernel vector of this matrix, the condensate condition is always fulfilled. The selection of this condensate set thus only depends on the attractivity condition, which can only be met when $0.5 - 1.5y > 0$:

$$A_{\text{example}} \cdot \boldsymbol{c}^{(iii)} = \begin{pmatrix} 0 & -1 & 2 & y & 3 \\ 1 & 0 & -1.5 & 0 & 0 \\ -2 & 1.5 & 0 & -0.5 & 0 \\ -y & 0 & 0.5 & 0 & 0 \\ -3 & 0 & 0 & 0 & 0 \end{pmatrix} \begin{pmatrix} 0 \\ 1 \\ 0 \\ a_1 \\ a_2 \end{pmatrix} = \begin{pmatrix} -1{+}a_1y{+}3a_2 \\ 0 \\ 1.5{-}0.5a_1 \\ 0 \\ 0 \end{pmatrix}. \tag{2.13}$$

  The condensation condition is fulfilled for every $a_1, a_2 > 0$. To additionally fulfill the attractivity condition, we need $-1 + a_1y + 3a_2 < 0$ and $1.5 - 0.5a_1 < 0$, putting a constraint on the two variables a_1, a_2. Substituting $1.5/0.5 < a_1$ in the first inequality, we find $-(0.5 - 1.5y) + 1.5a_2 < 0$, which is solvable when $0.5 - 1.5y > 0$. Thus, $\boldsymbol{c}^{(iii)}$ is a condensate vector when $1.5y - 0.5 > 0$. As, apart from the two restrictions of the inequalities, the values a_1 and a_2 can be chosen arbitrarily, the condensate vector is not unique.

From the previous section 2.2 we know that the condensate vector defines the unique set of condensates that survive in the ALVE dynamics. The above discussion of the three condensate sets I shows that the observations from the numerical integrations in Figure 1.3 can be made rigorous: For each of the three outcomes I, a condensate vector exists for suiting values of the rate y. Or, reversing the logic, the value of the expression $(0.5{-}1.5{\cdot}y) \gtreqless 0$ decides which set of condensates is chosen in the ALVE dynamics.

2.3 Coexistence of all states

After the initial extinction process, every ALVE dynamics ends up in the subsystem made up from the condensates. The interactions between the condensates and thus the dynamics after depletion depends on A_I. The condensation condition (2.2) requires that A_I has one or several strictly positive kernel vectors. In the following we show that this argument can be reversed: When the interaction matrix A has a strictly positive kernel vector, all states survive for all times and there is no extinction.

Let $\boldsymbol{p}$ be an element of the kernel of A. Then the Kullback-Leibler divergence (2.4) of the kernel element $\boldsymbol{p}$ to the trajectory $\boldsymbol{x}$,

$$D(\boldsymbol{p}||\boldsymbol{x}(t)) = \sum_{\substack{\alpha=1 \\ (p_\alpha \neq 0)}}^{S} p_\alpha \log\left(\frac{|p_\alpha|}{x_\alpha(t)}\right) = const. - \sum_{\substack{\alpha=1 \\ (p_\alpha \neq 0)}}^{S} p_\alpha \log\left(x_\alpha(t)\right) \ , \tag{2.14}$$

is conserved under the dynamics of the ALVE (2.1) due to the antisymmetry of matrix A,

$$\frac{\mathrm{d}}{\mathrm{d}t} D(\boldsymbol{p}||\boldsymbol{x}) = \sum_{\alpha} (A\boldsymbol{p})_\alpha x_\alpha = 0 \ . \tag{2.15}$$

Furthermore, when the kernel of A is degenerate, that is there exist several linear independent kernel vectors, each kernel element gives rise to a conserved quantity of the form (2.14), and the dimension of the kernel, $\dim(\mathrm{Ker}(A))$, determines how many such conserved quantities of form D exist; see [1] for details. If the kernel of A contains a strictly positive kernel element, $\boldsymbol{p} > 0$, the relative entropy (2.14) is conserved and positive for all times: $0 < D(\boldsymbol{p}||\boldsymbol{x}(t)) = D(\boldsymbol{p}||\boldsymbol{x}(0)) < \infty$. Thus, none of the state concentrations vanishes (otherwise, D would diverge in contradiction to the boundedness of D). In other words, if the kernel of A is strictly positive, all states coexist.

2.4 Characterization of the stationary state

If we are interested in the long-term dynamics of the ALVE, we must find a better understanding of how strictly positive kernel elements influence the dynamics. Here, progress is possible when the strictly positive kernel vector is unique, that is the kernel of A is one-dimensional. In the following we assume that A has a unique strictly positive kernel vector $\boldsymbol{c}$ upon normalization ($c_\alpha > 0$ for all α and $A\boldsymbol{c} = \boldsymbol{0}$, $\sum_\alpha c_\alpha = 1$, if not stated otherwise we sum over all states).

This vector $\boldsymbol{c}$ characterizes the long-time behavior of the ALVE, as can be seen from the following three statements proven below: (1) The masses in all sites of the RPS chain remain bounded away from 0 in the stationary state (none of the sites becomes depleted), (2) average masses in the stationary state are given by the strictly positive kernel vector $\boldsymbol{c}$ of A, and (3) fluctuations of masses in the stationary state are determined by $\boldsymbol{c}$ as well.

(1) The masses in all sites remain bounded away from 0. As shown in Section 2.3, from the strictly positive kernel vector we can deduce that all states of the ALVE are condensates and no state goes extinct. Additionally, the Kullback-Leibler divergence of the kernel vector to the masses $\boldsymbol{x}$, $D(\boldsymbol{c}||\boldsymbol{x})$ (2.4), is a conserved quantity of the ALVE.

(2) Average masses in the stationary state are given by the kernel vector c of A. Let us define the temporal average of the masses, $\langle x_\alpha \rangle_T := 1/T \int_0^T \mathrm{d}t\ x_\alpha$, and consider the quantity $\langle \partial_t \log(x_\alpha) \rangle_T$. On the one hand,

$$1/T \int_0^T \mathrm{d}t\ \partial_t \log(x_\alpha) = \frac{1}{T}(\log(x_\alpha)(T) - \log(x_\alpha)(0)) \xrightarrow{T\to\infty} 0\ , \tag{2.16}$$

and the convergence to 0 follows because $\log(x_\alpha)(T)$ is bounded, but $1/T$ converges to 0 as $T \to \infty$. On the other hand, employing Eq. (2.1) yields,

$$1/T \int_0^T \mathrm{d}t\ \partial_t \log(x_\alpha) = \sum_\beta a_{\alpha\beta} \langle x_\beta \rangle_T\ , \tag{2.17}$$

and, thus, $\langle \boldsymbol{x} \rangle_T$ converges to the kernel of A as $T \to \infty$. Because, $\boldsymbol{c}$ spans the kernel of A, the average masses in the stationary state are given by this kernel vector, that is, $\langle x_\alpha \rangle_\infty = c_\alpha$ for all initial conditions $x_\alpha(0) > 0$ for all α.
Additionally, when strictly positive, the condensate vector $\boldsymbol{c}$ is the unique fixed point $\boldsymbol{x}^*$ of the dynamics. When initialized at the fixed point, no dynamics of the ALVE takes place, $\partial_t \boldsymbol{x}^* = 0$. Thus, the temporal average of the ALVE dynamics approaches the stationary state, while the trajectory itself remains dynamic for all times, see also Figure 1.1.

(3) Fluctuations of masses in the stationary state are determined by the kernel vector c of A. In a similar manner as for the average masses, let us consider the quantity $\langle \partial_t x_\alpha \rangle_T$. On the one hand,

$$1/T \int_0^T \mathrm{d}t\ \partial_t x_\alpha = \frac{1}{T}(x_\alpha(T) - x_\alpha(0)) \xrightarrow{T\to\infty} 0\ . \tag{2.18}$$

On the other hand, upon employing the ALVE (2.1),

$$1/T \int_0^T \mathrm{d}t\ \partial_t x_\alpha = \sum_\beta a_{\alpha\beta} \langle x_\alpha x_\beta \rangle_T\ , \tag{2.19}$$

In other words, $\{\langle x_\alpha x_\beta \rangle_T\}_\beta$ as a function of β lies in the kernel of A as $T \to \infty$. Thus, $\langle x_\alpha x_\beta \rangle_\infty = const(\alpha) \cdot c_\beta$ for $\beta \neq \alpha$ with $\boldsymbol{c}$ again denoting the strictly positive kernel vector of A. With the same arguments one obtains $\langle x_\alpha x_\beta \rangle_T = const(\beta) \cdot c_\alpha$ for $\alpha \neq \beta$ and, thus, $\langle x_\alpha x_\beta \rangle_T \to const \cdot c_\alpha c_\beta$ as $T \to \infty$ for all $\alpha \neq \beta$. To compute the second moment of the

mass in the stationary state, $\langle x_\alpha^2\rangle_T \to \langle x_\alpha^2\rangle_\infty$ as $T \to \infty$, we exploit the normalization $\sum_\alpha x_\alpha = 1$ as follows:

$$\langle x_\alpha^2\rangle_T = \langle x_\alpha(1 - \sum_{\beta\neq\alpha} x_\beta)\rangle_T = \langle x_\alpha\rangle_T - \sum_{\beta\neq\alpha}\langle x_\alpha x_\beta\rangle_T \tag{2.20}$$

and, hence, in the stationary state $\langle x_\alpha^2\rangle_\infty = c_\alpha - const\cdot c_\alpha \sum_{\alpha\neq\beta} c_\beta$. By exploiting normalization $\sum_{\alpha\neq\beta} c_\beta = (1 - c_\alpha)$, the stationary second moment is written as

$$\langle x_\alpha^2\rangle_\infty = const\cdot c_\alpha^2 + (1 - const)c_\alpha \tag{2.21}$$

Consequently, the stationary state fluctuations ($\mathrm{Var}(x_\alpha)_\infty = \langle x_\alpha^2\rangle_\infty - \langle x_\alpha\rangle_\infty^2$) at site α are quantified as,

$$\mathrm{Var}(x_\alpha)_\infty = \sigma_{\alpha,\infty}^2 = (1 - const)c_\alpha(1 - c_\alpha)\ . \tag{2.22}$$

For completeness, the stationary correlations, $\mathrm{Corr}(\alpha,\beta)_\infty = \langle x_\alpha x_\beta\rangle_\infty - \langle x_\alpha\rangle_\infty\langle x_\beta\rangle_\infty$, between sites α and β are obtained as,

$$\mathrm{Corr}(\alpha,\beta)_\infty = -(1 - const)c_\alpha c_\beta\ . \tag{2.23}$$

Using the same method, also higher order correlations can be related to the unique strictly positive kernel vector. Considering $\langle\partial_t x_\alpha^k\rangle_T$ with $k \in \mathbb{N}^+$ is a positive integer, we find

$$1/T\int_0^T \mathrm{d}t\ \partial_t x_\alpha^k = \sum_\beta a_{\alpha\beta}\langle x_\alpha^k x_\beta\rangle_T \xrightarrow{T\to\infty} 0\ , \tag{2.24}$$

$$\Rightarrow \langle x_\alpha^k x_\beta\rangle_\infty = K_\alpha^k c_\beta\ . \tag{2.25}$$

Here, K_α^k is a constant.
Again, as the vector $\boldsymbol{x}$ lies in the simplex, performing the sum over β yields

$$\langle x_\alpha^{k+1}\rangle_\infty = \langle x_\alpha^k(1 - \sum_{\beta\neq\alpha} x_\beta)\rangle_\infty = \langle x_\alpha^k\rangle_\infty - K_\alpha^k(1 - c_\alpha)\ . \tag{2.26}$$

This results in a hierarchy of the correlations,

$$\langle x_\alpha^{k+1}\rangle_\infty = \langle x_\alpha^k\rangle_T + K_\alpha^k(c_\alpha - 1) \tag{2.27}$$

$$\Rightarrow \langle x_\alpha^{k+1}\rangle_\infty = c_\alpha + (1 - c_\alpha)\sum_{l=2}^{k} K_\alpha^l \tag{2.28}$$

In the last line, the hierarchy was repeatedly applied down to the known value $\langle x_\alpha\rangle_\infty = c_\alpha$. So far it is unclear how to obtain the constants K_α^l.

Note that all these derivations strongly depend on the uniqueness of the strictly positive kernel vector. When there is a continuum of strictly positive kernel vectors, only statement (1) remains.

2.A The index set of positive entries of the condensate vector is unique to an real, antisymmetric matrix

Here we show that although a real, antisymmetric matrix may have several condensate vectors, the index set of positive entries is unique. This property follows from the defining properties of the condensate vector, (2.2) and (2.3). We proof the assumption by contradiction:
Assume there is another condensate vector $\tilde{\boldsymbol{c}}$, satisfying condition (2.3) for an index set J that differs from I, such that $J \bigcap \bar{I} \neq \emptyset$. Then for any $\alpha \in J \bigcap \bar{I}$ we find

$$0 = c_\alpha (\mathbf{A}\tilde{\boldsymbol{c}})_\alpha \geq \sum_i \underbrace{c_\alpha}_{\geq 0} \underbrace{(\mathbf{A}\tilde{\boldsymbol{c}})_\alpha}_{\leq 0} = -\sum_\alpha \tilde{c}_\alpha (\mathbf{A}\boldsymbol{c})_\alpha = -\sum_{\alpha \in J \bigcap \bar{I}} \underbrace{\tilde{c}_\alpha}_{>0} \underbrace{(\mathbf{A}\boldsymbol{c})_\alpha}_{<0} > 0 \,, \tag{2.29}$$

which contradicts the assumption. For the case $\bar{J} \bigcap I \neq \emptyset$ the same argument leads to a contradiction as well, therefore the index set is unique.

Chapter 3

Networks and real antisymmetric Matrices

So far we have shown that the antisymmetric matrix that defines the coupling of the ALVE plays the central role in the ALVE dynamics. The condensate vector of an antisymmetric matrix defines which states become condensates. When the interaction matrix has a strictly positive kernel vector it is a condensate vector, and all states are condensates. Furthermore, if the strictly positive kernel vector is unique, it contains information about the long-time behavior of the system.
In this section we introduce basic properties of real antisymmetric matrices and their representation as weighted networks. This allows us to connect the kernel of an antisymmetric matrices to its network topological properties. As robustness of long-time behavior of the ALVE is the main focus of this thesis, the characterization of strictly positive kernel vectors through network topology plays a major role for the later results.

3.1 Antisymmetric matrices are equivalent to weighted networks

For our analysis of topological robustness and coexistence networks, we interpret the real antisymmetric matrix A as the antisymmetric adjacency matrix of a weighted network (also referred to as the skew-adjacency matrix of a weighted directed graph) as shown in Figures 1.3, 1.1 and Figure 3.1 (a). States in the ALVE correspond to nodes of the weighted network, and entries of the antisymmetric matrix A characterize the links between nodes. This mapping to a network enables us to separate the discussion of the network topology (direction of links) from the weights of the network (weights of links).

In general, a *network* (or directed graph) $\mathcal{N}$ consists of a set of (labeled) nodes (or vertices) $V(\mathcal{N}) = \{1, ..., S\}$ and a set of links (or edges) $E(\mathcal{N}) = \{(1 \to 2), \dots, (\alpha \to \beta), \dots\}$, each of which connects two nodes [53]. In a *weighted network*, each directed edge additionally has a (real positive) weight. Every antisymmetric matrix $A \in \mathbb{R}^{S\times S}$ can be

interpreted as weighted network $\mathcal{N}(A)$ (also called a weighted directed graph) of size S and with vertex-set $V(\mathcal{N}(A)) = \{1, ..., S\}$. In the following, we drop the prefix ('weighted') for simplicity. The weighted edge set of $\mathcal{N}(A)$ is obtained from the positive matrix entries. A nonzero entry of A indicates an edge, its sign the direction and its magnitude the edge weight. The matrix entry $a_{\beta\alpha} > 0$ translates to the edge $\alpha \to \beta$ with edge weight $w(\alpha \to \beta) \coloneqq a_{\beta\alpha}$, see Figure 3.1 (a). As A is antisymmetric, changing the sign of a matrix entry effectively reverses the direction of the corresponding edge while keeping the weight. If $a_{\alpha\beta} = a_{\beta\alpha} = 0$, nodes α and β are not connected. Naturally, two nodes are connected by at most one link and self-loops do not appear, such that we deal with simple networks here. The *network topology* of A is recovered by discarding the weights of the links, but keeping their direction. In other words, the network topology is the oriented graph without the weights.

Conversely, from a simple, weighted network $\mathcal{N}$ with S nodes, the antisymmetric adjacency matrix $A(\mathcal{N}) \in \mathbb{R}^{S\times S}$ is obtained by defining for every edge $\alpha \to \beta$ with weight $a_{\beta\alpha} > 0$ the matrix entries $A(\mathcal{N})_{\beta\alpha} = -A(\mathcal{N})_{\alpha\beta} = a_{\beta\alpha}$. Unconnected nodes are translated to zero entries in the matrix. Thus, the sign of an entry in the adjacency matrix translates to the direction of the edge (positive weight for incoming link, negative for outgoing link), and the absolute value denotes the magnitude of the weight.

Due to this equivalence in representation of real, antisymmetric matrices and networks, we use the terms interchangeably depending on the context.

3.2 Spectral properties of real antisymmetric matrices

For the analysis of the ALVE on a network, especially the kernel (or null space) is of great importance. In this Section, we collect some basic properties of antisymmetric matrices $A = -A^T \in \mathbb{R}^{S\times S}$ for later reference.

The antisymmetry of A restricts its spectral properties: The non-zero eigenvalues of A always occur as pairs of purely imaginary complex conjugate numbers, $\lambda = -\bar{\lambda}$, as can be seen from the scalar product of the eigenvector $A\boldsymbol{v} = \lambda\boldsymbol{v}$:

$$\langle \boldsymbol{v}, (A\boldsymbol{v})\rangle = \sum_{\alpha,\beta} \bar{v}_\alpha a_{\alpha\beta} v_\beta = \lambda\langle \boldsymbol{v}, \boldsymbol{v}\rangle = \lambda \ ,$$

$$\text{also, } \langle \boldsymbol{v}, (A\boldsymbol{v})\rangle = \overline{(-A\boldsymbol{v})}^T \boldsymbol{v} = -\bar{\lambda}\langle \boldsymbol{v}, \boldsymbol{v}\rangle = -\bar{\lambda} \ .$$

Especially, this implies that for the real matrix A both eigenvalues and eigenvectors are complex. The symmetry in the eigenvalues imposes a symmetry of the eigenvectors as well. Considering eigenvector and -value $\{\boldsymbol{v}, \lambda\}$, for its complex conjugate we find $A\bar{\boldsymbol{v}} = -\lambda\bar{\boldsymbol{v}}$, and thus a new pair of eigenvector and eigenvalue, $\{\bar{\boldsymbol{v}}, -\lambda\}$.
The real and imaginary part of an eigenvector $\boldsymbol{v} = \boldsymbol{s} + i\boldsymbol{t}$, are orthogonal, and A maps them onto each other, $A\boldsymbol{s} = -\mathrm{Im}(\lambda)\boldsymbol{t}$ and $A\boldsymbol{t} = \mathrm{Im}(\lambda)\boldsymbol{s}$ (for details see Section 3.A). The vectors $\boldsymbol{s}$ and $\boldsymbol{t}$ can be understood as conjugated generalized purely real eigenvectors. In other words, the antisymmetric matrix A divides the space of its image in two-dimensional subspaces, and A maps the base vectors of these subspaces onto each other.

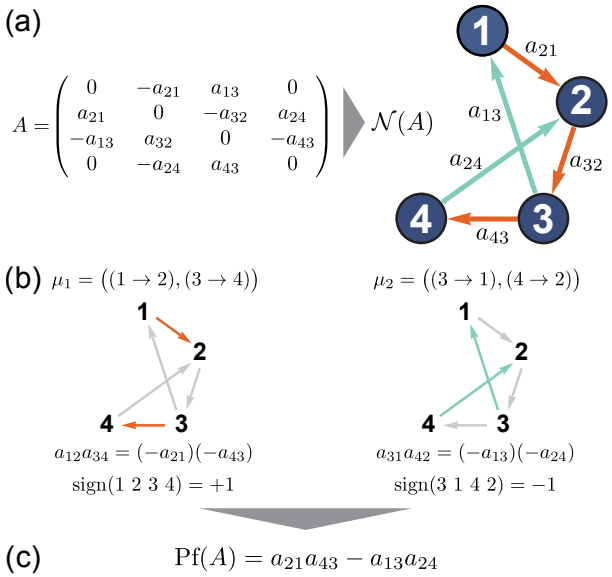

Figure 3.1: Graph-theoretical definition of the Pfaffian. (a) The antisymmetric matrix A and the corresponding, pretzel-like, weighted network $\mathcal{N}(A)$. (b) $\mathcal{N}(A)$ has two perfect matchings, $\mu_1 = \big((1 \to 2), (3 \to 4)\big)$ and $\mu_2 = \big((3 \to 1), (4 \to 2)\big)$. Each of the perfect matchings gives rise to a summand in the Pfaffian of A. Note that the graph-theoretical definition of the Pfaffian only includes negative matrix entries. Thus, the difference of the signs of the two summands arises from the network topology (via the permutations of the respective perfect matchings). The sign of a perfect matching depends on the number of transpositions needed to permute the indices of the matching's partition to the ordered partition $(1, 2, 3, 4)$. (c) The Pfaffian of A is the sum over the contributions stemming from all perfect matchings; see Equation (3.2). All signs in the final sum of the graph-theoretical definition of the Pfaffian are determined by the network topology alone.

From the conjugated eigenvectors, a unitary matrix $T^T T = 1$ can be constructed, which block diagonalizes A,

$$T^T A T = \begin{pmatrix} 0 & \lambda^1 & \dots & 0 & 0 & 0 & \dots & 0 \\ -\lambda^1 & 0 & \dots & 0 & 0 & 0 & \dots & 0 \\ \vdots & \vdots & \vdots & \vdots & \vdots & \vdots & \vdots & \vdots \\ 0 & 0 & \dots & 0 & \lambda^k & 0 & \dots & 0 \\ 0 & 0 & \dots & -\lambda^k & 0 & 0 & \dots & 0 \\ 0 & 0 & \dots & 0 & 0 & 0 & \dots & 0 \\ \vdots & \vdots & \vdots & \vdots & \vdots & \vdots & \vdots & \vdots \\ 0 & 0 & \dots & 0 & 0 & 0 & \dots & 0 \end{pmatrix},$$

see also Section 3.A.3.

The above analysis already shows that the image of a real antisymmetric matrix must be even dimensional. Consequently, the kernel (or nullspace) of an odd-sized antisymmetric matrix must be odd-dimensional. We refer to the kernel of an antisymmetric matrix as *degenerate* if the kernel dimension is greater than the minimal value 1 ($\dim(\mathrm{Ker}(A)) \geq 2$). These spectral properties also reflect in the determinant. When S is odd, its determinant is zero, $\mathrm{Det}(A) = \mathrm{Det}(-A^T) = (-1)^S \mathrm{Det}(A) = 0$. When A has no kernel vector, i.e., its

kernel is trivial, the determinant is the product of pairs of complex conjugated numbers, so $\mathrm{Det}(A) > 0$. For antisymmetric matrices, there is a determinant-like function called the *Pfaffian*, which we discuss in the next section.

3.3 The Pfaffian

The Pfaffian can be thought of as a determinant-like function tailored to antisymmetric matrices. The square of the Pfaffian of A equals its determinant, $\mathrm{Pf}(A)^2 = \mathrm{Det}(A)$ [54, 55, 56], indicating that the Pfaffian of an antisymmetric matrix can carry a sign as opposed to its determinant. As the determinant, the Pfaffian of odd sized matrices is always zero.

For even sized antisymmetric matrices, $S = 2n$, the Pfaffian is typically defined through a combinatorial formula

$$\mathrm{Pf}(A) \coloneqq \sum_{\gamma\in\Pi} \left(\mathrm{sign}(\sigma_\gamma) \prod_{k=1}^{n} a_{\gamma_k} \right), \tag{3.1}$$

where Π is the set of all partitions of $\{1, 2, \ldots, S = 2n\}$ into ordered pairs, for details see Section 3.B.1.
An intuitive understanding of the Pfaffian that is better suited for our purposes is obtained via the weighted network $\mathcal{N}(A)$ by considering all of its perfect matchings. This graph-theoretical interpretation of the Pfaffian presented in Section 3.3.2 has already been appreciated and applied in statistical physics to compute the entropy of systems in which dimer molecules are placed on regular lattice graphs [57, 58, 59, 60, 61]. The graph theoretical interpretation of the Pfaffian of A is based on perfect matchings of $\mathcal{N}(A)$ which we introduce next.

3.3.1 Perfect Matchings, near-perfect matchings, and factor-critical networks.

A *matching* of a network is a subset of its edge set $E' \subseteq E$ such that no two edges in E' share the same node. In other words, every node is covered by at most one edge of the matching E'. A matching that covers all nodes of a network is referred to as a *perfect matching* μ of a network [53]; see Figure 3.1(b). Consequently, the number of nodes in a network with a perfect matching is even. Because a perfect matching is a subset of the network's edges such that every node is covered exactly once, it can be interpreted as a partition of the set $\{1, ..., S = 2n\}$ into pairs. For networks with an odd number of nodes, one introduces the notion of a *near-perfect matching*, which is a matching that covers all but one node. Thus, a near-perfect matching of a network is a perfect matching of a subnetwork that is obtained by deleting one node from the network. An odd-sized network is called *factor-critical* if there exists a perfect matching for every subnetwork that is created by deleting one node from the network [53]; the simplest example of a factor critical network is a cycle of odd length, such as the RPS cycle in Figure 1.1. Adding edges

can only increase the number of near-perfect matchings, such that all networks obtained by adding edges to a cycle of odd length are also factor critical, for example see Figure 4.2(a).

3.3.2 Graph-theoretical definition of the Pfaffian.

The Pfaffian of an antisymmetric matrix A can be calculated via all perfect matchings of the network $\mathcal{N}(A)$. Here we follow the convention that a network's link $\alpha \to \beta$ gives rise to (a) the pair (α, β) in the partition corresponding to the perfect matching μ and to (b) the *negative* matrix entry $a_{\alpha\beta} < 0$. With these two conventions, the Pfaffian of the antisymmetric matrix A is computed as:

$$\mathrm{Pf}(A) = \sum_{\substack{\text{perf. match.} \\ \mu \in \mathcal{N}(A)}} \left(\mathrm{sign}(\sigma_\mu) \prod_{(\alpha\to\beta)\in\mu} a_{\alpha\beta} \right) , \tag{3.2}$$

in which the sum runs over all perfect matchings of the network $\mathcal{N}(A)$; see Figure 3.1. Thus, the Pfaffian is a sum over signed products of negative matrix entries, which are determined by the edges of each perfect matching. The permutation σ_μ denotes the partition of the node set $\{1, 2, \ldots, S = 2n\}$ obtained from the edges in the perfect matching μ:

$$\begin{aligned} \sigma_\mu &= \begin{pmatrix} 1 & 2 & 3 & 4 & \ldots & 2n-1 & 2n \\ (i_1, & j_1) & (i_2, & j_2) & \ldots & (i_n, & j_n) \end{pmatrix} , \\ &\equiv \begin{pmatrix} i_1 & j_1 & i_2 & j_2 & \ldots i_n & j_n \end{pmatrix} . \end{aligned}$$

$\mathrm{sign}(\sigma_\mu)$ is determined by the number of transpositions needed to permute the partition $(i_1, j_1, i_2, j_2, \ldots, i_n, j_n)$ into the partition $(1, 2, \ldots, S = 2n)$: $\mathrm{sign}(\sigma_\mu) = +1$ if the number of transpositions is even, and $\mathrm{sign}(\sigma_\mu) = -1$ if it is odd. For simplicity, we refer to $\mathrm{sign}(\sigma_\mu)$ as the sign of the perfect matching μ. In Section 3.B.2 we discuss why this graph-theoretical definition agrees with the "standard" (combinatorial) definition of the Pfaffian (3.1).

In direct comparison, the graph theoretical definition (3.2) has two main advantages over the combinatorial definition of the Pfaffian (3.1): By utilizing perfect matchings, the graph theoretical definition of the Pfaffian excludes all summands that contain matrix elements that are zero, thus reducing the number of terms in the Pfaffian to the relevant ones. The inclusion of the orientation of the edges allows to separate the sign of a summand from the matrix entries. As by definition (3.2) only negative entries enter each summand, the overall sign of a summand is solely provided by the sign of the permutation.

Example of the Pfaffian for a pretzel-like network. To illustrate the graph-theoretical definition of the Pfaffian, consider the pretzel-like interaction network sketched in Figure 3.1, whose antisymmetric adjacency matrix is:

$$A_{\text{pretzel}} = \begin{pmatrix} 0 & -a_{21} & a_{13} & 0 \\ a_{21} & 0 & -a_{32} & a_{24} \\ -a_{13} & a_{32} & 0 & -a_{43} \\ 0 & -a_{24} & a_{43} & 0 \end{pmatrix} . \tag{3.3}$$

There exist two perfect matchings of this network: $\mu_1 = \big((1 \to 2), (3 \to 4)\big)$ and $\mu_2 = \big((3 \to 1), (4 \to 2)\big)$ and the Pfaffian of A_{pretzel} is obtained via definition (3.2) as:

$$\begin{aligned} \text{Pf}(A_{\text{pretzel}}) &= \text{sign}(1\ 2\ 3\ 4)a_{12}a_{34} + \text{sign}(3\ 1\ 4\ 2)a_{31}a_{42}\ , \\ &= (+1)(-a_{21})(-a_{43}) + (-1)(-a_{13})(-a_{24})\ , \\ &= a_{21}a_{43} - a_{13}a_{24}\ . \end{aligned} \tag{3.4}$$

The kernel of A_{pretzel} is only nontrivial if the matrix entries of A_{pretzel} fulfill $\text{Pf}(A_{\text{pretzel}}) = a_{21}a_{43} - a_{13}a_{24} = 0$, that is, for a fine-tuned choice of weights.

3.3.3 Adjugate vector and adjugate matrix

By using the notion of the Pfaffian of an antisymmetric matrix A, an explicit analytical expression for the kernel of A is obtained for odd-sized matrices with kernel dimension 1 and even-sized matrices with kernel dimension 2 via the adjugate vector or the adjugate matrix of A, respectively [62].

The adjugate vector of A. If S is odd, the kernel of an antisymmetric matrix $A \in \mathbb{R}^{S\times S}$ is characterized by the *adjugate vector* $\boldsymbol{r} \in \mathbb{R}^S$ [63], which is defined as:

$$r_\alpha = (-1)^{\alpha+1}\text{Pf}(A_{\hat{\alpha}}) \quad ,\ \alpha = 1, \ldots, S\ . \tag{3.5}$$

Here, $A_{\hat{\alpha}}$ denotes the matrix obtained by deleting the αth row and column from A, or equivalently the network obtained by deleting the node α from $\mathcal{N}(A)$. The computation of the adjugate vector (3.5) via the Pfaffians of all submatrices $A_{\hat{i}}$ is reminiscent of Cramer's rule [63] adjusted to antisymmetric matrices. The adjugate vector is, thus, determined by all near-perfect matchings of $\mathcal{N}(A)$. The adjugate vector is a kernel vector of A if $\dim(\text{Ker}(A)) = 1$ and the zero-vector $\boldsymbol{r} = 0$ if $\dim(\text{Ker}(A)) = 3, 5, \cdots, S$ [62]. In any case, it is $A\boldsymbol{r} = 0$.

Example: The adjugate vector of an odd-sized cycle. With the graph-theoretical definition of the Pfaffian (3.2) we can compute the adjugate vector of an odd cycle as follows: The antisymmetric adjacency matrix of an odd cycle with S states, $A_{\text{odd-cycle}}$, reads

$$A_{\text{odd-cycle}} = \begin{pmatrix} 0 & -a_{21} & 0 & \ldots & a_{1,S} \\ a_{21} & 0 & -a_{32} & \ldots & 0 \\ \vdots & \ddots & \ddots & \ddots & \vdots \\ 0 & 0 & \ldots & 0 & -a_{S,S-1} \\ -a_{1,S} & 0 & \ldots & a_{S,S-1} & 0 \end{pmatrix}\ . \tag{3.6}$$

Every subnetwork of the odd cycle created by deleting one node is a path of length $S-1$ and thus has exactly one perfect matching. Consequently every component of the adjugate

vector consists of one product of matrix elements. All edges of the odd cycle connect nodes with different parity, apart from the edge $S \to 1$. Only when this edge $S \to 1$ is part of a near-perfect matching, the elements in the permutation of the near-perfect matching are not ordered in size, which is the case whenever an even node is deleted.

(i) α *even.* For example, the near-perfect matching upon deleting node 2 is $\mu_{\text{even}} = ((S \to 1), (3 \to 4), \ldots, (S-2 \to S-1))$. To order the corresponding permutation in size, one may shift the index S from the first to the last position by applying $S-2$ transpositions. Thus, $\text{sign}(\mu_{\text{even}}) = -1$. Therefore, for even α, the component of the adjugate vector, r_α, is obtained as (recall that $S = 2n+1$ here is odd):

$$\begin{aligned} r_\alpha &= (-1)^{1+\alpha}\text{sign}(\mu_{\text{even}})(-a_{1,S})(-a_{32})\ldots(-a_{\alpha-1,\alpha-2})(-a_{\alpha+2,\alpha+1})\ldots(-a_{S-1,S-2}) \ , \\ &= (-1)(-1)(-1)^{n \bmod 2} a_{1,S}a_{32}\ldots a_{\alpha-1,\alpha-2}a_{\alpha+2,\alpha+1}\ldots a_{S-1,S-2} \ . \end{aligned} \tag{3.7}$$

(ii) α *odd.* If, on the other hand, an odd node is deleted, an equal number of even and odd nodes remain in the network such that every edge of a perfect matching connects an even and an odd node. The edge $S \to 1$ is not part of the perfect matching μ_{odd} and, thus, the elements of the corresponding permutation are ordered in size, yielding the sign $+1$ for the permutation. Consequently, for odd i the adjugate vector is obtained as:

$$\begin{aligned} r_\alpha &= (-1)^{\alpha+1}\text{sign}(\mu_{\text{odd}})(-a_{21})(-a_{43})\ldots(-a_{\alpha-1,\alpha-2})(-a_{\alpha+2,\alpha+1})\ldots(-a_{S,S-1}) \ , \\ &= (+1)(+1)(-1)^{n \bmod 2} a_{21}a_{43}\ldots a_{\alpha-1,\alpha-2}a_{\alpha+2,\alpha+1}\ldots a_{S,S-1} \ . \end{aligned} \tag{3.8}$$

Therefore, the kernel of an odd-sized cycle is given by
$\text{Ker}(A) = \{(a_{32}a_{54}\cdots a_{S,S-1}, a_{43}a_{65}\cdots a_{1,S}, \ldots, a_{21}a_{43}\cdots a_{S-1,S-2})\}$.

The adjugate matrix of an even-sized antisymmetric matrix. The kernel of an even-dimensional antisymmetric matrix is characterized in terms of Pfaffians of submatrices as well. If S is even, the kernel of A is characterized by the *adjugate matrix* $R \in \mathbb{R}^{S\times S}$ [63], whose entries are defined as follows:

$$R_{\alpha\beta} = \text{sign}(\sigma_{\alpha\beta})\text{Pf}(A_{\hat{\alpha}\hat{\beta}}) \quad , \ \alpha, \beta = 1, \ldots, S \ . \tag{3.9}$$

Here, $A_{\hat{\alpha}\hat{\beta}}$ denotes the matrix obtained by deleting both the αth and βth row and column from A. In case $\alpha = \beta$, $A_{\hat{\alpha}\hat{\beta}} \coloneqq A_{\hat{\alpha}}$ and, thus, $\text{Pf}(A_{\hat{\alpha}\hat{\alpha}}) = 0$. Furthermore, $\text{sign}(\sigma_{\alpha\beta})$ denotes the signum of the permutation,

$$\begin{aligned} \sigma_{\alpha\beta} &\coloneqq \begin{pmatrix} 1 & 2 & 3 & 4 & \ldots & \alpha{-}1 & \alpha & \alpha{+}1 & \alpha{+}2 & \ldots & \beta{-}1 & \beta & \beta{+}1 & \ldots & 2n{-}1 & 2n \\ \alpha & \beta & 1 & 2 & \ldots & \alpha{-}3 & \alpha{-}2 & \alpha{-}1 & \alpha{+}1 & \ldots & \beta{-}2 & \beta{-}1 & \beta{+}1 & \ldots & 2n{-}1 & 2n \end{pmatrix} \ , \\ &\equiv \big(\alpha \ \beta 1 \ 2 \ \ldots 2n-1 \ 2n\big) \ , \end{aligned} \tag{3.10}$$

in which α and β are taken out of and put in front of the sequence $(1, 2, \ldots, 2n)$. The adjugate matrix comprises two linearly independent column vectors as kernel vectors if $\dim(\text{Ker}(A)) = 2$; and it is the zero-matrix if $\dim(\text{Ker}(A)) = 4, 6, \ldots, S$ [62]. In general,

the adjugate matrix can be thought of as the generalized inverse of the antisymmetric matrix A having the property $AR = -\mathrm{Pf}(A)\mathbb{1}_{S\times S}$ with $\mathbb{1}_{S\times S}$ denoting the unit matrix of size $S \times S$. If the kernel is trivial ($\dim(\mathrm{Ker}(A)) = 0$, that is, $\mathrm{Det}(A) > 0$), the antisymmetric matrix A is invertible and the adjugate matrix R is proportional to its inverse.

Example: The adjugate matrix of an even-sized cycle. For completeness, we also denote the elements of the adjugate matrix of an even-sized cycle, which are obtained in a similar manner as for the odd-sized cycle, but deleting two nodes from the network:

$$R_{\alpha\beta} = \begin{cases} 0 & \text{for } \alpha = \beta \\ 0 & \text{for } \beta - \alpha \text{ even} \\ (-1)^{n \bmod 2} a_{21} \dots a_{\alpha-1,\alpha-2} a_{\alpha+2,\alpha+1} \dots a_{\beta-1,\beta-2} a_{\beta+2,\beta+1} \dots a_{S,S-1} & \text{for } \beta - \alpha, \ \alpha \text{ odd} \\ (-1)(-1)^{n \bmod 2} a_{1,S} \dots a_{\alpha-1,\alpha-2} a_{\alpha+2,\alpha+1} \dots a_{\beta-1,\beta-2} a_{\beta+2,\beta+1} \dots a_{S-1,S-2} & \text{for } \beta - \alpha, \ \alpha \text{ even} \\ -R_{\beta\alpha} & \text{for } \beta < \alpha \ . \end{cases} \tag{3.11}$$

3.3.4 Minimal kernel dimension of a network topology determined by perfect matchings of subnetworks

Given a network topology, that is, a directed graph for which the magnitudes of the edge weights can be arbitrarily chosen, one may ask the following question: what is the lower bound for the kernel dimension of the antisymmetric adjacency matrices corresponding to that network topology? The lower bound for the kernel dimension in the set of all antisymmetric matrices that respect the specified network topology is referred to as the *minimal kernel dimension* of this network topology. Note that upon tuning the weights of a network topology, the Pfaffians of the antisymmetric adjacency matrix A or of submatrices of A may vanish and, thus, the dimension of the kernel may increase. In other words, tuning the weights on a given network topology can only increase the kernel dimension compared with the minimal kernel dimension of that network topology.

Factor-critical networks have minimal kernel dimension 1. First, consider a factor-critical network as depicted in Figure 4.3(a). Because the adjugate vector is not the zero-vector for some choice of weights (Figure 4.3(d)), the minimal kernel dimension of this network topology is 1. In general, the minimal kernel dimension of factor-critical networks is always 1; see below.

Example of a network topology with minimal kernel dimension 3. Consider now the exemplary network topology depicted in Figure 3.2(a), which is built from four 4-cycles connected at one single center node. For a generic choice of weights, the kernel of A has dimension 3, as validated by the three linearly independent kernel vectors:

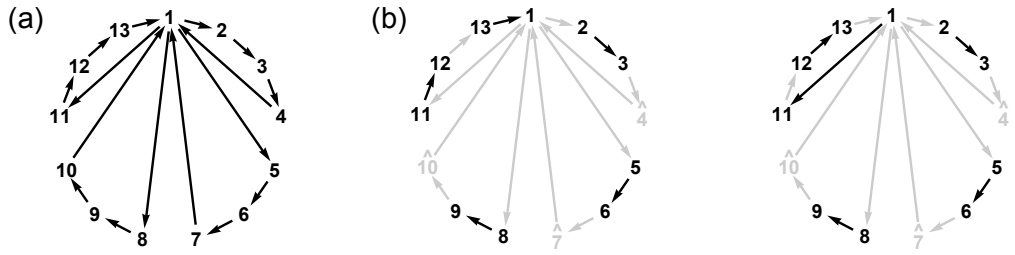

Figure 3.2: Example of a network topology with minimal kernel dimension 3. (a) Example of a network topology of 13 nodes, for which the minimal kernel dimension is 3. The network consists of four cycles of length four connected at one single center node (node 1). (b) Two exemplary perfect matchings, which arise after deleting three nodes. No perfect matching can be identified after removal of no, one, or two arbitrary node(s). As a consequence, the kernel dimension of the network's adjacency matrix for an arbitrary choice of weights is at least 3. No choice of weights can yield a one-dimensional kernel. In total, the minimal kernel dimension of this network topology is 3.

$$v_1 = \begin{pmatrix} 0 \\ a_{4,3}(a_{11,1}a_{13,12} - a_{12,11}a_{1,13}) \\ 0 \\ a_{3,2}(a_{11,1}a_{13,12} - a_{12,11}a_{1,13}) \\ 0 \\ 0 \\ 0 \\ 0 \\ 0 \\ 0 \\ -a_{13,12}(a_{2,1}a_{4,3} - a_{3,2}a_{1,4}) \\ 0 \\ -a_{12,11}(a_{2,1}a_{4,3} - a_{3,2}a_{1,4}) \end{pmatrix}, \quad v_2 = \begin{pmatrix} 0 \\ -a_{4,3}(a_{1,10}a_{9,8} - a_{8,1}a_{10,9}) \\ 0 \\ -a_{3,2}(a_{1,10}a_{9,8} - a_{8,1}a_{10,9}) \\ 0 \\ 0 \\ 0 \\ -a_{10,9}(a_{2,1}a_{4,3} - a_{3,2}a_{1,4}) \\ 0 \\ -a_{9,8}(a_{2,1}a_{4,3} - a_{3,2}a_{1,4}) \\ 0 \\ 0 \\ 0 \end{pmatrix}, \quad v_3 = \begin{pmatrix} 0 \\ a_{4,3}(a_{5,1}a_{7,6} - a_{6,5}a_{1,7}) \\ 0 \\ a_{3,2}(a_{5,1}a_{7,6} - a_{6,5}a_{1,7}) \\ -a_{7,6}(a_{2,1}a_{4,3} - a_{3,2}a_{1,4}) \\ 0 \\ -a_{6,5}(a_{2,1}a_{4,3} - a_{3,2}a_{1,4}) \\ 0 \\ 0 \\ 0 \\ 0 \\ 0 \\ 0 \end{pmatrix}.$$

Therefore, the minimal kernel dimension of the network topology in Figure 3.2(a) is 3. However, all three kernel vectors v_1, v_2, and v_3 have zero entries at index $1, 3, 6, 9$ and 12. No linear combination of these vectors is strictly positive for any choice of weights and, thus, this network is not a coexistence network. In other words, no choice of weights on this network topology can yield an antisymmetric adjacency matrix with kernel dimension smaller than 3. In fact, when all weights are chosen to be equal, the three kernel vectors vanish. In this case, the kernel dimension is 5.

Minimal kernel dimension is determined by occurrences of perfect matchings in subnetworks. In the following, we show that the minimal kernel dimension of a network topology equals the minimal number of nodes that need to be deleted such that a perfect matching exists in the remaining subnetwork. In other words, the kernel of A on the specified network topology is at least K-dimensional if it is necessary to delete at least K nodes from the network $\mathcal{N}(A)$ to obtain a perfect matching in the remaining subnetwork.

For example, a factor-critical network has a perfect matching upon removing any single node (the so-called near-perfect matchings). On the other hand, because factor-critical network are of odd size, they do not have a perfect matching. Thus, the minimal kernel

dimension of a factor-critical network is 1. The above example of four 4-cycles connected at a center node (Figure 3.2(a)) neither has a perfect matching nor does it have a perfect matching upon removing one arbitrary node or two arbitrary nodes. However, this network topology has perfect matchings after removal of three nodes as shown in Figure 3.2(b). Thus, the minimal kernel dimension of this network topology is 3.

To briefly rationalize the graph-theoretical characterization of the minimal kernel dimension, we express the characteristic polynomial of an arbitrary antisymmetric matrix A that respects a given network topology in terms of its principal minors. The characteristic polynomial of a matrix can be written as:

$$\det(A - \lambda \mathbb{1}_S) = \sum_{\alpha=0}^{S} c_\alpha \lambda^\alpha \ , \tag{3.12}$$

where the coefficients $c_\alpha \in \mathbb{R}$ in the expansion are given by [63]:

$$c_0 = \det(A) \ , \tag{3.13}$$

$$c_\alpha = \sum_{\substack{J \subseteq \{1,\dots,S\}, \\ |J|=\alpha}} (-1)^\alpha \det(A_{\hat{J}}) \quad , \ \alpha = 1, \dots, S-1 \ , \tag{3.14}$$

$$c_S = 1 \ . \tag{3.15}$$

Here, $A_{\hat{J}}$ denotes the submatrix of A (a principal minor) that is created by deleting the rows and columns with label $j_1, \dots, j_{|J|}$ (such that $J = \{j_1, \dots, j_{|J|}\}$) from A. In a graph-theoretical interpretation, $A_{\hat{J}}$ is the antisymmetric adjacency matrix of the subnetwork that is created by deleting the nodes J and their attached links from $\mathcal{N}(A)$. If it is necessary to delete at least K nodes from the network $\mathcal{N}(A)$ to obtain a perfect matching in a remaining subnetwork, the first K expansion coefficients $c_0, c_1, \dots, c_{K-1}$ are zero (because for antisymmetric matrices, the determinant is 0 if and only if the Pfaffian is 0). Upon tuning the weights of the network, also further expansion coefficients c_α with $\alpha \geq K$ may vanish and, thus, the kernel dimension can only be greater than K. Therefore, the kernel of A on the specified network topology is at least K-dimensional if it is necessary to delete at least K nodes from the network $\mathcal{N}(A)$ to obtain a perfect matching in a remaining subnetwork.

3.4 Minimal network topological requirement for coexistence of all states: Strongly connected network

Coexistence of all states in the ALVE (2.1) occurs when the interaction matrix A has a strictly positive kernel vector. In the example 2.2.2 we have seen that the kernel depends on the network topology, the interaction rates, or both. Intuitively, coexistence of interacting states can only occur when mass can flow from each states to every other, such that mass is not trapped in subsystems or single states. This intuition can be made rigorous and

gives a minimal requirement for the network topology of networks of condensates, as we show in the following.

In graph theory, a network is strongly connected if for all pairs of nodes α and β there is a directed path connecting α to β and, vice versa, a directed path connecting β to α [53]. Pictorially speaking, all states can coexist for all times ($x_\alpha \geq \epsilon > 0$ for all α for all times) if each state can (i) gain mass through a directed path from all other states and (ii) release mass through a directed path to all other states. The simplest example of a strongly connected network is a directed cycle.

To show that coexistence of all states requires a strongly connected network, we apply an argument by contradiction: Assume that A is the antisymmetric adjacency matrix of a network that is not strongly connected, but weakly connected (that is, there exists an undirected path connection all pairs of nodes). Furthermore, we assume that A has a positive kernel and, thus, coexistence of all states in the ALVE (2.1). Because the network is not strongly connected, the set of nodes V can be divided into two disjoint sets of nodes V_1 and V_2 ($V = V_1 \cup V_2$ and $V_1 \cap V_2 = \emptyset$), for which all edges between nodes of V_1 and nodes of V_2 are directed from V_2 to V_1. In other words, the network's antisymmetric adjacency matrix in a suitable labeling takes the form:

$$A = \begin{pmatrix} A_1 & A_{1\leftarrow 2} \\ -A_{1\leftarrow 2}^T & A_2 \end{pmatrix}, \tag{3.16}$$

with $(A_{1\leftarrow 2})_{\alpha\beta} \geq 0$ for all α, β denotes the weights of the edges that connect V_2 to V_1. Note also that $A_{1\leftarrow 2} \neq 0$ (if $A_{1\leftarrow 2} \equiv 0$, the network would be divided into two separated subnetworks without any connecting edges between V_1 and V_2, contradicting our assumption that the network is strongly connected). The antisymmetric matrices A_1 and A_2 characterize the weights connecting nodes solely within V_1 and V_2, respectively. Accordingly, we decompose the state vector into the chosen partitions V_1 and V_2 and write $\boldsymbol{x} = (\boldsymbol{x}_1, \boldsymbol{x}_2)$.

Let us now compute how the total mass in the states V_2 evolves in time:

$$\begin{aligned} \frac{\mathrm{d}}{\mathrm{d}t} \sum_{\alpha\in V_2} x_\alpha = \sum_{\alpha\in V_2} x_\alpha (A\boldsymbol{x})_\alpha &= \begin{pmatrix} 0^T & \boldsymbol{x}_2^T \end{pmatrix} \begin{pmatrix} A_1 & A_{1\leftarrow 2} \\ -A_{1\leftarrow 2}^T & A_2 \end{pmatrix} \begin{pmatrix} \boldsymbol{x}_1 \\ \boldsymbol{x}_2 \end{pmatrix} , \\ &= -\boldsymbol{x}_2^T A_{1\leftarrow 2}^T \boldsymbol{x}_1 + \boldsymbol{x}_2^T A_2 \boldsymbol{x}_2 = -\boldsymbol{x}_2^T A_{1\leftarrow 2}^T \boldsymbol{x}_1 . \end{aligned} \tag{3.17}$$

Since we assumed coexistence of all states ($x_\alpha \geq \epsilon > 0$ for all α for all times), we know

$$\frac{\mathrm{d}}{\mathrm{d}t} \sum_{\alpha\in V_2} x_\alpha = -\boldsymbol{x}_2^T A_{1\leftarrow 2}^T \boldsymbol{x}_1 \leq -Const \cdot \epsilon < 0 , \tag{3.18}$$

for some positive constant $Const > 0$, as $A_{1\leftarrow 2} \geq 0$ and all concentrations are positive $x_\alpha \geq 0$. Together with equation (3.18) it follows that all states V_2 go extinct over time. This result is intuitively understood because all edges between V_1 and V_2 are directed from V_2 to V_1, that is, mass can only flow from V_2 to V_1, but not in the opposite direction.

However, extinction of V_2 is in contradiction with our assumption that all states coexist. If a network is not strongly connected, all states cannot coexist. Therefore, strongly connected networks are necessary to obtain coexistence of all states in the ALVE (2.1). The simplest examples of strongly connected network are directed cycles and Hamiltonian networks (obtained by adding edges to a directed cycle). Hamiltonian networks are of relevance in Section 4.3.1.

3.A Properties of real antisymmetric matrices

3.A.1 Nonzero eigenvalues occur in pairs, the corresponding eigenvectors are conjugated and orthogonal

By complex conjugating the eigenvalue equation, we find

$$\overline{A\boldsymbol{x}} = \overline{\lambda\boldsymbol{x}} = -\lambda\overline{\boldsymbol{x}} = A\overline{\boldsymbol{x}} \ .$$

If $\boldsymbol{x}$ is an eigenvector of A with eigenvalue λ, then its complex conjugate $\overline{\boldsymbol{x}}$ is also an eigenvector of A with eigenvalue $-\lambda$.

We decompose the eigenvector $\boldsymbol{x}$ into its real and imaginary part (i denotes the imaginary unit):

$$\begin{aligned} \boldsymbol{x} = \boldsymbol{u} + i\boldsymbol{v} \ ; \ \ \bar{\boldsymbol{x}} = \boldsymbol{u} - i\boldsymbol{v} \\ A(\boldsymbol{u} + i\boldsymbol{v}) = i|\lambda|(\boldsymbol{u} + i\boldsymbol{v}) = -|\lambda|\boldsymbol{v} + i|\lambda|\boldsymbol{u} \\ A(\boldsymbol{u} - i\boldsymbol{v}) = -i|\lambda|(\boldsymbol{u} - i\boldsymbol{v}) = -|\lambda|\boldsymbol{v} - i|\lambda|\boldsymbol{u} \\ \Rightarrow A\boldsymbol{u} = -|\lambda|\boldsymbol{v} \ ; \ \ A\boldsymbol{v} = |\lambda|\boldsymbol{u} \end{aligned}$$

This decomposition reveals that the complex eigenvectors consists of real conjugated pairs of vectors $\boldsymbol{u}, \boldsymbol{v}$ that map onto each other with a factor $|\lambda|$ that corresponds to the eigenvalue. The antisymmetry of A implies that these 'generalized eigenvectors' are orthogonal to each other,

$$\boldsymbol{u}^T A\boldsymbol{u} = -\boldsymbol{u}^T A\boldsymbol{u} = -|\lambda|\boldsymbol{u}^T\boldsymbol{v} = 0 \ .$$

In the decomposition of the true eigenvalue $\boldsymbol{x}$, both of the generalized eigenvectors have the same norm,

$$\begin{aligned} i|\lambda|\langle\boldsymbol{x},\boldsymbol{x}\rangle = \langle\boldsymbol{x},(A\boldsymbol{x})\rangle &= (\boldsymbol{u}^T - i\boldsymbol{v}^T)A(\boldsymbol{u} + i\boldsymbol{v}) \\ &= \boldsymbol{u}^T A\boldsymbol{u} + \boldsymbol{v}^T A\boldsymbol{v} + i\boldsymbol{u}^T A\boldsymbol{v} - i\boldsymbol{v}^T A\boldsymbol{u} = 2i\boldsymbol{u}^T A\boldsymbol{v} \\ &= 2i|\lambda|\langle\boldsymbol{u},\boldsymbol{u}\rangle = 2i|\lambda|\langle\boldsymbol{v},\boldsymbol{v}\rangle \end{aligned}$$

3.A.2 The image dimension always even

From the previous calculations, we conclude that there is always an even number of eigenvalues. Summarizing, we have shown that the image $\mathrm{Im}\,(A)$ of a real antisymmetric matrix is always even dimensional. By the rank-nullity theorem ($\dim \mathrm{Ker}\,(A) + \dim \mathrm{Im}\,(A) = S$), for even-sized (odd-sized) real antisymmetric matrices, the kernel dimension is always even (odd), respectively.

Notably, for real, antisymmetric matrices of odd size, there is always a non-trivial kernel vector. This fact is of special importance for this thesis.

3.A.3 Bock-diagonalization for real, antisymmetric matrices

With the information derived above, we can block-diagonalize each A. Let $A = -A^T \in \mathbb{R}^{S\times S}$ be a real, antisymmetric matrix of size S. The matrix has $k \leq \lfloor S/2 \rfloor$ distinct eigenvalues. To every eigenvalue there is a pair of real conjugated eigenvectors $A\boldsymbol{u}^{(\alpha)} = -\lambda\boldsymbol{v}^{(\alpha)}, A\boldsymbol{v}^{(\alpha)} = \lambda\boldsymbol{u}^{(\alpha)}$ (we assume that $\boldsymbol{v}, \boldsymbol{u}$ are normalized). Additionally, the matrix has the orthonormal kernel vectors $\boldsymbol{r}^{\beta}$ with $\beta = \{1, ..., S-k\}$.

The vectors form a unitary transformation matrix $T = \left(\boldsymbol{u}^{(1)}, \boldsymbol{v}^{(1)}, ..., \boldsymbol{u}^{(k)}, \boldsymbol{v}^{(k)}, \boldsymbol{r}^{(1)}, .., \boldsymbol{r}^{(S-2k)}\right)$:

$$
\begin{aligned}
T^T A T &= \left(\boldsymbol{u}^{(1)}, \boldsymbol{v}^{(1)}, ..., \boldsymbol{v}^{(k)}, \boldsymbol{r}^{(1)}, .., \boldsymbol{r}^{(S-k)}\right)^T \left(-\lambda^1\boldsymbol{v}^{(1)}, \lambda^1\boldsymbol{u}^{(1)}, ..., \lambda^k\boldsymbol{u}^{(k)}, 0, .., 0\right) \\
&= \begin{pmatrix}
0 & \lambda^1 & ... & 0 & 0 & 0 & ... & 0 \\
-\lambda^1 & 0 & .. & 0 & 0 & 0 & ... & 0 \\
\vdots & \vdots & \vdots & \vdots & \vdots & \vdots & \vdots & \vdots \\
0 & 0 & ... & 0 & \lambda^k & 0 & ... & 0 \\
0 & 0 & ... & -\lambda^k & 0 & 0 & ... & 0 \\
0 & 0 & ... & 0 & 0 & 0 & ... & 0 \\
\vdots & \vdots & \vdots & \vdots & \vdots & \vdots & \vdots & \vdots \\
0 & 0 & ... & 0 & 0 & 0 & ... & 0
\end{pmatrix}
\end{aligned}
$$

3.B Properties of the Pfaffian

In the following, we provide background information for the Pfaffian. We elaborate on its combinatorial definition, present examples and show that the combinatorial and the graph theoretical definition of the Pfaffian agree. We close this chapter with the calculation of the Pfaffians of exemplary matrices.

3.B.1 Combinatorial definition of the Pfaffian

Because the Pfaffian of an antisymmetric matrix is central to our analysis, we present here its combinatorial definition for completeness. Let Π denote the set of all partitions of the set $\{1, 2, \ldots, S = 2n\}$ into ordered pairs. In other words, every partition $\gamma \in \Pi$ is pair-wisely ordered in the form $\gamma = \big((i_1, j_1), (i_2, j_2), \ldots, (i_n, j_n)\big)$ with $i_k < j_k$ for all k and

$i_k < i_l$ for all $k < l$. Note that there are $|\Pi| = (2n-1)\cdot(2n-3)\cdot\cdots\cdot 3\cdot 1 = (2n-1)!!$ different pair-wisely ordered partitions of the set $\{1,\ldots,S\}$. We define the permutation σ_γ of such a partition $\gamma \in \Pi$ as:

$$\sigma_\gamma \coloneqq \begin{pmatrix} 1 & 2 & 3 & 4 & \ldots & 2n-1 & 2n \\ (i_1 & j_1) & (i_2 & j_2) & \ldots & (i_n & j_n) \end{pmatrix} , \tag{3.19}$$

$$\equiv \begin{pmatrix} i_1 & j_1 & i_2 & j_2 & \ldots & i_n & j_n \end{pmatrix} . \tag{3.20}$$

With these notions, the Pfaffian of an antisymmetric matrix $A \in \mathbb{R}^{S\times S}$ of even size $S = 2n$ is defined as [54, 61]:

$$\mathrm{Pf}(A) \coloneqq \sum_{\gamma\in\Pi} \left(\mathrm{sign}(\sigma_\gamma) \prod_{k=1}^{n} a_{\alpha_k} \right) . \tag{3.21}$$

For an odd-sized antisymmetric matrix, the Pfaffian is 0. Because the elements of every partition γ are ordered pairs ($i < j$ for every pair $(i,j) \in \gamma$), every summand $\prod_{k=1}^{n} a_\gamma$ is a product of above-diagonal matrix entries of A. With this definition (3.1), one can show that $\mathrm{Pf}(A)^2 = \mathrm{Det}(A)$.

More generally, we define the permutation of a partition of an arbitrary, ordered set of size $2n$ by identifying the indices of its ordered elements with the elements of the index set $\{1,2,\ldots,2n\}$. In other words, a permutation of a partition of an arbitrary, ordered set of even size is understood as the permutation of the partition of the corresponding index set. For example, when calculating the Pfaffian of a submatrix $A_{\hat{\alpha}}$ (necessary for the adjugate vector), we consider permutations of the set $\{1,2,\ldots,\alpha-1,\alpha+1,\ldots,S\}$ with S odd. In this case, the sign of the permutation is determined by the number of transpositions necessary to order the elements in size.

For illustration, consider the pretzel-like interaction network sketched in Figure 3.1 with adjacency matrix (3.3) given in the main text. Using the combinatorial definition (3.1) to compute the Pfaffian of A_{pretzel} yields:

$$\mathrm{Pf}(A_{\mathrm{pretzel}}) = \begin{bmatrix} \mathrm{sign}(1\ 2\ 3\ 4)(-a_{21})(-a_{43}) \\ +\,\mathrm{sign}(1\ 3\ 2\ 4)a_{13}a_{24} \\ +\,\mathrm{sign}(1\ 4\ 2\ 3)\cdot 0\cdot(-a_{32}) \end{bmatrix} , \tag{3.22}$$

$$= (+1)(-a_{21})(-a_{43}) + (-1)a_{13}a_{24} ,$$

$$= a_{21}a_{43} - a_{13}a_{24} , \tag{3.23}$$

which agrees with the graph-theoretical (3.2) computation in Equation (3.4) in the main text.

Laplace-like formula of the Pfaffian. As can be seen from the above example, the computation of the Pfaffian of an antisymmetric matrix proceeds in a similar manner as the computation of the determinant of an arbitrary matrix, but is tailored to the antisymmetry

of the matrix through the notion of the Pfaffian. In this line of thought, it is not surprising that a recursive definition of the Pfaffian for an antisymmetric matrix of even size can be obtained (in the spirit of Laplace's formula for determinants) as [62, 56]:

$$\mathrm{Pf}(A) = \sum_{\alpha=2}^{S} (-1)^{\alpha} a_{1\alpha} \mathrm{Pf}(A_{\hat{1}\hat{\alpha}}) \ , \tag{3.24}$$

which we mention here for completeness.

3.B.2 Graph-theoretical and combinatorial definition agree.

The graph-theoretical definition of the Pfaffian (3.2) agrees with its combinatorial definition (3.1) for the following reason. If the weighted network $\mathcal{N}(A)$ is built from the antisymmetric adjacency matrix A, every perfect matching of the network $\mathcal{N}(A)$ corresponds to a distinct non-zero summand in the Pfaffian of A in the graph-theoretical definition (3.2). In the combinatorial definition (3.1) all matrix elements for the computation of the Pfaffian are taken from above the diagonal of A, whereas in the graph-theoretical definition only negative matrix elements are used (that is, from above or below the matrix diagonal). If a positive entry $a_{ji} > 0$ appears in a summand of the combinatorial definition of the Pfaffian (3.1), the negative matrix entry $a_{ij} = -a_{ji} < 0$ appears in the graph-theoretical definition (3.2). Additionally, the permutation of the corresponding partition changes by one transposition (i and j are swapped) such that the sign of the permutation in the combinatorial and graph-theoretical definition differs by a factor of -1. This compensates for the minus sign originating from the different sign of the matrix entry. Taken together, the graph-theoretical definition of the Pfaffian (3.2) and the combinatorial definition (3.1) are equivalent.

The graph-theoretical definition is suitable for our work on coexistence networks. The graph-theoretical definition of the Pfaffian (3.2) has the advantage over the combinatorial definition (3.1) in that it distinguishes between network topology and edge weights. The combinatorial definition (3.1) includes only above-diagonal entries of the antisymmetric matrix A. When A contains zero-entries, zero summands appear in the expression for the Pfaffian, which do not contribute to its value. In contrast, the graph-theoretical definition of the Pfaffian includes by construction only non-zero entries of A and, thus, contains only non-zero summands in the definition of the Pfaffian. In addition, all matrix elements of the summands occurring in the Pfaffian are negative such that the sign of each summand is determined only by the sign of the perfect matching alone. For these reasons, the graph-theoretical definition (3.2) distinguishes between edge-weights (negative matrix elements) and network topology (signs of matchings) and, thus, is suitable for our discussion of coexistence networks in the main text.

3.B.3 The Pfaffian of exemplary antisymmetric matrices

A general 2×2 antisymmetric matrix. As an example, consider an arbitrary antisymmetric 2×2 matrix (with $a_{12} > 0$),

$$A_2 = \begin{pmatrix} 0 & a_{12} \\ -a_{12} & 0 \end{pmatrix} . \tag{3.25}$$

The set of all pair-wisely ordered partitions of $\{1, 2\}$ is simply $\Pi = \{\big((1, 2)\big)\}$. Therefore, the Pfaffian of A_2 is given by

$$\mathrm{Pf}(A_2) = a_{12} . \tag{3.26}$$

A general 4×4 antisymmetric matrix. For an arbitrary antisymmetric 4×4 matrix (all above-diagonal entries are assumed to be positive),

$$A_4 = \begin{pmatrix} 0 & a_{12} & a_{13} & a_{14} \\ -a_{12} & 0 & a_{23} & a_{24} \\ -a_{13} & -a_{23} & 0 & a_{34} \\ -a_{14} & -a_{24} & -a_{34} & 0 \end{pmatrix} , \tag{3.27}$$

the set of all pair-wisely ordered partitions of the set $\{1, 2, 3, 4\}$ is given by
$\Pi = \{\big((1, 2), (3, 4)\big),\ \big((1, 3), (2, 4)\big),\ \big((1, 4), (2, 3)\big)\}$.
The Pfaffian of A_4 is obtained as:

$$\mathrm{Pf}(A_4) = (+1)a_{12}a_{34} + (-1)a_{13}a_{24} + (+1)a_{14}a_{23} . \tag{3.28}$$

The sign of the permutation was highlighted in front of the corresponding factor (for example, $\mathrm{sign}(1\ 3\ 2\ 4) = -1$).

A general 6×6 antisymmetric matrix. For a general antisymmetric 6×6 matrix A_6 (again all above-diagonal entries are assumed to be positive),

$$A_6 = \begin{pmatrix} 0 & a_{12} & a_{13} & a_{14} & a_{15} & a_{16} \\ -a_{12} & 0 & a_{23} & a_{24} & a_{25} & a_{26} \\ -a_{13} & -a_{23} & 0 & a_{34} & a_{35} & a_{36} \\ -a_{14} & -a_{24} & -a_{34} & 0 & a_{45} & a_{46} \\ -a_{15} & -a_{25} & -a_{35} & -a_{45} & 0 & a_{56} \\ -a_{16} & -a_{26} & -a_{36} & -a_{46} & -a_{56} & 0 \end{pmatrix} , \tag{3.29}$$

the Pfaffian is obtained as:

$$\mathrm{Pf}(A_6) = \begin{bmatrix} (+1)a_{12}a_{34}a_{56} + (-1)a_{12}a_{35}a_{46} \\ +(+1)a_{12}a_{36}a_{45} + (-1)a_{13}a_{24}a_{56} \\ +(+1)a_{13}a_{25}a_{46} + (-1)a_{13}a_{26}a_{45} \\ +(+1)a_{14}a_{23}a_{56} + (-1)a_{14}a_{25}a_{36} \\ +(+1)a_{14}a_{26}a_{35} + (-1)a_{15}a_{23}a_{46} \\ +(+1)a_{15}a_{24}a_{36} + (-1)a_{15}a_{26}a_{34} \\ +(+1)a_{16}a_{23}a_{45} + (-1)a_{16}a_{24}a_{35} \\ +(+1)a_{16}a_{25}a_{34} \end{bmatrix} . \tag{3.30}$$

Directed cycle of even size. For further illustration of how the Pfaffian is computed and to complete the statements from the previous Section, let us also consider a directed cycle of even length: $S \to 1 \to 2 \to 3 \to \cdots \to S-1 \to S$ (such that $a_{1,S}, a_{21}, a_{32}, \ldots, a_{S,S-1} > 0$ with $S = 2n$ even for $n = 2, 3, \ldots$) with according antisymmetric adjacency matrix $A_{\text{even-cycle}}$:

$$A_{\text{even-cycle}} = \begin{pmatrix} 0 & -a_{21} & 0 & \ldots & a_{1,S} \\ a_{21} & 0 & -a_{32} & \ldots & 0 \\ 0 & a_{32} & 0 & \ldots & 0 \\ \vdots & 0 & \ddots & \ddots & \vdots \\ 0 & \ldots & a_{S-1,S-2} & 0 & -a_{S,S-1} \\ -a_{1,S} & 0 & \ldots & a_{S,S-1} & 0 \end{pmatrix} . \tag{3.31}$$

The Pfaffian of the even-sized cycle is obtained as:

$$\mathrm{Pf}(A_{\text{even-cycle}}) = \quad (-1)^{n \bmod 2} a_{21}a_{43}\cdots a_{S,S-1} - (-1)^{n \bmod 2} a_{32}a_{54}\cdots a_{1,S} \ . \tag{3.32}$$

Chapter 4

Topologically robust coexistence and coexistence networks

To explore how the topology of interaction networks determines the robustness of dynamical systems, we study the antisymmetric Lotka-Volterra equation (ALVE) (2.1). In the ALVE, the strengths of pairwise interactions between strategies are defined by an antisymmetric matrix such that typically some strategies go extinct over time. Here we show that there also exist topologically robust zero-sum games, such as the rock-paper-scissors game, for which all strategies coexist for all choices of interaction strengths. We refer to such zero-sum games as *coexistence networks*. By mapping the long-time dynamics of the ALVE to the algebra of antisymmetric matrices, we identify simple graph-theoretical rules by which coexistence networks are identified and constructed. Examples are triangulations of cycles characterized by the golden ratio $\varphi = 1.6180...$, cycles with complete subnetworks, and non-Hamiltonian networks. In graph-theoretical terms, we extend the concept of a Pfaffian orientation from even-sized to odd-sized networks. Our results show that the topology of interaction networks alone can determine the long-time behavior of nonlinear dynamical systems, and may help to identify robust network motifs arising, for example, in ecology.

The results in this chapter were worked out together with *Johannes Knebel* and *Erwin Frey*. This chapter is adapted from the publication with the title "Topologically robust zero-sum games and Pfaffian orientation: How network topology determines the long-time dynamics of the antisymmetric Lotka-Volterra equation" [49] with minor changes to fit the shape of this thesis.

4.1 Introduction

The temporal behavior of models arising in nonequilibrium statistical physics are often adequately described in terms of nonlinear dynamical systems. How the qualitative long-time behavior of a dynamical system depends on the initial conditions, on the interaction of different degrees of freedom, and on the coupling parameters that determine the

interaction strengths remain central questions in theoretical physics and applied mathematics [64, 65, 4, 66]. In this chapter, we focus on the robustness of the qualitative long-time behavior of dynamical systems against arbitrary changes of the coupling parameters [67, 68, 69, 70, 16, 71, 72, 73, 74]. The antisymmetric Lotka-Volterra equation (ALVE) (2.1) is a well-suited dynamical system to study robustness properties. In the dynamics of the ALVE, typically some strategies go extinct over time (see Section 2.2). We investigated the conditions on a zero-sum game under which all strategies coexist *for all choices* of interaction strengths. For example, for the rock-paper-scissors zero sum game, all strategies coexist in an interacting population irrespective of the chosen interaction strengths (Section 1.1) . Since coexistence of all states depends only on the game's network topology, but not on the choice of interaction strengths, we refer to the rock-paper-scissors game as a *topologically robust zero-sum game* or a *coexistence network*; see Figure 4.1(a).

The existence of coexistence networks as well as their characterization are non-trivial because strategies typically go extinct for some choice of interaction strengths, see Section 2.2 and [1]. On the one hand, complete networks such as the rock-paper-scissors-lizard-spock game [1, 75, 76, 77, 78, 79] are not coexistence networks as coexistence of all states depends on the choice of weights; see Figure 4.1(b). On the other hand, cycles with an odd number of strategies, in which every strategy dominates exactly one strategy and is dominated by another ($1 \to 2 \to \cdots \to 2n-1 \to 1$), are coexistence networks [80, 81]. Additionally, for the network topology of a directed cycle of five states supplemented with the directed link in the inside of the cycle as depicted in Figure 4.1(a), coexistence of all states is observed for all choices of weights. We refer to the latter network topology as a *topologically robust zero-sum game* or a *coexistence network* because coexistence of all states in the ALVE (2.1) is robust against arbitrary changes of the weights on that network topology. In other words, coexistence of all states depends only on the network topology, but not on the specific values of the weights. Such coexistence networks with an arbitrary number of strategies beyond odd-sized cycles have not been characterized thus far.

4.2 Topologically robust coexistence and coexistence networks

Algebraic characterization of coexistence networks. A network is a *coexistence network* if its antisymmetric adjacency matrix has a strictly positive kernel element for all choices of weights that do not change the underlying network topology, that is, keeping the direction of links and not adding links to or removing links from the network. In algebraic terms, this question of a strictly positive kernel amounts to determining the conditions on an antisymmetric matrix under which its kernel remains strictly positive for all choices of the non-zero matrix entries (as long as their sign is kept). An antisymmetric matrix whose kernel is one-dimensional is a coexistence network if, for all choices of weights, all entries of the kernel vector have the same sign, such that the unique normalized kernel vector is always

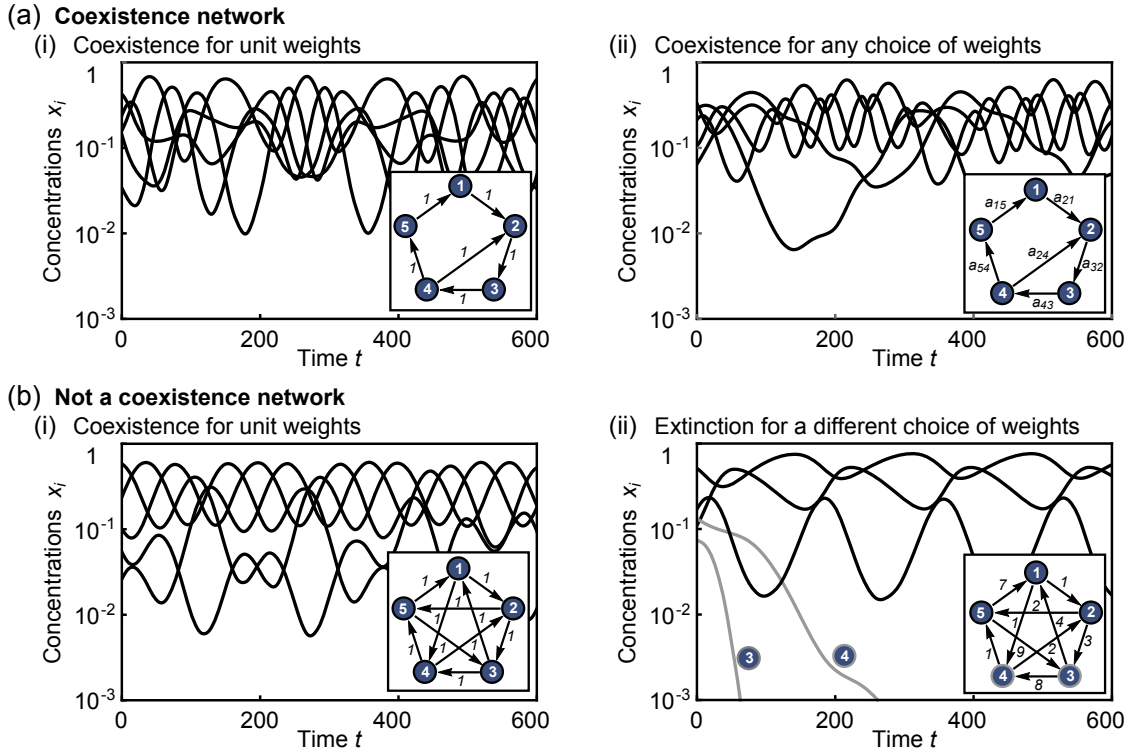

Figure 4.1: Coexistence networks in the antisymmetric Lotka-Volterra equation (ALVE) (2.1)**.** The long-time dynamics of the ALVE are independent of the initial conditions and two scenarios are possible for a state i (equivalently strategy): Either the state concentration vanishes ($x_i \to 0$ as $t \to \infty$; extinction and depletion) or it remains bounded away from 0 for all times ($x_i \geq Const > 0$ for all t; survival and condensation). Survival and extinction of states depend only on the weighted network defined by the network topology and the weights. (a) Trajectories of the ALVE for a directed cycle of 5 nodes with an interior edge from node 4 to 2 (see insets). All states coexist. This coexistence does not only occur for unit weights (i), but *for all choices* of weights on that network topology (ii). Such network topologies are called *coexistence networks* or *topologically robust zero-sum games*. (b) The vast majority of networks are not coexistence networks; here shown for the rock-paper-scissors-lizard-spock game (network topology of five states with two in-going and two out-going links for every node); see insets. (i) For unit weights, all states coexist, but states 3 and 4 go extinct for differently chosen weights (ii). Thus, coexistence in the rock-paper-scissors-lizard-spock game depends on the rates.

strictly positive. The mapping between the entries of a matrix and its kernel elements is, in general, not straightforwardly answered for arbitrary matrices. For antisymmetric matrices, nevertheless, analytical progress is possible as we show in Section 3.3.3. Before proceeding, we illustrate these algebraic insights with directed cycles of odd and even length as examples.

Example for coexistence networks: directed cycles. As an example for a coexistence network, consider the rock-paper-scissors network topology (that is, mass can only

flow in the directed cycle $1 \to 2 \to 3 \to 1$ such that $a_{13}, a_{21}, a_{32} > 0$, see also Section 1.1 and Figure 1.1). The antisymmetric adjacency matrix $A_{\text{3-cycle}}$ is given by:

$$A_{\text{3-cycle}} = \begin{pmatrix} 0 & -a_{21} & a_{13} \\ a_{21} & 0 & -a_{32} \\ -a_{13} & a_{32} & 0 \end{pmatrix} , \tag{4.1}$$

with kernel $\text{Ker}(A_{\text{3-cycle}}) = \{(a_{32}, a_{13}, a_{21})\}$ [1]. Consequently, the kernel of the rock-paper-scissors network topology is strictly positive and all states coexist in the ALVE for all times *for all choices* of weights as long as the rock-paper-scissors network topology is not altered. The above observation can be generalized to cycles of odd size, that is, to network topologies in which mass can only flow in the cycle $1 \to 2 \to 3 \to \cdots \to S-1 \to S \to 1$ for S odd (such that $a_{1,S}, a_{21}, a_{32}, \ldots, a_{S,S-1} > 0$, see (3.6)). The kernel of a cycle of odd size is obtained as $\text{Ker}(A) = \{(a_{32}a_{54} \cdots a_{S,S-1}, a_{43}a_{65} \cdots a_{1,S}, \ldots, a_{21}a_{43} \cdots a_{S-1,S-2})\}$ (see Section 3.3.3), which is again strictly positive for all choices of weights on the cyclic network topology. Thus, cycles of odd size are coexistence networks.

In contrast, directed cycles of even size have a non-trivial kernel only if the weights a_{ij} are fine-tuned. The determinant (in suiting labeling) is given by $\text{Det}(A_{\text{even-cycle}}) = (a_{21}a_{43} \ldots a_{S,S-1} - a_{32}a_{54} \ldots a_{1,S})^2$, which is zero only for specific choices of weights; see Section 3.3 and Section 3.B.3. Thus, for cycles of even size, the occurrence of a strictly positive kernel depends on the choice of matrix entries. Cycles of even size are not coexistence networks. In the following, we further explore this possibly counter-intuitive behavior between even and odd dimension. The discussion of odd-sized directed cycles as examples of coexistence networks is extended in Section 4.3 to Hamiltonian networks, which have a directed cycle through all nodes, and generalized to non-Hamiltonian networks (that is, network topologies without a cycle).

Coexistence networks can be found using the adjugate vector. In our work, we use the adjugate vector to characterize coexistence networks of odd size S. The adjugate vector of an antisymmetric matrix A can be calculated from the Pfaffians of all submatrices of size $S-1$, see Section 3.3.3. A network A whose kernel is one-dimensional for all choices of weights is a coexistence network if its adjugate vector is always strictly positive, that is, if all entries of the adjugate vector have the same sign independent of the weights (if $\boldsymbol{r}$ is a kernel vector of A, so is $-\boldsymbol{r}$). For further details on the influence of the network topology on the kernel dimension of the network's adjacency matrix see also Section 3.3.4.

Figure 4.2(a) illustrates the connection between coexistence networks and the graph-theoretical interpretation of the adjugate vector for an exemplary cycle of five states with two additional interior edges. The adjugate vector is computed by identifying the near-perfect matchings of the network and their signs. A necessary condition to obtain a strictly positive adjugate vector is that the network is factor-critical. Only if the network is factor-critical can the adjugate vector have non-vanishing values in all of its components. The

[1] Note that we do not distinguish notationally between column and row vectors in this manuscript if the meaning is clear from the context.

sign of the αth component of the adjugate vector, r_α, is determined by the signs of the near-perfect matchings and by whether the index α is even or odd; see Equations (3.2) and (3.5). Both contributions determine whether all summands occurring in the adjugate vector have the same sign or not and, thus, whether the one-dimensional kernel is strictly positive or not for all choices of weights.

Examples for the algebraic characterization. As was shown above, simple directed cycles of odd length are coexistence networks (see Figure 4.2(b)(i)), while cycles of even length are not. The directed cycle with one additional interior edge depicted in Figure 4.2(b)(ii) is a coexistence network as well; see also Figure 4.1(a). The interior edge $(4 \to 2)$ creates one new near-perfect matching $\big((4 \to 2), (5 \to 1)\big)$ that gives rise to an entry in the third component of the adjugate vector. The corresponding permutation has the same sign as the permutation of the near-perfect matching $\big((4 \to 5), (1 \to 2)\big)$. Therefore, the kernel of A remains strictly positive for all choices of weights, and this network is a coexistence network. Note that if the direction of this edge is reversed to $(2 \to 4)$, the sign of the near-perfect matching will be negative and the adjugate vector could have a negative entry in the third component upon choosing suitable weights. Hence, the resulting network is not a coexistence network. Figure 4.2(b)(iii) shows the complete network of five nodes (see also Figure 4.1(b)). This network is factor-critical, but not a coexistence network. As indicated above, factor-criticality is not sufficient to obtain a coexistence network; in addition to factor-criticality, the signs of all summands in all entries of the adjugate vector need to be the same to give rise to a coexistence network.

Coexistence networks must be strongly connected. In Section 3.4 we have shown that coexistence of all states is only possible if the underlying network is strongly connected. Intuitively speaking, this means that mass can flow from each state to every other state. The simplest example of a strongly connected network is a directed cycle, such as the rock-paper-scissors network. The fact that coexistence networks are strongly connected has further implications for the underlying topology of coexistence networks. An undirected graph admits a strong orientation (that is, a choice of the direction of all edges such that the resulting directed network is strongly connected) if and only if it has an ear-decomposition [82]. Pictorially speaking, a graph has an ear-decomposition if it can be decomposed to a cycle by successively detaching paths, which are connected to the graph with both ends as 'ears' without crossing any other paths. Notably, Lovasz [83] showed that all factor-critical graphs can always be oriented to be strongly connected. As introduced in Section 3.3.1 a network is factor critical if every subnetwork with of size $S - 1$ (all subnetworks obtained by deleting one node from the original network) has a perfect matching. We employed this fact for our numerical search of coexistence networks starting from undirected graphs; see Section 4.A.2.

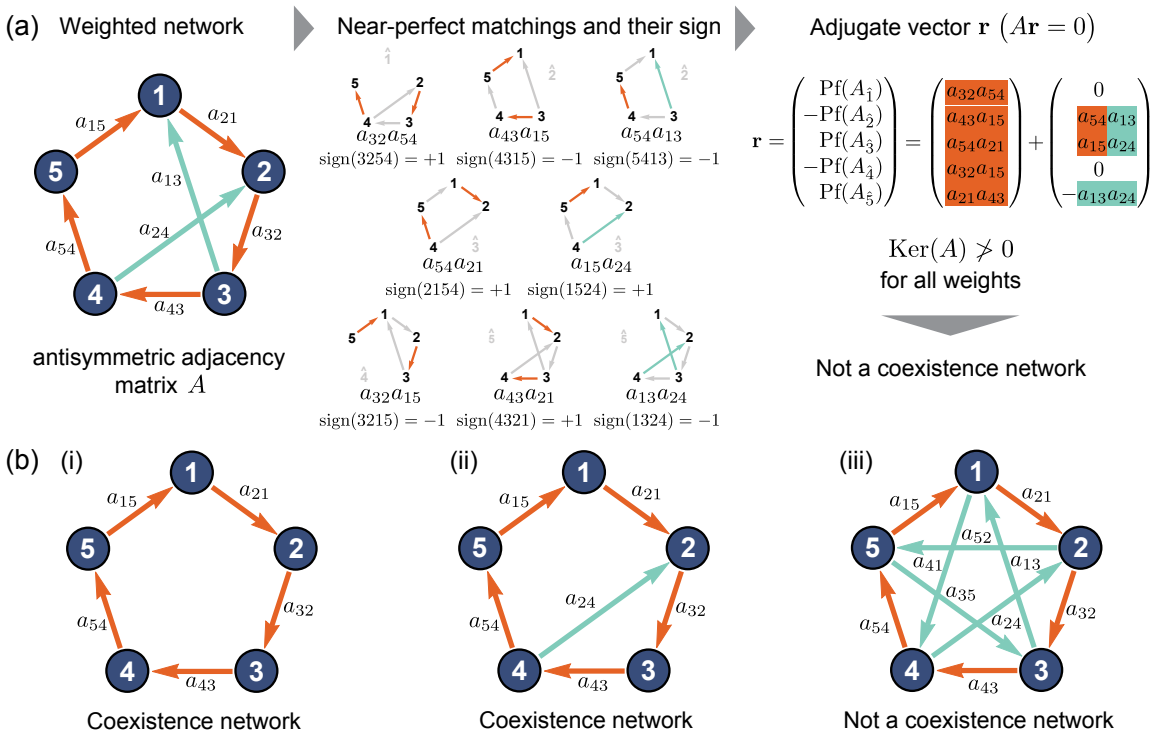

Figure 4.2: Algebraic characterization of coexistence networks via the adjugate vector of A. (a) Algebraic determination of coexistence networks; here illustrated for a cycle of five nodes (orange edges) with the two additional interior edges $(4, 2)$ and $(3, 1)$ (cyan edges). The network is factor-critical. The entries of the adjugate vector are calculated via the near-perfect matchings of the network and their signs (here, eight near-perfect matchings in total); see Figure 3.1 for details of the computation. The near-perfect matching $\big((3 \to 1), (4 \to 2)\big)$ creates the negative summand $(-a_{13}a_{24})$. Thus, the weights can be chosen such that the kernel of A is not strictly positive. Therefore, this network is not a coexistence network. Note that by setting one of the two or both cyan matrix entries to zero, the resulting network topology is a coexistence network. (b)(i) Cycles of odd length are coexistence networks because their adjugate vector is always strictly positive, whereas cycles of even length are not. (ii) The cycle with five nodes and the additional interior edge $(4, 2)$ is a coexistence network as is inferred from the adjugate vector in (a) by setting $a_{13} = 0$. (iii) The complete network of five nodes is not a coexistence network; see also Figure 4.1(b). Additional near-perfect matchings arise through the interior edges $(5, 3), (1, 4)$, and $(2, 5)$.

4.3 Coexistence networks

Overview of this section. In this section, we present graph-theoretical rules for how to construct coexistence networks. Recall that for coexistence networks, coexistence of all states in the ALVE (2.1) is robust against arbitrary changes of the weights (the defining interaction strengths) on the given network topology; see Section 4.2. We begin our analysis with coexistence networks that have a one-dimensional kernel for all choices of weights. For such networks, the vector of steady state concentrations of the ALVE (2.1) is given by

the unique normalized kernel vector as described in Section 2.4.

First, we introduce Hamiltonian coexistence networks, which are coexistence networks with a directed cycle through all nodes and, thus, generalize directed cycles of odd size. In Section 4.3.1 we present the two *coexistence conditions* on the network topology (cycle condition (4.2) and crossing condition (4.3)) with which all Hamiltonian coexistence networks are identified. The proof of these conditions exploits the connection between the adjugate vector (3.5) of an antisymmetric matrix and near-perfect matchings of its network topology; details are deferred to Section 4.C. In Section 4.3.2, we show how network topologies without a Hamiltonian cycle can be obtained from Hamiltonian coexistence networks by deleting suitable links from the cycle. For networks with up to 9 nodes, we numerically verify that all coexistence networks are obtained from Hamiltonian coexistence networks this way; see Section 4.3.3. At present, our numerical enumerations are limited to networks of 9 nodes because of the vastly growing number of network topologies with more nodes. We also briefly discuss the possibility of coexistence networks with a degenerate kernel ($\dim(\mathrm{Ker}(A)) = 2, 3, \dots$), even though we did not find any for $S \leq 9$. We present examples for the construction of coexistence networks in Section 4.4, applications of our results are discussed in Section 4.5.

4.3.1 Hamiltonian coexistence networks

Conditions for Hamiltonian coexistence networks. We now present a scheme to identify Hamiltonian coexistence networks of odd size $S = 2n - 1$ ($n = 2, 3, \dots$). A Hamiltonian network $\mathcal{N}(A)$ contains at least one directed cycle, that is, a directed closed path passing exactly once through all nodes. Thus, its edge-set $E(\mathcal{N})$ can be split into the edges that constitute one such Hamiltonian cycle, E_{cycle}, and all other interior edges in the cycle, E_{in}, such that $E(\mathcal{N}) = E_{\mathrm{cycle}} \cup E_{\mathrm{in}}$ with $E_{\mathrm{cycle}} \cap E_{\mathrm{in}} = \emptyset$. An ascending labeling of the network can be chosen such that $E_{\mathrm{cycle}} = \{(1,2), (2,3), ..., (\alpha, \alpha+1), ..., (S,1)\}$; see Figure 4.3.

With this assignment of the edges of the Hamiltonian network into cycle edges and interior edges, we identified the following necessary and sufficient conditions for a Hamiltonian network to be a coexistence network. The coexistence conditions are stated first, before we illustrate, discuss, and prove them. A Hamiltonian network with the chosen ascending labeling of the cycle $E_{\mathrm{cycle}} = \{(1,2), (2,3), ..., (\alpha, \alpha+1), ..., (S,1)\}$ is a coexistence network *if and only if* its interior edges fulfill the following two *coexistence conditions*:

1. *Cycle condition:* For every interior edge $(\alpha, \beta) \in E_{\mathrm{in}}$ it holds that:

$$\begin{aligned} &(\alpha, \beta) \text{ is ascending and } \beta - \alpha \text{ is odd,} \\ &(\alpha, \beta) \text{ is descending and } \alpha - \beta \text{ is even.} \end{aligned} \tag{4.2}$$

   An edge $(\alpha, \beta) \in E_{\mathrm{in}}$ is called *ascending* (with respect to the labeling of the Hamiltonian cycle) if $\alpha < \beta$, and *descending* if $\alpha > \beta$; see Figure 4.3.

2. *Crossing condition:* For every pair of crossing interior edges $\{(\alpha,\beta),(\mu,\nu)\} \subseteq E_{\text{in}}$ it holds that:

$$\begin{aligned} &(\alpha,\beta) \text{ and } (\mu,\nu) \text{ cross each other,} \\ &\text{and } \min(|\alpha-\mu|,|\beta-\nu|) \text{ is even.} \end{aligned} \tag{4.3}$$

Two interior edges $(\alpha,\beta),(\mu,\nu) \in E_{\text{in}}$ are called *crossing* if $\min(\mu,\nu) < \alpha < \max(\mu,\nu)$ or $\min(\mu,\nu) < \beta < \max(\mu,\nu)$. If the Hamiltonian network is drawn in the two-dimensional plane, crossing edges cross in the interior of the cycle; see Figure 4.3.

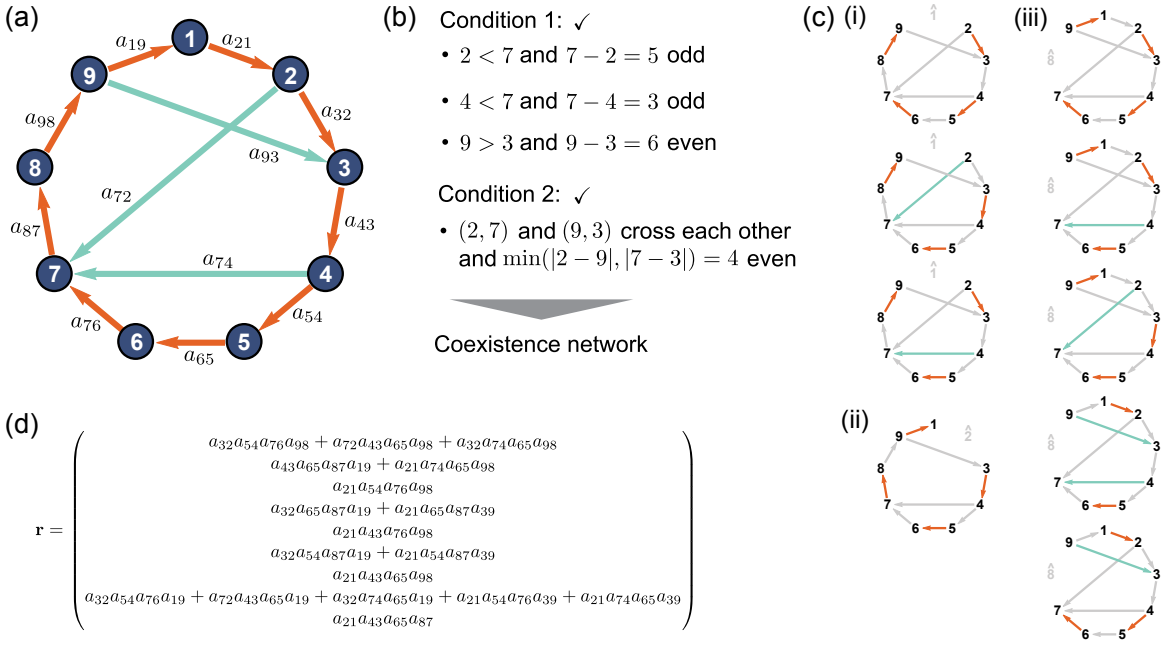

Figure 4.3: Graph-theoretical conditions for Hamiltonian coexistence networks. (a) Hamiltonian network $\mathcal{N}^{(9)}$ of 9 nodes consisting of edges from the Hamiltonian cycle (orange) and interior edges $(2,7),(4,7)$, and $(9,3)$ (cyan). (b) We identified the cycle condition (4.2) and the crossing condition (4.3) to check whether a network topology is a coexistence network. These conditions are both necessary and sufficient. The cycle condition ensures that only cycles of odd length are created within the Hamiltonian cycle through any interior edge. The crossing condition ensures that two crossing cycles share only an odd number of nodes connected by an even number of edges. It follows that $\mathcal{N}^{(9)}$ is a coexistence network. (c) Near-perfect matchings contributing to the first, second, and eighth component of the adjugate vector (3.5). Crossing edges do not contribute to the same near-perfect matching. (d) The component-wise calculation of the adjugate vector $\mathbf{r}$ confirms that the network topology $\mathcal{N}^{(9)}$ in (a) is a coexistence network because all vector components are strictly positive for all choices of weights.

Illustration of the conditions. The cycle condition (4.2) governs the relation of interior edges with the Hamiltonian cycle, while the crossing condition (4.3) governs the relation of interior edges to each other. Fulfillment of the cycle condition (4.2) ensures that interior

edges only create directed subcycles of odd length (due to S being odd). If the difference between start and end node of an interior edge is odd, the direction of the interior edge needs to be ascending with respect to the Hamiltonian cycle to ensure a strictly positive kernel. In contrast, if the difference is even, the edge needs to be descending. Taken together, Hamiltonian coexistence networks do not have even cycles. The crossing condition (4.3) ensures that no two crossing edges occur in the same near-perfect matching. This is the case if and only if the minimal difference between end and start nodes of crossing edges is even. In other words, the two directed cycles of odd length created by every pair of interior edges share an odd number of nodes that are connected by an even number of edges. In Section 4.C, we prove that the coexistence conditions (4.2) and (4.3) are both sufficient and necessary for Hamiltonian coexistence networks.

Example of a coexistence network. To illustrate both the above conditions and the ideas of the proof, we consider an exemplary Hamiltonian network $\mathcal{N}^{(9)} = E^{(9)}_{\text{cycle}} \cup E^{(9)}_{\text{in}}$ of 9 nodes, constituted by the Hamiltonian cycle $E^{(9)}_{\text{cycle}} = \{(1,2),(2,3),\dots(9,1)\}$ and three interior edges $E^{(9)}_{\text{in}} = \{(2,7),(4,7),(9,3)\}$; see Figure 4.3(a) for a sketch.

First, the coexistence conditions (4.2) and (4.3) for a Hamiltonian coexistence network are fulfilled (Figure 4.3(b)). The cycle condition (4.2) is fulfilled for all interior edges: (i) the interior edge $(2,7)$ is ascending because $2 < 7$ and their difference is odd, (ii) the interior edge $(4,7)$ is ascending because $4 < 7$ and the difference is odd, (iii) the interior edge $(9,3)$ is descending because $9 > 3$ and the difference is even. The crossing condition (4.3) is fulfilled for the two crossing edges $(9,3)$ and $(2,7)$ (no other interior edges cross each other) because $\min(|9-2|,|3-7|) = 4$, which is even. Thus, we conclude from the coexistence conditions that the Hamiltonian network $\mathcal{N}^{(9)}$ is a coexistence network.

Component-wise calculation of the adjugate vector confirms coexistence network. To verify that the kernel of the antisymmetric matrix of $\mathcal{N}^{(9)}$ is indeed strictly positive as claimed above, we now explicitly calculate the adjugate vector (3.5) and check the sign of all entries. This algebraic check illustrates the main ideas underlying the proof presented in Section 4.C. For illustration, we write out the near-perfect matchings for the first, second, and eighth component of the adjugate vector (3.5) and discuss their sign; see Figure 4.3(c).

The first component r_1 is calculated as the Pfaffian of the submatrix $A_{\hat{1}}$. The summands contributing to $\text{Pf}(A_{\hat{1}})$ originate from the near-perfect matchings of $\mathcal{N}^{(9)}$ for which the first node is removed, that is, the perfect matchings of the subnetwork $\mathcal{N}(A_{\hat{1}})$. Three such near-perfect matchings exist (see Figure 4.3(c)(i)):

$$\begin{aligned}
\mu_{\hat{1},1} &= \big((2\to 3),(4\to 5),(6\to 7),(8\to 9)\big)\ ,\\
\mu_{\hat{1},2} &= \big((2\to 7),(3\to 4),(5\to 6),(8\to 9)\big)\ ,\\
\mu_{\hat{1},3} &= \big((2\to 3),(4\to 7),(5\to 6),(8\to 9)\big)\ .
\end{aligned}$$

The first of the above near-perfect matchings, $\mu_{\hat{1},1}$, comprises only edges from the Hamiltonian cycle. The two other near-perfect matchings, $\mu_{\hat{1},2}$ and $\mu_{\hat{1},3}$, include contributions

from the Hamiltonian cycle and, in addition, one interior edge. Thus, r_1 is computed as:

$$\begin{aligned} r_1 &= (-1)^{1+1}\mathrm{Pf}(A_{\hat{1}}), \\ &= \begin{bmatrix} \mathrm{sign}\,(2\ 3\ 4\ 5\ 6\ 7\ 8\ 9)\, a_{23}a_{45}a_{67}a_{89} \\ +\mathrm{sign}\,(2\ 7\ 3\ 4\ 5\ 6\ 8\ 9)\, a_{27}a_{34}a_{56}a_{89} \\ +\mathrm{sign}\,(2\ 3\ 4\ 7\ 5\ 6\ 8\ 9)\, a_{23}a_{47}a_{56}a_{89} \end{bmatrix}, \\ &= (+1)a_{32}a_{54}a_{76}a_{98} + (+1)a_{72}a_{43}a_{65}a_{98} \\ &\quad + (+1)a_{32}a_{74}a_{65}a_{98}\ . \end{aligned}$$

The sign of the near-perfect matchings is calculated via the number of transpositions to order its elements in size.

The permutation $\mu_{\hat{1},1}$ is already ordered in size and, thus, equals the identity permutation $\mu_{\hat{1},1} = (2\ 3\ \ldots\ 8\ 9) = \sigma_{\mathbb{1}}$. For odd components of the adjugate vector, the permutation containing only edges from E_{cycle} always equals the identity permutation and, thus, has the sign $+1$. The first component of the adjugate vector is strictly positive because the permutations corresponding to $\mu_{\hat{1},2}$ and $\mu_{\hat{1},3}$ are ordered by an even number of transpositions, such that r_1 contains three positive summands.

For the second component, r_2, there exists only one perfect matching of $\mathcal{N}(A_{\hat{2}})$, which contains only edges from the Hamiltonian cycle; see Figure 4.3(c)(ii):

$$\mu_{\hat{2},1} = \big((3 \to 4), (5 \to 6), (7 \to 8), (9 \to 1)\big)\ .$$

Interior edges do not contribute to any near-perfect matching of $\mathcal{N}^{(9)}$ for which node 2 is removed. In general, it is both the placement of the interior edges relative to each other and their placement relative to the deleted node that determines whether additional near-perfect matching arise or not. For r_2, it follows:

$$\begin{aligned} r_2 &= (-1)^{1+2}\mathrm{Pf}(A_{\hat{2}})\ , \\ &= (-1)\ \mathrm{sign}\,(3\ 4\ 5\ 6\ 7\ 8\ 9\ 1)\, a_{34}a_{56}a_{78}a_{91}\ , \\ &= a_{43}a_{65}a_{87}a_{19}\ . \end{aligned} \tag{4.4}$$

For other even components of the adjugate vector, the permutation of the near-perfect matching containing only edges from E_{cycle} is also not ordered in size in the same way as for r_2. The identity permutation $\sigma_{\mathbb{1}} = (1\ 2\ \ldots \alpha - 1\ \alpha + 1\ \ldots S)$ is achieved with an odd number of transpositions, resulting in the sign -1. This minus sign is balanced by the prefactor $(-1)^{1+\alpha}$ in the adjugate vector. Therefore, all summands in all components, which arise from near-perfect matching with only edges from the Hamiltonian cycle, have the same sign.

Similarly, all other components of the adjugate vector are calculated from which r_8 as an instructive component is further discussed in the following. There exist five near-perfect

matchings of $\mathcal{N}^{(9)}$ upon omitting node 8; see Figure 4.3(c)(iii):

$$\begin{aligned}
\mu_{\hat{8},1} &= \big((2 \to 3), (4 \to 5), (6 \to 7), (9 \to 1)\big) \ , \\
\mu_{\hat{8},2} &= \big((2 \to 7), (3 \to 4), (5 \to 6), (9 \to 1)\big) \ , \\
\mu_{\hat{8},3} &= \big((2 \to 3), (4 \to 7), (5 \to 6), (9 \to 1)\big) \ , \\
\mu_{\hat{8},4} &= \big((1 \to 2), (4 \to 5), (6 \to 7), (9 \to 3)\big) \ , \\
\mu_{\hat{8},5} &= \big((1 \to 2), (4 \to 7), (5 \to 6), (9 \to 3)\big) \ .
\end{aligned} \tag{4.5}$$

Again, the first near-perfect matching $\mu_{\hat{8},1}$ comprises only edges stemming from the Hamiltonian cycle, while $\mu_{\hat{8},2}, \mu_{\hat{8},3}$ and $\mu_{\hat{8},4}$ involve contributions from the Hamiltonian cycle and exactly one interior edge. The corresponding permutations have the same sign because an even number of transpositions maps the partitions to the partition stemming from $\mu_{\hat{8},1}$; similarly as for the discussion of r_1. The near-perfect matching $\mu_{\hat{8},5}$, however, contains the two non-crossing interior edges $(4,7)$ and $(9,3)$. The sign of the permutation equals the sign of the identity permutation (which corresponds to the ordered set) because each interior edge fulfills the cycle condition (4.2) and, thus, can be transferred to the partition stemming from $\mu_{\hat{8},1}$ by an even number of transpositions. This reasoning can be generalized to any number of interior, non-crossing edges occurring in the same near-perfect matching. The eighth component of the adjugate vector is, thus, obtained as:

$$\begin{aligned}
r_8 &= (-1)^{1+8}\mathrm{Pf}(A_{\hat{8}}) \ , \\
&= (-1) \cdot \begin{bmatrix}
\ \ \mathrm{sign}\,(2\ 3\ 4\ 5\ 6\ 7\ 9\ 1)\, a_{23}a_{45}a_{67}a_{91} \\
+\mathrm{sign}\,(2\ 7\ 3\ 4\ 5\ 6\ 9\ 1)\, a_{27}a_{34}a_{56}a_{91} \\
+\mathrm{sign}\,(2\ 3\ 4\ 7\ 5\ 6\ 9\ 1)\, a_{23}a_{47}a_{56}a_{91} \\
+\mathrm{sign}\,(1\ 2\ 4\ 5\ 6\ 7\ 9\ 3)\, a_{12}a_{45}a_{67}a_{93} \\
+\mathrm{sign}\,(1\ 2\ 4\ 7\ 5\ 6\ 9\ 3)\, a_{12}a_{47}a_{56}a_{93}
\end{bmatrix} \ , \\
&= a_{32}a_{54}a_{76}a_{19} + a_{72}a_{43}a_{65}a_{19} + a_{32}a_{74}a_{65}a_{19} \\
&\quad + a_{21}a_{54}a_{76}a_{39} + a_{21}a_{74}a_{65}a_{39} \ .
\end{aligned} \tag{4.6}$$

In total, the adjugate vector for the Hamiltonian network $\mathcal{N}^{(9)}$ is written out for all components in Figure 4.3(d). The adjugate vector of $\mathcal{N}^{(9)}$ is not the zero-vector for any choice of non-vanishing weights, such that the kernel of $A(\mathcal{N}^{(9)})$ is one-dimensional for all choices of weights; see Section 3.3.3. The network topology of $\mathcal{N}^{(9)}$ determines the signs of all summands in all entries and components of the adjugate vector (4.7). Because all these summands have the same sign, the kernel is strictly positive for all choices of weights and, thus, the network topology $\mathcal{N}^{(9)}$ is a coexistence network.

In summary, the decomposition of the edge-set into edges from the cycle and interior edges, $\mathcal{N}^{(9)} = E^{(9)}_{\mathrm{cycle}} \cup E^{(9)}_{\mathrm{in}}$, leads to a separation of all near-perfect matchings into two sets. The first set consists of all near-perfect matchings containing only edges of the Hamiltonian cycle E_{cycle}. These near-perfect matchings are identical to the near-perfect matchings of a directed cycle of size S. Analogous to the adjugate vector of odd cycles, the

signs of these near-perfect matchings alternate such that the corresponding contributions to the adjugate vector (3.5) have the same sign ($\mathrm{sign}(\mathrm{Pf}(A_{\hat{\alpha}})) = (-1)^{\alpha-\beta}\mathrm{sign}(\mathrm{Pf}(A_{\hat{\beta}}))$), see Section 4.2. The second set consists of all near-perfect matchings containing one or several interior edges E_{in}. The cycle condition (4.2) and the crossing condition (4.3) together ensure that the signs of all near-perfect matchings excluding the same node are identical. Thus, $\mathcal{N}^{(9)}$ is a coexistence network.

Edge-wise decomposition of the adjugate vector. To establish the coexistence conditions (4.2) and (4.3) for coexistence networks, it is also insightful to partition the adjugate vector into contributions arising from the presence of interior edges. For example, the adjugate vector of the network $\mathcal{N}^{(9)}$ in Figure 4.3(a) can be written as:

$$
\begin{aligned}
\boldsymbol{r} &= \boldsymbol{r}_{\mathrm{cycle}} + \boldsymbol{r}_{\mathrm{in}} \ , \\
&= \boldsymbol{r}_{\mathrm{cycle}} + \boldsymbol{r}_{2\to 7} + \boldsymbol{r}_{4\to 7} + \boldsymbol{r}_{9\to 3} + \boldsymbol{r}_{4\to 7,9\to 3} \ , \\
&= \begin{pmatrix} a_{32}a_{54}a_{76}a_{98} \\ a_{43}a_{65}a_{87}a_{19} \\ a_{21}a_{54}a_{76}a_{98} \\ a_{32}a_{65}a_{87}a_{19} \\ a_{21}a_{43}a_{76}a_{98} \\ a_{32}a_{54}a_{87}a_{19} \\ a_{21}a_{43}a_{65}a_{98} \\ a_{32}a_{54}a_{76}a_{19} \\ a_{21}a_{43}a_{65}a_{87} \end{pmatrix} + \begin{pmatrix} a_{72}a_{43}a_{65}a_{98} \\ 0 \\ 0 \\ 0 \\ 0 \\ 0 \\ 0 \\ a_{72}a_{43}a_{65}a_{19} \\ 0 \end{pmatrix} + \begin{pmatrix} a_{32}a_{74}a_{65}a_{98} \\ 0 \\ a_{21}a_{74}a_{65}a_{98} \\ 0 \\ 0 \\ 0 \\ 0 \\ a_{32}a_{74}a_{65}a_{19} \\ 0 \end{pmatrix} + \begin{pmatrix} 0 \\ 0 \\ 0 \\ a_{21}a_{65}a_{87}a_{39} \\ 0 \\ a_{21}a_{54}a_{87}a_{39} \\ 0 \\ a_{21}a_{54}a_{76}a_{39} \\ 0 \end{pmatrix} + \begin{pmatrix} 0 \\ 0 \\ 0 \\ 0 \\ 0 \\ 0 \\ 0 \\ a_{21}a_{74}a_{65}a_{39} \\ 0 \end{pmatrix} .
\end{aligned}
\tag{4.7}
$$

The contribution of the Hamiltonian cycle to the adjugate vector is denoted as $\boldsymbol{r}_{\mathrm{cycle}}$, which is the adjugate vector of a directed cycle of 9 nodes in the ascending labeling. The contributions from near-perfect matchings of one interior edge and edges from the cycle are denoted as $\boldsymbol{r}_{2\to 7}, \boldsymbol{r}_{4\to 7}$ and $\boldsymbol{r}_{9\to 3}$. The remaining contribution $\boldsymbol{r}_{4\to 7,9\to 3}$ arises because these two non-crossing interior edges occur together in a near-perfect matching. $\boldsymbol{r}_{\mathrm{in}}$ summarizes all contributions to the adjugate vector that stem from near-perfect matchings and include one or several interior edges. In this edge-wise notation, the contribution of a single interior edge to the adjugate vector can be suitably discussed: whether it creates one or several near-perfect matchings, whether these matchings arise through combinations with edges of the Hamiltonian cycle only or in combination with further interior edges, and whether their signs agree with the near-perfect matching stemming from the cycle.

Necessity of the conditions. As demonstrated by the previous example, every Hamiltonian network in which all internal edges fulfill the coexistence conditions (4.2) and (4.3) is a coexistence network. Furthermore, the coexistence conditions are not only sufficient, but also necessary to obtain a coexistence network. By reversing the direction of an edge, the signs of the respective summands occurring in the adjugate vector change because of an additional transposition in the permutation. Thus, every Hamiltonian network not fulfilling conditions (4.2) and (4.3) is not a coexistence network; see Section 4.C.

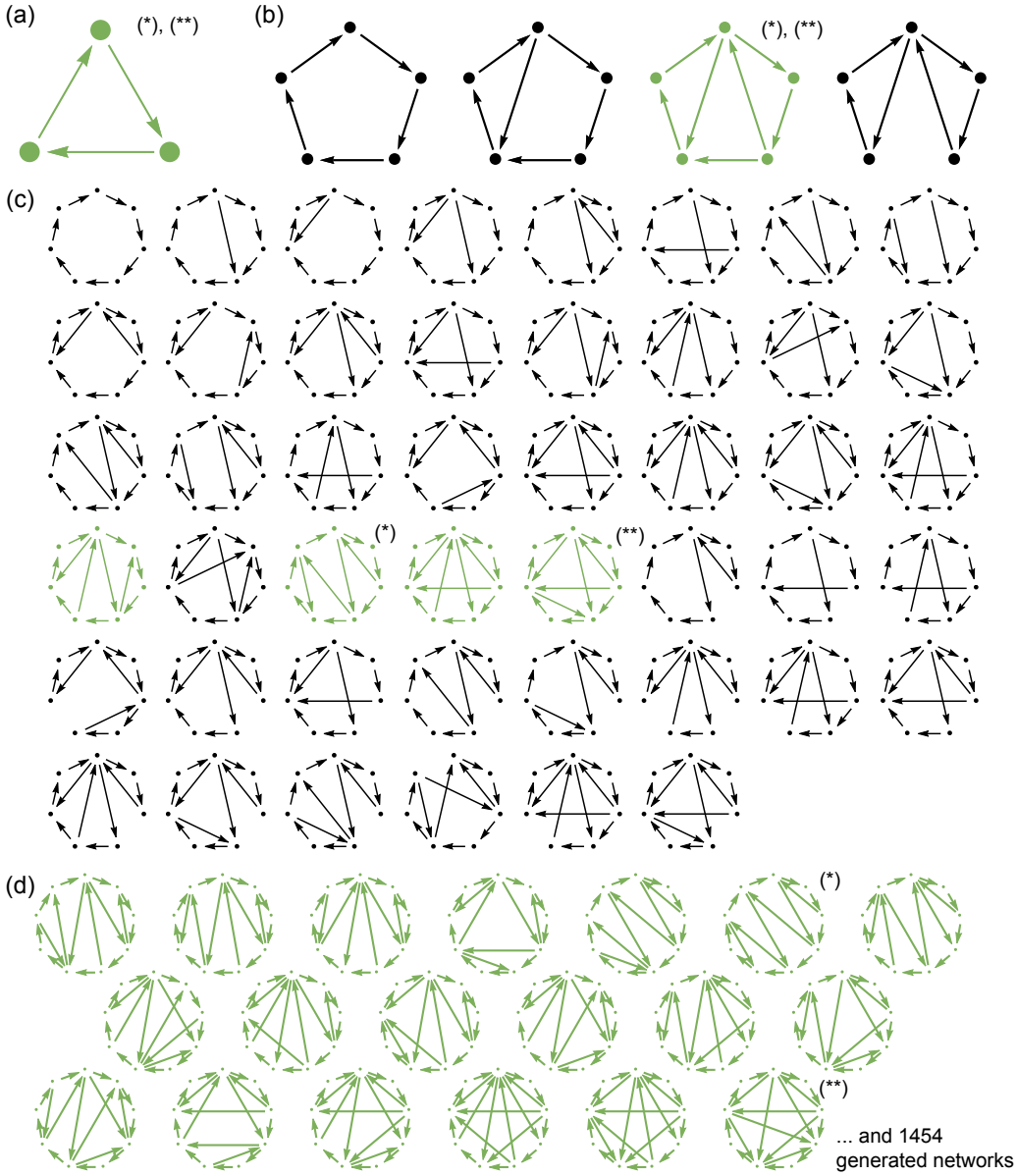

Figure 4.4: All coexistence networks with up to 9 nodes. We determined all coexistence networks for up to $S \leq 9$ by establishing all Hamiltonian coexistence networks via the graph-theoretical coexistence conditions (4.2) and (4.3) and deleting suitable edges; see Section 4.3.3. (a)-(c) All coexistence networks for $S = 3, 5$, and 7 nodes. Coexistence networks are, for example, cycles, concatenations of smaller coexistence networks, and so-called generating coexistence networks (green color). Generating coexistence networks have a saturated number of edges: Upon adding any further edge to their network topology, they are no longer coexistence networks. (*) denotes specific triangulations of cycles that are discussed in Section 4.4.1. These are dilute networks, but the total number of near-perfect matchings grows exponentially fast with the number of nodes S at a rate characterized by the golden ratio $\varphi = 1.6180...$; see Equation (4.10). (**) denotes cycles with complete subnetworks; see Section 4.4.2. These networks are dense, but the total number of near-perfect matchings grows only polynomially as $\sim S^3$. (d) Generating coexistence networks with 9 nodes. Upon deleting suitable edges from these generating coexistence networks, all other 1454 coexistence networks for $S \leq 9$ are generated.

4.3.2 Non-Hamiltonian coexistence networks

Non-Hamiltonian coexistence networks can be generated by deleting suitable links from Hamiltonian coexistence networks. To illustrate this approach, consider the network topology that is obtained by deleting the cycle edge $(2,3)$ from the above-studied Hamiltonian network $\mathcal{N}^{(9)}$ (equivalently, by setting $a_{32} = 0$ in $A(\mathcal{N}^{(9)})$). The resulting network $\mathcal{N}^{(9)}\backslash\{(2,3)\}$ is not Hamiltonian because no directed cycle passes through all of the network's nodes. The adjugate vector of this non-Hamiltonian network is obtained from the adjugate vector (4.7) by setting all entries $a_{32} = 0$.

Even though six previously existing near-perfect matchings vanish upon deleting the edge $(2,3)$ (four near-perfect matchings from the cycle, and two involving the interior edge $(4,7)$), all components of the resulting adjugate vector are different from 0 and all summands in all components have the same sign. In other words, the kernel of the corresponding antisymmetric matrix is still strictly positive for all choices of weights due to the contributions from the previously interior edges. Thus, the non-Hamiltonian network topology $\mathcal{N}^{(9)}\backslash\{(2,3)\}$ is a coexistence network.

In general, deleting edges from a Hamiltonian coexistence network can only decrease the number of its near-perfect matchings. Note that the resulting network does not have to be factor-critical or strongly connected (for example, upon deleting the edge $(5,6)$ from $\mathcal{N}^{(9)}$, $A_4^\downarrow$ does not have a perfect matching). However, as long as the network remains factor-critical upon removing edges, it remains a coexistence network. This can be seen as follows: Removing edges from the network leads to removing summands in the adjugate vector. On the other hand, factor-criticality of the remaining network ensures that for every component at least one perfect matching and, thus, one summand in every component of the adjugate vector, remains. Potentially non-Hamiltonian coexistence networks arise if edges are deleted from the defining Hamiltonian cycle of a Hamiltonian coexistence network as illustrated for the network topology $\mathcal{N}^{(9)}\backslash\{(2,3)\}$. The smallest non-Hamiltonian coexistence network has five nodes; see Figure 4.4(b). It is constituted of two 3-cycles that are trivially concatenated at one node. The smallest nontrivial non-Hamiltonian coexistence networks, which are *not* obtained by concatenating smaller coexistence networks at single nodes, have seven nodes; see Figure 4.4(c).

4.3.3 All coexistence networks with up to 9 nodes

Numerical methods. In order to support our theoretical findings from above, we numerically determined all coexistence networks for up to 9 nodes with two different methods. In our first method, we used the coexistence conditions (4.2) and (4.3) to successively build Hamiltonian coexistence networks, and deleted suitable edges to generate both all Hamiltonian and also non-Hamiltonian coexistence networks; see Section 4.A.1 for details. Through a second method, we determined all coexistence networks in an algebraic manner. This approach explicitly exploits the notion of the adjugate vector (3.5) of an antisymmetric matrix; see Section 4.A.2. Only networks with up to 9 nodes were considered in our study. Investigation of networks with a larger number of nodes was limited by the com-

putational effort to identify isomorphic networks (see Section 4.A.1 for details). Crucially, our numerical results confirm that both methods yield the same coexistence networks for up to 9 states, which also numerically confirms the validity of the coexistence conditions for Hamiltonian coexistence networks.

All coexistence networks for $S \leq 9$. The obtained list of coexistence networks for three, five, and seven nodes are shown in Figure 4.4(a)-(c). Coexistence networks depicted in green indicate so-called *generating coexistence networks*. A generating coexistence network is Hamiltonian and has a saturated number of edges: Upon adding any further edge to this network topology, it is not a coexistence network any longer. In general, every Hamiltonian coexistence network can be generated from a generating coexistence network by deleting suitable interior edges. Our numerical enumerations show that for $S \leq 9$ also all non-Hamiltonian coexistence networks can be created from generating coexistence networks by deleting suitable interior and cycle edges. For $S = 7$ nodes, for example, four generating coexistence networks exist; see Figure 4.4(c). All other Hamiltonian coexistence networks as well as all non-Hamiltonian are obtained from the four generating coexistence networks by deleting suitable edges. The specific form of two of these generating coexistence networks is further discussed in the next Section 4.4. Because of the large number of coexistence networks for $S = 9$ (in total 1473 coexistence networks), only the generating coexistence networks are depicted in Figure 4.4(d), from which again all coexistence networks are obtained. Whether also for $S \geq 10$ all non-Hamiltonian coexistence networks can be created from generating coexistence networks remains open at present. Furthermore, it is an interesting question to us, whether all coexistence networks can be obtained by concatenating and fusing Hamiltonian coexistence networks of smaller size.

Do coexistence networks with a degenerate kernel exist? Our numerical simulations of coexistence networks with $S \leq 9$ nodes did not yield any coexistence network with a kernel dimension other than $\dim(\mathrm{Ker}(A)) = 1$. In other words, all coexistence networks, which we identified thus far, are odd-sized and have a strictly positive adjugate vector (3.5). In Section 4.B.1, we show that coexistence networks with a two-dimensional kernel do not exist. Whether coexistence networks with a degenerate kernel ($\dim(\mathrm{Ker}(A)) > 2$) exist, remains an open question to us at present.

4.4 Specific generating coexistence networks

In the following, we discuss two examples of classes of generating coexistence networks. These two exemplary classes are chosen because of their simple topological structure that can be constructed for arbitrary odd size. Furthermore, they illustrate the importance of topology for both the complexity and diversity of coexistence networks. Applications of these insights are further discussed in Section 4.5. The first class of coexistence networks comprises specific triangulations of odd cycles; see Figure 4.5(a). As an application of the correspondence between the adjugate vector and the steady state concentrations of

the ALVE (2.1), we propose a protocol to dynamically measure the golden ratio and the Fibonacci numbers by using these triangulations. The second class comprises coexistence networks, which are fully connected on the subnetwork of all odd nodes; see Figure 4.5(b). Applications of these and other coexistence networks are discussed in Section 4.5.

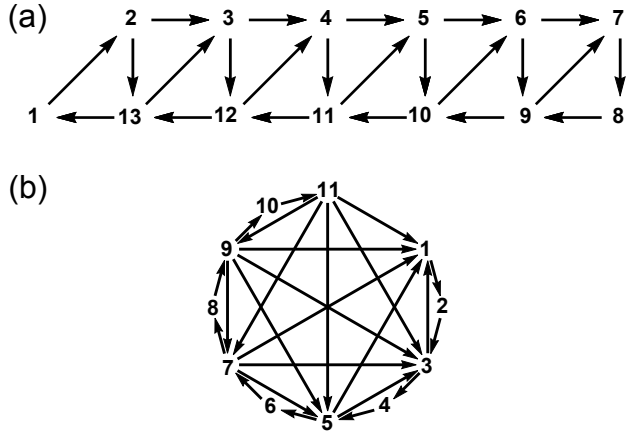

Figure 4.5: Specific generating coexistence networks. (a) Triangulation of a cycle of size $S = 13$. The orientation of the interior edges is chosen such that the network is a generating coexistence network. The adjugate vector is obtained as $\boldsymbol{r}^{(13)} = (13, 8, 5, 6, 6, 5, 8, 13, 8, 10, 9, 10, 8)$ if unit weights are chosen. Each entry equals the number of near-perfect matchings if the corresponding node is deleted from the network. The ratio of its first two entries converges to the golden ratio $\varphi = 1.6180...$ as $S = 2n - 1 \to \infty$. The total number of near-perfect matchings in the network is obtained from the sum over all entries of this adjugate vector and grows exponentially fast at a rate characterized by φ; see Equation (4.10). (b) Cycle of size $S = 11$ with a complete subnetwork on the odd nodes. The adjugate vector for unit weights is obtained as $\boldsymbol{r}^{(11)} = (1, 5, 1, 8, 1, 9, 1, 8, 1, 5, 1)$. Such networks are dense (1/4 of all possible edges are realized as $S \gg 1$, as opposed to the triangulations for which only $\sim 4/S$ of all possible edges are realized). Even though these networks are dense, the number of near-perfect matchings grows only polynomially with the system size S.

4.4.1 Triangulations of cycles

Triangulations of cycles are dilute networks. A triangulation of a cycle is created by adding the maximal amount of internal edges such that no crossing edges occur. That is, the cycle is divided into triangles. Every triangulation of an odd-sized cycle can be oriented to be a Hamiltonian coexistence network because interior edges in a triangulation do not cross each other and, thus, can always be oriented to fulfill the cycle condition (4.2). Here, we consider a specific class of triangulations of odd-sized cycles, which give rise to generating coexistence networks; see Figure 4.5(a) and the networks indicated with (*) in Figure 4.4. These triangulations are created by adding to a cycle of odd size S the ascending edges $(2, S), (3, S-1), (4, S-2), \ldots, ((S-1)/2, (S-1)/2+3)$ and the descending edges $(S, 3), (S-1, 4), \ldots, ((S-1)/2+3, (S-1)/2+1)$. In other words, this triangulation is

obtained from merging the two directed paths $S \to 1 \to 2 \to 3 \cdots \to S-1 \to S$ (in total, S edges that form the cycle) and $2 \to S \to 3 \to S-1 \to \ldots...(S-1)/2 \to (S-1)/2+3 \to (S-1)/2+1$ (in total, $S-3$ interior edges that triangulate the cycle). Note that the total number of edges in a triangulation grows as $\sim 2S$ for $S \gg 1$. Compared to a complete network of S nodes (with $\binom{S}{2} \sim S^2/2$ edges), only $\sim 4/S$ of the possible edges are realized in a triangulation for $S \gg 1$. Heuristically speaking, triangulations are dilute (or sparse) network topologies.

These triangulations are generating coexistence networks. Triangulations that are built in the above manner are coexistence networks because they are Hamiltonian networks, and all of their interior edges fulfill the coexistence conditions. The cycle condition (4.2) is fulfilled because every interior edge does not create any even-sized cycle, and the crossing condition (4.3) is trivially fulfilled because no two interior edges cross each other. A network topology, in which an arbitrary interior edge is added to this triangulation, will not be a coexistence network any longer, which can be seen as follows. For every node α of the network, there is a neighboring node ($\alpha+1$ or $\alpha-1$) that is both starting and end point of two different interior edges. Because of the way in which these triangulations are created, every additional interior edge starting or ending in α crosses at least one neighboring interior edge such that the distance between starting and end points is 1. Therefore, the crossing condition is violated in triangulations with an additional interior edge. Taken together, the presented triangulations of odd cycles are generating coexistence networks.

Counting the total number of near-perfect matchings by choosing unit rates. It is worth calculating the adjugate vector for these triangulations explicitly for unit weights. Upon setting all weights to 1 in a coexistence network, the αth component of the adjugate vector r_α counts the number of near-perfect matchings for node α, that is, the number of perfect matchings when node α is removed from the coexistence network; see also Figure 4.6 for an illustration. Because the constructed triangulations are coexistence networks, the adjugate vector is strictly positive for all choices of weights. With unit rates, the sum over all entries of the adjugate vector, $|\sum_\alpha r_\alpha|$, counts the total number of near-perfect matchings in the coexistence network. Note that this procedure to count the number of near-perfect matchings can be applied to any undirected graph for which an orientation as a coexistence network can be found. We refer to such an orientation as a Pfaffian orientation of an odd-sized graph; see Section 4.5.3 for a detailed discussion of this application in the context of the dimer problem in statistical physics.

Number of near-perfect matchings for triangulations is characterized by the golden ratio. We found that the adjugate vector of the triangulation of a cycle of odd size $S = 2n-1$ ($n = 2, 3, \ldots$) with chosen unit weights is analytically computed as (see

Section 4.D.1 for details):

$$r_\alpha = \begin{cases} F(n) & \text{, for } \alpha = 1 \text{ ,} \\ F(n+1-\alpha)F(\alpha-1) & \text{, for } \alpha = 2,\ldots,n \text{ ,} \\ F(2n+1-\alpha)F(\alpha-n) & \text{, for } \alpha = n+1,\ldots,2n-1 \text{ ,} \end{cases} \tag{4.8}$$

where $F(k)$ denotes the kth Fibonacci number with $F(0) = 0, F(1) = 1$, and $F(k+1) = F(k) + F(k-1)$, a linear recursive sequence as discussed in Section 6.E. For example, the adjugate vector of the triangulation of the cycle of size $S = 13$ ($n = 7$) is obtained as $\boldsymbol{r}^{(13)} = (13, 8, 5, 6, 6, 5, 8, 13, 8, 10, 9, 10, 8)$. The Fibonacci numbers arise in this context because of the iterative decomposition of the triangulations into the so-called ladder graphs [84]; see Section 4.D.1. The total number of near-perfect matchings #(npm) for the triangulation of an odd-sized cycle is calculated (by applying the convolution expansion for Fibonacci numbers [84, 85]) as:

$$\#(\text{npm}) = nF(n)\frac{1}{5}\left(3\frac{F(n+1)}{F(n)} + 1 + \frac{1}{n}\right) \text{ ,} \tag{4.9}$$

which grows asymptotically as:

$$\#(\text{npm}) \sim \frac{3\varphi+1}{5\sqrt{5}} n \mathrm{e}^{\ln\varphi\cdot n} \quad \text{, for } n \gg 1. \tag{4.10}$$

Here, $\varphi = 1/2\left(1+\sqrt{5}\right)$ denotes the golden ratio. Note that the ratio of two consecutive Fibonacci numbers converges to the golden ratio ($F(n+1)/F(n) \to \varphi$ and $F(n) \sim \varphi^n/\sqrt{5}$ as $n \to \infty$). In other words, the total number of near-perfect matchings grows exponentially fast with the system size $S = 2n-1$ at a rate determined by the golden ratio φ; see Section 4.5.3 for discussion.

Dynamical measurement of the Fibonacci numbers and the golden ratio. Interestingly, these results on the triangulations of cycles of odd size $S = 2n-1$ suggest a recipe to *dynamically measure* the Fibonacci numbers and the golden ratio that we present in the following. Recall from Section 2.4 that, if the kernel of A is one-dimensional, the adjugate vector determines the kernel element and, after normalization, equals the steady state concentrations $\langle \boldsymbol{x} \rangle_T = \frac{1}{T}\int_0^T \mathrm{d}s\ \boldsymbol{x}(s)$ in the ALVE (2.1) as $t \to \infty$. Therefore, after normalization, the entries of the adjugate vector (4.8) denote the steady state concentrations of the evolutionary zero-sum game that is defined by the triangulation of an odd-sized cycle as $\langle x_i \rangle_\infty \coloneqq \lim_{t\to\infty}\langle x_i\rangle_t = r_i/\#(\text{npm})$. Note also that, because all entries r_i of the adjugate vector (4.8) scale as $r_i \sim \mathcal{O}(\varphi^n)$ or $\sim \mathcal{O}(\varphi^{n+1})$ as $n \gg 1$ for all i, the trajectory defined by the ALVE (2.1) remains in the center of the $(S-1)$-simplex Δ_{S-1}.

As an application of the correspondence between the adjugate vector and the steady state concentrations, one may carry out the following protocol to dynamically measure the golden ratio and the Fibonacci numbers:

1. Pick a number $n = 2, 3, \ldots$.

2. Construct the triangulation of the cycle $\mathcal{N}_{\text{triang}}$ of (odd) size $S = 2n - 1$ by merging the two directed paths $S \to 1 \to 2 \to 3 \cdots \to S - 1 \to S$ and $2 \to S \to 3 \to S - 1 \to \ldots ...(S-1)/2 \to (S-1)/2 + 3 \to (S-1)/2 + 1$ as illustrated in Figure 4.5. Choose unit weights for every edge. $A(\mathcal{N}_{\text{triang}})$ denotes the antisymmetric adjacency matrix of the constructed weighted network.

3. Simulate the evolutionary zero-sum game defined by $A(\mathcal{N}_{\text{triang}})$, that is, numerically integrate the ALVE (2.1) specified by $A(\mathcal{N}_{\text{triang}})$.

4. Measure the long-time average of all state concentrations $\langle \boldsymbol{x} \rangle_t = \frac{1}{t} \int_0^t \mathrm{d}s \; \boldsymbol{x}(s)$ for $t \gg 1$.

5. Compute approximate values of:

   - the golden ratio φ by computing the ratio $\langle x_1 \rangle_t / \langle x_2 \rangle_t$, which converges to $F(n)/F(n-1)$ as $t \to \infty$ (and $F(n)/F(n-1) \to \varphi$ as $n \to \infty$);
   - the Fibonacci number $F(k)$ by computing the ratio $\prod_{l=1}^{k} \langle x_{n+l} \rangle_t / \langle x_l \rangle_t$ for $k = 1, 2, \ldots, n-1$, which converges to $F(k)$ as $t \to \infty$. $F(n)$ is obtained by computing the ratio $\langle x_{n+1} \rangle_t / \langle x_n \rangle_t \prod_{l=1}^{k} \langle x_{n+l} \rangle_t / \langle x_l \rangle_t$ as $t \to \infty$.

     The Fibonacci numbers can also be computed more efficiently by successively computing the ratios $\langle x_{n+1} \rangle_t / \langle x_1 \rangle_t$ (converging to $F(1)$ as $t \to \infty$), $F(1) \langle x_{n+2} \rangle_t / \langle x_2 \rangle_t$ (converging to $F(2)$ as $t \to \infty$), continuing with $F(k-1) \langle x_{n+k} \rangle_t / \langle x_k \rangle_t$ (converging to $F(k)$ as $t \to \infty$) for $k = 1, 2, \ldots, n-1$, and finally computing $F(n-1) \langle x_{n+1} \rangle_t / \langle x_n \rangle_t$ (converging to $F(n)$ as $t \to \infty$).

Even though we are not aware of any real-world application of the above protocol and the procedure is not numerically efficient, this measurement of the Fibonacci numbers and the golden ratio with a dynamical system is an interesting number-theoretical observation.

Topological phase transitions in triangulations of cycles. Triangulations of cycles can be constructed in such a way that the network is translationally invariant, apart from the boundary, see Figure 4.5(a). Exploiting (i) that the triangulation of a cycle is a coexistence network and (ii) that the network has a regular structure makes this a good example to analyze topological phase transitions in the ALVE. Here, due to (i) the condensate vector provides insight into the dynamics as it is the asymptotic limit of the temporal average occupation of the nodes. As the triangulation is a coexistence network. we can choose the weights arbitrarily together with (ii), the network is a finite one dimensional lattice. In this setting, we find that the change of a control parameter leads to polarization in the condensate vector, a phenomenon which can be understood in the framework of topological phase transitions as known from condensed matter physics. The details of this analysis are presented in Chapter 5 and Chapter 6.

4.4.2 Cycles with complete subnetworks

Cycles with complete subnetworks are dense networks. Odd-sized cycles with complete subnetworks on the odd nodes are generating coexistence networks as well; see Figure 4.5(b) and the networks indicated with (**) in Figure 4.4. These network topologies are built by starting from an odd-sized cycle of size $S = 2n-1$ in ascending labeling $S = 2n-1 \to 1 \to 2 \to \cdots \to 2n-2 \to 2n-1$ and adding descending edges between all pairs of odd nodes, that is, $E_{\text{in}} = \{(2n-1, 2n-3), (2n-1, 2n-5), \ldots (2n-1, 1), (2n-3, 2n-5), \ldots, (2n-3, 1), \ldots, (3, 1)\}$. Thus, the number of interior edges is given by $\binom{n}{2} - 1$ (the complete network on the odd nodes with $\binom{n}{2}$ edges minus the cycle edge $(S, 1)$). The total number of edges in this network topology grows as $(S-1)(S+9)/8$ such that a ratio of $(1+9/S)/4$ of the possible edges are realized compared with a complete network in which all possible edges are realized. This ratio scales as $\sim 1/4$ for $S \gg 1$. Thus, these network topologies are dense network topologies (that is, with a macroscopic number of edges).

Cycles with complete subnetworks are generating coexistence networks. These cycles with complete subnetworks on the odd nodes are coexistence networks because they are Hamiltonian networks, and the coexistence conditions are fulfilled by construction: Every interior edge is descending and the difference between start and end node is even (the cycle condition (4.2) is fulfilled), and the minimal distance between the starting nodes and end nodes of two crossing edges is always even (the crossing condition (4.3) is fulfilled). Upon adding another arbitrary edge, the network topology is not a coexistence network any longer, which can be seen as follows. Any further edge (k, l) needs to either start or end in an even node (or both). Therefore, the added edge would cross the interior edge connecting the two neighboring odd nodes (connecting either nodes $k-1$ and $k+1$, or $l-1$ and $l+1$). Thus, the minimal distance between the start and end nodes of the added edge and the crossing edge is always 1, which is not even. In other words, every additional interior edge creates a network in which the crossing condition is violated. In total, the cycle with a complete subnetwork on the odd nodes is a generating coexistence network.

Number of near-perfect matchings for cycles with complete subnetworks grows polynomially slowly. To further characterize cycles with complete subnetworks of size $S = 2n-1$ ($n = 2, 3, \ldots$), we computed the total number of near-perfect matchings by setting all weights equal to 1 and calculating the adjugate vector (3.5) as described before. We found that the adjugate vector is obtained as (see Section 4.D.2 for details):

$$r_i = \begin{cases} 1 & \text{, for } i \text{ odd ,} \\ \frac{i(n-i/2)}{2} & \text{, for } i \text{ even .} \end{cases} \tag{4.11}$$

For example, the adjugate vector of the network topology of size $S = 11$ ($n = 6$) is obtained as $\boldsymbol{r}^{(11)} = (1, 5, 1, 8, 1, 9, 1, 8, 1, 5, 1)$; see Figure 4.5. The total number of near-perfect matchings is computed as:

$$\#(\text{npm}) = n + \frac{1}{6}(n-1)n(n+1) \ , \tag{4.12}$$

which grows polynomially as $\sim n^3/6$ for $n \gg 1$.

Summary. In this section we have investigated specific triangulations of odd-sized cycles that are dilute networks (with $\sim 4/S$ edges realized of all possible edges), but their number of near-perfect matchings grows exponentially fast with S at a rate characterized by the golden ratio. Additionally, we have shown that, even though odd-sized cycles with complete subnetworks on the odd nodes are dense network topologies (1/4 of all possible edges are realized as $S \gg 1$), the number of their near-perfect matchings grows only polynomially $\sim S^3$ with the system size. This different scaling behavior between the two classes of network topologies underlines the importance of the topology of a network. The number of near-perfect matchings of a network, and thus the structure of the adjugate vector, mainly depends on the arrangement of internal edges, but only secondary on their number. Topology matters.

4.5 Applications of coexistence networks

In the following, we present applications of our results on coexistence networks in different contexts. We outline applications of coexistence networks for the ALVE, which was our initial motivation of this work. These applications include topologically robust zero-sum games in evolutionary game theory and topologically robust quantum networks for non-interacting bosons in driven-dissipative systems. Furthermore, our results on coexistence networks find also applications for symmetric zero-sum games in the field of game theory and for the dimer problem for odd-sized graphs in statistical physics.

4.5.1 The ALVE and coexistence networks: Topologically robust coexistence in evolutionary game theory and driven-dissipative bosonic systems

The ALVE has applications in physics and biology. The ALVE was originally studied in the context of population biology by Volterra [19, 86], and has recently gained attention (i) as the replicator equation for zero-sum games (in the field of evolutionary game theory) and (ii) as the equation of motion for non-interacting bosons in driven-dissipative systems (in the field of open quantum systems) [27, 25, 2, 37, 38, 87, 19, 88, 86, 89, 90, 91, 20, 92, 93]. Furthermore, the ALVE occurs in the fields of plasma physics and chemical kinetics as summarized in reference [2]. In the following, we outline applications of coexistence networks to evolutionary game theory and open quantum systems.

Replicator dynamics for symmetric zero-sum games. In the context of evolutionary game theory, the ALVE is derived as the replicator equation of zero-sum games [27, 25, 2, 92]. States correspond to pure strategies (labeled by $\alpha = 1, \ldots, S$) that are played by agents in a well-mixed population. Agents interact pair-wisely with each other through a prescribed symmetric zero-sum game (antisymmetric payoff matrix A such that the value of the game is zero) or, equivalently, by a weighted network. The payoff gained or lost in each interaction translates to fitness and determines the rate at which agents of a certain strategy reproduce. The ALVE describes the temporal evolution of the fraction of agents

x_α playing strategy α in an infinitely large population. Depending on the entries of the payoff matrix, one typically observes the survival of certain strategies in the population and the extinction of others at long times [28, 1, 89, 90, 91]. In other words, some of the strategies will not be played by the agents of the population at long times while other strategies survive and constitute the so-called evolutionary stable set of strategies [25].

Topologically robust evolutionary zero-sum games. Our work was originally motivated by the observation of zero-sum games in evolutionary game theory for which all strategies coexist *for all choices* of interaction strengths. The rock-paper-scissors zero-sum game [25, 94, 95, 87] and cycles with an odd number of strategies are coexistence networks [80, 81], and we asked whether other coexistence networks with a more complex interaction structure exist. Our results on how to determine these coexistence networks as described in Section 4.3 are not trivial because strategies typically go extinct for some choice of interaction strengths [1]. Coexistence networks as determined in this work may give rise to topologically robust zero-sum games in evolutionary game theory. Irrespective of the chosen interaction strengths, all strategies will be played in the population. No extinction can ever occur on these network topologies.

Condensation dynamics in driven-dissipative, bosonic systems. In the context of open quantum systems, the ALVE describes the condensation dynamics of non-interacting bosons in driven-dissipative systems [37, 2, 38]. In a theoretical model that was proposed only recently [37], a system of non-interacting bosons is weakly coupled to a heat bath and driven by an external, time-periodic potential (a so-called Floquet system [96, 97, 98]). On a coarse-grained time scale, the dynamics of this open quantum system becomes incoherent [37, 38]. In other words, in this effective description the temporal evolution of such a driven-dissipative quantum system is captured by a classical stochastic process. Each state $\alpha = 1, \ldots, S$ corresponds to a quantum Floquet state and the fraction of bosons in this state is given by the concentration x_α. Even though the bosons transition incoherently between the different quantum states, the transition rates still reflect the quantum statistics of the bosons: The more bosons occupy a quantum Floquet state, the higher is the rate for other bosons to jump into this state, reflecting the fact that bosons tend to congregate due to their indistinguishability. Furthermore, the differences of forward and backward jump rates between any two states are characterized by an antisymmetric matrix A, whose entries depend on microscopic properties of the system, the heat bath, and the coupling between the two. Due to these dynamics, certain quantum Floquet states become condensates over time, that is, bosons congregate in a subset of the possible states, while other states become depleted. It was shown [2] that the ALVE captures this condensation on the leading-order time scale. Whether a state becomes a condensate or a depleted state depends on the antisymmetric matrix A alone. This theoretical observation can be understood as a generalization of the Bose-Einstein condensation in thermodynamic equilibrium to a condensation of bosons in nonequilibrium [37], which has stimulated further research recently [99, 100, 101, 40, 102].

Topologically robust bosonic quantum networks. Coexistence networks as determined in this work give rise to topologically robust quantum networks, in which all states are condensates and no state becomes depleted, irrespective of how the individual jump rates

are tuned. However, coexistence networks cannot be complete networks (see the list of coexistence networks in Figure 4.4 and the networks in Figure 4.5 for illustration). It is straightforward to show that some transitions between states need to be forbidden (or forward and backward jump rate need to be equal) in order to create a coexistence network. Once it is possible to engineer the topology of such transition networks for non-interacting bosons in driven-dissipative systems, topologically robust quantum networks, in which none of the states becomes depleted, might be observable.

4.5.2 Game theory and coexistence networks: Stability of optimal, totally mixed strategies in symmetric zero-sum games

Our results on coexistence networks may also gain significance in the field of game theory for symmetric zero-sum games and so-called tournaments [103, 104, 105, 106] that we outline in the following.

Symmetric zero-sum games in game theory. Tournaments are typically introduced as symmetric two-player zero-sum games on fully connected networks of size S with unit payoff. In other words, all pairs of different nodes of the game's network (representing the S actions that the two players pick from) are connected by a directed edge with weight $+1$ (representing the dominance relation between the actions; that is, the payoff matrix is antisymmetric, $A = -A^T$, and all off-diagonal entries are ± 1) [103, 104, 105, 106]. Tournament games were introduced as a generalization of the rock-paper-scissors game with unit weights [103]. More generally, *weighted tournaments* are symmetric zero-sum games on a fully connected network with arbitrary payoff (that is, the payoff matrix is antisymmetric and all off-diagonal entries are non-zero) [107], while *weak tournaments* are characterized by unit payoff on an arbitrary network topology (that is, the payoff matrix is antisymmetric, off-diagonal entries may be zero and non-zero entries are ± 1) [108]. If neither the game's underlying network topology nor the weights of the payoff are restricted, one simply refers to the game as a *symmetric zero-sum game* characterized by the antisymmetric payoff matrix $A = -A^T \in \mathbb{R}^{S\times S}$. The results of our work apply to such symmetric zero-sum games.

Optimal strategies in symmetric zero-sum games. For symmetric zero-sum games, one is typically interested in so-called optimal sets of actions (or briefly an *optimal strategy*), in which "optimal" may have different meanings depending on the context [105, 109]. For example, an optimal set of actions may denote a probability vector ($\boldsymbol{p}^* \in \Delta_{S-1}$, that is, $\boldsymbol{p}^* \in \mathbb{R}^S$, $\boldsymbol{p}^* \geq 0$, and $\sum_{i=1}^S p_i = 1$), whose ith entry denotes the probability to play the ith action, and that maximizes the player's minimum expected payoff against all other sets of actions (a so-called *mixed Nash equilibrium* of the symmetric game [110, 111]). For a symmetric zero-sum game, it is straightforward to show that a normalized positive kernel vector $\boldsymbol{p}^* \geq 0$ of the payoff matrix ($A\boldsymbol{p}^* = 0$) is an optimal strategy. A single action of this optimal strategy is referred to as essential if it is chosen with non-vanishing probability ($p_i^* > 0$). In other words, in an infinitely repeated game, it is reasonable to choose an essential action. If all actions of the optimal strategy are essential ($\boldsymbol{p}^* > 0$), the optimal

strategy is called *totally mixed* [104]; that is, all actions are played. One central result obtained for odd-sized tournaments is that an optimal, totally mixed strategy always exists and is unique. In other words, there exists a unique way to optimize the player's payoff in odd-sized tournament games and all possible actions must be played [103, 112]. Recent research results further characterized optimal, totally mixed strategies and extended this concept to other types of games [113, 107, 114, 105, 108, 104, 115, 116].

Stability of optimal, totally mixed strategies in coexistence networks. Our results on coexistence networks contribute to this line of research by identifying the symmetric zero-sum games whose optimal, totally mixed strategies are stable. An optimal, totally mixed strategy of a game is referred to as *stable* if all actions remain essential for any change of the payoff on the game's network topology [117]. In other words, arbitrary changes of the payoff values do not change the fact that all actions are essential (even though their specific probability to be played may change). In our work, we determined and characterized those antisymmetric matrices (defining the game's network topology) whose kernel remains one-dimensional and strictly positive for all choices of off-diagonal entries. Therefore, coexistence networks define symmetric zero-sum games for which the optimal strategy is totally mixed for any choice of payoff values; see Section 4.3. The list of coexistence networks in Figure 4.4 depicts the network topologies of such games for $S \leq 9$.

Note that, apart from the rock-paper-scissors game, none of the coexistence networks are complete graphs as already mentioned above. Instead, our discussion of coexistence networks in Section 4.4 exemplifies how symmetric zero-sum games with an arbitrary number of nodes can be constructed to have a unique optimal, totally mixed strategy for all choices of payoff values. These games include, for example, cycles with S edges, triangulations of cycles with $\sim 2S$ edges, and cycles with complete subnetworks and $\sim \frac{1}{4}S^2$ edges; see Sections 4.2 and 4.4. The stability of optimal strategies against arbitrary changes of payoff values in symmetric zero-sum games is, in general, an interesting topic for further research, for example, when the optimal strategy is not totally mixed or not unique.

4.5.3 Graph theory and coexistence networks: Pfaffian orientation and the dimer problem of odd-sized graphs

One interesting application of our results on coexistence networks relates to the so-called dimer problem in statistical physics: How many configurations do exist that completely cover the edges of a lattice graph of even size with non-overlapping dimer molecules? In graph theory and combinatorial mathematics, the dimer problem is connected to counting the number of perfect matchings for a given even-sized graph, and motivated the introduction of the so-called Pfaffian orientation of even-sized graphs [57, 118, 58, 59]. As we explain in the following, our results obtained in this manuscript suggest a possibility to extend the concept of the Pfaffian orientation from even-sized to odd-sized graphs; see also Figure 4.6 for an illustration. This way, our results facilitate the study of closed-packed dimer configurations on odd-sized graphs and may stimulate further research in this direction.

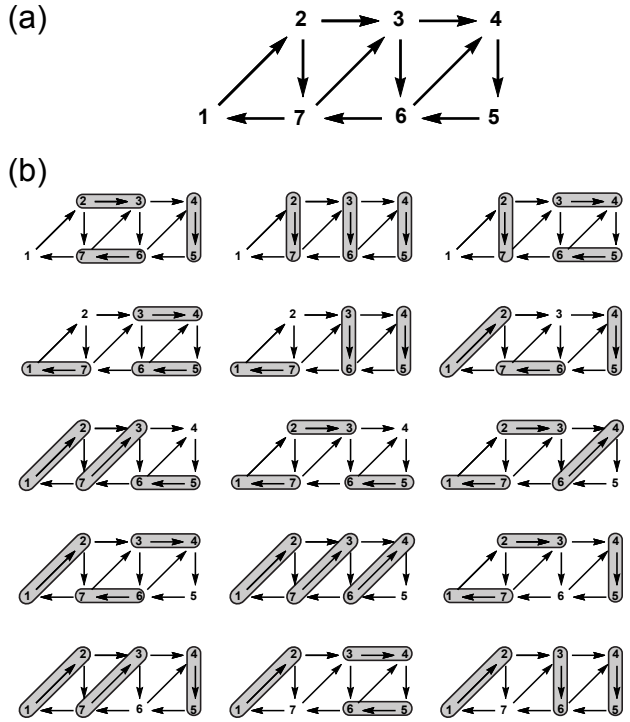

Figure 4.6: The dimer problem for graphs of odd size. (a) What is the number of closest-packing configurations with dimers (so-called dimer coverings) for the triangulation of a cycle of size $S = 7$? A closest-packing configuration is a covering of the graph that leaves only one node of the graph uncovered. Our results obtained in Section 4.3 show that this question can be answered for all factor-critical coexistence networks. (b) All possible dimer coverings of the triangulation in (a) are depicted. Each closest-packing configuration with one uncovered node corresponds to one near-perfect matching of the triangulation. In total, 15 near-perfect matchings exist. The number of near-perfect matchings excluding node i equals the ith component of the adjugate vector of the chosen directed graph (the Pfaffian orientation of the network topology) upon setting all weights to one. Here, the adjugate vector is obtained as $\boldsymbol{r}^{(7)} = (3, 2, 1, 2, 3, 2, 2)$ for unit weights; see Equation (4.8). The total number of dimer coverings for the triangulation of a cycle grows exponentially fast with the number of nodes S at a rate characterized by the golden ratio $\varphi = 1.6180...$; see Section 4.4.1 for details.

The dimer problem in statistical physics. Starting with the work of Kasteleyn, Fisher, and Temperley [57, 118, 58, 59], the graph-theoretical interpretation of the Pfaffian (3.2) has been appreciated and applied in statistical physics to compute the entropy of dimer molecules adsorbed on lattices. Such systems are typically defined by regular lattice graphs of even size on which dimer molecules cover the graph's vacancies. Every dimer molecule covers two connected nodes of the graph and dimers do not overlap. Of specific interest are closed-packing configurations (so-called dimer coverings), for which every node of the graph is covered exactly once by a dimer and the graph is completely filled. The partition function counts the total number of such dimer coverings and its computation is often

referred to as the *dimer problem*. The contribution of a dimer covering to the partition function may be weighted by introducing edge weights to the graph.

Counting the number of dimer coverings of regular lattice graphs was first motivated in statistical physics by the adsorption of dimer molecules on two-dimensional surfaces. Kasteleyn, Fisher, and co-workers [57, 118, 119] also established a connection of the two-dimensional dimer problem to the two-dimensional Ising model. Notably, the dimer problem gained fresh attention through the work of Rokhsar and Kivelson [120] to describe the so-called short-range resonating valence bond ground state in the field of superconductivity; see, for example, reference [121] for a concise description of the physical background and on how the quantum dimer problem relates to the classical dimer problem described above. All of these physical applications continue to stimulate the research of dimer statistics on lattices and networks in the fields of statistical physics and graph theory; see below.

Pfaffian orientation of even-sized graphs. From a mathematical point of view, counting the number of dimer configurations that cover the whole graph amounts to counting the number of perfect matchings of that graph. As it was motivated in Section 3.3.2, the Pfaffian (3.2) can be thought of as the sum of the signed perfect matchings of a graph. Therefore, to count the number of perfect matchings, it suffices to find an orientation of that graph (that is, assigning every edge a direction) such that every perfect matching has the same sign. Such an orientation of an even-sized graph is referred to as a *Pfaffian orientation* [83]. Thus, upon assigning every directed edge the weight $+1$ on a Pfaffian orientation of the graph, the value of the Pfaffian of its antisymmetric adjacency matrix equals the number of perfect matchings. In other words, the Pfaffian of a graph's antisymmetric adjacency matrix in a chosen Pfaffian orientation equals the partition function for the dimer problem on that graph.

Two questions are of specific interest for the dimer problem: (i) Which graphs admit a Pfaffian orientation? (ii) If a Pfaffian orientation of a graph exists, how many perfect matchings exist on that graph?

Question (i). Kasteleyn showed that every *planar graph* has a Pfaffian orientation [118]. A planar graph can be drawn in the two-dimensional plane such that no two edges intersect. To find a Pfaffian orientation of a planar graph, one can orient the graph's edges such that each face (regions bounded by the graph's edges) has an odd number of lines oriented clockwise. Such an orientation can be found in polynomial time [55]. Ever since this result for planar graphs was established, progress has also been made for Pfaffian orientations of more general graphs [122, 123, 124, 125, 61]. For example, it was shown that a graph of even size has a Pfaffian orientation if and only if it can be drawn in the two-dimensional plane (possibly with crossings) such that every perfect matching intersects itself an even number of times [125, 61].

Question (ii). If a graph has a Pfaffian orientation, the number of perfect matchings can be efficiently calculated; see reference [61] for a review and details on the computational complexity of this task. Analytical expressions for the partition function were first obtained for the square lattice by Kasteleyn, Temperley, and Fisher [57, 58, 59], have been computed for other regular lattices [126, 60, 121, 127, 128, 129, 130, 131, 132, 133, 134], such as the honeycomb, triangular, and kagome lattice since then (see [60] for a review), and for other

geometries [124, 135, 136] and scale-free networks [137, 138].

Pfaffian orientation and dimer problem of odd-sized, factor-critical graphs. Our results on coexistence networks suggest that the above concept of a Pfaffian orientation can be generalized to odd-sized, factor-critical graphs. For a given factor-critical graph of odd size one may consider closest-packing configurations with dimers (that is, a dimer covering), which leave only one node of the graph uncovered; see Figure 4.6. The total number of near-perfect matchings of that graph relates, as above, to the partition function of the dimer problem.

A natural generalization of the concept of a Pfaffian orientation from even-sized to odd-sized graphs is obtained in the following sense. In Section 4.3, we constructed those networks $\mathcal{N}(A)$ for which (i) every subnetwork $\mathcal{N}(A_{\hat{\alpha}})$ has a Pfaffian orientation for all α and, moreover, (ii) the signs of the corresponding orientations fulfill the sign-condition $\mathrm{sign}(\mathrm{Pf}(A_{\hat{\alpha}})) = (-1)^{\alpha-\beta}\mathrm{sign}(\mathrm{Pf}(A_{\hat{\beta}}))$ for all α and β. These two conditions originate from the notion of the adjugate vector $\boldsymbol{r}$ (3.5) of an odd-sized antisymmetric matrix A. We emphasize that the sign-condition (ii) imposes a strong condition on the network topology: The signs of all summands in all near-perfect matchings of a network need to be aligned, and not just the sign of the summands of a single perfect matching as for the Pfaffian orientation of an even-sized graph. Thus, networks that fulfill conditions (i) and (ii) can be understood as odd-sized graphs with a Pfaffian orientation.

Factor-critical coexistence networks (see Section 4.3) are networks with a Pfaffian orientation in the above sense because perfect matchings (that is, closest-packing dimer configurations) exist for every node removed from the graph and all of their signs are aligned in the sense of the above conditions (i) and (ii). We note that all coexistence networks that we have found thus far are factor-critical; see Section 4.3.3. The total number of near-perfect matchings can be computed by assigning unit weights to all edges of a factor-critical coexistence network and by computing the adjugate vector of the antisymmetric adjacency matrix. As was demonstrated in Section 4.4, the αth component of the adjugate vector, r_α, then counts the number of perfect matchings when node α is removed. The sum over all components of the adjugate vector, $\sum_\alpha |r_\alpha|$, counts the total number of near-perfect matchings in the factor-critical coexistence network.

As an example for a planar graph, we computed the number of near-perfect matchings for specific triangulations of an odd-sized cycle; see Section 4.4.1 and Figure 4.5(a). We showed that the number of near-perfect matchings #(npm) grows as $\sim n\mathrm{e}^{\ln\varphi\cdot n}$ for $n \gg 1$. Consequently, the entropy of adsorption per dimer molecule on that triangulation of the cycle is given by:

$$s = \lim_{D\to\infty} \frac{1}{D} \ln(\#(\mathrm{npm})) \ , \tag{4.13}$$

$$= \ln\varphi \approx 0.4812... \ . \tag{4.14}$$

Here, D denotes the maximal number of dimers on the graph and is equal to $D = n - 1 = (S-1)/2$ in the notation of Section 4.4.1; $\varphi = 1/2\left(1+\sqrt{5}\right)$ denotes the value of the golden ratio. Notably, the value of the entropy per dimer $s = \ln\varphi \approx 0.4812...$ for the triangulation of the cycle, which is an effectively one-dimensional lattice, lies above the

value of the two-dimensional honeycomb lattice ($s \approx 0.3230$) [126], but below the two-dimensional triangular lattice of even size ($s \approx 0.8571$) [121]; see, for example, Table 1 in reference [60] for further comparison.

Outlook. It will be interesting to extend our results on the Pfaffian orientation and the dimer problem of odd-sized graphs to two-dimensional lattices and non-planar graphs of odd size (see example in Section 4.4.2), and to explore possible phase transitions that might occur upon choosing anisotropic dimer weights.

4.6 Summary and conclusion

After having discussed applications of both coexistence networks and related concepts in Section 4.5, we provide a brief summary of our results and conclude.

Summary of coexistence networks. In this chapter, we introduced the notion of *coexistence networks*, that is, networks which show coexistence of all states in the antisymmetric Lotka-Volterra equation (ALVE) (2.1) as a consequence of the network topology alone. We determined coexistence networks by mapping the question about the dynamical system of the ALVE to an algebraic question of the antisymmetric matrix A, which defines the interactions between the states. By exploiting tools from graph theory related to antisymmetric matrices, we identified coexistence networks.

In detail, we showed that coexistence of all states in the ALVE is independent of the initial conditions and only depends on the antisymmetric matrix A, which defines the interactions between the states. We identified coexistence networks as networks whose weighted adjacency matrix has a strictly positive kernel element for all choices of weights. For matrices A with a one-dimensional kernel, a non-trivial kernel element is computed as the adjugate vector via the Pfaffians of submatrices. Exploiting the graph-theoretical interpretation of the Pfaffian, we characterized the kernel of A in terms of network topological properties, namely by all near-perfect matchings of the network defined by A. This interpretation enabled us to formulate conditions with which to identify Hamiltonian coexistence networks. With these results we, first, constructed Hamiltonian coexistence networks as generalizations of odd-sized, directed cycles. Second, by deleting edges from Hamiltonian coexistence networks, we also constructed non-Hamiltonian coexistence networks. A numerical survey of coexistence networks with up to 9 nodes verifies our results; see Figure 4.4 for an overview. Our results strongly depend on the antisymmetry of the matrix A, which is justified in the context of the applications discussed above. The validity of our results and extensions to more general replicator equations, as occurring in theoretical ecology, are the focus of future research.

Summary of applications of coexistence networks. With respect to the ALVE, we outlined applications in the fields of evolutionary game theory as *topologically robust zero-sum games*. In the context of driven-dissipative systems of non-interacting bosons, topologically robust quantum networks might be an interesting application. The algebraic results of our work include the characterization of antisymmetric matrices whose kernel remains strictly positive for all choices of weights that respect the sign structure of the matrix. We

discussed the applications of our findings in the field of game theory for the stability of optimal, totally mixed strategies in symmetric zero-sum games. Furthermore, coexistence networks suggest the introduction of a Pfaffian orientation for odd-sized graphs to study the dimer problem on such graphs.

Methodological approach and outlook. Besides these specific applications of coexistence networks, we emphasize the methodological approach with which we studied the long-time behavior of the ALVE. With a suitable mapping from the dynamical system to an algebraic problem (via a Lyapunov function or a conserved quantity) and by solving the algebraic problem with a graph-theoretical approach, we characterized topologically robust coexistence in the ALVE. It might be possible to generalize this approach to study topologically stable attractors of general Lotka-Volterra systems on arbitrary networks [6, 7, 139] or in other population-dynamical models [140, 141, 142].

Overall, we believe that the results of this work will stimulate further research to investigate the interplay between interaction topologies and nonlinear dynamical systems. Ultimately, such studies will help to characterize the long-time behavior of nonequilibrium systems.

4.A Numerical methods for the determination of coexistence networks

We numerically determined all coexistence networks for $S \leq 9$ nodes with two different methods. In our first approach, we used conditions (4.2) and (4.3) to constructively generate all coexistence networks. The second approach consisted of algebraically determining all coexistence networks to verify the results of the first approach.

4.A.1 Method 1: Construction of coexistence networks via conditions (4.2) and (4.3)

To generate coexistence networks, we implemented conditions (4.2) and (4.3) as a constructive algorithm. By successively adding edges fulfilling both conditions to a cycle of odd size ($S \to 1 \to 2 \to \cdots \to S$), we constructed an exhaustive list of Hamiltonian coexistence networks. From that list, we deleted network duplicates, that is, isomorphic network topologies. Only networks with up to 9 nodes were considered because of the limiting computing time needed to identify the vast number of both possible network duplicates (naively there are $S!$ ways to label S nodes) and network isomorphisms.

Note that in our understanding two networks are isomorphic if one network is equal to the other after reversing all of its edges and/or suitably relabeling its nodes. In other words, a graph isomorphism is expressed in terms of multiplication with -1 and/or simultaneous reordering of row and column vectors of the antisymmetric adjacency matrix. This notion of isomorphism of network topologies is justified by the algebraic properties of the antisymmetric adjacency matrix. A relabeling of all nodes is achieved by multiplying the antisymmetric matrix with permutation matrices, whose eigenvalues are ± 1 only; see [143]. Therefore, algebraic characteristics such as positivity of the kernel and spectrum do not change under such operations for an antisymmetric matrix.

4.A.2 Method 2: Algebraic determination of coexistence networks via the adjugate vector (3.5)

Additionally, we determined all coexistence networks for up to networks of 9 nodes through a second, algebraic approach. For all possible orientations of all connected, undirected graphs, we examined whether a strictly positive kernel of the antisymmetric adjacency matrix is obtained for all choices of weights. Starting from databases containing all undirected graphs, we exploited, first, necessary conditions for coexistence networks with an one-dimensional kernel and, second, the notion of the adjugate vector (3.5) to find all orientations of undirected graphs that form coexistence networks.

We started with a list of all connected, undirected graphs with $S \leq 9$ nodes. In reference [144], complete lists are available for up to $S = 10$ nodes; the number of undirected graphs grows super-exponentially for larger S. For every undirected graph in that list, we

examined whether it admits an orientation yielding a coexistence network through a sieve of necessary conditions that is outlined in the following.

(i) First, we checked whether the graph can be oriented such that it is strongly connected (in the graph-theoretical literature referred to as *2-edge-connected* [83, 82]). Every network that is not strongly connected cannot admit an orientation yielding a coexistence network and, thus, does not have to be considered further; see Section 3.4.

(ii) If the (undirected) graph can be oriented to be strongly connected, we checked whether it admits at least one near-perfect matching. For graphs having at least one near-perfect matching, the kernel of the antisymmetric adjacency matrix is structurally one-dimensional and is given by the adjugate vector (see Section 3.3.4). Thus far, we have not found any coexistence network whose kernel is not one-dimensional; see Section 4.3.3.

(iii) Next, we checked whether the (undirected) graph is factor-critical. An undirected graph having a near-perfect matching, but not being factor-critical has at least one zero-entry in its adjugate vector (3.5) irrespective of the orientation of that graph. Thus, such a graph cannot be oriented to be a coexistence network. For factor-critical graphs, however, every component of the adjugate vector (3.5) has at least one non-vanishing summand irrespective of the orientation; see Section 3.3.2.

(iv) Only for factor-critical graphs did we search for an orientation such that all summands occurring in the adjugate vector (3.5) have the same sign; see Section 3.4. To this end, we computed all near-perfect matchings from the above-diagonal matrix elements. By choosing $+1, -1$ as matrix entries, the signs of all summands for all orientations were tested, and all coexistence networks were determined.

Carrying out the described procedure for all connected, undirected graphs with $S \leq 9$ nodes yields all coexistence networks (up to graph isomorphisms; see above). The list obtained through our algebraic approach agrees with the list of coexistence networks that was constructed as described in Section 4.A.1 (see also Figure 4.4. of the main text).

4.B Topological constraints for coexistence networks

In the following we introduce some constraints that the network topology puts on the kernel vectors of its corresponding matrix. As for coexistence networks the kernel is vital, these constraints give exclusion conditions for networks to be topologically robust.

4.B.1 No coexistence networks with a two-dimensional kernel

Overview. If the dimension of the kernel of a network's antisymmetric adjacency matrix is zero, the network does not have non-trivial kernel elements and, thus, no strictly positive kernel vectors. Consequently, this network topology cannot be a coexistence network. In

case of a one-dimensional kernel, we identified coexistence networks through the adjugate vector (3.5). Sufficient and necessary conditions for Hamiltonian coexistence networks of odd size were determined and all coexistence networks with up to 9 nodes were identified; see Sections 4.3.1-4.3.3 of the main text. Here we supplement the statements from the main text (see Section 4.3.3) by showing that there are no coexistence networks with a two-dimensional kernel $\dim(\mathrm{Ker}(A)) = 2$. We employ the adjugate matrix (3.9) to show this result. Whether coexistence networks with a high-dimensional kernel $\dim(\mathrm{Ker}(A)) \geq 3$ exist, remains open at present.

Proof: No coexistence networks with a two-dimensional kernel. We use an argument by contradiction to show that coexistence networks cannot have a two-dimensional kernel. Assume that $\mathcal{N}(A)$ is a coexistence network with a two-dimensional kernel (its minimal kernel dimension is 2). Thus, A has a strictly positive kernel vector for every choice of weights. We choose the rates such that indeed $\dim(\mathrm{Ker}(A)) = 2$ and it is possible to choose two strictly positive kernel vectors u and v that are linear independent and form a basis of the kernel of A.

For antisymmetric matrices with a two-dimensional kernel, the kernel vectors can be calculated with help of the adjugate matrix (3.9). If the kernel of A is two-dimensional, the antisymmetric adjugate matrix has nonzero entries, its rank is 2, and two linearly independent column vectors form a basis of the kernel space. We denote the column vectors of the adjugate matrix R as $\boldsymbol{r}^{(\beta)}$ ($\beta = 1, \ldots, S$) with elements $r_\alpha^{(\beta)} = R_{\alpha\beta}$ for $\alpha, \beta = 1, \ldots, S$.

Because the column vector of the adjugate matrix are kernel vectors of A (see Section 3.3.3), they can be expressed as linear combinations of u and v: $r_i^\beta = \mu^{(\beta)} u_\alpha^{(\beta)} + \nu^{(\beta)} v_\alpha^{(\beta)}$. From the antisymmetry of the adjugate matrix ($r_{\beta\beta} = 0$), it follows that:

$$\nu^{(\beta)} = -\mu^{(\beta)} \frac{v_\beta}{u_\beta} \ , \ \text{for all } \beta = 1, \ldots, S \ . \tag{4.15}$$

By assumption, the network has a two-dimensional kernel (or higher dimension) for all choices of weights. Thus, the Pfaffian of A is always zero and the network has no perfect matching; see Section 3.3.2.

Because the network is a coexistence network, it is strongly connected; see Section 3.4. In particular, for every node γ, one finds another node δ that is connected to γ. In the following we show that $R_{\gamma\delta} = R_{\delta\gamma} = 0$ follows. Because nodes γ and δ are connected, the network created by deleting these nodes, $A_{\hat{\delta}\hat{\gamma}}$, has no perfect matching. If $A_{\hat{\delta}\hat{\gamma}}$ had a perfect matching, A would have a perfect matching as well (by combining the perfect matching of $A_{\hat{\delta}\hat{\gamma}}$ together with the edge connecting δ and γ); which is in contradiction to the assumption that the minimal kernel dimension is 2. Therefore, $\mathrm{Pf}(A_{\hat{\delta}\hat{\gamma}}) = 0$ and $R_{\delta\gamma} = R_{\gamma\delta} = 0$ as claimed. Furthermore, it follows that $R_{\delta\gamma} = r_\delta^{(\gamma)} = \mu^{(\gamma)} u_\alpha + \nu^{(\gamma)} v_\alpha = 0$, and with Equation (4.15) for index k: $0 = \mu^{(\gamma)} u_\alpha - \mu^{(\gamma)} \frac{v_\gamma}{u_\gamma} v_\alpha = 0$. If $\mu^{(\gamma)} = 0$, it also follows that $\boldsymbol{r}^{(\gamma)} = \boldsymbol{0}$, which is in contradiction to $\dim(\mathrm{Ker}(A)) = 2$ because γ is arbitrary. As a

consequence, if node γ and δ are connected, it follows that:

$$u_\gamma u_\delta - v_\delta v_\gamma = 0 \ . \tag{4.16}$$

This argument can be carried out iteratively for all pairs of connected nodes. This way, it follows that for any two nodes γ and δ, which are connected via a path of arbitrary length, it holds $u_\gamma u_\delta - v_\delta v_\gamma = 0$.

Because the network is strongly connected, one finds indeed for every pair of nodes γ and δ a path in the network that connects the two nodes, that is, $u_\gamma u_\delta - v_\delta v_\gamma = 0$ for all γ, δ. Therefore, the two vectors $\boldsymbol{u}$ and $\boldsymbol{v}$ are *not* linearly independent, which is in contradiction to the assumption at the beginning. In other words, the network A cannot be a coexistence network and have a two-dimensional kernel. This proves that coexistence networks with a two-dimensional kernel do not exist.

Outlook: Do coexistence networks with minimal kernel dimension ≥ 3 exist? Our numerical simulations of coexistence networks with up to 9 nodes (see Section 4.3.3) show that network topologies that give rise to high-dimensional kernels ($\dim(\mathrm{Ker}(A)) \geq 3$) are not coexistence networks. In other words, we have not found any coexistence network with minimal kernel dimension different from 1 thus far. At present, it remains to us an open question for future research, whether this numerical observation generalizes to networks with $S \geq 10$: Do coexistence networks exist whose minimal kernel dimension is ≥ 3?

4.C Proof of the conditions for Hamiltonian coexistence networks

In the following, we provide the proof for the main results stated in Section 4.3: A Hamiltonian network is a coexistence network if and only if in an ascending labeling all interior edges fulfill the coexistence conditions, that is the cycle condition (4.2) and the crossing condition (4.3).

4.C.1 Set-up of the proof

Notation: adjugate vector $\boldsymbol{r} = \boldsymbol{r}_{\mathbf{cycle}} + \boldsymbol{r}_{\mathbf{in}}$. Recall that we label the nodes of a Hamiltonian network $E(\mathcal{N}) = E_{\mathrm{cycle}} \cup E_{\mathrm{in}}$ with $E_{\mathrm{cycle}} \cap E_{\mathrm{in}} = \emptyset$ in an ascending manner such that the Hamiltonian cycle is given by the edge-set $E_{\mathrm{cycle}} = \{(1,2),(2,3),\ldots,(S-1,S),(S,1)\}$. Similar to the example in Section 4.3.1, we separate the adjugate vector of this network into two components, such that $\boldsymbol{r} = \boldsymbol{r}_{\mathrm{cycle}} + \boldsymbol{r}_{\mathrm{in}}$. In this notation, $\boldsymbol{r}_{\mathrm{cycle}}$ contains only contributions from the edges that form the Hamiltonian cycle E_{cycle}. The vector $\boldsymbol{r}_{\mathrm{in}}$ contains all contributions stemming from the interior edges E_{in}. This separation is always possible because the presence of (near-)perfect matchings containing only cycle edges is not altered by interior edges. Adding interior edges only leads to additional near-perfect matchings.

$\boldsymbol{r}_{\text{cycle}}$ as the reference for the comparison of signs. Since an odd cycle is a coexistence network (see also Section (4.2)), all components of $\boldsymbol{r}_{\text{cycle}}$ have the same sign. As a consequence, a Hamiltonian network is a coexistence network if for every deleted node i all permutations of all near-perfect matchings have the same sign as the permutation of the near-perfect matching containing only edges of the cycle. This way, we compare all summands in $r_{\text{in},i}$ with the one summand in $r_{\text{cycle},i}$. If these signs agree for every component, the signs of all summands agree because they do so for $\boldsymbol{r}_{\text{cycle}}$. Effectively, the adjugate vector of the cycle $\boldsymbol{r}_{\text{cycle}}$ serves as a reference for the signs that are induced by the interior edges through near-perfect matchings.

Notation: relabel nodes such that $\hat{\alpha} \to \hat{S}$. Note that the property of being a coexistence network is independent of the order in which the nodes of the network are labeled. In algebraic terms, a relabeling of the nodes is achieved by multiplying the adjacency matrix with permutation matrices, which does not change the spectral properties of the network and the structural properties of the kernel. Therefore, if all signs in the adjugate vector are equal in one selected labeling, the signs are equal in every labeling. For convenience, we relabel the nodes of the system such that the node, which is not part of the near-perfect matching, has the index S by shifting the node labels as $\alpha \to S, \alpha + 1 \to 1, \ldots$. This shift facilitates an easier comparison of signs because the permutation corresponding to the perfect matching of the cycle after relabeling is the identity (that is, $(1\ 2\ \ldots\ S-1)$) and, thus, has the sign $(+1)$.

Directed paths contribute to near-perfect matchings if they are even-sized. Furthermore, we denote the set of edges of the network, from which the αth node was deleted, as $E_{\text{cycle},\hat{\alpha}}$ and after relabeling as $E_{\text{cycle},\hat{S}}$. After relabeling, the remaining edges of $E_{\text{cycle},\hat{S}}$ form a directed path from 1 to $S-1$. In the following, we also denote such a directed path as $P[1, S-1] = \{(1,2),(2,3),\ldots,(S-2,S-1)\}$. In general, a directed path $P[\alpha,\beta] = \{(\alpha,\alpha+1),(\alpha+1,\alpha+2),\ldots,(\beta-1,\beta)\}$ has a perfect matching if the number of nodes in the path $|P| = \beta - \alpha + 1$ is even and, thus, $\beta - \alpha$ is odd. Thus, only directed paths of even length contribute to perfect matchings.

Structure of the proof. First, we prove that a Hamiltonian coexistence network is a coexistence network if the coexistence conditions (4.2) and (4.3) are fulfilled. We show that the permutations all near-perfect matchings which contain (one or several) interior edges have the same sign as the near-perfect matching of the cycle. This step proves that the coexistence conditions are sufficient; see Section 4.C.2. Second, we consider all cases in which interior edges do not fulfill the coexistence conditions. We show that, under this assumption, near-perfect matchings arise that have a different sign than the near-perfect matching of the cycle. This step proves that the coexistence conditions are necessary; see

Section 4.C.3.

4.C.2 Sufficiency of the conditions (9) and (10) for coexistence networks

First, we show that a Hamiltonian network is a coexistence network if all of its interior edges E_{in} fulfill the coexistence conditions (4.2) and (4.3). To show sufficiency of the conditions, we assume a Hamiltonian network in which all interior edges fulfill the coexistence conditions. We investigate all near-perfect matchings that can arise through the presence of interior edges and discuss their sign as follows. For the subnetwork created by deleting node i (denoted by $A_{\hat{i}}$) we (i) relabel the nodes in the manner mentioned above, such that $\hat{i} \to \hat{S}$, (ii) analyze for every subset $U \subseteq E_{\text{in}}$ whether it can be completed to a perfect matching of $A_{\hat{S}}$ using only edges from $E_{\text{cycle},\hat{S}}$ (that is, the edges of the cycle that remain after deleting node i and after relabeling $\hat{i} \to \hat{S}$), (iii) then determine the sign of the resulting perfect matching, (iv) and compare the sign with the sign of the perfect matching of $A_{\hat{i}}$ that includes only edges from $E_{\text{cycle},\hat{i}}$ (that is, the near-perfect matching of the cycle; its sign is referred to as $\text{sign}(\sigma_{\mathbb{1}})$). We discuss all cases for possible subsets of interior edges $U \subseteq E_{\text{in}}$ in the following.

Trivial cases: $U = \emptyset$, $\hat{S} \in U$, and interior edges starting or ending in the same node. For the case $U = \emptyset$, there are no contributions from interior edges to any near-perfect matching of the network. When the deleted vertex $\hat{S}$ is part of an edge in U, a near-perfect matching including all edges in U and excluding S does not exist. Furthermore, when two or more edges in U share the same node, they cannot be part of the same perfect matching. In the following, these trivial cases are disregarded.

U contains a single edge ($|U| = 1$). The simplest case, for which interior edges can contribute to the network's near-perfect matchings is $|U| = 1$. In this case, only the cycle condition (4.2) applies to the edge in U, but not the crossing condition (4.3). For this case, we denote $U = \{e\}$ with $e = (e_{\text{start}}, e_{\text{end}})$ after relabeling of the cycle ($\hat{\alpha} \to \hat{S}$) and discuss the contribution of edge e to a perfect matching of $A_{\hat{S}}$.

If the nodes of the interior edge e contribute to the perfect matching of $A_{\hat{S}}$, the unmatched nodes are $\{1, 2, \ldots, S-1\} \backslash \{e_{\text{start}}, e_{\text{end}}\}$. After deleting e, the remaining edges of E_{cycle} form three paths:
$X = P[1, \min(e_{\text{start}}, e_{\text{end}}) - 1]$,
$Y = P[\min(e_{\text{start}}, e_{\text{end}}) + 1, \max(e_{\text{start}}, e_{\text{end}}) - 1]$, and
$Z = P[\max(e_{\text{start}}, e_{\text{end}}) + 1, S - 1]$; see Figure 4.7(b).
A perfect matching of $A_{\hat{S}}$ including e is possible if and only if all three created paths have a perfect matching on their own, that is, the difference between highest and lowest node is

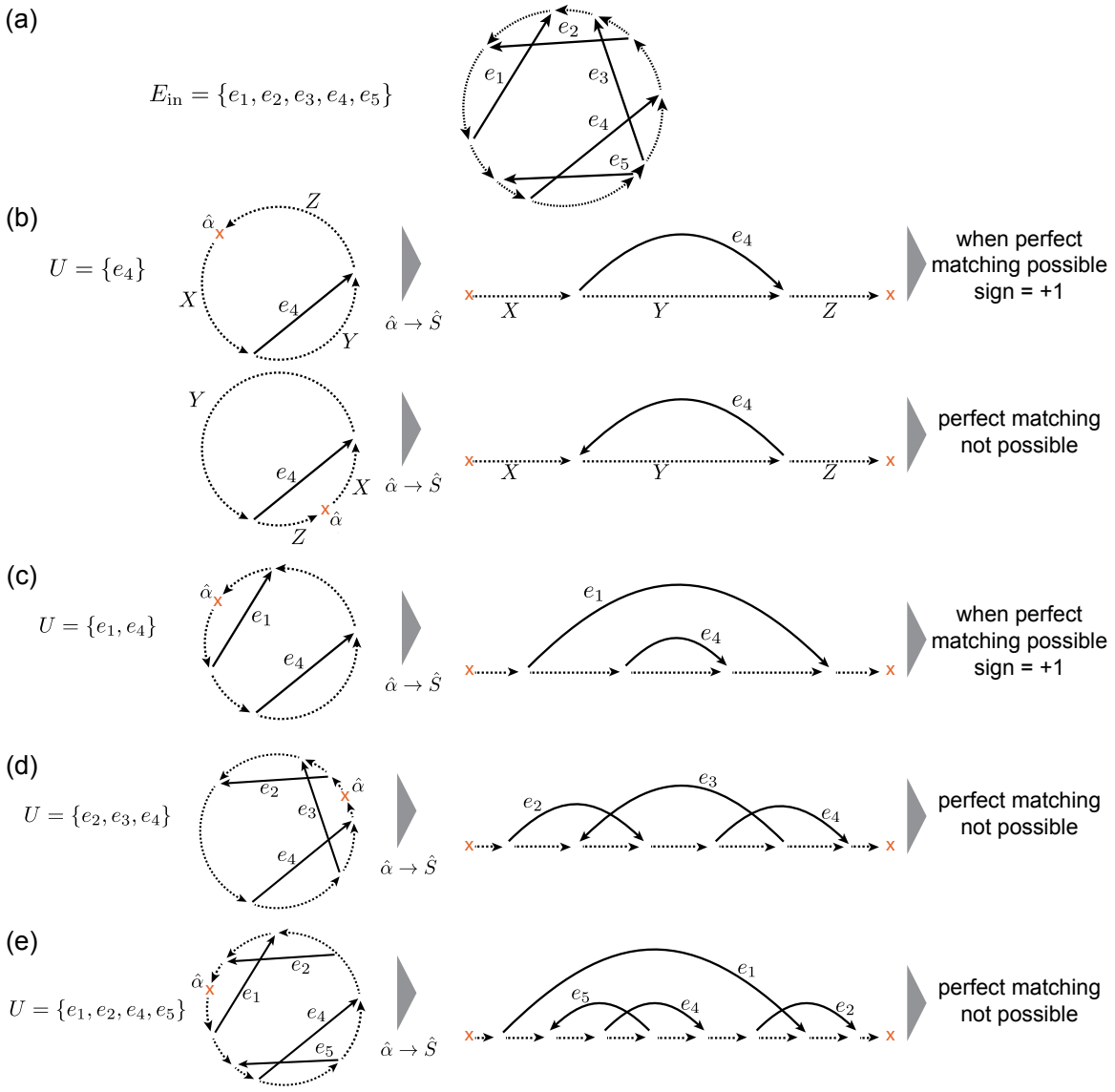

Figure 4.7: Illustration of important steps of the proof for Hamiltonian coexistence networks. (a) Hamiltonian network with internal edges $e_1, ..., e_5$. This network is a coexistence network if for every subset $U \subseteq E_{\text{in}}$ and relative to every deleted vertex $\hat{\alpha} \to \hat{S}$ all near-perfect matchings have a positive sign. (b) Case of a single edge, $|U| = 1$: The edge e_4 is either ascending or descending, depending on its position relative to the deleted vertex. (c) Case of covering edges: Both vertices of the edge e_4 lie between start- and end-vertex of e_1, such that edge e_1 covers the edge e_4. Since both edges are ascending, a perfect matching exists with sign +1. (d) Case of crossing edges: The edges e_2, e_3, and e_4 form a crossing set. Thus, a perfect matching does not exist. The lowest descending edge is e_3 because it does not cover any other descending edges. (e) Case of two crossing sets: The crossing set consisting of e_1 and e_2 covers the crossing set of e_4 and e_5.

odd for each of the three paths (the number of vertices in the paths, $|X|, |Y|$, and $|Z|$, are even; that is, the paths X, Y, and Z are of even length). We distinguish two cases in the following: the edge e is ascending or descending (again, meant after relabeling $\hat{\alpha} \to \hat{S}$).

- *Case (i): the edge e is ascending: all near-perfect matchings have the same sign as the near-perfect matching stemming from the cycle.* In this case, $e_{\text{start}} < e_{\text{end}}$ and $e_{\text{end}} - e_{\text{start}}$ is odd (by the cycle condition (4.2)). Therefore, $(e_{\text{end}} - 1) - (e_{\text{start}} + 1)$ is odd and Y has a perfect matching. The perfect matching of $A_{\hat{S}}$ including the edge e does indeed exist if, in addition, $|X|$ and $|Z|$ are even.

  If this perfect matching exists, its corresponding permutation has the same sign as the perfect matching stemming from the cycle. If the paths X, Y and Z are of even length, e_{start} is odd and e_{end} is even. The permutation corresponding to a perfect matching induced by e is given by:

$$\sigma_{\alpha_e} = (e_{\text{start}}\ e_{\text{end}}\ 1\ 2\ \ldots\ e_{\text{start}} - 1\ e_{\text{start}} + 1\ \ldots\ e_{\text{end}} - 1\ e_{\text{end}} + 1\ \ldots\ S - 1)\ .$$

  The sign of this perfect matching of $A_{\hat{S}}$ is determined by the number of transpositions necessary to transform the permutation into the identity permutation ($\sigma_{\mathbb{1}}$), and is computed as:

$$\begin{aligned}
\text{sign}(\sigma_{\alpha_e}) &= \text{sign}(e_{\text{start}}\ e_{\text{end}}\ 1\ \ldots\ e_{\text{start}} - 1\ e_{\text{start}} + 1\ \ldots\ e_{\text{end}} - 1\ e_{\text{end}} + 1\ \ldots\ S - 1)\ , \\
&= (-1)^{(2\cdot((e_{\text{start}}-1)+1))}\ \text{sign}(1\ \ldots\ e_{\text{start}} - 1\ e_{\text{start}}\ e_{\text{end}}\ e_{\text{start}} + 1\ \ldots \\
&\qquad \ldots\ e_{\text{end}} - 1\ e_{\text{end}} + 1\ \ldots\ S - 1)\ , \\
&= (-1)^{((e_{\text{end}}-1)-(e_{\text{start}}+1)+1)}\text{sign}(1\ \ldots\ e_{\text{start}} - 1\ e_{\text{start}}\ e_{\text{start}} + 1 \ldots \\
&\qquad \ldots\ e_{\text{end}} - 1\ e_{\text{end}}\ e_{\text{end}} + 1\ \ldots\ S - 1)\ , \\
&= (+1)\text{sign}(\sigma_{\mathbb{1}}) = +1\ .
\end{aligned}$$

  In other words, all near-perfect matchings arising from a single ascending interior edge have the same sign as the near-perfect matching that is constituted by edges from E_{cycle} only.

- *Case (ii): the edge e is descending: no contribution to a near-perfect matching.* In this case, $e_{\text{end}} < e_{\text{start}}$ and $e_{\text{start}} - e_{\text{end}}$ is even (according to the cycle condition (4.2)). Thus, Y is of odd length, and e cannot contribute to a perfect matching of $A_{\hat{S}}$ as a single interior edge. For later purposes, note that for a descending edge, start node, e_{start}, and end node, e_{end}, have the same parity.

U contains several edges ($|U| > 1$). Next, we consider the case that the set $U \subseteq E_{\text{in}}$ contains several edges fulfilling the coexistence conditions (4.2) and (4.3). First, we study the possibility that all interior edges in U do not cross each other. In this case the cycle condition (4.2) ensures that all near-perfect matchings that can possibly arise have the

same sign as the near-perfect matching stemming from the edges of the cycle. Second, we study the cases in which interior edges cross each other and the crossing condition (4.3). becomes relevant. In particular, we introduce the notion of a crossing set $E_\times \subseteq E_{\text{in}}$. We show that no near-perfect matchings are created if U contains exactly two crossing edges. This result is generalized to any $U \subseteq E_{\text{in}}$ that contains a crossing set.

- *None of the edges in U cross each other.* In generalization of the reasoning for $|U| = 1$, a near-perfect matching can only arise from all non-crossing edges in U and edges of the cycle if all created paths are of even length. Two different cases can occur.

  - *Case (i): All non-crossing edges in U are ascending: all near-perfect matchings have the same sign as the near-perfect matching stemming from the cycle.* If all edges in U are ascending, for all of its edges, the path between start and end node is of even length (following the cycle condition (4.2), as above). When U contains k ascending edges, after deleting all edges of U, the remaining edges of E_{cycle} form $2k + 1$ paths (possibly of zero length), see Figure 4.7(c). Since the edges do not cross, the length of every path is either determined by the vertices of an ascending edge (similar to Y in the case $|U| = 1$) or by the relative placement of two ascending edges (similar to X and Z in the case $|U| = 1$). As argued before, ascending edges lead to a path of even length, such that only the relative placement of edges determines whether a perfect matching of $A_{\hat{S}}$ exists. The sign of the permutation corresponding to such a perfect matching is equal to the sign of the perfect matching stemming from E_{cycle} because an even number of transpositions is needed to order its elements in size (all paths are of even length). In particular, all nodes of interior ascending edges can be ordered in size by pair-wisely ordering them with an even number of transpositions. For example, if $e_1 = (e_{1,\text{start}}\ e_{1,\text{end}})$ and $e_2 = (e_{2,\text{start}}\ e_{2,\text{end}})$ with $e_{2,\text{end}} < e_{1,\text{start}}$, four transpositions are needed to order these indices in size:

$$\begin{aligned}\text{sign}(e_{2,\text{start}}\ e_{2,\text{end}}\ e_{1,\text{start}}\ e_{1,\text{end}}\ 1\ \ldots\ S-1) = \\ = (-1)^{(2\cdot 2)}\text{sign}(e_{1,\text{start}}\ e_{1,\text{end}}\ e_{2,\text{start}}\ e_{2,\text{end}}\ 1\ \ldots\ S-1)\ .\end{aligned}$$

    If, on the other hand, $e_{2,\text{start}} < e_{1,\text{start}}$ and $e_{1,\text{end}} < e_{2,\text{end}}$ (the vertices of e_1 lie between the vertices of e_2, e_2 covers e_1), two transpositions are necessary to order these nodes in size (see Figure 4.7(c)):

$$\begin{aligned}\text{sign}(e_{2,\text{start}}\ e_{1,\text{start}}\ e_{1,\text{end}}\ \ e_{2,\text{end}}\ 1\ \ldots\ S-1) = \\ = (-1)^{(2\cdot 1)}\text{sign}(e_{1,\text{start}}\ e_{1,\text{end}}\ e_{2,\text{start}}\ e_{2,\text{end}}\ 1\ \ldots\ S-1)\ .\end{aligned}$$

    This way, all nodes of the interior ascending edges can be ordered in size by pairwisely ordering them with an even number of transpositions. Because all paths stemming from cycle edges are of even length, further ordering the ordered nodes from interior edges within the nodes of the cycle edges involves an

even number of transpositions. Thus, an overall even number of transpositions is needed to order the elements of the partition corresponding to the perfect matching in size.

– *Case (ii): U contains at least one non-crossing descending edge: no contribution to near-perfect matchings.* If at least one non-crossing descending edge is contained in U, one path of odd length is created for every arrangement of non-crossing edges. This path of odd length cannot contribute to a near-perfect matching of the network.

- *Definition of a crossing set $E_\times$.* All edges in U that are related by condition (4.3) form a so-called crossing set $E_\times$. Pictorially speaking, in a crossing set all edges are related by the crossing condition. More precisely, all pairs of edges in a crossing set $f, g \in E_\times$ either cross each other (their relative placement is explicitly constrained by the crossing condition (4.3), or there exists a series of edges $f, e_1, ..., e_l, g \in E_\times$ that consecutively cross each other (the relative placement of f and g is implicitly constrained by the intermediate edges $e_1, ..., e_l$). For example, in Figure 4.7(d) the edges e_2 and e_4 are contained in one crossing set because both edges cross the edge e_3. Thus, $E_\times = \{e_2, e_3, e_4\}$ is a crossing set. In Figure 4.7(e), the set U consists of two disjoint crossing sets $U = E_\times^{(1)} \cup E_\times^{(2)}$ with $E_\times^{(1)} = \{e_1, e_2\}$ and $E_\times^{(2)} = \{e_4, e_5\}$. Note also that the edges e_2 and e_4 belong to one crossing set for the choice of U as depicted in Figure 4.7(d), but not for the choice of U in Figure 4.7(e). Hence, both the occurrence and the elements of crossing sets do not only depend on the interior edges of a network, but also on the choice of U from which near-perfect matchings of the network are constructed.

  Consequences of the crossing condition (4.3) *for the relative placement of two crossing edges.* We briefly discuss the consequences of the crossing condition for the relative placement of two crossing edges. One pair of crossing edges divides a cycle into four paths $P_1, \ldots, P_4$, as illustrated in Figure 4.8. Because the crossing condition is fulfilled in the chosen ascending labeling of the cycle, either $|P_2|$ or $|P_4|$ is the shortest path length either between the start points or between the end points. Thus, either $|P_2|$ or $|P_4|$ is odd, or both are odd. Furthermore, because every interior edge also fulfills the cycle condition (4.2), only directed cycles of odd length are created when combining every single interior edge with the Hamiltonian cycle. Thus, both $|P_4|+|P_1|+3$ (the cycle consists of the start and end node of e_1, the nodes constituting P_4, the end node of e_2 and the nodes constituting P_1) and $|P_1|+|P_2|+3$ are odd; see Figure 4.8(a). Consequently, the numbers of nodes in each of the three paths P_1, P_2, and P_4 are odd. It follows that $|P_3|$ is even because the overall number of nodes in the system $|P_1| + |P_2| + |P_3| + |P_4| + 4$ is odd. In total, two crossing interior edges create two cycles of odd length that share an odd number of nodes.

  The same consequences for the placement of crossing edges are, of course, obtained if one considers an explicit labeling of the cycle with reference to the deleted index $\hat{\alpha} \to \hat{S}$ as depicted in Figure 4.8(b)(i)-(iv). Depending on the position of the deleted

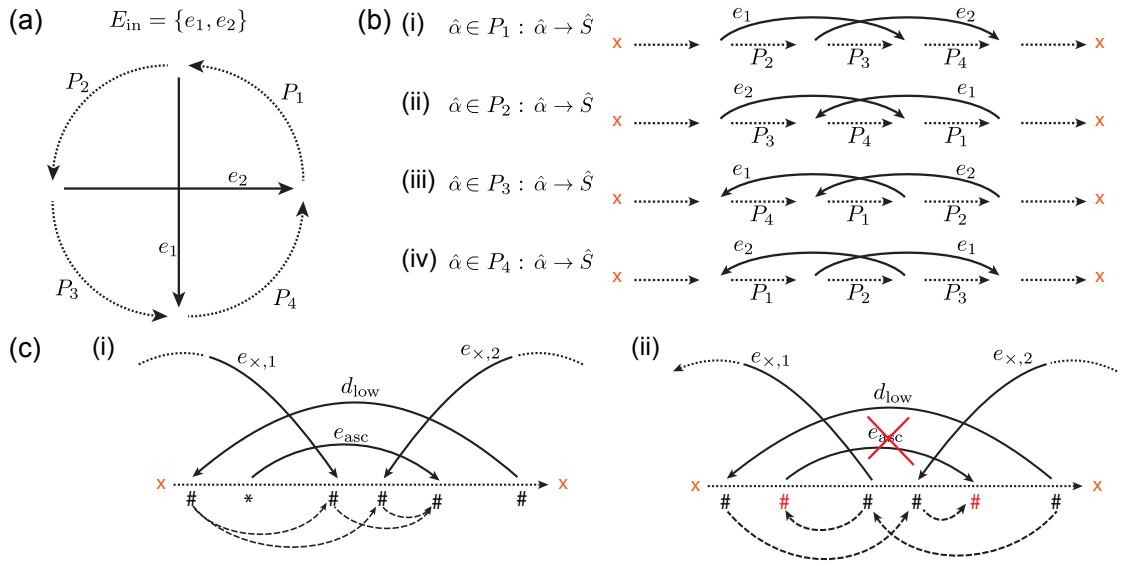

Figure 4.8: (a) Schematic illustration of Hamiltonian coexistence network with two crossing edges e_1 and e_2. $P_1, \ldots, P_4$ are the paths constituted by the edges of E_{cycle} that do not include any vertices of e_1 and e_2. (b) Because the network is a coexistence network, the crossing condition (4.3) is fulfilled for every ascending labeling. Thus, for the deletion of every vertex i that is not part of e_1 and e_2, after relabeling $\alpha \to S$, fulfillment of the crossing condition constraints the length of the paths $P_1, \ldots, P_4$. Hence, $|P_1|, |P_2|$ and $|P_4|$ are odd and P_3 is even. (c) The lowest descending edge d_{low} does not cover other descending edges. The edges $e_{\times,1}$ and $e_{\times,4}$ cross both d_{low} and e_{asc}, such that all edges form one crossing set. On the left, (i), the edges $e_{\times,1}$ and $e_{\times,2}$ both end between the vertices of a covered ascending edge and fulfill the crossing condition pair-wisely, indicated by # and $*$ as placeholders for the vertices' parity (odd and even). On the right, (ii), the edge $e_{\times,1}$ starts and the edge $e_{\times,2}$ ends between the vertices of a covered ascending edge. In this arrangement, the crossing condition cannot be pair-wisely fulfilled.

node $\hat{S}$, the two crossing edges e_1 and e_2 are arranged differently with respect to each other. In line with the above arguments, it follows that the node of edge e_2 that lies between the nodes of e_1 has the same parity as its counterpart of e_1 irrespective of the labeling.

U contains only two crossing edges ($U = E_\times$ and $|E_\times| = 2$): no contribution to near-perfect matchings. Now, we discuss whether near-perfect matchings arise in case U contains exactly two crossing edges; see Figure 4.8(a). Because the crossing edges fulfill the coexistence conditions (4.2) and (4.3), either P_2 or P_4 build up the minimal distance between the two edges. After deleting the nodes of the edges e_1 and e_2 (as contributions to the near-perfect matching of the network $\mathcal{N}(A_{\hat{S}})$), either path P_2 remains or path P_4 remains, or both paths remain to be matched, Figure 4.8(b). Because both P_2 and P_4 have an odd number of nodes (see above), they do not have a perfect matching. Therefore, there does not exist any near-perfect matching that contains a single pair of crossing edges.

U contains only one crossing set of several ascending edges ($U = E_\times$ and $|U| \geq 3$ and $e_{i,start} < e_{i,end}$ for all $i = 1, \ldots |U|$): no contribution to near-perfect matchings. When all edges in U are ascending (again, ascending is meant after relabeling as above) and form a single crossing set, the above reasoning can be readily generalized. In particular, all start nodes have the same parity (for example, even) and all end nodes have the opposite parity (in this example, odd). The two lowest nodes of these ascending edges are start nodes and, thus, have the same parity. Therefore, these two start nodes enclose a path with an odd number of nodes, which does not have a perfect matching. Thus, a near-perfect matching containing a crossing set with only ascending edges does not exist.

U contains only one crossing set with at least one descending edge ($U = E_\times$ and $|U| \geq 3$ and $e_{i,start} > e_{i,end}$ for at least one $i \in \{1, \ldots |E_\times|\}$): no contribution to near-perfect matchings. First, we discuss some implications of the coexistence conditions (4.2) and (4.3) for relative placement of an arbitrary edge crossing a descending edge. For a descending edge d the cycle condition (4.2) implies that both of its nodes have the same parity; see above. From the crossing condition (4.3) it follows that, if an arbitrary edge e crosses a descending edge d, the node of e that is placed between end and start node of d has the same parity as the nodes of d. For example, in Figure 4.8(b)(ii), the end node of e_2 has the same parity as both nodes of e_1. For the configuration of crossing descending edges (as depicted in Figure 4.8(b)(iii)), the coexistence conditions imply that all nodes of the two edges have the same parity because the start-node of e_1 lies between end and start node of e_2, and because e_1 is descending.

We now use these arguments to show that a crossing set with at least one descending edge is not part of a near-perfect matching. In any crossing set $E_\times$ with descending edges we find (at least) one descending edge, to which we refer as d_{low}, that does not cover any other descending edges. In other words, there is no other descending edge in $E_\times$ for which both nodes lie between $d_{\text{low,end}}$ and $d_{\text{low,start}}$. Two cases can occur for this descending edge d_{low}.

- *Case (i): The descending edge d_{low} does not cover any ascending edges: no contribution to near-perfect matchings.* In this case d_{low} does not cover any descending or ascending edges (see Figure 4.7). Thus, any node that is covered by the edge d_{low} and that is part of an edge of $E_\times$ belongs to an edge that crosses d_{low}. As a consequence of the crossing condition (4.3), all of these nodes have the same parity and, thus, enclose paths of odd length. Therefore, this arrangement of crossing edges cannot be completed to form a perfect matching.
- *Case (ii): The descending edge d_{low} covers ascending edges: no contribution to near-perfect matchings.* In the following we show that every crossing set U in which a descending edge covers ascending edges leads to at least one odd path and thus cannot be part of a near-perfect matching.

First, we consider the case that d_{low} covers only non-crossing ascending edges, see Figure 4.8. Recall that U contains only one crossing set, such that there are edges $e_{\times,i}$ that cross both d_{low} and the covered ascending edge e_{asc}. A pairwise fulfillment of the crossing condition (4.3) enforces that either all start or all end vertices of the edges $e_{\times,i}$ lie between the vertices of e_{asc}, see Figure 4.8 (c)(i). When the start vertex of $e_{\times,1}$ and the end vertex of $e_{\times,2}$ lie between the vertices of e_{asc} an arrangement consistent with the crossing condition cannot exist, see Figure 4.8 (c)(ii). Thus, either the two highest vertices of U that lie between the vertices of d_{low} (in case all $e_{\times,i}$ end between the vertices of e_{asc}) or the two lowest vertices (in case all $e_{\times,i}$ start between the vertices of e_{asc}) have the same parity. The arrangement leads to paths of odd length and cannot give rise to a perfect matching.

The same argument holds when d_{low} covers a crossing set of ascending edges $E_{\times,\text{asc}}$. As stated above, in a crossing set consisting only of ascending edges all start vertices have the same parity, while all end-vertices have the other parity. As above, in an arrangement consistent with the crossing condition the edges $e_{\times,i}$ that cross both d_{low} and $E_{\times,\text{asc}}$ either all start or all end between the vertices of $E_{\times,\text{asc}}$. Hence, either the two highest vertices of $E_{\times,\text{asc}} \cup e_{\times,i}$, or the two lowest vertices of $E_{\times,\text{asc}} \cup e_{\times,i}$ (or both) have the same parity.

These arguments show that every crossing set containing at least one descending edge enclose at least one path of odd length. Therefore, this arrangement of edges cannot be completed to form a perfect matching.

Thus, for all cases of a single crossing set $E_\times \subseteq U$ for which all interior edges fulfill the coexistence conditions (4.2) and (4.3), no contributions to near-perfect matchings occur. Therefore, no contributions to the adjugate vector arise through a single crossing set.

- *U contains several crossing sets and single edges: no contribution to near-perfect matchings.* The above result for one crossing set readily generalizes to a set U that consists of several crossing sets and further non-crossing edges. Note that every U can be decomposed into pair-wisely disjoint sets of crossing sets and sets of single edges. If a crossing set is contained in U, there exists a path of odd length between two nodes of edges contained in the crossing set. Thus, this path does not have a perfect matching, neither when its nodes are ordered (that is, if the path consists of edges from the cycle), nor when it its nodes are permuted (that is, if edges from the crossing set cover other edges). We conclude that a near-perfect matching cannot contain arbitrary combinations crossing edges.

If the coexistence conditions (4.2) **and** (4.3) **are fulfilled, the network is a coexistence network.** In total, we have shown that for a network in which all interior edges satisfy the coexistence conditions, the adjugate vector consists of summands all of which have the same sign. Thus, the network topology is a coexistence network. In particular, it

was shown that through the cycle condition (4.2) only ascending single edges contribute to near-perfect matchings, but not descending edges. The resulting near-perfect matchings have the same sign as the near-perfect matching stemming from the Hamiltonian cycle. The crossing condition (4.3) implies that crossing edges do not occur in a near-perfect matching.

4.C.3 Necessity of the conditions (4.2) and (4.3) for coexistence networks

In the second part of this proof, we show that the conditions (4.2) and (4.3) are also necessary for coexistence networks. To this end, we show that a Hamiltonian network $\mathcal{N}$ with edge-set $E(\mathcal{N}) = E_{\text{cycle}} \cup E_{\text{in}}$ is not a coexistence network if either condition (4.2) or condition (4.3) is not fulfilled.

Condition (4.2) is not fulfilled for one interior edge: at least one induced near-perfect matching has a different sign than the near-perfect matching stemming from the cycle. Assume that there is an edge $e \in E_{\text{in}}$ that violates condition (4.2). We choose the component of the adjugate vector such that after relabeling $\hat{i} \to \hat{S}$ the edge has the form $e = (e_{\text{start}}, e_{\text{end}}) = (e_{\text{start}}, 1)$ with $2 < e_{\text{start}} < S-1$, and consider perfect matchings of $A_{\hat{S}}$. In this labeling, e is descending. Thus, violating the cycle condition (4.2) implies that e_{start} is even. Deleting the nodes e_{start} and $e_{\text{end}} = 1$ from $E_{\text{cycle},\hat{S}}$ creates the two separated paths $P[2, e_{\text{start}} - 1]$ and $P[e_{\text{start}} + 1, S - 1]$. Both paths are of even length and, thus, have perfect matchings. Therefore, a summand that includes the edge e contributes to the Sth component of the adjugate vector (3.5).

However, this summand has the opposite sign than the summand stemming from the Hamiltonian cycle alone, as we show in the following. To determine the sign of the perfect matching arising from the interior edge e for the Sth node deleted, we compute the number of transpositions needed to obtain the identity permutation:

$$\begin{aligned}
\text{sign}[\sigma_{\alpha_e}] &= \text{sign}(e_{\text{start}}\ 1\ 2\ \dots\ S-1) = -\text{sign}(1\ e_{\text{start}}\ 2\ \dots\ S-1)\ , \\
&= -(-1)^{((e_{\text{start}}-1)-1+1)}\text{sign}(1\ 2\ \dots\ e_{\text{start}}-1\ e_{\text{start}}\ e_{\text{start}}-1\ \dots\ S-1)\ , \\
&= -\text{sign}(\sigma_{\mathbb{1}}) = -1\ .
\end{aligned}$$

Thus, the interior edge e contributes with a summand to the adjugate vector that has a different sign than the identity permutation. Therefore, if a network contains at least one interior edge violating the cycle condition, at least one summand in one component of the adjugate vector has the opposite sign compared to the contribution stemming from the cycle in that component of the adjugate vector (3.5). Such a network is not a coexistence network.

The crossing condition (4.3) **is not fulfilled for two crossing edges: at least one induced near-perfect matching has a different sign than the near-perfect matching stemming from the cycle.** Next, we consider a network with interior edges E_{in} that fulfill the cycle condition, but violate the crossing condition. In other words, there exist two edges $e_1, e_2 \in E_{\text{in}}$ that do not fulfill the crossing condition. We choose the component of the adjugate vector such that after relabeling $\hat{i} \to \hat{S}$ the edges take the form $e_{1,\text{end}} = 1 < e_{2,\text{end}} < e_{1,\text{start}} < e_{2,\text{start}} < S$. fulfilling the cycle condition and violating the crossing condition implies that $e_{1,\text{end}}$ is odd, whereas $e_{2,\text{start}}$ and $e_{2,\text{end}}$ are even. In this labeling, we consider now the edges of $E_{\text{cycle},\hat{S}}$, that is, perfect matchings of $A_{\hat{S}}$. By deleting all edges that contain the nodes of e_1 and e_2 from $E_{\text{cycle},\hat{S}}$, the paths $P[2, e_{2,\text{end}} - 1], P[e_{2,\text{end}} + 1, e_{1,\text{start}} - 1], P[e_{1,\text{start}} + 1, e_{2,\text{start}} - 1]$, and $P[e_{2,\text{start}} + 1, S - 1]$ remain. Because for every path start node and end node have different parity, all paths contain an even number of nodes. In other words, a near-perfect matching of $A_{\hat{S}}$ is possible.

The sign of the permutation of that near-perfect matching is obtained as follows:

$$
\begin{aligned}
\operatorname{sign}(\sigma_{\alpha_{e_1,e_2}}) &= \operatorname{sign}(e_{1,\text{start}}\ 1\ e_{2,\text{start}}\ e_{2,\text{end}}\ 2\ \dots\ S-1) = \operatorname{sign}(1, e_{1,\text{start}}\ e_{2,\text{end}}, e_{2,\text{start}}\ 2\ \dots\ S-1)\ , \\
&= (-1)^3 \operatorname{sign}(1\ e_{2,\text{end}}\ e_{1,\text{start}}\ e_{2,\text{start}}\ 2\ \dots\ S-1)\ , \\
&= -(-1)^{((e_{2,\text{start}}-1)-3)} \operatorname{sign}(1\ e_{2,\text{end}}\ e_{1,\text{start}}\ 2\ \dots\ e_{2,\text{end}}-1\ e_{2,\text{end}}+1 \dots \\
&\qquad\qquad \dots\ e_{1,\text{start}}-1\ e_{1,\text{start}}+1\ \dots\ e_{2,\text{start}}\ \dots\ S-1)\ , \\
&= -(-1)^{((e_{1,\text{start}}-1)-2)} \operatorname{sign}(1\ e_{2,\text{end}}\ 2\ \dots\ e_{2,\text{end}}-1\ e_{2,\text{end}}+1\ \dots\ e_{1,\text{start}}\ \dots\ S-1)\ , \\
&= -(-1)^{((e_{2,\text{end}}-1)-1)} \operatorname{sign}(1\ 2\ \dots\ e_{2,\text{end}}\ \dots\ S-1)\ , \\
&= -\operatorname{sign}(\sigma_{\mathbb{1}}) = -1\ .
\end{aligned}
$$

Thus, if two interior edges of a given network do not fulfill the crossing condition, at least one near-perfect matching exists that has a different sign than the corresponding near-perfect matching of the cycle. Thus, such a network is not a coexistence network.

If the coexistence conditions (4.2) **or** (4.3) **are not fulfilled, the network is not a coexistence network.** In total, we have shown that the existence of (i) one interior edge that does not fulfill the cycle condition (4.2) or (ii) two interior edges that fulfill the cycle condition, but not the crossing condition (4.3) implies that the network is not a coexistence network. Thus, the coexistence conditions are necessary for a Hamiltonian network to be a coexistence network.

4.D Calculation of the number of near-perfect matchings for selected coexistence networks

Here we supplement the derivation of the adjugate vectors for the generating coexistence networks with unit rates given in (4.8) and (4.11), respectively, as stated in Section 4.4

of the main text. More explicitly, for both networks we derive the number of near-perfect matchings. Exploiting that both examples suffice the coexistence conditions (4.2) and (4.3), the number of near-perfect matchings excluding vertex i equals the ith entry of the adjugate vector for unit rates.

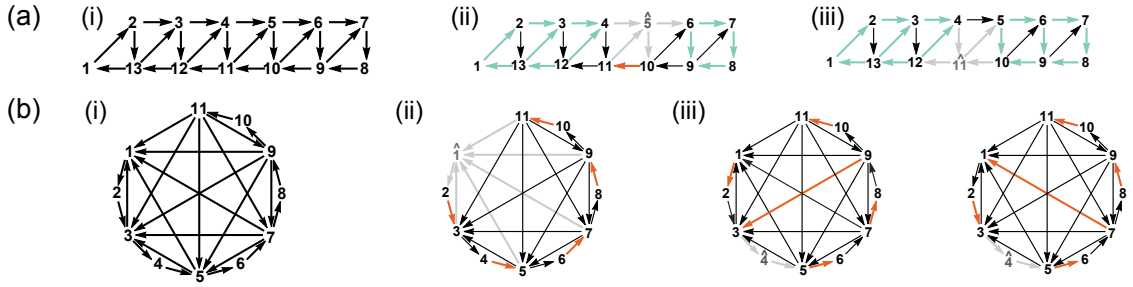

Figure 4.9: Exemplary sketches for the calculation of the number of near-perfect matchings for (a) the triangulation of the cycle, and (b) the cycles with complete subnetwork. (a) The triangulation of the cycle with $S = 11$ nodes is shown in (a)(i). Depending on the position of the deleted node, the whole network is separated either such that two ladder-graphs (highlighted in blue) and one additional edge (orange) contribute to perfect matchings ((a)(ii), for the nodes $\{2, 3, 4, 5, 6, 7\}$), or such that only two ladder graphs (blue) contribute ((a)(iii), for the nodes $\{8, 9, 10, 11, 1\}$). (b)(i) The cycle of $S = 11$ nodes with a complete subnetwork on the odd nodes is shown. When deleting odd nodes, only one near-perfect matching exists consisting only of edges of the cycle (ii). When deleting an even node, every near-perfect matching contains one edge between odd nodes (iii). The deleted node effectively divides the subnetwork into two partitions; in the depicted example $\{1, 2, 3\}$ and $\{5, 6, 7, 8, 9, 10, 11\}$. Every pair of one odd node from each partition gives rise to one near-perfect matching. Thus, in the depicted example, there are $2 \cdot 4 = 8$ near-perfect matchings.

4.D.1 Near-perfect matchings for the triangulation of the cycle

In the following we derive the number of near-perfect matchings of the triangulation of an odd cycle as specified in Equation (4.8) in Section 4.4.1.

For this calculation, it is helpful to introduce so-called ladder graphs and their number of perfect matchings. The ladder graphs with $2, 4$, and 6 vertices are a single edge, a rectangle, and a domino tile, respectively, see Section 6.B.1. In general, a ladder graph with $2T$ vertices consists of T rungs and $2(T-1)$ rails. The number of perfect matchings of a A ladder graph with $2T$ vertices has $F(T+1)$ perfect matchings, where $F(n)$ is the nth Fibonacci number. This can be shown inductively by considering the additional perfect matchings arising when augmenting the graph by one rung and two rails [84].

Note that the triangulation of an odd cycle presented in Section 4.4.1 can be thought of as a superposition of two ladder graphs, see Figure 4.9(a)(i). One of the two ladder graphs consists of the vertices $2, \dots, S$ and the ascending edges on these vertices (that is, $2 \to S, 3 \to S-1, \dots$), the other ladder graph is diagonally placed over the first one and

contains the vertices $1, \ldots, \frac{(S+1)}{2}, \frac{(S+1)}{2}+2, \ldots, S$ and all edges of the cycle together with all descending edges on these vertices. Additionally, note that for a ladder graph with diagonal edges (for example, the subnetwork formed by the vertices $2, \ldots, 13$ in Figure 4.9(a)(i)), the diagonal edges do not contribute to any perfect matchings. In other words, the number of perfect matchings of a ladder graph with diagonal edges with $2T$ vertices is $F(T+1)$ as well.

Using these observations, the components of the adjugate vector for the triangulation of the cycle with unit rates are calculated as the number of perfect matchings of the subnetworks created by deleting each node. Upon deleting node 1 from the network, a network with $S-1 = 2n-2$ vertices remains. This graph is a ladder graph with $2(n-1)$ vertices and additional diagonal edges. Thus, it has $F(n)$ perfect matchings. Because the network is a coexistence network, the number of perfect matchings equals the entry of the first component of the adjugate vector with unit rates, that is, $r_1 = F(n)$.
In case one of the vertices $\alpha = 2, \ldots, n$ is deleted, the network is divided into two parts that can be viewed as two ladder graphs with $2(\alpha-2)$ and $2(n-\alpha)$ vertices (ignoring diagonal edges that cannot contribute to perfect matchings). The two ladder graphs are connected by three edges, see Figure 4.9(a)(ii). Every combination of perfect matchings of the two separated ladder graphs is a perfect matching of the full graph, such that $r_\alpha = F(\alpha-1)F(n-\alpha+1)$.
The remaining matrix entries $\alpha = n+1, \ldots, 2n-1$ are calculated in a similar way. Deleting one of these vertices divides the remaining network into two ladder graphs with $2(2n-\alpha)$ and $2(\alpha-n-1)$ vertices (see Figure 4.9(a)(iii)), such that the corresponding components of the adjugate vector are $r_\alpha = F(2n-\alpha+1)F(\alpha-n)$. Taken together, the adjugate vector for the triangulation of a cycle with unit rates is given by Equation (4.8).

Using the convolution formula for Fibonacci numbers [85],

$$\sum_{k=0}^{n} F(k)F(n-k) = \frac{1}{5}(n(F(n-1)+F(n+1)) - F(n)),$$

the total number of near-perfect matchings is

$$\begin{aligned}
&\sum_{\alpha=2}^{n} F(\alpha-1)F(n-(\alpha-1)) + \left(\sum_{\alpha=n+1}^{2n-1} F(n-(\alpha-n)+1)F(\alpha-n) + F(n)\right) = \\
&\qquad = \sum_{\alpha=0}^{n} F(\alpha)F(n-\alpha) + \sum_{\alpha=1}^{n+1} F(n+1-\alpha)F(\alpha)\ , \\
&\qquad = \frac{1}{5}(n(F(n-1)+F(n+1)) - F(n)) + \frac{1}{5}((n+1)(F(n)+F(n+2)) - F(n+1))\ , \\
&\qquad = \frac{1}{5}\left(n(3F(n+1)+F(n)) + F(n)\right) = \frac{1}{5}nF(n)\left(3\frac{F(n+1)}{F(n)} + 1 + \frac{1}{n}\right),
\end{aligned}$$

as stated in Equation (4.9) the main text.

4.D.2 Number of near-perfect matchings in a cycle with complete subnetwork on odd nodes

Here we supplement the calculation of the form of the adjugate vector given in Equation (4.11) in Section 4.4.2. The form of the adjugate vector of an odd cycle with a complete subnetwork on the odd nodes can be understood as follows; see Figure 4.9(b)(i) for illustration.

Upon deleting an odd node $2k-1$ ($k = 1, \ldots, n$) from the network, the only perfect matching that covers all remaining nodes consists of edges from the Hamiltonian cycle. In detail, the perfect matching is $\mu_{\widehat{2k-1}} = \big((2k \to 2k+1), (2k+2 \to 2k+3), \ldots, (S-1 \to S), (1 \to 2), (3 \to 4), \ldots (2k-3 \to 2k-2)\big)$, see Figure 4.9(b)(ii). Thus, with unit rates, for odd i the components of the adjugate vector are $r_i = 1$.

When deleting an even node $\alpha = 2k$ ($k = 1, \ldots, n-1$) from the network topology, the remaining network contains the edges of the cycle $1 \to \cdots \to \alpha - 1$, $\alpha + 1 \to \cdots \to S$, and edges connecting all pairs of odd vertices. In total, the remaining subnetwork has $n-1$ odd nodes and $n-3$ even nodes. Each perfect matching thus contains one edge connecting two odd vertices. There are $\frac{\alpha-1+1}{2} \cdot \frac{S-\alpha+1}{2} = \frac{\alpha(n-\alpha/2)}{2}$ possibilities for choosing odd edges such that the remaining paths consisting of edges from the cycle have a perfect matching; two such possibilities are shown in Figure 4.9(b)(iii). Thus, for unit weights, for even α the component of the adjugate vector are $r_\alpha = \frac{\alpha(n-\alpha/2)}{2}$.
Taken together, the adjugate vector for the cycle with complete subnetwork on the odd nodes with unit rates is given by Equation (18).

Chapter 5

Topological phase transition in coupled rock-paper-scissors cycles

A hallmark of topological phases is the occurrence of topologically protected modes at the system's boundary. Here we find topological phases in the antisymmetric Lotka-Volterra equation (ALVE). The ALVE is a nonlinear dynamical system and describes, e.g., the evolutionary dynamics of a rock-paper-scissors cycle. On a one-dimensional chain of rock-paper-scissor cycles, topological phases become manifest as robust polarization states. At the transition point between left and right polarization, solitary waves are observed. This topological phase transition lies in symmetry class D within the "ten-fold way" classification as also realized by 1D topological superconductors.
This chapter has been published together with *Johannes Knebel* and *Erwin Frey* under the title of the "Topological phase transition in coupled rock-paper-scissors cycles" [50]. Minor changes have been made to fit the form of this thesis.

Overview and organization of this chapter In Chapter 4, we showed that there are topologically robust zero sum games, that is networks for which all states coexist for all time for every choice of rates. Apart from the focus on hamiltonian coexistence networks, we mentioned that large coexistence networks can be constructed by concatenating smaller coexistence networks such that they share one node 4.3.2.

Here, we construct a one-dimensional lattice by concatenating several copies of the same rock-paper-scissors cycle to create a chain. The phenomenology of the ALVE dynamics on this network shows characteristics of a topological phase transition.

In Section 5.1, we introduce the basic phenomenological traits of a topological phase transition in 1 dimension, as well as a short repetition of the ALVE. Next, we define the RPS chain in Section 5.2. In Section 5.3, we show that the phenomenology of the ALVE dynamics on the RPS chain resembles a topological phase transition. The connection between the phenomenology and a topological phase transition is made rigorous in Section 5.4, where we two different interpretations of the transition. The derivations and detailed calculations are collected in the Appendix 5.A

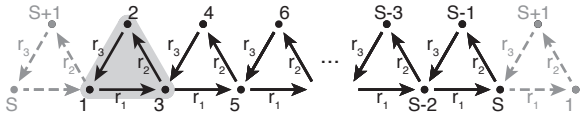

Figure 5.1: One-dimensional chain of rock-paper-scissors cycles. The interactions on the S sites of the RPS chain (one single RPS cycle highlighted) are captured by the antisymmetric matrix A in Eq. (5.1). An arrow from one site to another indicates that mass is transported in this direction at rate $r_1, r_2, r_3 > 0$ following the ALVE (2.1); the skewness $r = r_2/r_3$ defines the control parameter. The auxiliary site $S+1$ facilitates periodic boundary conditions (dashed lines) within the framework of topological band theory.

5.1 Introduction

Topological phases were discovered in condensed matter physics [145, 146, 147, 148, 149] and recently extended to classical physics, for example, as topological mechanical metamaterials [150, 151, 152, 153, 154]. From a phenomenological point of view, topological phases are paramount for the following characteristics [148, 149]: (i) *Localization*–dynamical excitations become localized at the system's boundary; (ii) *Robustness*–these boundary modes are robust against perturbations of the system's parameters and noise; (iii) *Phase transition*–at the transition point between the topological phases, the dynamical mode expands throughout the whole system. From a theoretical point of view, topological phases are determined by nontrivial topological properties of the system's bulk, which are classified in terms of the system's symmetries. These properties give rise to gapless boundary modes and explain the observations (i)-(iii) [148, 149, 153].

Thus far, the study of topological phases and their realization in soft-matter [155, 156, 157, 158] and biological systems [159, 160] has only started to develop, with recent focus on active matter and fluid dynamics [161, 162, 163, 164] and stochastic model systems [165, 166, 167, 168]. As to what extent topological phases may determine the behavior of dynamical systems that arise, for example, in population dynamics was, however, not addressed. Ultimately, it would be interesting to design biological set-ups with nontrivial topological properties so that one obtains robust dynamical modes with the above characteristics (i)-(iii).

In this chapter, we make a step in this direction by showing that topological phases can be realized with the antisymmetric Lotka-Volterra equation (ALVE). The ALVE is a conceptually important model for studying coexistence in population dynamics [19, 88] and also describes the condensation of non-interacting bosons in driven-dissipative set-ups [37, 2]. In population dynamics, the ALVE governs, for example, the evolutionary dynamics of the rock-paper-scissors game, in which each of the three strategies dominates one strategy and is dominated by another one, such that all strategies coexist [25, 87, 169, 36].

As introduced in Section 2.1 the ALVE is defined as (2.1)

$$\tfrac{\mathrm{d}}{\mathrm{d}t} x_\alpha = x_\alpha \textstyle\sum_{\beta=1}^{S} a_{\alpha\beta} x_\beta \ , \quad \alpha = 1 \ldots, S \ .$$

The real-valued $S \times S$ matrix $A = \{a_{\alpha\beta}\}$ is antisymmetric ($a_{\alpha\beta} = -a_{\beta\alpha}$) and defines how mass is transported between two sites in a nonlinear interaction $\sim x_\alpha x_\beta$.

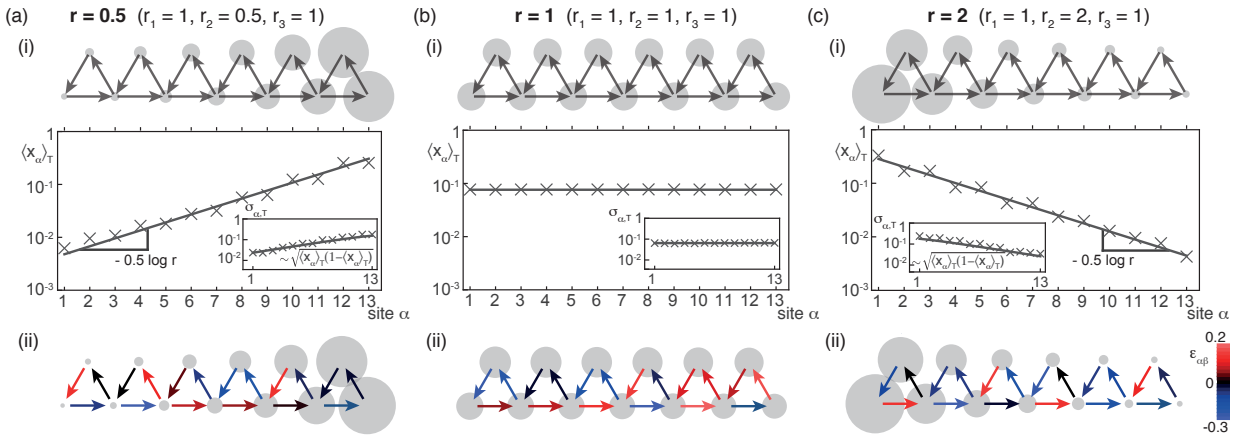

Figure 5.2: Polarization of mass to the boundary. (a-c)(i) Temporal mass averages $\langle x_\alpha \rangle_T$ from single realizations of the ALVE (2.1) are depicted on the RPS chain (disk size encodes magnitude) and on lin-log scale for $T = 5000$. Mass becomes polarized to the right for $r < 1$ and to the left for $r > 1$. For $r = 1$, mass is uniformly distributed on the whole chain. Polarization is no state of rest (non-vanishing fluctuations $\sigma_{\alpha,T}$ around the averages; insets). (a-c)(ii) Polarization is robust against perturbations ($\epsilon_{\alpha\beta}$ uniformly sampled in $[-0.30, 0.20]$) with the same characteristics as without perturbations.

Here we study the ALVE on a one-dimensional chain of coupled rock-paper-scissors cycles ("RPS chain", see Figure 5.1). We observe behaviors resembling key features of a topological phase transition: (i) mass polarizes to the right or left boundary of the RPS chain independent of the initial conditions; (ii) polarization is robust against perturbations of the model parameters; (iii) at the transition between left and right polarization, the overall mass expands on the whole chain and, moreover, solitary waves are observed. To explain these dynamics, we relate polarization of the ALVE (2.1) to properties of the antisymmetric matrix A. We show that the RPS chain encompasses a gap in the spectrum of A and an intrinsic "particle-hole symmetry" and, thus, falls into the symmetry class D within the "ten-fold way" classification scheme of gapped free-fermion systems [149]. Hence, left and right polarization are distinguished by a $\mathbb{Z}_2$ invariant characterizing the topological phase transition. Intriguingly, the topological polarization states are entirely nonlinear that cannot be rationalized within the framework of linear wave theory. We envision that the described mechanism might guide one path to design topological phases in nonlinear dynamical systems accessible to biological experiments.

5.2 Model

The RPS chain is composed of RPS cycles coupled in one dimension (Figure 5.1) and represented by the antisymmetric matrix of size $S = 2n - 1$,

$$A = \begin{pmatrix} 0 & r_3 & -r_1 & 0 & 0 & \dots & 0 & 0 & 0 \\ -r_3 & 0 & r_2 & 0 & 0 & \dots & 0 & 0 & 0 \\ r_1 & -r_2 & 0 & r_3 & -r_1 & \dots & 0 & 0 & 0 \\ 0 & 0 & -r_3 & 0 & r_2 & \dots & 0 & 0 & 0 \\ 0 & 0 & r_1 & -r_2 & 0 & \dots & 0 & 0 & 0 \\ \vdots & \vdots & \vdots & \vdots & \vdots & \ddots & \vdots & \vdots & \vdots \\ 0 & 0 & 0 & 0 & 0 & \dots & 0 & r_3 & -r_1 \\ 0 & 0 & 0 & 0 & 0 & \dots & -r_3 & 0 & r_2 \\ 0 & 0 & 0 & 0 & 0 & \dots & r_1 & -r_2 & 0 \end{pmatrix}, \tag{5.1}$$

with rate constants $r_1, r_2, r_3 > 0$. The resulting network can be understood as a concatenation of RPS cycles which are coexistence networks, such that the RPS chain is a coexistence network as well 4.3.2. In our numerical simulations of the ALVE (2.1), time is rescaled such that $r_1 = 1$. The ratio $r := r_2/r_3$ serves as the control parameter for the dynamics and is referred to as *skewness*, see also Figure 1.1. The RPS chain can be thought of as a one-dimensional chain of nonlinear oscillators because each isolated RPS cycle represents a local oscillator in which mass oscillates between the different sites. For $r \neq 1$, mass is skewed towards certain sites within a single oscillating RPS cycle.

The initial masses in the ALVE (2.1) are normalized ($\sum_\alpha x_{0,\alpha} = 1$) and strictly positive ($x_{0,\alpha} > 0$ for all α such that the chain does not become disconnected or shortened). Due to the antisymmetry of A, the total mass is conserved for all times $t \geq 0$, see Section 2.1 Furthermore, all masses remain bounded away from 0 ($x_\alpha \geq const > 0$, for all α) for all times for any choice of rates $r_1, r_2, r_3 > 0$ [2, 49].

5.3 Phenomenology

In the numerical simulations of the RPS chain, we observed a surprisingly rich dynamics for how the mass is distributed depending on the skewness r.

(i) *Localization.* For skewness $r < 1$, the overall mass on the RPS chain becomes polarized to the right boundary over time irrespective of the initial conditions (Figure 5.2(a)(i)), whereas for $r > 1$, mass polarizes to the left (Figure 5.2(c)(i)). Polarization becomes manifest as an exponential decay of the average mass per site from the boundary into the bulk. We quantify this polarization by averaging the mass at every site over a time window $T \gg 1$, $\langle x_\alpha \rangle_T = 1/T \int_0^T \mathrm{d}t\, x_\alpha(t)$ as introduced in Section 2.4. We observed that, for $r \neq 1$, average masses decay from the boundary into the bulk as $\langle x_\alpha \rangle_T \sim \exp(-\alpha/l_p)$ for $\alpha \geq 1$, numerically consistent with $l_p = 2/\ln r$ as the penetration depth. Such polarization arises for any initial mass distribution and is already visible for a small system size of $S = 13$ (Figure 5.2). Remarkably, the skewness $r = r_2/r_3$ alone determines whether the total mass polarizes to the left or right boundary of the chain. The values of all other parameters affect only the quantitative, but not the qualitative long-time behavior; see Figure 5.5 and 5.6.

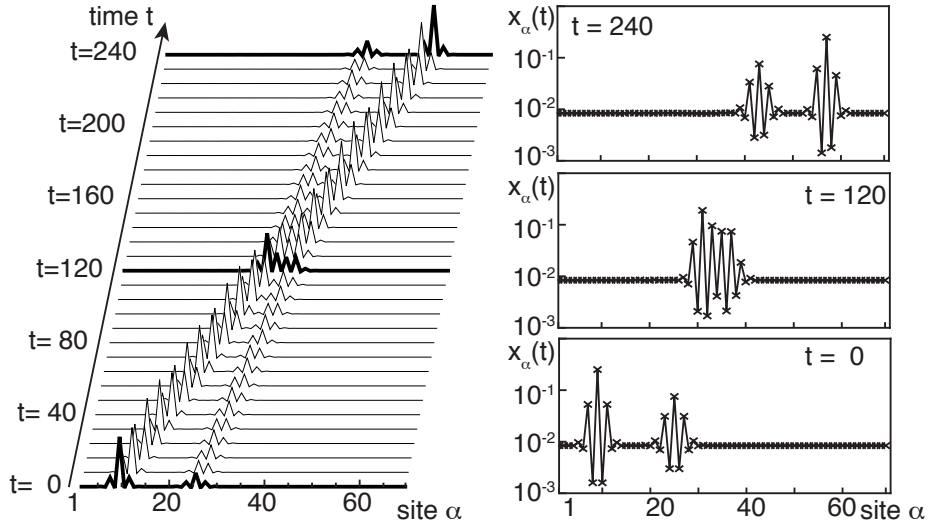

Figure 5.3: Solitary waves at the transition point $r = 1$**.** The suitably prepared wave package ($t = 0$) remains localized and travels along the (here periodic) RPS chain ($S = 80$) without changing its shape. In an interaction with another solitary wave ($t = 120$), the shapes of both wave packages remain unchanged afterwards ($t = 240$). The initial wave packages were numerically obtained from the dispersion of a single mass peak.

The ALVE (2.1) is a deterministic dynamical system that approaches a stationary state at large times. This stationary state can be characterized by the average masses per site, $\langle x_\alpha \rangle_T$ (see above) and the fluctuations around the averages within a framework of thermodynamic equilibrium [88]. To quantify the fluctuations at site α, we measured the standard deviation $\sigma_{\alpha,T} = \sqrt{\langle x_\alpha^2 \rangle_T - \langle x_\alpha \rangle_T^2}$ (Figure 5.2(a,c)(i)) which also decay exponentially into the bulk from the boundary, where the mass is localized, see Section 2.4.

(ii) *Robustness.* Polarization is robust against perturbations of the model parameters. For example, Figure 5.2(a,c)(ii) illustrates the polarization of mass to the boundary when the positive matrix entries are perturbed as $a'_{\alpha\beta} = a_{\alpha\beta}(1 + \epsilon_{\alpha\beta})$; for $a_{\alpha\beta} < 0$, the entry $a'_{\alpha\beta}$ is obtained as $a'_{\alpha\beta} = -a'_{\beta\alpha}$ such that the perturbed matrix A' is antisymmetric. Here, all $\epsilon_{\alpha\beta}$ are independently drawn from the same uniform distribution (all realizations need to be greater than -1 to preserve the network topology of a RPS chain), see details in Section 5.A.2. As another example, we found that mass also becomes localized when additional couplings are introduced. Such extensions of the RPS-chain are discussed in Chapter 6

(iii) *Phase transition.* For $r = 1$, the average masses expand throughout the whole chain, marking the transition point between the two polarization states. In the stationary state, the overall mass is on average uniformly distributed on the chain with $\langle x_\alpha \rangle_T = 1/S$ for all α. More generally, from our numerical simulations it turns out that it is not possible to tune any set of rate constants on the RPS chain such that one passes from polarization at one boundary to polarization at the other boundary without crossing a transition point at which the average masses expand throughout the whole chain.

Furthermore, we observed solitary mass waves at the transition point $r = 1$. Mass packages that are suitably initialized at a few neighboring sites show soliton-like properties (Figure 5.3): They are spatially confined; their shape does not change; and after an interaction with other solitary waves, their shape and speed remains unchanged [170, 171]. It will be interesting to further characterize these solitary waves and connect them to already known solitons in similar set-ups [47, 42, 41, 172, 173, 174], see also Section 6.6

5.4 Analysis.

Taken together, the combination of the observations of (i) localization, (ii) robustness, and (iii) phase transition share characteristic features of a topological phase transition underlying the behavior of the ALVE (2.1) on the RPS chain. In the following, we make this hypothesis rigorous. First, we outline how fixed points $\boldsymbol{x}^*$ of the ALVE ($\partial_t \boldsymbol{x}|_{\boldsymbol{x}^*} = 0$) are determined by strictly positive kernel vectors of A. Second, we derive the qualitative changes in the dynamics from the bulk properties of A within the framework of topological band theory. Third, we explicitly compute the kernel vector of A and thereby confirm the results obtained from the topological band theory approach.

5.4.1 Fixed points.

By construction the RPS chain is a coexistence network as introduced in Chapter 4, such that the adjugate vector is the unique strictly positive kernel vector of A 4.4.1, $A\boldsymbol{c} = \boldsymbol{0}$ with $c_\alpha > 0$ for all α and $\sum_\alpha c_\alpha = 1$. This vector gives rise to the fixed point $\boldsymbol{x}^* = \boldsymbol{c}$ of the ALVE (2.1), and no further fixed points with $x^*_\alpha > 0$ for all α exist 2.3. The existence of a unique vector $\boldsymbol{c}$ derives from the cyclic structure of the concatenated RPS cycles; the explicit form of $\boldsymbol{c}$ is given below in Eq. (5.3). Recall that the strictly positive kernel vector ensures that the quantity $E = x_1^{c_1} \dots x_S^{c_S} = \exp(\sum_\alpha c_\alpha \log x_\alpha)$ is conserved, see Section 2.3. For such cases, we have shown in Section 2.4 that the average masses are given by the value of the fixed point $\langle x_\alpha \rangle_\infty = c_\alpha$ for all initial conditions, see also [25, 2]. This way, the long-time dynamics on the RPS chain (average masses $\langle \boldsymbol{x} \rangle_\infty$) are determined by algebraic properties of A (kernel vector $\boldsymbol{c}$).

5.4.2 Topological band theory.

To further characterize the algebraic properties of A, the RPS chain is extended by the auxiliary site $S + 1$ and periodic boundary conditions (PBC) are employed (Figure 5.1). The corresponding antisymmetric matrix, A_{PBC}, is of size $2n$ and block-circulant (that is, translationally invariant) [175, 176]. To relate our approach to condensed matter physics, we define the "RPS Hamiltonian" $H := iA_{\mathrm{PBC}}$ (i denotes the imaginary unit), which is a Hermitian matrix ($H^\dagger = H$) with only real eigenvalues. Below, we analyze H in the framework of topological band theory [177].

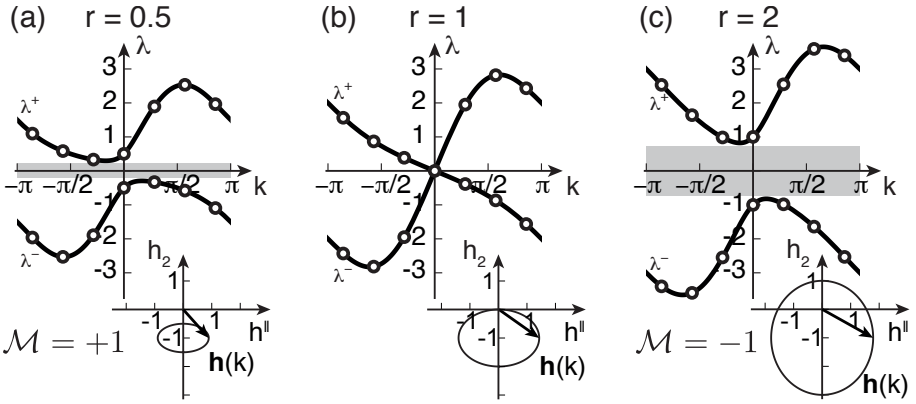

Figure 5.4: Topological phase transition on the RPS chain. Point-symmetric band structure of the RPS Hamiltonian (white dots denote eigenvalues of H for $S = 14$) with a spectral gap for $r \neq 1$ (gray shade). The band structures for $r < 1$ and $r > 1$ are topologically distinct in how the eigenvectors change within the Brillouin zone, which is quantified by the topological invariant $\mathcal{M}$ and visualized by whether $\boldsymbol{h}(k)$ winds around 0. As $\boldsymbol{h}(k)$ lies in a plane, a two dimensional projection is shown here, see Section 5.B.

The spectrum of H is characterized by its band structure. Starting from the eigenvalue equation for H and exploiting translational invariance, the eigenvectors of H can be decomposed into a plane wave part and a within-cell alignment part $\tilde{\boldsymbol{u}}(k)$, which fulfills the much simpler eigenvalue equation $\lambda(k)\tilde{\boldsymbol{u}}(k) = \tilde{H}(k)\tilde{\boldsymbol{u}}(k)$ for the Fourier-transformed Hamiltonian $\tilde{H}$; k denotes the wave number in the Brillouin zone ($k = \frac{2\pi}{n}l$ and $l = \lfloor\frac{n}{2}\rfloor, \ldots, 0, 1, \ldots, \lfloor\frac{n}{2}\rfloor - 1$). For the RPS chain, one finds,

$$\tilde{H} = \begin{pmatrix} 2r_1 \sin k & -r_2 \sin k + i(r_3 - r_2 \cos k) \\ -r_2 \sin k - i(r_3 - r_2 \cos k) & 0 \end{pmatrix}, \tag{5.2}$$

which can be written as $\tilde{H}(k) = \boldsymbol{h}(k) \cdot \boldsymbol{\sigma}$, with $\boldsymbol{h}(k) = (h_0(k), h_1(k), h_2(k), h_3(k)) = (r_1 \sin k, -r_2 \sin k, -r_3 + r_2 \cos k, r_1 \sin k)$; $\boldsymbol{\sigma} = (\sigma_0, \sigma_1, \sigma_2, \sigma_3)$ denotes the Pauli matrices with σ_0 as the 2×2 identity matrix [178], see Section 5.B.1.

How the spectral and topological properties of H depend on the control parameter r can be derived from Eq. (5.2); see Figure 5.4. First, the spectrum of H exhibits two bands of eigenvalues, λ^+ and λ^-, on the Brillouin zone $k \in [-\pi, \pi)$ since the unit cell is constituted of two sites connected by one edge ($2m + 1 \to 2m$). For $r \neq 1$, the two bands are separated by a spectral gap that closes only for $r = 1$ at $k = 0$.

Second, the spectrum of H is point-symmetric with respect to the origin, $\lambda^+(k) = -\lambda^-(-k)$. This property follows from the intrinsic "particle-hole symmetry" of H because it is defined by a real-valued antisymmetric matrix. In formal terms, H fulfills the operator identity $\mathcal{C}\tilde{H}(k)\mathcal{C}^{-1} = -\tilde{H}(-k)$, with $\mathcal{C} := \sigma_0 \circ \kappa$ and κ as the complex conjugation operator. However, H does not have time-reversal or chiral symmetry. Thus, the RPS Hamiltonian H falls into symmetry class D in one dimension within the "ten-fold way" classification scheme of gapped free-fermion systems [149]. In fact, H can be interpreted as a Bogoliubov-de Gennes mean-field description of superconductivity in the Majorana representation [179,

180, 181, 149].

Gapped Hamiltonians in the symmetry class D in 1D admit topological phases that are characterized by a $\mathbb{Z}_2$ invariant [179, 181, 149]. This invariant, $\mathcal{M}$, is the sign of the Pfaffian of A_{PBC} and can be computed from $\tilde{H}$ as $\mathcal{M} = \mathrm{sign}(1 - r^2)$ [181]. Thus, a topological phase transition occurs at $r = 1$: for $r < 1$, the RPS Hamiltonian H is in the "topologically trivial phase" ($\mathcal{M} = +1$); for $r > 1$, the "topologically non-trivial phase" is attained ($\mathcal{M} = -1$); see insets of Figure 5.4 for an illustration. In other words, the two phases ($r < 1$ and $r > 1$) are topologically distinct in that they cannot be smoothly deformed into one another without closing the spectral gap.

Through the so-called bulk-boundary correspondence [150, 149], topological properties of the bulk (periodic RPS chain with $S + 1$ sites) become manifest at the boundary of the open system (open RPS chain with S sites). More precisely, upon removing the auxiliary site $S + 1$ and returning to the open RPS chain, the spectral gap for $r \neq 1$ is populated by a zero eigenvalue with a corresponding, topologically protected, strictly positive kernel vector, whose entries are localized at the boundary of the RPS chain, see Section 5.B.2. This bulk-boundary correspondence is made rigorous by introducing a Toeplitz matrix as an intermediary between the two matrices A and A_{PBC} and applying the Szegő-Widom theorem [182, 183, 184]. We conclude that the polarization states of the ALVE (2.1) correspond to gapless boundary modes. Thus, left and right polarization constitute topologically distinct stationary states, which cannot be transformed into each other without passing through the phase transition at $r = 1$.

5.4.3 Kernel vectors.

Finally, we briefly present the exact form of the kernel vector $\boldsymbol{c}$ of A. To determine $\boldsymbol{c}$, we employed the graph-theoretical interpretation of the Pfaffian, such that the kernel of A is related to the network representation of A in Figure 5.1; see [49] and Section 3.3.2. As a result, the kernel vector $\boldsymbol{c} = (c_1, \ldots, c_{2n-1})$ can be written as:

$$\begin{pmatrix} c_{2m-1} \\ c_{2m} \end{pmatrix} = \frac{1}{C} \begin{pmatrix} r_2 \\ r_1 \end{pmatrix} r^{-(m-1)} \ , \quad m = 1, \ldots, n-1 \ , \tag{5.3}$$

and $c_{2n-1} = r_2 r^{-(n-1)}/C$; C denotes the normalization constant and ensures $\sum_\alpha c_\alpha = 1$. Thus, average masses $\langle \boldsymbol{x} \rangle_\infty = \boldsymbol{c}$ decay as $c_\alpha \sim \exp(-\alpha/l_p)$ with penetration depth $l_p = 2/\ln r$ from the boundary (analogously for $r < 1$); see Figure 5.2. This explicit construction of the kernel vector agrees with the result obtained within the approach of topological band theory and, thus, confirms the topological nature of the transition at $r = 1$.

5.5 Discussion

In this Chapter, we report a topological phase transition in the stationary state of the ALVE (2.1) on the RPS chain. Stationary states are linked to strictly positive kernel vectors of the defining antisymmetric matrix. These kernel vectors are topologically protected and

give rise to robust polarization of mass. Notably, these topological phases are entirely nonlinear in that they cannot be understood as the superposition of linear waves.

We envision that the results of this work could be extended to specific higher dimensions. In 2D, the symmetry class D of the "ten-fold way" classification admits topological phases characterized by the Chern number, whereas in 3D no topological phase transition occurs [149]. In 2D, such a topological phase should be observable as a unidirectional flow of mass at the system's boundary. Possible lattices might be constructed as two-dimensional carpets of RPS cycles as extensions of the chain.

Beyond the observation of topological phases in the ALVE, one might generalize this approach to other dynamical systems in biological physics, whose attractors are nonlinear oscillators or limit cycles [185], and ecology [186]. Here we employed the ALVE on RPS cycles as the constituting building blocks, but other local oscillators may serve equally well. By suitably coupling these oscillators in the spirit of this work, we believe that topological phases as robust dynamical modes in biological systems could be designed.

5.A Appendix to RPS-chain

Figures 5.5 and 5.6 provide additional numerical simulation data that accompany Figure 5.2 from the main text.

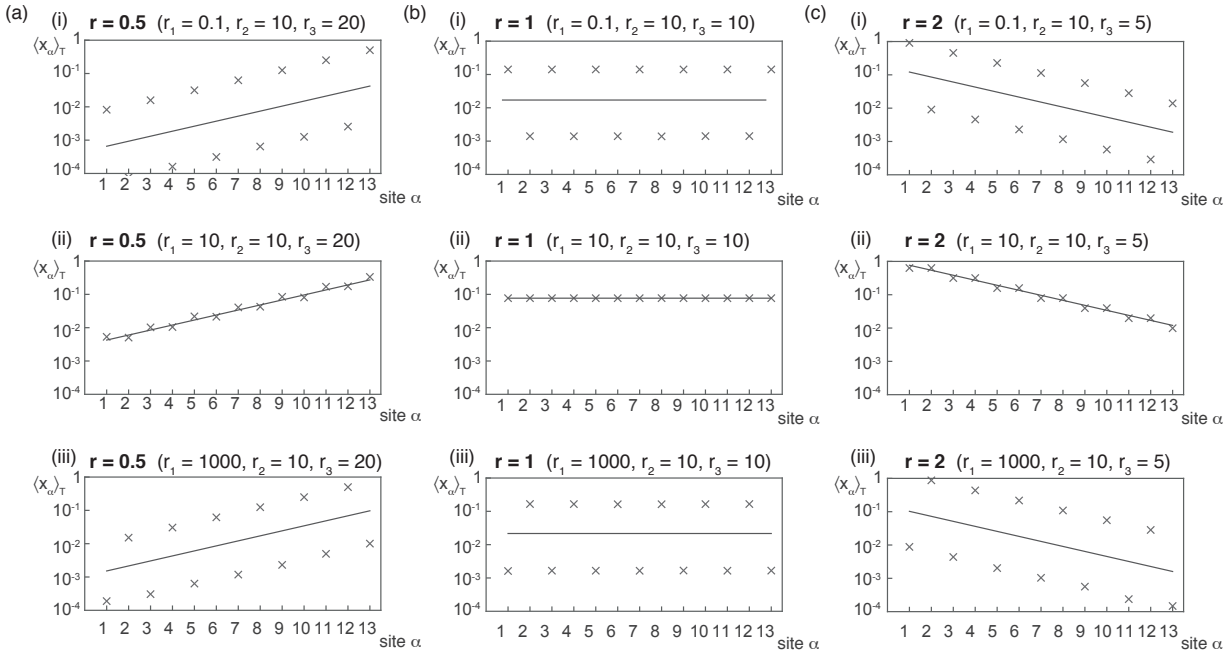

Figure 5.5: Polarization of mass to the boundary does not depend on the parameter r_1. Same organization of the plots as in Figure 5.2 with (a) $r = 0.5$, (b) $r = 1$, and (c) $r = 2$. Temporal averages $\langle x_\alpha \rangle_T$ are obtained from single realizations of the ALVE (equation 2.1) for $T = 5000$; plotted on lin-log scale. Mass becomes polarized to the right for $r < 1$ and to the left for $r > 1$, irrespective of the precise values of r_1. The parameter r_1 determines how the mass balance shifts within a single cell of the RPS chain: mass shifts to the odd states for $r_1 < r_2$ (i), to an equal distribution between even and odd states for $r_1 = r_2$ (ii), and to the even states for $r_1 > r_2$ (iii).

5.A.1 Computation of the strictly positive kernel vector of A

Here we calculate the adjugate vector of the RPS chain. The RPS chain consists of RPS cycles that share one node. As such it is a coexistence network, see Section 4.3.2, and the entries of the unique kernel vector which can be calculated as the adjugate vector are strictly positive for all choices of rates.

The αth component of the adjugate vector is calculated using all perfect matchings of the subnetwork $A_{\widehat{\alpha}}$ that is obtained from A by deleting the αth node, see Section 3.3.3. All signs of the adjugate vector share the same sign due to the RPS chain being a coexistence network. Thus the calculation of the adjugate vector simplifies to the determination of all perfect matchings. Figure 5.7 shows that every component of the adjugate vector only has

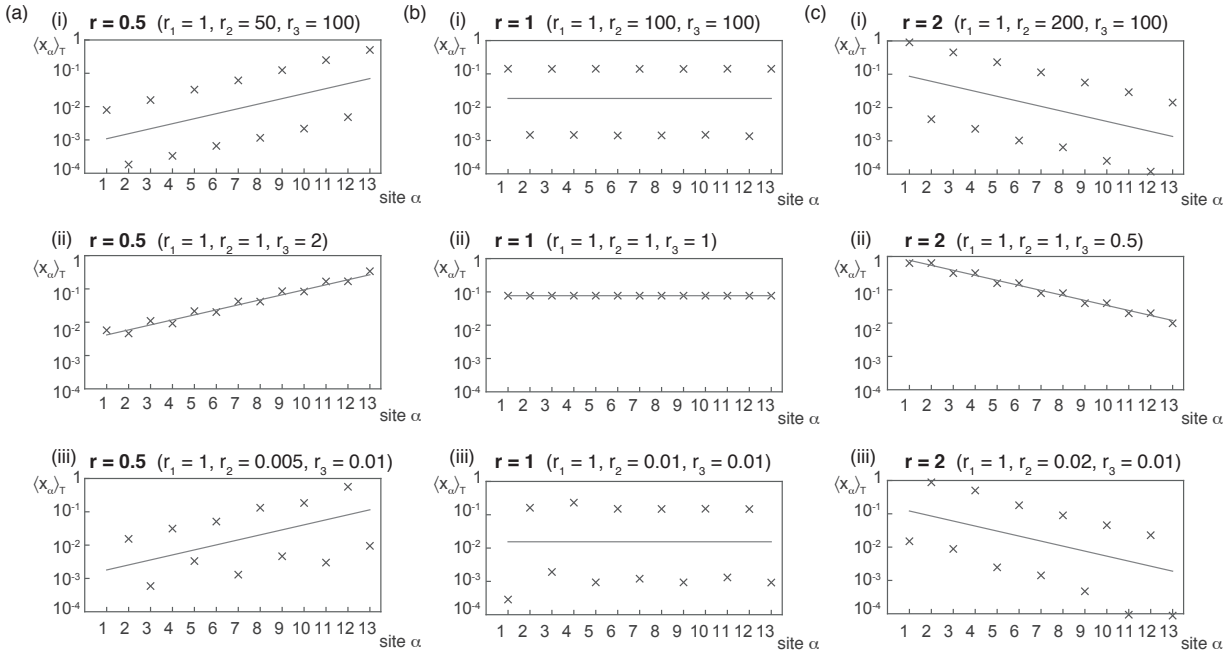

Figure 5.6: Polarization of mass to the boundary does not depend on the precise values of r_2 or r_3, but only on their ratio $r = r_2/r_3$. Same organization of the plots as in Figure 5.2 of the main text with (a) $r = 0.5$, (b) $r = 1$, and (c) $r = 2$. Temporal mass averages $\langle x_\alpha \rangle_T$ are obtained from single realizations of the ALVE (Eq. (1) of the main text) for $T = 5000$; plotted on lin-log scale. Mass becomes polarized to the right for $r < 1$ and to the left for $r > 1$, irrespective of the precise values of r_2 and r_3.

one summand corresponding to the single near-perfect matching. The adjugate vector is

$$\boldsymbol{v} = (r_2^{n-1}, r_1 r_2^{n-2}, r_2^{n-2} r_3, r_1 r_2^{n-3} r_3, \ldots, r_2^{n-m} r_3^{m-1}, r_1 r_2^{n-m-1} r_3^{m-1}, \ldots, r_2 r_3^{n-2}, r_1 r_3^{n-2}, r_3^{n-1})^T \,. \tag{5.4}$$

Because the adjugate vector is not the zero-vector, the kernel of A is one-dimensional and the adjugate vector spans the kernel. Therefore, upon normalizing with the sum over all entries C',

$$C' = \textstyle\sum_\alpha v_\alpha = \sum_{j=0}^{n-1} r_2^{n-1-j} r_3^j + \sum_{j=0}^{n-2} r_1 r_2^{n-2-j} r_3^j \tag{5.5}$$

$$= r_2^{n-1} \frac{1 - r^{-n}}{1 - 1/r} + r_3^{n-2} r_1 \frac{1 - r^{n-1}}{1 - r} = r_2^{n-2} \frac{r_2(1 - r^{-n}) + r_1(1 - r^{1-n})}{1 - 1/r} \,, \tag{5.6}$$

the kernel vector $c_\alpha = v_\alpha / C'$ is unique and strictly positive in all components α, and can be written as (see Eq. (5.3) of the main text):

$$\begin{pmatrix} c_{2m-1} \\ c_{2m} \end{pmatrix} = \frac{r_2^{n-m-1} r_3^{m-1}}{C'} \begin{pmatrix} r_2 \\ r_1 \end{pmatrix} = \frac{r_2^{n-2}}{C'} \begin{pmatrix} r_2 \\ r_1 \end{pmatrix} r^{-(m-1)} = \frac{r_3^{n-1}}{C' r_2} \begin{pmatrix} r_2 \\ r_1 \end{pmatrix} r^{n-m} \,, \tag{5.7}$$

for $m = 1, \ldots, n-1$ and $c_{2n-1} = r_3^{n-1}/C' = \frac{1}{C'} r_2^{n-1} r^{-(n-1)}$, and recall $r = r_2/r_3$. The normalization constant C as provided in the main text is obtained as $C = C'/r_2^{n-2}$.

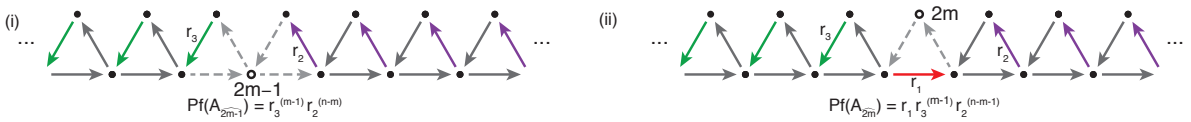

Figure 5.7: Calculation of the adjugate vector of A for the RPS chain. (i) The $(2m-1)$th component of the adjugate vector, v_{2m-1}, is calculated as the Pfaffian of the subnetwork obtained by deleting node $(2m-1)$ and determining all perfect matchings of the resulting network. For the RPS chain, only one perfect matching contributes as indicated by the green and purple arrows. (ii) Analogously, for the $2m$-th component, only one perfect matching contributes as indicated by the green, red, and purple arrows.

5.A.2 Robustness against perturbation of the model parameters

Polarization is robust against perturbations of the model parameters. This characteristics follows from the result that polarization on the RPS chain is a topological phase. Here we supplement the statements from the main text to provide a qualitative feeling for the order of magnitude against which polarization on the RPS chain is robust. To this end, we employ a perturbation of the *positive* matrix entries (5.1) as $a'_{\alpha\beta} = a_{\alpha\beta}(1 + \epsilon_{\alpha\beta})$; for $a_{\alpha\beta} < 0$, the perturbed entry $a'_{\alpha\beta}$ is obtained as $a'_{\alpha\beta} = -a'_{\beta\alpha}$ such that the perturbed matrix A' is antisymmetric. Furthermore, we assume that the perturbations $\epsilon_{\alpha\beta}$ are independently sampled from an identical probability distribution whose probability mass is centered sufficiently enough around the mean (relatively small variance in relation to the system size n and the distance of the skewness r to the critical value $r = 1$). Furthermore, we assume that all realizations of the perturbations fulfill $\epsilon_{\alpha\beta} > -1$, the mean of the distribution, $\langle\epsilon\rangle$, fulfills $\langle\epsilon\rangle \leq 1/n$, and the system size n is large.

For one realization of the perturbed rates, one may compute the adjugate vector of the perturbed system, $\boldsymbol{v}^\epsilon$, along the lines leading to Eq. (5.4) and obtains, for example, for the first component $v_1^\epsilon = v_1(1+\epsilon_{32})(1+\epsilon_{54})\dots(1+\epsilon_{S,S-1})$. If all realizations of the perturbations $\epsilon_{\alpha\beta} > -1$, then the perturbed component v_1^ϵ has the same sign as the unperturbed component v_1. Consequently, the RPS topology is not changed by the perturbations and the kernel vector of the perturbed system A' is strictly positive.

If, in addition, the perturbations are sampled from a probability distribution such that the mean fulfills $|\langle\epsilon\rangle| \leq 1/n$, the same polarization pattern emerges as for the unperturbed system for $n \gg 1$. This can be seen from the expansion of the adjugate vector; for example, the first component scales as $v_1^\epsilon \sim v_1\big(1 + (n-1)\bar{\epsilon}_{(n-1)}\big) + \mathcal{O}(v_1 n^2 \epsilon_{\alpha_1\beta_1}\epsilon_{\alpha_2\beta_2})$ and $\bar{\epsilon}_{(n-1)} = (\epsilon_{32} + \epsilon_{54} + \dots + \epsilon_{S,S-1})/(n-1)$ denoting the partial sample average, that is, the sample average of the perturbations contributing to v_1. For large enough systems, $n \gg 1$, this partial sample average approaches the mean $\langle\epsilon\rangle$ of the probability distribution. Hence, the corrections to v_1 are of the same order of magnitude as v_1 because we assumed $|\langle\epsilon\rangle| \lesssim 1/n$.

If the distribution is sufficiently centered around the mean (its variance is small enough), the corrections to most components of the adjugate vector of the perturbed system A' are of the same order of magnitude as the unperturbed component. Thus, the exponential

decay of mass on the chain is observable. In other words, the magnitude of the admissible variance of the perturbation distribution is constrained by the system size n and the value of r: the smaller the system size n and the closer the value of r is to the critical point $r = 1$, the more likely it is that a realization from a fixed perturbation distribution yields a loss of polarization.

In total, the same polarization pattern emerges for the perturbed system as for the unperturbed system with a high probability.

Estimate for robustness against perturbations. Here we give a back-of-the-envelope calculation for the robustness of the topological phase against perturbations of the rates, $a'_{\alpha\beta} = -a'_{\beta\alpha} = a_{\alpha\beta}(1 + \epsilon_{\alpha\beta})$, in the topologically phase, $r < 1$.

Assume that we choose perturbations $\epsilon_{\alpha\beta}$ from the discrete probability distribution $p(x) = 0.5(\delta(x-k) + \delta(x+k))$. In words, the perturbation takes one of the two values $\pm k$ with equal probability. This distribution has mean zero and variance k^2.

From the adjugate vector (5.4), we can read off a 'local polarization' $r_{\alpha,\mathrm{loc}}$, which describes the mass shift between two neighboring cells, as

$$r_{\alpha,\mathrm{loc}} = \frac{a_{2\alpha,2\alpha+1}}{a_{2\alpha-1,2\alpha}} \,. \tag{5.8}$$

In this setting, the overall control parameter r can be interpreted as the average of the local phase: For the unperturbed system $r = r_{\alpha,\mathrm{loc}}$ for all α. However, when adding the perturbation as defined above, we find

$$r_{\alpha,\mathrm{loc}} = \frac{r_2(1 + \epsilon_{2\alpha,2\alpha+1})}{r_3(1 + \epsilon_{2\alpha-1,2\alpha})} = r\frac{(1 + \epsilon_{2\alpha,2\alpha+1})}{(1 + \epsilon_{2\alpha-1,2\alpha})} \,. \tag{5.9}$$

In a large system (the fluctuation around the mean is neglected), the average control parameter is

$$\langle r_{\mathrm{loc}} \rangle = \sum_{\alpha} r\frac{(1 + \epsilon_{2\alpha,2\alpha+1})}{(1 + \epsilon_{2\alpha-1,2\alpha})} = r\frac{1}{4}\left(\frac{1+k}{1+k} + \frac{1-k}{1+k} + \frac{1+k}{1-k} + \frac{1-k}{1-k}\right) = \frac{r}{1-k^2} \tag{5.10}$$

On average the perturbation increases the average control parameter. The variance of the distribution is

$$\frac{\mathrm{var}(r_{\mathrm{loc}})}{r^2} = \frac{4k^2(2+k^2)}{3(k^2-1)^2} \tag{5.11}$$

From the law of large numbers, we assume that the sum over discrete random variables approaches a Gaussian distribution. For a Gaussian, a deviation of more than two standard deviations is unlikely (less than 5%). We search for a the magnitude of noise k that is admissible for the perturbed RPS chain to stay in the initial phase $r < 1$, i.e. the largest k with

$$\langle r_{loc,i} \rangle + 2\sqrt{\mathrm{var}(r_{\mathrm{loc}})} = r\left(\frac{1 + 4k\sqrt{k^2+2}/\sqrt{3}}{(1-k^2)}\right) < 1$$

Lowering the bound for r, we find

$$\frac{(1-k^2)}{1+4k\sqrt{k^2+2}/\sqrt{3}} > \frac{(1-k^2)}{1+4k} > \frac{1-k}{1+3k} > r \tag{5.12}$$

$$\Rightarrow k < \frac{1-r}{1+3r} \, . \tag{5.13}$$

The farther the system is from the point of the topological transition $r = 1$, the more robust it is against perturbations of the rates. For example, for the system in Figure 5.2, we find for $r = 0.5$ that a perturbation with discrete noise with the magnitude $k = 0.2$ is admissible.

Although this calculation gives a rough estimate about the robustness against perturbations, it is vastly simplified and can give no closed answer to the question how robust a system of finite size is.

5.B Topological band theory of the RPS Hamiltonian

5.B.1 Spectral properties of the RPS Hamiltonian

(1) RPS chain of $S+1$ sites with periodic boundary conditions. To make analytical progress within the framework of topological band theory, we extend the RPS chain by one additional site $S + 1 = 2n$ with periodic boundary conditions as described in the main text. This way, the corresponding antisymmetric interaction matrix $A_{\mathrm{PBC}} \in \mathbb{R}^{2n\times 2n}$ extends the antisymmetric matrix A by one row and column. Because of the periodic boundary conditions, A_{PBC} is an antisymmetric block-circulant matrix (compare with A in Eq. (5.1)):

$$A_{\mathrm{PBC}} = \begin{pmatrix} A_0 & A_1 & 0 & 0 & \dots & 0 & A_{-1} \\ A_{-1} & A_0 & A_1 & 0 & \dots & 0 & 0 \\ 0 & A_{-1} & A_0 & A_1 & \dots & 0 & 0 \\ \vdots & \vdots & \vdots & \vdots & \ddots & \vdots & \vdots \\ 0 & 0 & 0 & 0 & \dots & A_0 & A_1 \\ A_1 & 0 & 0 & 0 & \dots & A_{-1} & A_0 \end{pmatrix} = Circ(A_0, A_1, 0, \dots, 0, A_{-1}) \, , \tag{5.14}$$

with the 2×2 block-matrices:

$$A_0 = \begin{pmatrix} 0 & r_3 \\ -r_3 & 0 \end{pmatrix} = -A_0^T, \; A_1 = \begin{pmatrix} -r_1 & 0 \\ r_2 & 0 \end{pmatrix} = -A_{-1}^T \, . \tag{5.15}$$

In this notion, the unit cell of the RPS chain may be interpreted as follows: the transition between sites $x\alpha \to 2\alpha - 1$ for $\alpha = 1, \dots, n$ (with transition rate r_3) define the inter-cellular coupling, encoded by A_0; see Figure 5.1 . These unit cells are coupled by the transition rates r_1 and r_2 with each other and define the intra-cellular couplings, encoded by $A_1 = -A_{-1}^T$. To connect our analysis to results from condensed matter physics, we

defined in the main text the RPS Hamiltonian $H := iA_{\mathrm{PBC}}$, which is a Hermitian matrix ($H^\dagger = H$) with only real eigenvalues. Accordingly, $H_0 := iA_0$, $H_1 := iA_1$, and $H_{-1} := iA_{-1}$ are defined.

(2) Fourier transform of the RPS Hamiltonian. Because H is a translationally invariant matrix, its spectrum can be computed explicitly. To determine the spectrum of H, we start from the eigenvalue equation as follows:

$$\lambda^{(\kappa)} u_\alpha^{(\kappa)} = \sum_{\beta=1}^{2n} H_{\alpha\beta} u_\beta^{(\kappa)} \ , \ \kappa = 1, \ldots, 2n \ , \tag{5.16}$$

in which $\boldsymbol{u} \in \mathbb{R}^{2n}$ is an eigenvector to the eigenvalue λ, and κ labels the different eigenvectors. Please note that the eigenvalues come in pairs of $\pm\lambda$ because H is Hermitian. To exploit translational invariance of H in the spirit of band theory in condensed matter physics, we compute its Fourier transform through the following steps. First, the ansatz for the eigenvector $\boldsymbol{u}$,

$$u_\alpha^{(\kappa)} = u_{2\alpha'+\alpha''+1}^{(\kappa)} = \tilde{u}^{(\alpha'')}(k) \cdot e^{ik\alpha'} \ , \tag{5.17}$$

is employed with $\alpha = 2\alpha' + \alpha'' + 1$. This ansatz decomposes the eigenvector into a plane wave part, $e^{ik\alpha'}$, and a within-cell alignment part, $\tilde{u}^{(\alpha'')}(k)$. Here $\alpha' = 0, \ldots, n-1$ labels the unit cell and $\alpha'' = 0, 1$ the within-cell position of the lattice site. The momentum $k = \frac{2\pi}{n} l$ is a rescaled version of the index κ with $l = -\lfloor \frac{n}{2} \rfloor, \ldots, -1, 0, 1, \ldots, \lfloor \frac{n}{2} \rfloor - 1$.

Because H is a block-circulant matrix (and, thus, H is translationally invariant), its entries are given as $H_{\alpha\beta} = H_{2\alpha'+\alpha''+1, 2\beta'+\beta''+1} = \left(H_{\alpha'-\beta'}\right)_{\alpha'',\beta''}$ with $\alpha'', \beta'' = 0, 1$ and $\alpha', \beta' = 0, \ldots, n-1$. Note that only H_{-1}, H_0, H_1 are non-zero, see Eq. (5.14), and that the blocks H_l are cyclic in the index l, that is, $H_l = H_{n+l}$. With these definitions and properties, the eigenvalue equation (5.16) reduces to:

$$\lambda(k) \tilde{u}^{(\alpha'')}(k) = \sum_{\beta''=0,1} \tilde{H}(k)_{\alpha'',\beta''} \cdot \tilde{u}^{(\beta'')}(k) \ , \tag{5.18}$$

with $\tilde{H}(k) := \sum_{l=0}^{n-1} H_l e^{ikl}$ as the Fourier transform of the Hamiltonian H.

In summary, the eigenvectors of H as defined in Equation (5.16) can be decomposed into a plane wave part $e^{ik\alpha'}$ and a polarization part $\tilde{u}^{(\alpha'')}(k)$ (see Equation (5.17)). The polarization part fulfills the much simpler eigenvalue equation (5.18) for the Fourier transform of the Hamiltonian, which is a 2×2 matrix in this case. The eigenvalues can be directly inferred from Equation (5.18) through $\lambda^{(\kappa)} = \lambda(k)$. The Fourier transform of the

Hamiltonian for the RPS chain is obtained as follows (see Eq. (5.2) in the main text):

$$\tilde{H}(k) = e^{-ik}(-H_1^T) + H_0 + e^{ik}H_1 \ , \tag{5.19}$$

$$= \begin{pmatrix} ir_1(e^{-ik} - e^{ik}) & ir_3 - ir_2e^{-ik} \\ -ir_3 + ir_2e^{ik} & 0 \end{pmatrix} \ , \tag{5.20}$$

$$= \begin{pmatrix} 2r_1 \sin k & -r_2 \sin k + ir_3 - ir_2 \cos k \\ -r_2 \sin k - ir_3 + ir_2 \cos k & 0 \end{pmatrix} \ , \tag{5.21}$$

$$= \begin{pmatrix} h_0 + h_3 & h_1 - ih_2 \\ h_1 + ih_2 & h_0 - h_3 \end{pmatrix} = \begin{pmatrix} r_1 \sin k \\ -r_2 \sin k \\ -r_3 + r_2 \cos k \\ r_1 \sin k \end{pmatrix} \cdot \boldsymbol{\sigma} = \begin{pmatrix} h_0(k) \\ h_1(k) \\ h_2(k) \\ h_3(k) \end{pmatrix} \cdot \boldsymbol{\sigma} \ = \boldsymbol{h} \cdot \boldsymbol{\sigma} \ , \tag{5.22}$$

where, in the last line, we used the compact notation $\boldsymbol{\sigma} = (\sigma_0, \sigma_1, \sigma_2, \sigma_3)^T$ of the Pauli matrices:

$$\sigma_0 = \begin{pmatrix} 1 & 0 \\ 0 & 1 \end{pmatrix} \ \sigma_1 = \begin{pmatrix} 0 & 1 \\ 1 & 0 \end{pmatrix} \ \sigma_2 = \begin{pmatrix} 0 & -i \\ i & 0 \end{pmatrix} \ \sigma_3 = \begin{pmatrix} 1 & 0 \\ 0 & -1 \end{pmatrix} \ . \tag{5.23}$$

(3) Symmetries of the RPS Hamiltonian. $\tilde{H}$ has an inherent "particle hole symmetry" as mentioned in the main text. With the unitary operator $\mathcal{C} = \sigma_0 \circ \kappa$, where σ_0 is the identity matrix and κ is the complex conjugation, this symmetry is understood in the sense that $\sigma_0 \circ \kappa\tilde{H}(k) + \tilde{H}(-k)\sigma_0 \circ \kappa = \kappa\tilde{H}(k) + \tilde{H}(-k) = 0$ (as an operator equality) if applied to some matrix. This particle-hole symmetry of $\tilde{H}$ originates from the definition of the RPS Hamiltonian $H = iA_{\mathrm{PBC}}$ via the real-valued antisymmetric matrix A and the definition of the Fourier transform. As a consequence, the spectrum of $\tilde{H}$, and thus H, is point-symmetric to the origin, $\lambda(k) = -\lambda(-k)$; see Figure 5.4 .

(4) Spectrum of the RPS Hamiltonian. For completeness, we briefly mention explicitly the spectral properties of the RPS Hamiltonian and its Fourier transform. The determinant of $\tilde{H}$ is given by:

$$\det \tilde{H}(k) = h_0(k)^2 - h_1(k)^2 - h_2(k)^2 - h_3(k)^2 = -\big(r_2^2 \sin^2 k + (r_3 - r_2 \cos k)^2\big) \leq 0 \ . \tag{5.24}$$

Therefore, the determinant is 0 only if $r_2 = r_3$ (that is, $r = 1$) and at $k = 0$. In other words, $\tilde{H}$ has a non-trivial kernel only if $r = 1$. The trace of $\tilde{H}$ is given by $\mathrm{tr}(\tilde{H}) = 2h_0$. Thus, the eigenvalues of $\tilde{H}$ are obtained in two bands λ^+ and λ^- as follows:

$$\lambda^{\pm}(k) = \mathrm{tr}(\tilde{H})/2 \pm \sqrt{(\mathrm{tr}(\tilde{H}))^2/4 - \det \tilde{H}} = h_0(k) \pm \sqrt{h_1(k)^2 + h_2(k)^2 + h_3(k)^2} \ , \tag{5.25}$$

$$= r_1 \sin k \pm \sqrt{(r_1^2 + r_2^2)\sin^2 k + (r_3 - r_2 \cos k)^2} \ . \tag{5.26}$$

The value of r_1 only affects the eigenvalues of $\tilde{H}$ as a global shift and this shift vanishes for $k = 0$. As already seen from the determinant, the eigenvalues are only 0 for $r = 1$ at $k = 0$.

(5) Eigenvectors of the RPS Hamiltonian. The eigenvectors, $\tilde{\boldsymbol{u}}^{\pm}(k)$, of $\tilde{H}$ corresponding to $\lambda^{\pm}(k)$, k real-valued, can be written as follows (not normalized):

$$\tilde{\boldsymbol{u}}^{\pm}(k) = \begin{pmatrix} \lambda^{\pm}(k) - h_0(k) + h_3(k) \\ h_1(k) + ih_2(k) \end{pmatrix} = \begin{pmatrix} h_3(k) \pm \sqrt{h_1(k)^2 + h_2(k)^2 + h_3(k)^2} \\ h_1(k) + ih_2(k) \end{pmatrix} , \tag{5.27}$$

$$= \begin{pmatrix} r_1 \sin k \pm \sqrt{(r_1^2 + r_2^2)\sin^2 k + (r_3 - r_2 \cos k)^2} \\ -r_2 \sin k + i(r_3 - r_2 \cos k) \end{pmatrix} . \tag{5.28}$$

(6) Heuristic bulk-boundary correspondence. The RPS Hamiltonian $\tilde{H}$ has eigenvalues $\lambda^{\pm}(k)$ for only real k values; see above. However, for the *imaginary* values $k_{\pm} = \pm i \ln r$, that is $e^{ik_+} = 1/r$ and $e^{ik_-} = r$, one checks that $\det \tilde{H}(k_{\pm}) = 0$ (equivalently, $\lambda^{-}(k_{\pm}) = 0$) as $k_{\pm}$ would give rise to additional zero eigenvalues of $\tilde{H}$ (and, thus, H). Indeed, it turns out that the value of $k_+ = i \ln r$ gives rise to the kernel vector of the RPS chain defined by the antisymmetric matrix A in Eq. (5.1). The correspondence between the "suppressed" zero eigenvalue of H defined by the imaginary momentum k_+ and the realized zero eigenvalue and corresponding eigenvector of A is governed by the so-called bulk-boundary correspondence. Below, we supplement the main text with a heuristic picture of how the kernel vector of A emerges from the "suppressed" eigenvector corresponding to $\lambda^{-}(k_+)$. The mathematical details of this connection between the periodic RPS chain, defined by A_{PBC} and H, and the finite RPS chain, defined by A, are outlined in the main text and described further below.

The corresponding vectors $\tilde{\boldsymbol{w}}^{\pm}$ fulfilling the eigenvalue equation of $\tilde{H}$ for the values of $k_{\pm}$ are obtained as a solution to the equation $\tilde{H}(k_{\pm})\tilde{\boldsymbol{w}}^{\pm} = \boldsymbol{0}$ as follows:

$$\tilde{\boldsymbol{w}}^{+}(k_+ = i \ln r) = \begin{pmatrix} r_2 \\ r_1 \end{pmatrix} \quad \text{, and } \quad \tilde{\boldsymbol{w}}^{-}(k_- = -i \ln r) = \begin{pmatrix} 0 \\ 1 \end{pmatrix} . \tag{5.29}$$

Only the vector $\tilde{\boldsymbol{w}}^{+}$ is strictly positive and may give rise to a strictly positive kernel vector of A; see further below. If $\tilde{\boldsymbol{w}}^{+}$ is treated as an eigenvector of $\tilde{H}$, one can anticipate the polarization behavior of the RPS chain from the form of the corresponding eigenvector $\boldsymbol{w}^{+}$ of H that was introduced in Eq. (5.17):

$$\begin{pmatrix} w^{+}_{2\alpha'} \\ w^{+}_{2\alpha'+1} \end{pmatrix} = \begin{pmatrix} r_2 \\ r_1 \end{pmatrix} \cdot e^{ik_+\alpha'} = \begin{pmatrix} r_2 \\ r_1 \end{pmatrix} \cdot r^{-\alpha'} \text{ , for } \alpha' = 0, \ldots, n-1 , \tag{5.30}$$

in which the same functional form as the algebraically calculated kernel vector in Eq. (4) of the main text is apparent. In other words, the plane wave part $e^{ik\alpha'}$ with k_+ becomes the polarization part $e^{-\ln r \cdot \alpha'} \sim e^{-\ln r \cdot \alpha/2} = e^{-\alpha/l_p}$ with the penetration depth $p_l = 2/\ln r$

as observed in the simulations, see main text and Figure 5.2 . It also follows that for $r > 1$ mass will get polarized to the left, whereas for $r < 1$ polarization occurs to the right boundary of the RPS chain.

(7) Projection of the vector $\boldsymbol{h}(k)$ in Figure 5.4 . In Figure 5.4 , we plotted the projection of the vector $\boldsymbol{h}(k)$, which characterizes the Fourier-transformed Hamiltonian $\tilde{H}$, to analyze the manifold that is mapped out by its eigenvectors as a function of k. Because h_0 does not contribute to the form of the eigenvectors, only the three components $h_1(k), h_2(k), h_3(k)$ need to be considered for this discussion. The curve traced out by the vector $(h_1(k), h_2(k), h_3(k)) = (-r_2 \sin k, -r_3 + r_2 \cos k, r_1 \sin k)$ for $k \in [-\pi, \pi)$ lies in the plane with normal vector $\boldsymbol{n} = (r_1, 0, r_2)$ as one checks that $\boldsymbol{n} \cdot (h_1(k), h_2(k), h_3(k)) = 0$ for all k. Thus, instead of plotting $(h_1(k), h_2(k), h_3(k))$, we plotted the first two components of the vector $(h^{\parallel}(k), h_2(k), 0)$ in that plane defined by $\boldsymbol{n}$. This projection is obtained via the rotation matrix $T \in \mathbb{R}^{3\times 3}$ ($T^T T = T T^T = \mathbb{1}$):

$$T = \begin{pmatrix} -\frac{r_1}{\sqrt{r_1^2+r_2^2}} & 0 & \frac{r_2}{\sqrt{r_1^2+r_2^2}} \\ 0 & 1 & 0 \\ \frac{r_1}{\sqrt{r_1^2+r_2^2}} & 0 & \frac{r_2}{\sqrt{r_1^2+r_2^2}} \end{pmatrix} , \tag{5.31}$$

applied to the vector $(h_1(k), h_2(k), h_3(k))$:

$$\begin{pmatrix} h^{\parallel}(k) \\ h_2(k) \\ 0 \end{pmatrix} := T \cdot \begin{pmatrix} h_1(k) \\ h_2(k) \\ h_3(k) \end{pmatrix} = \begin{pmatrix} -\frac{r_1}{\sqrt{r_1^2+r_2^2}} & 0 & \frac{r_2}{\sqrt{r_1^2+r_2^2}} \\ 0 & 1 & 0 \\ \frac{r_1}{\sqrt{r_1^2+r_2^2}} & 0 & \frac{r_2}{\sqrt{r_1^2+r_2^2}} \end{pmatrix} \cdot \begin{pmatrix} -r_2 \sin k \\ -r_3 + r_2 \cos k \\ r_1 \sin k \end{pmatrix} = \begin{pmatrix} \frac{2r_1 r_2}{\sqrt{r_1^2+r_2^2}} \sin k \\ -r_3 + r_2 \cos k \\ 0 \end{pmatrix} . \tag{5.32}$$

5.B.2 Explicit bulk-boundary correspondence

Above, we heuristically explained that a "suppressed" zero eigenvalue of the RPS Hamiltonian H, or equivalently A_{PBC}, becomes a zero eigenvalue of A with a corresponding strictly positive kernel vector. Here we make this heuristic explanation rigorous by introducing an intermediary matrix between the block-circulant matrix A_{PBC} and A, and apply the so-called Szegő-Widom theorem [184, 182]. The three different systems that we discuss here are visualized in Figure 5.8 and are summarized as follows (we use the subscript n in the matrices from now on to highlight the system size):

- *The RPS chain* on $S = 2n - 1$ sites, see Figure 5.8(a); defined by the antisymmetric matrix A_n in equation (5.1) .
- *The left-boundary RPS chain* on $S + 1 = 2n$ sites, but both sites S and $S + 1$ are not connected to site 1, that is, this system has the same left boundary as the RPS chain (thus, "LB" as subscript), but a different right boundary, see Figure 5.8(b); defined by the antisymmetric matrix $A_{\mathrm{LB},n}$, which is a block-Toeplitz matrix [176].

This block-Toeplitz matrix represents the bridge to analyze the boundary properties of the RPS chain starting from the properties of the periodic RPS chain.

- *The periodic RPS chain* on $S+1=2n$ sites with periodic boundary conditions (sites S and $S+1$ are also connected to site 1 in a rock-paper-scissors cycle), see Figure 5.8 (c); defined by the antisymmetric matrix $A_{\mathrm{PBC},n}$ in Eq. (5.14), which is a block-circulant matrix, and represents the bulk properties of the RPS chain.

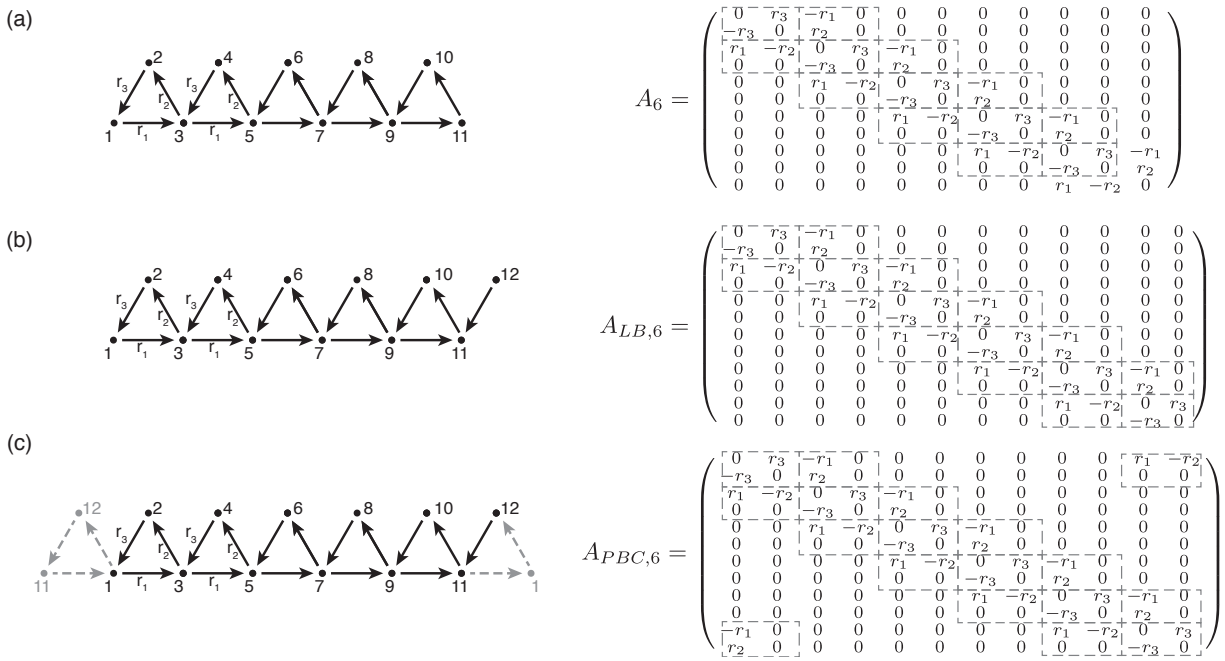

Figure 5.8: Visualization of the three different set-ups of the RPS chain, exemplified for $n=6$. (a) RPS chain on $S=2n-1$ sites defined by the antisymmetric matrix A_n. (b) Left-boundary RPS chain on $S+1=2n$ sites defined by the antisymmetric matrix $A_{\mathrm{LB},n}$, which is a block-Toeplitz matrix [176]. (c) Periodic RPS chain on $S+1=2n$ sites with periodic boundary conditions defined by the antisymmetric matrix $A_{\mathrm{PBC},n}$, which is a block-circulant matrix.

The goal is to explain the emergence of a strictly positive kernel vector of A_n with polarization to the boundary, which follows from the bulk properties of the RPS chain $A_{\mathrm{PBC},n}$. To this end, we proceed in four steps:

(1) We introduce the left-boundary RPS chain, defined by $A_{\mathrm{LB},n}$. We show that, by virtue of the Szegő-Widom theorem, two eigenvalues approach 0 as $n\to\infty$ if $r>1$. In other words, the left-boundary RPS chain has two "asymptotic" zero eigenvalues for $r>1$, which represents the essence of the bulk-boundary correspondence.

(2) We show that the vector $\boldsymbol{u}^+$ as obtained in Eq. (5.30), which fulfills the eigenvalue equation of H to the "suppressed" zero eigenvalue at value $k=i\ln r$, is indeed such an asymptotic kernel vector of $A_{\mathrm{LB},n}$.

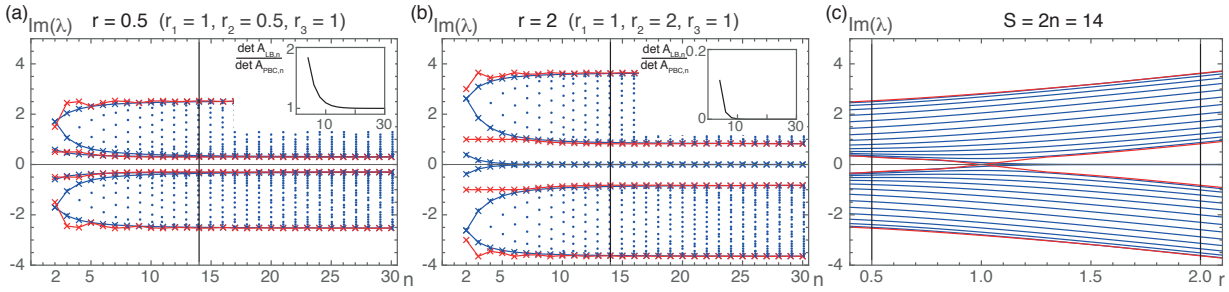

Figure 5.9: Bulk-boundary correspondence becomes apparent for the left-boundary RPS chain in that two asymptotic zero eigenvalues emerge as the system size $n \to \infty$ if $r > 1$. (a) Imaginary part of the eigenvalues of $A_{\mathrm{LB},n}$ (for $r = 0.5 < 1$) indicated by blue dots depending on the system size $S = 2n$. Largest and smallest eigenvalues above and below 0 are depicted as solid lines; red line indicates largest and smallest eigenvalues of $A_{\mathrm{PBC},n}$. The spectral gap of the Toeplitz matrix remains the same as for periodic RPS chain such that $\det(A_{\mathrm{LB},n})/\det(A_{\mathrm{PBC},n}) \to 1$ as $n \to \infty$; see inset. (b) Same plot as for (a) but with parameter $r = 2 > 1$. Two eigenvalues appear in the spectral gap and approach 0 as the system size increases such that $\det(A_{\mathrm{LB},n})/\det(A_{\mathrm{PBC},n}) \to 0$ as $n \to \infty$. Thus, the behavior of the $\det(A_{\mathrm{LB},n})$ is qualitatively different from the circulant matrix $A_{\mathrm{PBC},n}$ in that two asymptotic kernel vectors arise for the left-boundary RPS chain. One of these kernel vectors gives rise to the polarization state of the RPS chain. (c) Spectrum of the Toeplitz matrix for system size $n = 14$ (indicated as black vertical lines in (a) and (b)) for different values of the control parameter r ($r_1 = r_3 = 1$, r_2 is varied; $r = 0.5$ and $r = 2$ are depicted in (a) and (b), indicated by black vertical lines in (c)). For $r < 1$, all eigenvalues of the Toeplitz matrix (blue lines) lie between the largest and smallest eigenvalues of the circulant matrix (red lines) above and below 0. For $r > 1$, the circulant matrix again has a spectral gap, whereas the Toeplitz matrix has a pair of eigenvalues that approach zero as $n \to \infty$.

(3) This strictly positive vector $\boldsymbol{u}^+$ gives rise to the strictly positive kernel vector of A_n, which is unique upon normalization and reflects polarization to the left.

(4) The same arguments can be carried out for a right-boundary RPS chain, defined by $A_{\mathrm{RB},n}$, showing that the same vector $\boldsymbol{u}^+$ gives rise to the strictly positive kernel vector of A_n. This time, however, polarization to the right for $r < 1$ follows.

(1) Asymptotic zero eigenvalues for the left-boundary Toeplitz matrix for $r > 1$. In the spectrum of the Toeplitz matrix A_{LB}, a pair of zero eigenvalues emerges as n increases for $r > 1$ as opposed to the gapped spectrum of the circulant matrix A_{PBC}, whereas for $r < 1$ the spectra between A_{LB} and A_{PBC} develop similarly; see Figure 5.9.

More precisely, one may apply the so-called Szegő-Widom theorem for block-Toeplitz matrices, as detailed in reference [182], to the matrix $A_{\mathrm{LB},n}$. From this theorem it follows that the ratio between the determinants of the left-boundary RPS chain and the periodic RPS chain, $\det(A_{\mathrm{LB},n})/\det(A_{\mathrm{PBC},n})$, approaches a constant $E(\tilde{H})$, which only depends on the Fourier transform $\tilde{H}$, as $n \to \infty$. If E is non-zero, both the spectra of $A_{\mathrm{PBC},n}$ and $A_{\mathrm{LB},n}$ behave similarly and $A_{\mathrm{LB},n}$ is well approximated by $A_{\mathrm{PBC},n}$, loosely speaking. However,

when $E = 0$, the spectra of $A_{\mathrm{PBC},n}$ and $A_{\mathrm{LB},n}$ differ qualitatively, and this case is linked with topologically non-trivial behavior [182, 183].

For the RPS chain, the ratio of the two determinants can be explicitly computed. For example by applying the graph-theoretical formulation of the Pfaffian, the Pfaffian of both the block-Toeplitz and the block-circulant matrix, $A_{\mathrm{LB},n}$ and $A_{\mathrm{PBC},n}$, are calculated as follows:

$$\mathrm{Pf}(A_{\mathrm{LB},n}) = \mathrm{sign}\big(\begin{pmatrix}1 & 2 & 3 & 4 & ... & S & S+1\end{pmatrix}\big)\, r_3^n = (+1) r_3^n \,, \tag{5.33}$$

$$\begin{aligned}\mathrm{Pf}(A_{\mathrm{PBC},n}) &= \mathrm{sign}\big(\begin{pmatrix}1 & 2 & 3 & 4 & ... & S & S+1\end{pmatrix}\big) r_3^n + \mathrm{sign}\big(\begin{pmatrix}S+1 & 1 & 2 & 3 & 4 & ... & S\end{pmatrix}\big) r_2^n \\ &= r_3^n - r_2^n \,.\end{aligned} \tag{5.34}$$

Thus, one obtains for the fraction of the determinants:

$$\frac{\det A_{\mathrm{LB},n}}{\det A_{\mathrm{PBC},n}} = \frac{r_3^{2n}}{(r_3^n - r_2^n)^2} = \frac{1}{(1-r^n)^2} \xrightarrow{n\to\infty} \begin{cases} 0 & \text{for } r > 1 \\ 1 & \text{for } r < 1 \,. \end{cases} \tag{5.35}$$

In the topologically trivial phase ($\mathcal{M} = +1$, $r < 1$), one finds that the determinants behave asymptotically qualitatively similar, whereas in the topologically non-trivial case ($\mathcal{M} = -1$, $r > 1$), one encounters the case $E = 0$ and the determinants differ in their qualitative behavior as $n \to \infty$. Notably, while the determinant of the Toeplitz matrix, $\det A_{\mathrm{LB},n} = r_3^{2n}$, is always nonzero, with increasing size n, a pair of eigenvalues approaches zero. Thus, the corresponding eigenvectors become asymptotic kernel vectors of $\det A_{\mathrm{LB},n}$ as $n \to \infty$; see Figure 5.9.

(2) Asymptotic kernel vector of the left-boundary Toeplitz matrix for $r > 1$. To determine the asymptotic kernel vectors, one may check the vector $\boldsymbol{u}^+$ of the RPS Hamiltonian in Eq. (5.30). This vector is a promising candidate for an asymptotic kernel vector because it fulfills the eigenvalue equation for H at an imaginary value of $k_+ = i \ln r$ for which $\lambda(k_+) = 0$ and is a strictly positive vector. To this end, one computes:

$$A_{\mathrm{LB},n}\boldsymbol{u}^+ = \begin{pmatrix} 0 & r_3 & -r_1 & 0 & ... & 0 & 0 \\ -r_3 & 0 & r_2 & 0 & ... & 0 & 0 \\ r_1 & -r_2 & 0 & r_3 & ... & 0 & 0 \\ 0 & 0 & -r_3 & 0 & ... & 0 & 0 \\ \vdots & \vdots & \vdots & \vdots & \ddots & \vdots & \vdots \\ 0 & 0 & 0 & 0 & ... & 0 & 0 \\ 0 & 0 & 0 & 0 & ... & 0 & r_3 \\ 0 & 0 & 0 & 0 & ... & -r_3 & 0 \end{pmatrix} \cdot \begin{pmatrix} r_3 \\ r_1 r_3 / r_2 \\ r_3^2 / r_2 \\ r_1 r_3^2 / r_2^2 \\ \vdots \\ r_1 r_3^{n-1} / r_2^{n-1} \\ r_3^n / r_2^{n-1} \\ r_1 r_3^n / r_2^n \end{pmatrix} = \begin{pmatrix} 0 \\ 0 \\ 0 \\ 0 \\ \vdots \\ 0 \\ r_3 r_1 / r^n \\ -r_3^2 / r^{n-1} \end{pmatrix} . \tag{5.36}$$

Indeed, if $r > 1$, the "suppressed" kernel vector $\boldsymbol{u}^+$ of H is an "asymptotic" kernel vector of the Toeplitz matrix, that is $A_{\mathrm{LB},n}\boldsymbol{u}^+ \to \boldsymbol{0}$ as $n \to \infty$. In particular, $\boldsymbol{u}^+$ is strictly positive. Note that the second asymptotic kernel vector of $A_{\mathrm{LB},n}$ is not provided by the vector $\boldsymbol{u}^-$ because $A_{\mathrm{LB},n}\boldsymbol{u}^- = (r_3, 0, 0, \ldots, 0)$ does not approach $\boldsymbol{0}$ as $n \to \infty$.

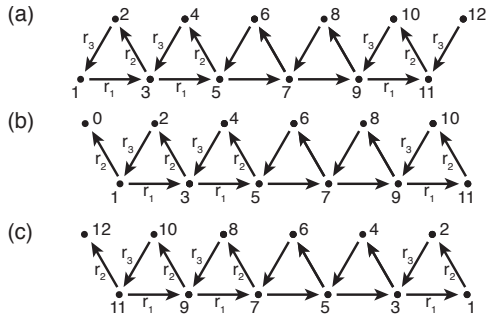

$$A_{0,LB} = \begin{pmatrix} 0 & r_3 \\ -r_3 & 0 \end{pmatrix} \qquad A_{1,LB} = \begin{pmatrix} -r_1 & 0 \\ r_2 & 0 \end{pmatrix}$$

$$A_{0,RB} = \begin{pmatrix} 0 & -r_2 \\ r_2 & 0 \end{pmatrix} \qquad A_{1,RB} = \begin{pmatrix} r_1 & 0 \\ -r_3 & 0 \end{pmatrix}$$

Figure 5.10: Toeplitz matrices of the left-boundary and the right-boundary RPS chain. (a) Left-boundary RPS chain, defined by $A_{\mathrm{LB},n}$ through the block matrices $A_{0,\mathrm{LB}}$ and $A_{1,\mathrm{LB}}$; see Eq. (5.15). (b) Right-boundary RPS chain. (c) Right-boundary RPS chain with relabeled lattices sites such that the same analysis as for the left-boundary RPS chain can be applied. This system is defined by defined by $A_{\mathrm{RB},n}$ through the block matrices $A_{0,\mathrm{RB}}$ and $A_{1,\mathrm{RB}}$ such that the roles between r_2 and r_3 are swapped and an overall minus sign is obtained.

(3) The asymptotic kernel vector gives rise to the left-polarization kernel vector of the RPS chain for $r > 1$. Importantly, $\boldsymbol{u}^+$ gives rise to the single kernel vector of A, if site $S+1$ is removed from the left-boundary RPS chain to obtain back the original RPS chain of S sites. This way, one obtains the matrix A_n from $A_{\mathrm{LB},n}$ by removing the last column and row. Similarly, the vector that is obtained from $\boldsymbol{u}^+$ by removing the last entry is the unique kernel vector of A_n upon normalization. This kernel vector reflects polarization of mass to the left boundary for the case $r > 1$.

(4) The vector $\boldsymbol{u}^+$ *gives rise to the right-polarization kernel vector of the RPS chain for* $r < 1$ *if the right-boundary RPS chain is considered.* The same arguments (1)-(3) can be made for a right-boundary system as depicted in Figure 5.10(b). Instead of implementing the correct boundary on the left side of the RPS chain (left-boundary RPS chain, defined $A_{\mathrm{LB},n}$; see Figure 5.10(a)), one may equally well implement the correct boundary at the right side of the RPS chain (see Figure 5.10(b)). After relabeling of the lattice sites $\alpha \mapsto 2n - \alpha$, one obtains the right-boundary RPS chain, defined by $A_{\mathrm{RB},n}$; see Figure 5.10(c). This relabeling has the advantage that the analysis above for the left-boundary RPS chain can be applied directly to the right-boundary RPS chain. The difference between $A_{\mathrm{RB},n}$ and $A_{\mathrm{LB},n}$ is that the roles between the rates r_3 and r_2 are swapped and that $A_{\mathrm{RB},n}$ carries an overall minus sign as compared with $A_{\mathrm{LB},n}$.

With these preparatory steps one can apply all steps of the above analysis for the left-boundary system to the right-boundary system. It follows that the same vector $\boldsymbol{u}^+$ gives rise to the strictly positive kernel vector of A_n, this time, however for the case $r_3/r_2 = 1/r > 1$, that is $r < 1$. Since the labeling starts with site 1 from the right, one also obtains polarization to the right instead of polarization to the left. In summary, the bulk-boundary correspondence yields polarization to the left boundary of the RPS chain if $r > 1$ and to the right boundary if $r < 1$.

Chapter 6

Topological phases beyond rock-paper-scissors chains

In this chapter we show that the topological phase transition of the RPS chain introduced in Chapter 5 is robust against changes in the network topology. We study two augmentations of the RPS chain:
The diamond chain is a coexistence network obtained as a triangulation of a directed cycle (see Section 4.4.1), and can be interpreted as a RPS chain with one additional coupling between neighboring unit cells. For the diamond chain, we find a similar phenomenology as for the RPS chain: Depending on one control parameter, the average overall mass polarizes to the boundaries of the system. This polarization is robust against perturbations of the rates. At the transition point, solitary waves are observed. However, in contrast to the previous chapter, the mathematical details of the diamond chain are more involved: Although the framework for topological phases predicts the correct qualitative behavior, quantitative characteristics like the penetration depth of the polarization cannot be read off from the Fourier transform, but require a graph-theoretical analysis of the network. Polarization in the diamond chain is an asymptotic behavior in the bulk: The exponential decay causing the polarization emerges at some distance from the boundaries.
We also present the K_4 chain, an augmentation of the diamond chain that includes all possible interactions between the vertices of neighboring unit cells. The topological phase transition observed in the diamond chain can also be found in the K_4 chain. Additionally, the K_4 chain can exhibit extinction, which results in a decay of the chain into smaller subsystems whose size depends sensitively on the chosen rates. Notably, extinction only occurs in the topologically non-trivial phase.
Finally, we derive that the ALVE on a one-dimensional chain at the critical point can be reformulated as a differential difference equation. The resulting equations have a similar structure as prominent model systems in the study of solitary waves in integrable systems.

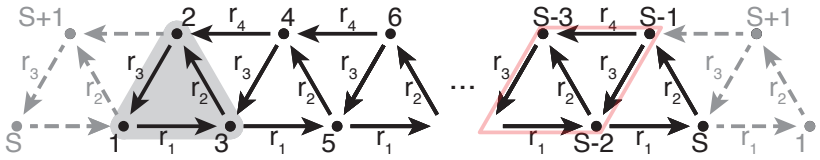

Figure 6.1: The one-dimensional diamond chain The network can be understood as a one dimensional lattice with a two-element unit cell that contains rock paper scissors cycles (highlighted in grey). We call this network a diamond chain for the diamond graph (as known from graph theory [53]) (light red). An arrow from one site to another indicates that mass is transported in this direction at rate $r_1, ..., r_4 > 0$ following the ALVE 2.1. The auxiliary site $S + 1$ facilitates periodic boundary conditions (dashed lines) within the framework of topological band theory.

6.1 The diamond chain

The diamond chain is a finite one dimensional lattice created from a unit cell containing two interacting states and coupling between neighboring unit cells. The coupling is chosen in such a way that mass flow in both directions of the chain is possible, see Figure 6.1. The name has its origin in graph theory where a square with one diagonal is called a 'diamond graph'. This motif is formed here by two neighboring unit cells (marked in light red in Figure 6.1). The diamond chain is represented by the antisymmetric matrix of size $S = 2n - 1$,

$$A = \begin{pmatrix} 0 & r_3 & -r_1 & 0 & 0 & ... & 0 & 0 & 0 & 0 & 0 \\ -r_3 & 0 & r_2 & r_4 & 0 & ... & 0 & 0 & 0 & 0 & 0 \\ r_1 & -r_2 & 0 & r_3 & -r_1 & ... & 0 & 0 & 0 & 0 & 0 \\ 0 & -r_4 & -r_3 & 0 & r_2 & ... & 0 & 0 & 0 & 0 & 0 \\ 0 & 0 & r_1 & -r_2 & 0 & ... & 0 & 0 & 0 & 0 & 0 \\ \vdots & \vdots & \vdots & \vdots & \vdots & \ddots & \ddots & \vdots & \vdots & \vdots & \\ 0 & 0 & 0 & 0 & 0 & ... & 0 & r_3 & -r_1 & 0 & 0 \\ 0 & 0 & 0 & 0 & 0 & ... & -r_3 & 0 & r_2 & r_4 & 0 \\ 0 & 0 & 0 & 0 & 0 & ... & r_1 & -r_2 & 0 & r_3 & -r_1 \\ 0 & 0 & 0 & 0 & 0 & ... & 0 & -r_4 & -r_3 & 0 & r_2 \\ 0 & 0 & 0 & 0 & 0 & ... & 0 & 0 & r_1 & -r_2 & 0 \end{pmatrix}, \tag{6.1}$$

with rate constants $r_1, r_2, r_3, r_4 > 0$. The qualitative phenomenology of the ALVE on this chain is controlled by the skewness $r := \frac{r_2}{r_3}$. The remaining values r_1, r_4, have only minor impact for the global phenomenology, that is polarization, but influence the strength of polarization.

Relation to the previous chapters In Chapter 4.4.1 we introduced the network topology of the diamond chain as a triangulation of a directed cycle that is oriented to be a coexistence network. As such, the diamond chain has a strictly positive kernel vector for all rates. Exploiting the regular structure (in its interior the network is translationally invariant) we can study topological phase transitions in the ALVE dynamics.
The diamond chain can also be understood as an extension of the RPS chain, where one additional coupling between neighboring unit cells is included. By setting $r_4 = 0$, we recover the RPS chain discussed in Chapter 5.

6.2 Phenomenology

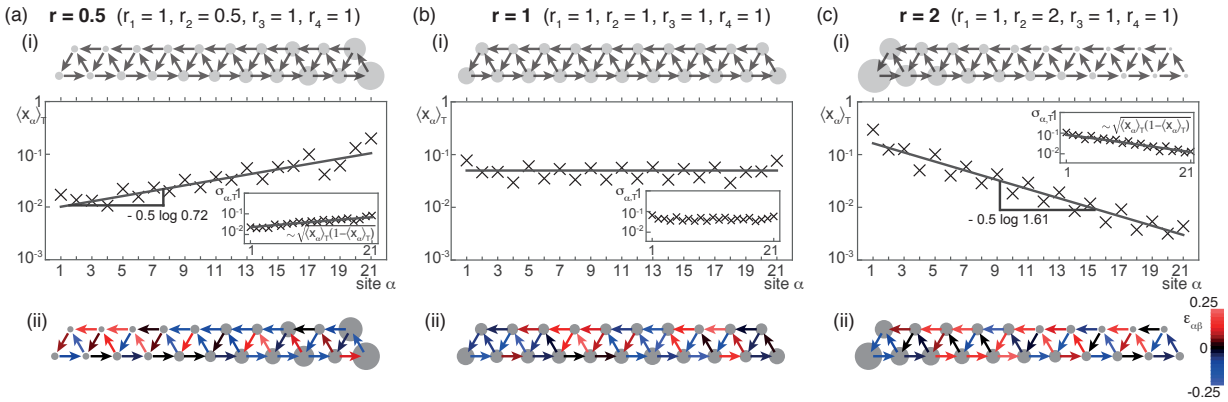

Figure 6.2: Polarization of mass to the boundary (a-c)(i) The temporal mass averages $\langle x_\alpha \rangle$ of single numerical integrations of the ALVE (2.1) are shown on the diamond chain (S = 21) as the disk size. The polarization becomes visible as exponential decay to the right for $r < 1$ and to the left for $r > 1$ (shown here on a lin-log scale). For $r = 1$, the average mass is uniformly distributed on the whole chain. While the penetration depth only depends indirectly on r, its sign and thus polarization is decided by $r \gtrless 1$. Polarization is no state of rest (non-vanishing fluctuations $\sigma_{\alpha,T}$ around the averages; insets). (a-c) (ii) Polarization is robust against perturbations of the individual rates ($\epsilon_{\alpha,\beta}$ uniformly sampled in $[-0.25, 0.25]$) with the same characteristics as without perturbations.

Numerical integrations of the ALVE dynamics on the diamond chain reveal a rich phenomenology, comparable to that of the RPS chain. Dependent on a single control parameter we observe robust polarization of mass as shown in Figure 6.2. At the transition, mass is uniformly distributed over the system and solitary waves are observed. Recall that in the ALVE dynamics the total mass is conserved. As the diamond chain is a coexistence network, all states coexist for all times ($x_\alpha > Const. > 0$ for all α) when $x_{0,\alpha} > 0$ for all α.

Localization Depending on the skewness $r = \frac{r_2}{r_3}$, the average mass in the system polarizes to the edge of the chain, see Figure 6.2 (a-c) (i). The ALVE dynamics itself does not fixate, but polarization becomes visible as the temporal average occupation $\langle x_\alpha \rangle_T$ over a long period $T \gg 1$.

Mass penetrates the system from the boundary, asymptotically reaching exponential decay $\langle x_\alpha \rangle_T \sim e^{-\alpha/l_p}$ in the bulk. The penetration depth $l_p = 2/\ln r'$ depends on the skewness only indirectly as $r' = \frac{r_2+\sqrt{r_2^2+4r_1r_4}}{r_3+\sqrt{r_3^2+4r_1r_4}}$. Note that, while the magnitude of the penetration depth, that is, the polarization strength, is also influenced by the values r_1 and r_4, the sign of l_p, and thus the polarization, only depends on wether $r \gtrless 1$, as shown in Figure 6.10.

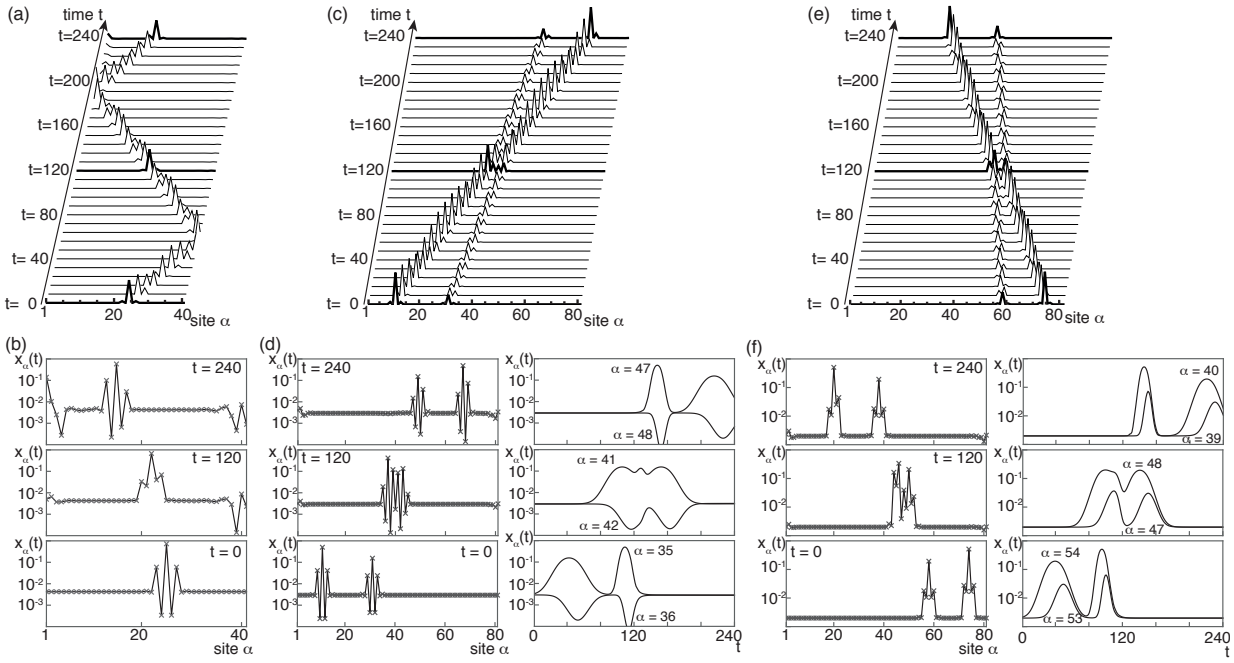

Figure 6.3: Solitary waves in the diamond chain at the topological transition At $r = 1$, a suitably initialized peak of mass remains localized and travels along the diamond chain. In a finite system a peak is imperfectly reflected at the boundary (a). Peaks can either travel from left to right (c)-(d) or from right to left (e)-(f). After a collision with a peak traveling in the same direction, shape and speed remain unchanged, (c)-(f). Compared to the average occupation in the system, the right-moving peak consists of positive and negative deflections (d), while the left-moving peak consists of positive deflections only (f). Through reflection at the boundaries, the right-moving peak is transformed into a left-moving peak and vice versa (a)-(b).

Robustness The polarization is robust against perturbations of the systems rates. In Figure 6.2 (a-c) (ii) we show that the polarization remains when the interaction strengths are perturbed as $a'_{\alpha\beta} = -a'_{\beta\alpha} = a_{\alpha\beta}(1 + \epsilon_{\alpha\beta})$. The perturbations $\epsilon_{\alpha\beta}$ are independently drawn from the same uniform distribution centered around 0 such that the network topology remains unchanged (all $\epsilon_{\alpha\beta} > -1$)[1]. Additionally, the polarization is observed when adding an additional coupling between neighboring unit cells r_5, as shown Section 6.5.

Solitary waves At the transition point, $r = 1$, we observe solitary waves in the system. A suitably initialized peak of mass travels through the system without changing its shape; two such peaks traveling at different speeds pass through each other seemingly without changing shape. Both of these observations are characteristic for solitary waves and by no means trivial for nonlinear dynamical systems [170]. Numerically, we found two different kinds of solitary waves:
Forward moving waves consist of positive deflections on the odd and negative deflections

[1] A nonzero center $\epsilon_0 \neq 0$ for the distribution can be absorbed in redefined rates and noise as $a_{\alpha\beta}(1 + \epsilon_{\alpha\beta}) = a_{\alpha\beta}(1 + \epsilon_0)(1 + \epsilon_{\alpha\beta}/(1 + \epsilon_0)) = \tilde{a}_{\alpha\beta}(1 + \tilde{\epsilon}_{\alpha\beta})$

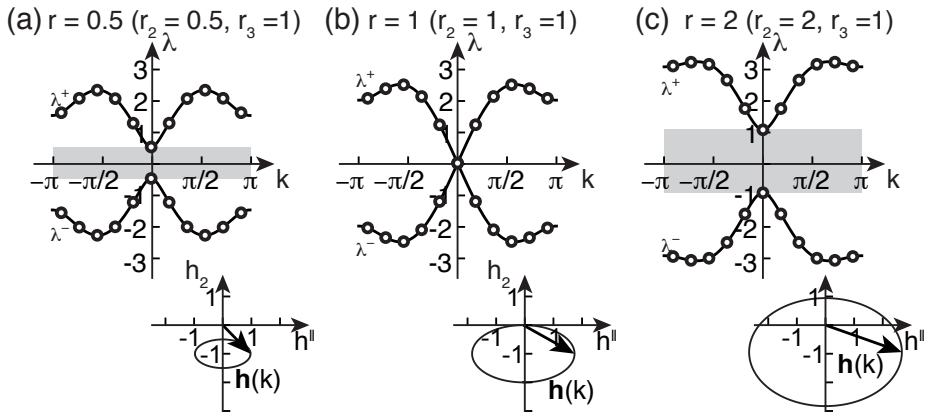

Figure 6.4: The spectra of the Fourier transform of the diamond Hamiltonian $\tilde{H}$ are shown with $r_1 = r_4 = 1$. Although the spectra for $r_2 < 1$ (a) and $r_2 > 1$ (c) both have a bandgap (grey), only for $r_2 > 1$ the system is topologically nontrivial as indicated by the winding of the origin by the contour of $\boldsymbol{h}(k)$ (insets). At the transition point $r = 1$ (b), the bandgap closes, coinciding with the contour $\boldsymbol{h}(k)$ passing through the origin.

on the even sites compared to the system's mean as shown in Figure 6.3 (a). Backward moving solitons are built from positive deflections both on odd and even sites compared to the systems mean, see Figure 6.3 (b).

With the rates $r_1, ..., r_4 = 1$, the ALVE 2.1 can be reformulated as a differential difference equation closely related to the relativistic Toda lattice, as shown in Section 6.6.

6.3 Analysis

Analogous for the RPS chain in Chapter 5, polarization in the ALVE on the diamond chain can be understood in the framework of topological phase transitions as known from condensed matter physics. To this end, we again consider a closed system, where to the original system A an additional state is added and periodic boundary conditions apply as indicated in grey in Figure 6.1. The resulting block-circulant matrix A_{PBC} is of size $2n$ ($n > 2$) and translationally invariant.

6.3.1 Topological condensed matter approach

We define the diamond-Hamiltonian $H = iA_{PBC}$, which is hermitian $H^\dagger = H$ with real eigenvalues that occur in pairs, $\pm\lambda$, see also Section 3.2. In the following, we analyze this Hamiltonian in the framework of topological band theory. Spectrum and eigenvectors of H can be obtained from spectrum and eigenvectors of the Fourier transformed Hamiltonian $\tilde{H}(k)$, where k denotes the wave number of the Brillouin zone ($k = \frac{2\pi}{n}l$ and $l = -\lfloor\frac{n}{2}\rfloor, ..., 0, 1, ..., \lfloor\frac{n}{2}\rfloor$). The Fourier transformed Hamiltonian reads

$$\tilde{H}(k) = \begin{pmatrix} 2r_1 \sin k & ir_3 - r_2 \sin k - ir_2 \cos k \\ -ir_3 - r_2 \sin k + ir_2 \cos k & -2r_4 \sin k \end{pmatrix} . \tag{6.2}$$

Projecting the Hamiltonian on the Pauli matrices $\sigma = (\sigma_0, \sigma_1, \sigma_2, \sigma_3)$ (as done in Section 5.B.1), we find $\tilde{H} = \mathbf{h}(k) \cdot \sigma$ with $\mathbf{h}(k) = ((r_1 - r_4)\sin k, -r_2 \sin k, -r_3 + r_2 \cos k, (r_1 + r_4)\sin k)$.
The spectrum of H and its dependence on the control parameter r as shown in Figure 6.4 can be derived from Eq. (6.2) as shown in Section 6.A. As the unit cell is constituted of two sites, the spectrum has two bands of eigenvalues $\lambda^{\pm}$. For $r \neq 1$, the bands are separated by a bandgap that closes only for $r = 1$ at $k = 0$.

Topological invariant In order identify and classify the topological phases of the diamond chain, we must first identify its topological class according to the "ten-fold way" classification scheme [148]. This classification is based on three unitary symmetries ("chiral", "particle hole" and "time reversal" [153, 149]) and predicts the topological invariant of a system. From the three canonical symmetries, the diamond chain only has a "particle hole symmetry", which is revealed by the operator $\mathcal{C} = \sigma_0 \circ \kappa$ (κ is the complex conjugation operator) with $\mathcal{C}^{-1}\mathcal{C} = +1$. Applied to the Hamiltonian, we find $\mathcal{C}\tilde{H}(k)\tilde{C}^{-1} = -\tilde{H}(-k)$, proving the "particle hole symmetry". For $r_1 = r_4$, the spectrum is additionally mirror symmetric along the x- and y-axis, i.e., $\lambda^{\pm}(k) = \lambda^{\pm}(-k) = -\lambda^{\mp}(-k)$. However, as there is no accompanying unitary operator to go with this symmetry, this does not influence the topological class.

Summarizing, the periodic diamond chain is in the symmetry class D. The topological invariant for 1D systems in this class can be calculated as the Pfaffian invariant[179] that is closely related to the Berry phase [181]. Simply speaking, the Pfaffian invariant equals the sign of the Pfaffian of H_{PBC}. The topological invariant is calculated as

$$\mathcal{M} = \operatorname{sign}\left(\operatorname{Pf}(\tilde{H}(0))\operatorname{Pf}(\tilde{H}(\pi))\right) \tag{6.3}$$

$$= \operatorname{sign}\left(1 - \left(\frac{r_2}{r_3}\right)^2\right) = \begin{cases} +1 & \text{for } r < 1 \\ -1 & \text{for } r > 1 \end{cases} . \tag{6.4}$$

Here, $\mathcal{M} = -1$ denotes the topologically nontrivial phase. The topological invariant can also be read of from the contour traced by $\boldsymbol{h}(k)$ for $k \in [0, 2\pi]$. In the topologically nontrivial phase the curve $\boldsymbol{h}(k)$ winds around the origin, see Figure 6.4, insets.

Topological condensed matter theory predicts that a semi-infinite system with a sharp boundary in the topologically nontrivial phase has an edge mode, that is a kernel vector that is localized at the boundary. For the ALVE, this means that the mass of the system polarizes to the left boundary when $\mathcal{M} = -1$.

In the numerical integrations we observe that when $\mathcal{M} = +1$, mass polarizes to the right boundary. This switch of polarization from the left to the right boundary when leaving the topologically nontrivial phase is a consequence of the symmetry between intra-size coupling (r_3) and inter-size coupling (r_2). By switching the roles of unit cell ($r_3 : \ 2m \to 2m-1$) and coupling ($r_2 : \ 2m+1 \to 2m$) we also exchange the topological invariant: As A consists of $S = 2n - 1$, i.e., $n - 1$ *and a half* unit cell, a non-trivial left boundary implies a trivial right-boundary and vice versa.

6.3.2 Algebraical approach: The Szegő-Widom theorem

As we are ultimately interested in the properties of a real antisymmetric matrix, we can alternatively find an algebraic interpretation for the topological phase transition that occurs when $r = 1$. Polarization can be understood by introducing a Toeplitz matrix A_{LB} of size $2n$ as an intermediary between the diamond chain A ($S = 2n - 1$) and the periodic system A_{PBC} ($S = 2n$). The Szegő-Widom theorem gives insight into the relation of the determinant of a circulant matrix (periodic system) and the corresponding open system (Toeplitz matrix). The situation when the fraction of determinants of the circulant and Toeplitz matrix is zero in the limit of infinite systems ($n \to \infty$) is associated with a topological phase transition [182, 183]. In the topologically nontrivial case, A_{LB} has a pair of eigenvectors that approach zero for $n \to \infty$, such that (in contrast to the circulant matrix), the Toeplitz matrix, has a zero mode.

For the diamond chain, looking at the fraction of determinants, we find

$$\frac{\det T_n}{\det C_n} \xrightarrow{S\to\infty} \begin{cases} 1 & \text{for } r < 1 \\ 0 & \text{for } r > 1 \end{cases} \tag{6.5}$$

Details of the calculation are presented in Section 6.B. Simply speaking, when the fraction of determinants approaches a nonzero constant, the two systems have similar spectral properties: The open system A_{LB} does not 'feel' the boundary. In contrast, when the fraction of determinants approaches zero, one pair of eigenvalues of A_{LB} approaches zero, indicating the appearance of an asymptotic zero mode. This zero mode is localized at the boundary, and can be extrapolated from the adjugate vector of A.

6.4 Condensate vector

The kernel vector of the coupling matrix A gives key informations about the long-time dynamics of the ALVE: The condensate vector is not only the stationary state of the ALVE ($\boldsymbol{x}^* = \boldsymbol{c}$ implies $\partial_t x_\alpha^* = 0$), but its entries equal the temporal average occupation of each site, $c_\alpha = \langle x_\alpha \rangle_\infty$ and its fluctuations 2.4.

The kernel vector of A can be calculated as the adjugate vector that makes use of Pfaffians of subnetworks, see the detailed calculations in Section 6.4. The Pfaffians of subnetworks can be expressed as linear recursive polynomials in their size m,

$$f_m(a, b) = a f_{m-1}(a, b) + b f_{m-2}(a, b) \; . \tag{6.6}$$

For the diamond chain, the variables a and b are functions of the transition rates r_1, r_2, r_3, r_4.

The kernel vector $\boldsymbol{c} = (c_1, \ldots, c_{2n-1})$ of the diamond chain reads

$$\begin{pmatrix} c_{2m-1} \\ c_{2m} \end{pmatrix} = \frac{1}{C} \begin{pmatrix} f_m(r_3, r_1 r_4) f_{n-m+1}(r_2, r_1 r_4) \\ f_m(r_3, r_1 r_4) r_1 f_{n-m}(r_2, r_1 r_4) \end{pmatrix}, \; m = 1, ..., n-1 \; . \tag{6.7}$$

and $c_{2n-1} = \frac{1}{C} f_{n+1}(r_3, r_1 r_4) f_1(r_2, r_1 r_4)$. Here, C denotes the normalization constant that ensures $\sum_\alpha c_\alpha = 1$. Details of the calculation are presented in Section 6.B.1.

Asymptotic behavior: exponential decay. The condensate vector is constructed as a combination of two sequences. The first sequence, $f_m(r_3, r_1r_4)$, increases with the index in such a way that both states of a unit cell (e.g., $2m-1$ and $2m$) receive the same contribution. The recursive series is initialized at the boundary, where it ensures the boundary condition.
On the other hand, the sequence $f_{n-m+1}(r_2, r_1r_4)$ starts at the final state and increases with decreasing index. Here, the two states of neighboring unit cells, $2m+1$ and $2m$, receive the same factor. This sequence proceeds from right to left, ensuring the boundary condition at the final state.

For large m, the linear recursive sequences $f_m(a,b)$ approach the asymptotically exponential behavior $f_m(a,b) \sim (\phi_+(a,b))^m = (a/2 + \sqrt{a^2/4+b})^m$, see Section 6.E. In the bulk of a large enough system, for both sequences the distance from their initial value at the boundary are large enough such that they are well approximated by their asymptotic behavior. Inserting the asymptotics in the condensate vector (6.7), in the bulk we find an exponential decay of $c_\alpha \sim \exp(-\alpha/l_p)$. The penetration depth, $l_p = 2/\ln r'$, is calculated as $r' = \frac{r_2+\sqrt{r_2^2+4r_1r_4}}{r_3+\sqrt{r_3^2+4r_1r_4}}$. This is precisely the decay observed in the numerical integrations in Figure 6.2

Asymptotic zero mode of a semi-infinite system. From the condensate vector, we can also extrapolate the asymptotic zero mode of a semi-infinite system whose existence is predicted by the topological analysis 6.3.

We assume that the semi-infinite system has a left boundary and is infinitely large, that is the right boundary is shifted to infinity. It can thus be understood as the infinite size limit of the original system A. The asymptotic kernel vector for this semi-infinite system, $\boldsymbol{c}_\infty$, has the form

$$\begin{pmatrix} c_{\infty,2m-1} \\ c_{\infty,2m} \end{pmatrix} = \frac{f_m(r_3, r_1r_4)}{\phi_+(r_2, r_1r_4)^m} \begin{pmatrix} \phi_+(r_2, r_1r_4) \\ r_1 \end{pmatrix} . \tag{6.8}$$

Here, the linear recursive polynomial $f_m(r_3, r_1r_4)$ secures that the boundary condition at he left boundary is fulfilled, while the contribution $1/\phi_+(r_2, r_1r_4)^m$ is the asymptotic of the sequence securing the right-boundary condition in the finite system. Taken together, this vector is no kernel vector of a finite system of any size as the right boundary condition is not fulfilled. Thus, it is an asymptotic kernel vector that fulfills left boundary condition and extends infinitely to the right as a decaying sequence.

Discussion. The sign of the penetration depth and thus the polarization is decided by the sign of $\ln r'$. When $r' < 1$ overall mass in the system polarizes to the right, when $r' > 1$, mass polarizes to the left. Although the sign of l_p does not directly depends on r, the phases $r \gtrless 1$ directly correspond to $r' \gtrless 1$. The topological phases identified using the framework of topological band theory translate directly to the polarizations that arise from r'. Although the rates r_1, r_4 do not influence the orientation of polarization (left or

right), they can drastically influence its strength. When $r_1, r_4 \gg r_2, r_3$, r' is driven close to the transition point ($r' \to 1$) and polarization may be barely noticeable in a finite system, see Figure 6.10.

6.5 The K_4 chain

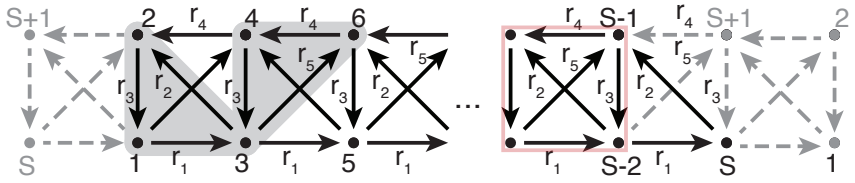

Figure 6.5: The K_4 chain. The network is obtained from the diamond chain by adding an additional interaction $2m + 2 \to 2m$ with rate r_5. The name derives from the graph theoretical motif of the complete graph with four vertices K_4 [53] (highlighted in light red). The K_4 chain can be though of as two RPS chains layered on top of each other. The RPS cycles are highlighted in grey.

As already mentioned in Section 6.2, the observations found for the diamond chain persists when including an additional interaction $2m \xrightarrow{r_5} 2(m-1)$, see Figure 6.5. The resulting network can be thought of as two RPS chains layered on top of each other. As all connections between all vertices of neighboring unit cells are realized, this network is the most general one dimensional chain with a two element unit cell. Note that the K_4 chain is not a coexistence network as it contains crossing edges (with rates r_2 and r_5) that disagree with the crossing condition (4.3), for details see Section 6.C.1. Thus, depending on the transition rates $r_1, \ldots, r_5$, we observe both coexistence of all states, or extinction and thus decomposition into disconnected subsystems, see Section 6.C.

6.5.1 Topological invariant and phenomenology

As for the diamond chain, we can define a Hamiltonian H and perform a Fourier transform, see Section 6.A. For the topological invariant we find

$$\mathcal{M} = \operatorname{sign}\left(1 - \left(\frac{r_2 + r_5}{r_3}\right)^2\right) , \tag{6.9}$$

indicating that the value of the control parameter $\tilde{r} = \frac{r_2+r_5}{r_3}$ sets the topological phase, with topologically nontrivial behavior for $\tilde{r} > 1$.

Indeed, we observe the same qualitative behavior as for the diamond chain and the RPS chain:
Dependent on $\tilde{r}$, we find robust polarization of the average mass $\langle x_\alpha \rangle_\infty$, with asymptotic exponential decay $\langle x_\alpha \rangle_\infty \sim e^{-\alpha/l_p}$ from the boundary into the bulk, with a transition without polarization at $\tilde{r} = 1$. As penetration depth we find $l_p = 2/r'$ with

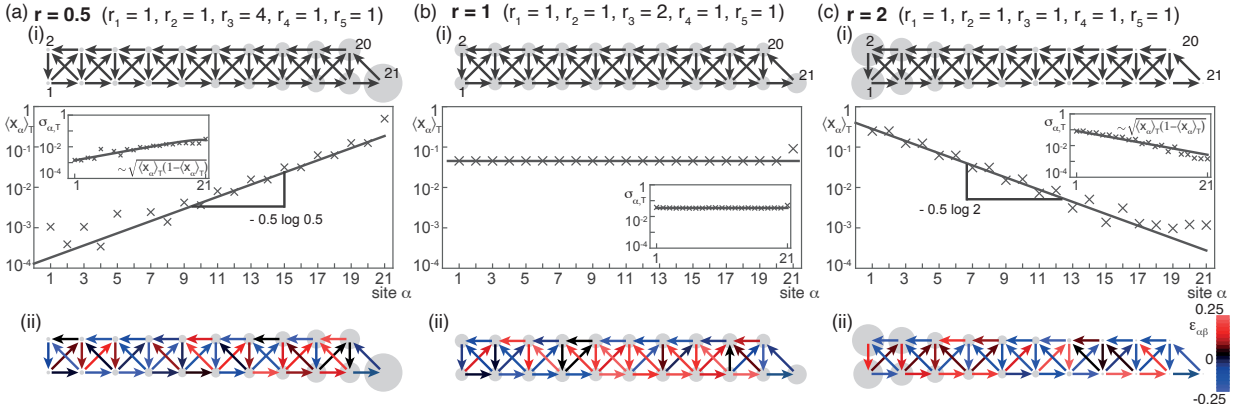

Figure 6.6: Polarization of mass in the K_4 chain The K_4 chain shows the same phenomenology as the diamond and the RPS chain. The temporal mass averages $\langle x_\alpha \rangle$ of single numerical integrations of the ALVE (2.1) are polarized to the right for $r < 1$ and to the left for $r > 1$ on a lin-log scale. For $r = 1$, the average mass is uniformly distributed on the whole chain. The slope in the lin-log plot is $-0.5 \log \frac{(r_2+r_5)+\sqrt{(r_2+r_5)^2+4(r_1r_4-r_2r_5)}}{r_3+\sqrt{r_3^2+4(r_1r_4-r_2r_5)}}$. Polarization is no state of rest (non-vanishing fluctuations $\sigma_{\alpha,T}$ around the averages; insets). (a-c) (ii) Polarization is robust against perturbations of the individual rates ($\epsilon_{\alpha,\beta}$ uniformly sampled in $[-0.25, 0.25]$) with the same characteristics as without perturbations.

$r' = \frac{(r_2+r_5)+\sqrt{(r_2+r_5)^2+4(r_1r_4-r_2r_5)}}{r_3+\sqrt{r_3^2+4(r_1r_4-r_2r_5)}}$, see Figure 6.6. These numerical findings are backed by the adjugate vector, for details see Section 6.B.1.

6.5.2 Extinction in the K_4 chain

As a new feature, in the dynamics of the K_4 chain extinction can occur. Dependent on the rates, states go extinct such that the chain dissects into disconnected subnetworks. The size of the remaining disconnected subnetworks depends on the rates alone and is independent of the system size. Simply speaking, the rates define a maximum sustainable size for which a subnetworks kernel vector is strictly positive.

If all states survive or not is decided by sign and magnitude of the expression $r_3^2/2 + r_1r_4 - r_2r_5$, as shown in Figure 6.7:

- For $r_3^2/2 + r_1r_4 - r_2r_5 > 0$, all states survive, see Figure 6.7(a),
- when $r_3^2/4 + r_1r_4 < r_2r_5 < r_3^2$, the chain decomposes into disconnected chunks whose size depends sensitively on the magnitude of r_2r_5, see Figure 6.7(b-c).
- Finally, when $r_3^2 < r_2r_5$, the K_4 chain separates into disconnected RPS cycles, see Figure 6.7(d).

The subsystems are unconnected, separated by the extinction of one RPS cycle. Interestingly, extinction occurs only in the topologically nontrivial phase $r < 1$, when mass polarizes to the left.

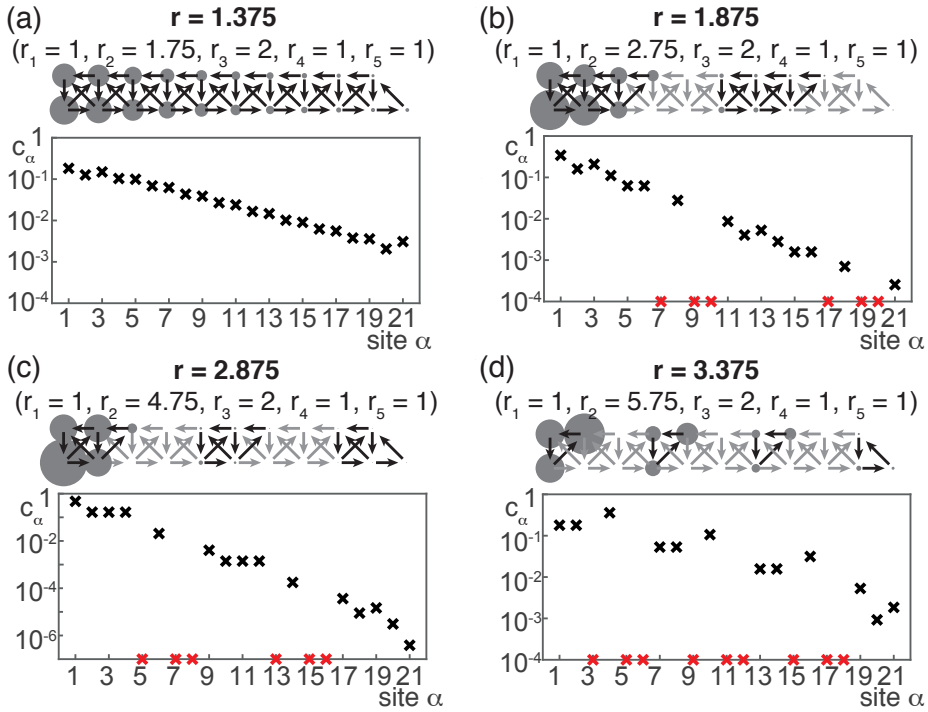

Figure 6.7: Extinction in the K_4 chain In the topologically nontrivial phase ($r > 1$), in the K_4 chain, extinction and condensation is possible. When increasing $r_2 r_5$ (here, r_5 is kept constant), the system transitions from coexistence of all states (a) to separation into disconnected chunks whose size depends sensitively on the rates (b-c). Below the critical value, $r_2 r_5 > r_1 r_4 + r_3^2$, the chain separates into disconnected RPS cycles (d).

Extinction in the K_4 chain can be understood on the basis of the condensate vector. As for the diamond chain, also for its augmented version the adjugate vector consists of a product of linear recursive polynomials, see Section 6.B.1. Simply speaking, extinction in the K_4 chain occurs when the adjugate vector contains zero or negative entries. In this case, the system divides into the largest subsystems for which the adjugate vector has only positive entries. The size of these subsystems depends on the first appearance of a nonpositive value in the linear recursive sequences that make up the adjugate vector, for details see Section 6.C. Summarizing, for specific choices of parameters, in the K_4 chain extinction occurs. For every choice of parameters $r_1, ..., r_5$ there is a largest size (between three and infinity) for which the condensate vector has no negative entries. This size determines the size of subsystems that survive.

Variants of 1D chains. Combining the topological invariant calculated above with the adjugate vector (calculated analogous to the adjugate vector of the diamond chain in Section 6.B.2) allows us to generalize the predictions of topological phases to arbitrary one dimensional lattices with two element unit cells. First, we discuss the topological phase, which, for the K_4 chain, is decided by $\text{sign}\left(1 - \left(\frac{r_2+r_5}{r_3}\right)^2\right)$. As long as we preserve

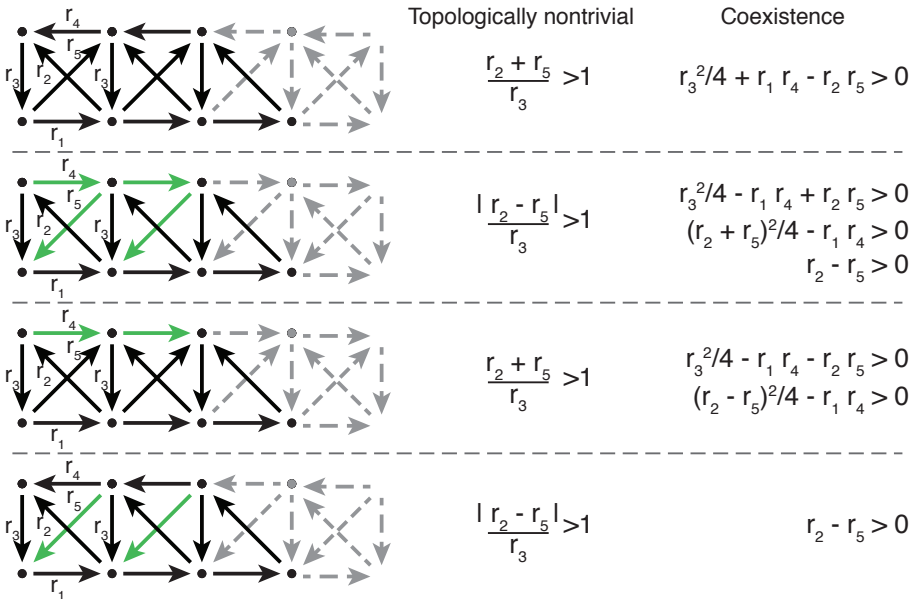

Figure 6.8: Properties of different 1D lattices Changing the direction of arrows, i.e., the network topology, can affect coexistence and topological phase. Three variants in the network topology are presented in comparison to the K_4 chain (top). In the network on the left, the arrows which direction is changed compared to the K_4 chain are highlighted in green. When the expression in the center column is fulfilled, the system is topologically nontrivial ($\mathcal{M} = -1$). The expressions in the right column indicates wether all states coexist.

the network topology, that is, all variables $r_1, ..., r_5$ can only be positive, the topological phase is decided thus decided by $r_2 + r_5 \gtrless r_3$. However, here we extrapolate the results discussed so far to changed network topologies. For example, inverting the direction of the interactions between vertices $2m$ and $2m + 2$, or, equivalently changing the sign of r_4, does not influence the topological phase. When the interaction identified by r_5 is flipped, the topological phase is decided by $\frac{|r_2+r_5|}{r_3} \gtrless 1$, as a result of the square in the topological invariant. The topological non-trivial phases for more network topologies derived from the K_4 chain by inverting interactions are shown in Figure 6.8 in the center column. The same argument can be applied to the condensate vector, which is calculated in analogy to the diamond chain in Section 6.B.2. For the K_4 chain, the adjugate vector consists of the linear recursive sequences $f_m(r_3, r_1r_4 - r_2r_5)$ and $f_m(r_2 + r_5, r_1r_4 - r_2r_5)$. For arbitrarily large systems, coexistence of all states occurs when both sequences are strictly positive for all indices m. As shown in Section 6.E, for a linear recursive sequence $f_m(a, b)$ this is the case when $a^2/4+b > 0$. For the K_4 chain network topology, only the sequence $f_m(r_3, r_1r_4-r_2r_5)$ can obtain negative values, deciding over coexistence and extinction. However, when the network topology is manipulated, both sequences can inhibit coexistence of all states. For example, inverting both interactions r_4 and r_5, the restrictions for coexistence amount to $r_3^2/4-(r_1r_4-r_2r_5) > 0$ and $(r_2+r_5)^2/4-r_1r_4$. In this case, also the initial value of a must be positive, adding $(r_2-r_5) > 0$ to the restrictions. In total, the conditions for coexistence

in arbitrarily large chains derived from the K_4 chain by inverting interactions are shown in Figure 6.8 in the right column. Note that the conditions presented in Figure 6.8 also apply when either reversing all edges (an overall minus sign does not change the properties of the matrix) or exchanging labels of odd and even states (simultaneously reordering matrix rows and columns does not change matrix properties). For networks where only unidirectional mass flow is possible, e.g., mass always flows to the lower row of vertices which is oriented to the right, coexistence of all states is never possible as the network is no longer strongly connected, see Section 3.4.

6.6 Differential difference equations and solitonic waves

In this section we will shortly derive the differential difference equations that arise from diamond chain and K_4 chain at the respective critical points. The study of differential difference equations and their solutions has a long tradition in soliton physics and the study of integrable systems [187, 171, 170, 41]. We numerically found solitonic waves for both the diamond chain and its augmented version at the critical point $r = 1$. Reformulated as a differential difference equation, these equations resemble prominent examples such as the relativistic Toda lattice and the Volterra lattice. We hope that the results presented here inspire further studies.

In order to derive a differential equation for traveling waves, we assume that the temporal evolution of all odd states and of all even states is identical, but shifted in time. For an infinite one dimensional chain, all states with odd index (even index) have the same interaction topology, thus for the odd (even) states we introduce a universal function $x_{2m-1} = u(\zeta_m)$ ($x_{2m} = v(\zeta_m)$), respectively. Here, $\zeta_m = c_1 m + c_2 t + \delta$, where c_1 is the spatial shift between states, c_2 is the speed of the wave and δ is an arbitrary offset.

In this condensed form, the one dimensional chains reduce to the differential difference equation

$$\begin{pmatrix} x_{2m-1}(t) \\ x_{2m}(t) \end{pmatrix} = \begin{pmatrix} u(\zeta(m,t)) \\ v(\zeta(m,t)) \end{pmatrix} = \begin{pmatrix} u_m \\ v_m \end{pmatrix} , \tag{6.10}$$

$$\frac{\mathrm{d}}{\mathrm{d}t} \begin{pmatrix} u_m \\ v_m \end{pmatrix} = \begin{pmatrix} u_m(r_2(v_m - v_{m-1}) + r_5(v_m - v_{m+1}) + r_1(u_{m-1} - u_{m+1})) \\ v_m(r_2(u_{m+1} - u_m) + r_5(u_{m-1} - u_m) + r_4(v_{m+1} - v_{m-1})) \end{pmatrix} . \tag{6.11}$$

Here, the constants r_1, r_2, r_4, r_5 are included to highlight which contributions arises from which edge. Note that the rate $r_3 = r_2 + r_5$, such that the system is at the transition point between the topological phases.

Setting $r_1 = r_2 = 1$ and $r_4 = r_5 = 0$ one recovers the differential difference equation of the RPS chain. Reversing the interaction $r_1 = -1$, yields the DDE for the relativistic Toda lattice, a famous example in the study of solitons in integrable lattices [48, 188].

With the rates $r_1 = r_2 = r_4 = 1$ and $r_5 = 0$ (corresponding to the diamond lattice) we achieve a DDE which has the surprising phenomenology of two classes of positive solitonic waves traveling in opposite directions.

Finally, choosing $r_1 = r_2 = r_4 = r_5 = 1$ yields the DDE for the K_4 chain. This equation has interesting properties by itself which will be discussed in the following.

The DDE for the K_4 chain at the critical point corresponds to the rates $r_1, r_2, r_4, r_5 = 1$ and $r_3 = 2$. For this case we find

$$\frac{\mathrm{d}}{\mathrm{d}t}\begin{pmatrix} u_m \\ v_m \end{pmatrix} = \begin{pmatrix} u_m(v_m - v_{m-1} + (v_m - v_{m+1}) + u_{m-1} - u_{m+1}) \\ v_m(u_{m+1} - u_m + (u_{m-1} - u_m) + (v_{m+1} - v_{m-1})) \end{pmatrix} \tag{6.12}$$

A transformation of variables yields

$$\frac{\mathrm{d}}{\mathrm{d}t}\begin{pmatrix} x_m \\ y_m \end{pmatrix} = \begin{pmatrix} u_m + v_m \\ u_m - v_m \end{pmatrix} = \begin{pmatrix} y_{m-1}x_m - x_{m+1}y_m \\ y_m(y_{m-1} - y_m) - x_m(x_{m+1} - x_m) \end{pmatrix} \tag{6.13}$$

Assuming $x_m = 0$, the system simplifies to $\partial_t y_m = y_m(y_{m-1} - y_m)$. Note that this assumption is unphysical for the context in which the ALVE is usually applied as negative occupation of states is not possible.
However, we mention this setting here as a traveling wave solution can be found using the hyperbolic tangent ansatz [172, 188]:

$$y_m = c_2\left(\frac{1}{\tanh(c_1)} - \tanh(c_1 m + c_2 t + \delta)\right). \tag{6.14}$$

The results stated here are meant to give an idea on how to approach an analysis of solitonic waves in the ALVE and hopefully inspire future studies.

6.7 Summary of the results

In this chapter we extended the observations and the analysis of the RPS chain to general one dimensional chains with a two element unit cell. We focused on two examples, the diamond chain and the K_4 chain, that can be viewed as successive augmentations of the RPS chain. The ALVE dynamics on these chains shows the same qualitative behavior as for the RPS chain: We observe robust polarization of the average mass that depends on a control parameter, and solitary waves at the transition point.

A full analytic treatment is possible on the basis of the adjugate vector that consists of linear recursive sequences. The exponential polarization emerges as the asymptotic behavior of the linear recursive sequences away from the boundaries in the bulk. Thus, in contrast to the RPS chain, the full dynamics cannot be understood solely on the basis of the Fourier transform of the periodic network.

As a new feature, we find extinction in the K_4 chain. Beyond a threshold value, the K_4 chain dissects through extinction into subsystems whose size sensitively depends on the rates. Interestingly, extinction only occurs in the topologically nontrivial phase. We use the results for the K_4 chain to predict the control parameter and critical point of topological phase transitions for other network topologies of one dimensional chains.

Finally, we derived differential difference equations for the diamond and the K_4 chain at the critical point and give an (unphysical) example for a traveling wave solution.

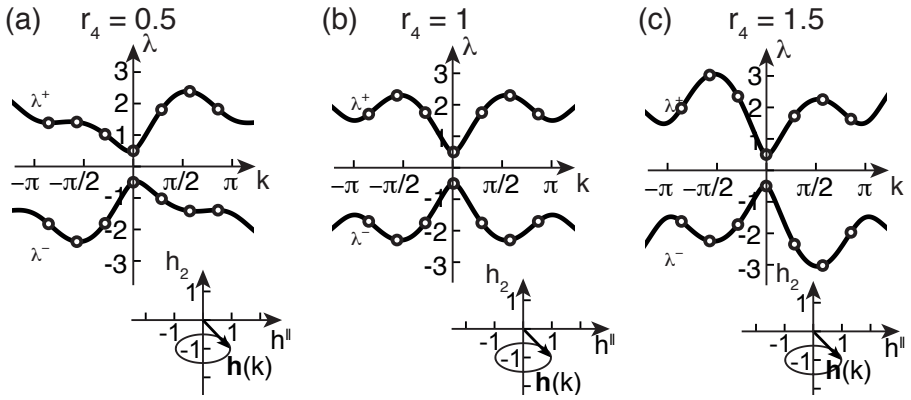

Figure 6.9: With fixed values $r_1 = 1, r_2 = 0.5, r_3 = 1$, the shape of the spectrum changes when varying r_4. However, the topology does not change. Although for $r_4 = 1$ the spectrum becomes point symmetric (as one would expect in a system with chiral symmetry), there is no accompanying symmetry operator of the Hamiltonian such that the symmetry class of the Hamiltonian remains unchanged.

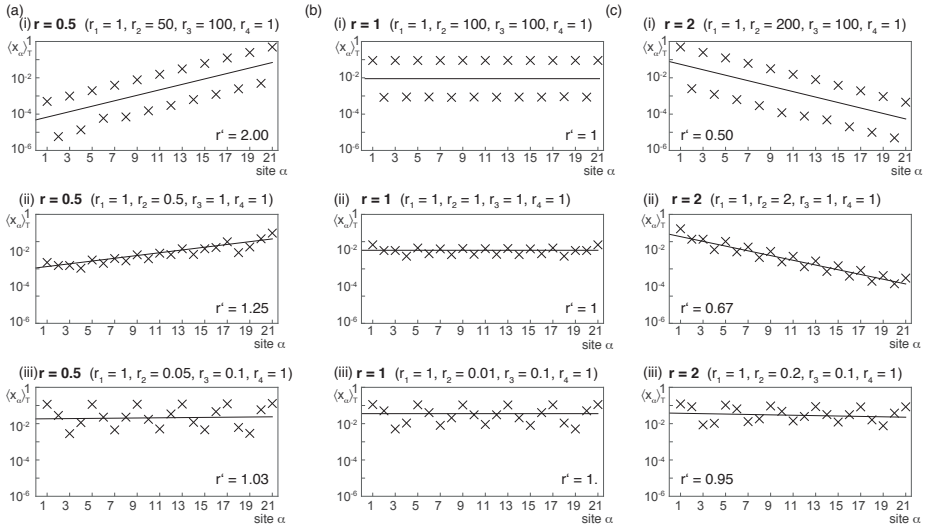

Figure 6.10: The relative magnitude of r_1, r_4 in relation to r_2, r_3 does not change the topological phase, however, it influences the distance to the critical point and thus the strength of polarization.

6.A Calculation of the topological invariant of the diamond chain and the K_4 chain

Here we derive the Fourier transformed Hamiltonian of the K_4 chain and calculate its topological invariant. When setting $r_5 = 0$ the results simplify to the case of the diamond chain.

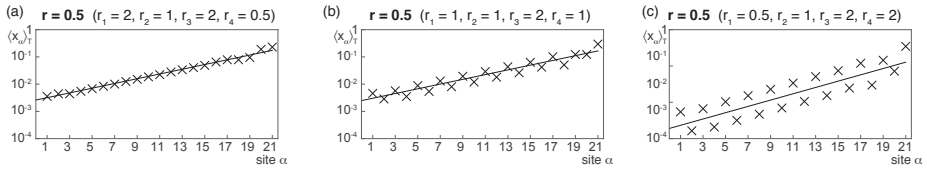

Figure 6.11: The influence of r_1, r_4 on the penetration depth $l_p = 2/\ln r'$ comes only from the product $r_1 r_4$. When keeping the product constant and varying the values, the polarization strength is not changed, while the distribution of mass in one unit cell is shifted. Increasing r_4 in relation to r_2 shifts mass from the even sites (a) to the odd sites (c).

The periodic chain corresponds to a block circulant matrix. We introduce a block circulant matrix A_{PBC} which corresponds to the 1D K_4 chain with periodic boundary conditions as indicated with the grey arrows in Figure 6.5. Generally, a circulant matrix is defined by a generating vector $\boldsymbol{c} = \begin{pmatrix} c_0 & c_1 & \dots & c_{S-1} \end{pmatrix}$ such that $(C)_{kl} = c_{l-k}$ where we assume periodicity, $c_{-k} = c_{S-k}$. In the given case, as we are studying a block circulant matrix, each of the generating elements a_k is a 2×2 block matrix. As A_{PBC} is an antisymmetric matrix, we require $a_k = -a_{-k}^T$.

For the K_4 chain, there are only interactions between neighboring unit cells, such that the only nonzero entries in the generating vector are a_0 (which defines the coupling in one unit cell) and $a_1 = -a_{-1}^T = -a_{S-1}^T$ (containing the coupling between neighboring unit cells). A matrix of this form, where only a diagonal band consisting of the main diagonal and possibly some off-diagonals are nonzero, is also called a block banded matrix [189].

Taken together, we find (cf. also matrix A (6.1))

$$a_0 = \begin{pmatrix} 0 & r_3 \\ -r_3 & 0 \end{pmatrix} = -a_0^T \tag{6.15}$$

$$a_1 = \begin{pmatrix} -r_1 & -r_5 \\ r_2 & r_4 \end{pmatrix} = -a_{-1}^T \, . \tag{6.16}$$

As A is an antisymmetric matrix, its eigenvalues are purely imaginary, see Section 3.2. To facilitate the analysis of the Fourier transform, the Hamiltonian $H = iA_{PBS}$ is introduced. The Hamiltonian is also block circulant with the blocks $H_m = iA_m$, and hermitian, such that its eigenvalues are real.

Calculation of the Fourier transform of the periodic system and its properties. From the blocks of the circulant matrix it is straightforward to calculate the Fourier trans-

form of H,

$$\tilde{H}(k) = e^{-ik}(-H_1^T) + H_0 + e^{ik}H_1 \tag{6.17}$$

$$= \begin{pmatrix} ir_1(e^{-ik} - e^{ik}) & ir_3 - ir_5e^{ik} - ir_2e^{-ik} \\ -ir_3 + ir_5e^{-ik} + ir_2e^{ik} & ir_4(e^{ik} - e^{-ik}) \end{pmatrix} \tag{6.18}$$

$$= \begin{pmatrix} 2r_1 \sin k & ir_3 + \sin k(r_5 - r_2) - i\cos k(r_5 + r_2) \\ -ir_3 + \sin k(r_5 - r_2) + i\cos k(r_5 + r_2) & -2r_4 \sin k \end{pmatrix}, \tag{6.19}$$

$$= \begin{pmatrix} (r_1 - r_4)\sin k \\ (r_5 - r_2)\sin k \\ -r_3 + (r_2 + r_5)\cos k \\ (r_1 + r_4)\sin k \end{pmatrix} \cdot \boldsymbol{\sigma} = \boldsymbol{h} \cdot \boldsymbol{\sigma} \tag{6.20}$$

The Fourier transform is periodic in $k \to k + 2\pi$, the values of k depend on the size of the system $S = 2n$ as $k = \frac{2\pi}{n}l$ and $l = -\lfloor \frac{n}{2} \rfloor, ..., 0, 1, ..., \lfloor \frac{n}{2} \rfloor$.

The last line contains the projection of $\tilde{H}(k)$ onto the Pauli matrices $\sigma_0, ..., \sigma_3$. From $\boldsymbol{h}$ the determinant and the eigenvectors can be directly read off [149]:

$$\det \tilde{H}(k) = h_0^2 - h_1^2 - h_2^2 - h_3^2 = -4r_1r_4 \sin k^2 - (r_5 - r_2)^2 \sin k^2 - ((r_2 + r_5)\cos k - r_3)^2 , \tag{6.21}$$

$$\lambda_\pm = h_0 \pm \sqrt{h_1^2 + h_2^2 + h_3^2} \tag{6.22}$$

$$= (r_1 - r_4)\sin k \pm \sqrt{(r_2 - r_5)^3 \sin k^2 + ((r_2 + r_5)\cos k - r_3)^2 + (r_1 + r_4)^2 \sin k^2}$$

$$\boldsymbol{r}^\pm(k) = \frac{1}{\sqrt{2|h|^2 \pm 2h_3\sqrt{|h|^2}}} \begin{pmatrix} \pm\sqrt{|h|^2} + h_3 \\ h_1 + ih_2 \end{pmatrix} . \tag{6.23}$$

The two bands of the spectrum are shown in Figure 6.4 for the two topological phases and the transition point. The determinant is either zero at the topological transition $(r_2 + r_3) = r_3$ when $k = 0$, or for specific complex values, see Section 6.A.1.

Note that h_0 is neglectable: It contributes to the eigenvectors only as a shift, and not at all to the eigenvectors and thus the topological invariant. The insets in Figure 6.4 are plots of the second and third component of the rotation

$$T \cdot \boldsymbol{h} = \begin{pmatrix} \frac{r_1+r_4}{\sqrt{(r_1+r_4)^2+(r_2-r_5)^2}} & 0 & \frac{(r_5-r_2)}{\sqrt{(r_1+r_4)^2+(r_2-r_5)^2}} \\ 0 & 1 & 0 \\ -\frac{r_1+r_4}{\sqrt{(r_1+r_4)^2+(r_2-r_5)^2}} & 0 & \frac{(r_5-r_2)}{\sqrt{(r_1+r_4)^2+(r_2-r_5)^2}} \end{pmatrix} \cdot \begin{pmatrix} h_1 \\ h_2 \\ h_3 \end{pmatrix} = \begin{pmatrix} \frac{2(r_5-r_2)(r_1+r_4)\sin k}{\sqrt{(r_1+r_4)^2+(r_2-r_5)^2}} \\ -r_3 + (r_2 + r_5)\cos k \\ 0 \end{pmatrix} \cdot \tag{6.24}$$

where $r_5 = 0$ to fit the diamond chain.

Finding the symmetry class. The classification of a topological hamiltonian is carried out by analysis of its unitary symmetries. The K_4 chain (and with it the diamond chain) only has a "particle hole symmetry", which puts it in symmetry class D.

The "particle hole symmetry" is an intrinsic property of all antisymmetric matrices and revealed by the unitary operator $\mathcal{C} = \sigma_0 \cdot \kappa, \mathcal{C}^{-1}\mathcal{C} = 1$:

$$\tilde{H}(k) = H_0 + \sum_{j=1}^{d} \left(e^{ijk} H_j - e^{-ijk} H_j^T\right) \tag{6.25}$$

$$\kappa\tilde{H}(k) = -H_0 - \sum_{j=1}^{d} \left(e^{-ijk} H_j - e^{ijk} H_j^T\right) = -\tilde{H}(-k) \tag{6.26}$$

$$\Rightarrow \mathcal{C} \cdot \tilde{H}(k) + \tilde{H}(-k) \cdot \mathcal{C} = 0, \tag{6.27}$$

where the last line reads as an operator identity.
For 2×2 Hamiltonians in class D, the topological invariant is calculated as the so-called Pfaffian invariance [181, 179]:

$$\mathcal{M} = -\text{sign}\left(\text{Pf}(\tilde{H}(0))\text{Pf}(\tilde{H}(\pi))\right) \tag{6.28}$$

$$= \text{sign}\left((r_3 - (r_5 + r_2))(r_3 + (r_5 + r_2))\right) \tag{6.29}$$

$$= \text{sign}\left(r_3^2 - (r_2 + r_5)^2\right) \tag{6.30}$$

$$= \text{sign}\left(1 - \left(\frac{r_2 + r_5}{r_3}\right)^2\right) . \tag{6.31}$$

This equation both identifies the control parameter of our system and, for given rates, predicts the topological phase.

6.A.1 Complex zeros of the Fourier transformed Hamiltonian

In this section we calculate the (complex) values for k for which the Hamiltonian has a zero mode. These values are determined from $\det \tilde{H}(k) \stackrel{!}{=} 0$. From the solutions k' of this equation we can read off the decay rate of the polarization.

$$\begin{aligned}\det(\tilde{H}) =& r_1 r_4 (e^{ik} - e^{-ik})^2 - (r_3 - r_2 e^{-ik} - r_5 e^{ik})(r_3 - r_2 e^{ik} - r_5 e^{-ik}) \\ =& \left[(r_1 r_4 - r_2 r_5) r'^2 + r_3(r_2 + r_5) r'\right] + \left[(r_1 r_4 - r_2 r_5) r'^{-2} + r_3(r_2 + r_5) r'^{-1}\right] \\ & - r_3^2 - r_2^2 - r_5^2 - 2 r_1 r_4 \stackrel{!}{=} 0 \ ,\end{aligned} \tag{6.32}$$

where we used the shorthand $r' = e^{ik}$. In case $r'_{\pm,\pm} = \frac{\phi_\pm(r_2+r_5, r_1 r_4 - r_2 r_5)}{\phi_\pm(r_3, r_1 r_4 - r_2 r_5)}$, where $\phi_\pm^2(a,b) - a\phi - b = 0$, the following identity applies:

$$b\frac{\phi^2(a,b)}{\phi^2(c,b)} + bc\frac{\phi(a,b)}{\phi(c,b)} = a\phi(a,b) - c\phi(c,b) + b + c^2 \tag{6.33}$$

Using this identity in equation (6.32), we find that for each of the four values $k = -i \ln r'_{\pm,\pm}$, the Hamiltonian has a kernel vector.

Interestingly, the correct decay observed in the ALVE, $r'_{+,+} = \frac{\phi_\pm(r_2+r_5, r_1r_4-r_2r_5)}{\phi_\pm(r_3, r_1r_4-r_2r_5)}$, is a complex zero of the determinant of $\tilde{H}$. However, in contrast to the RPS chain, Section 5.B.1, there is no way of finding the correct of the four solutions without further analysis of the matrix, as the exponential decay is an asymptotic property.

6.B Calculation of the kernel vectors

6.B.1 Kernel vector of the diamond chain

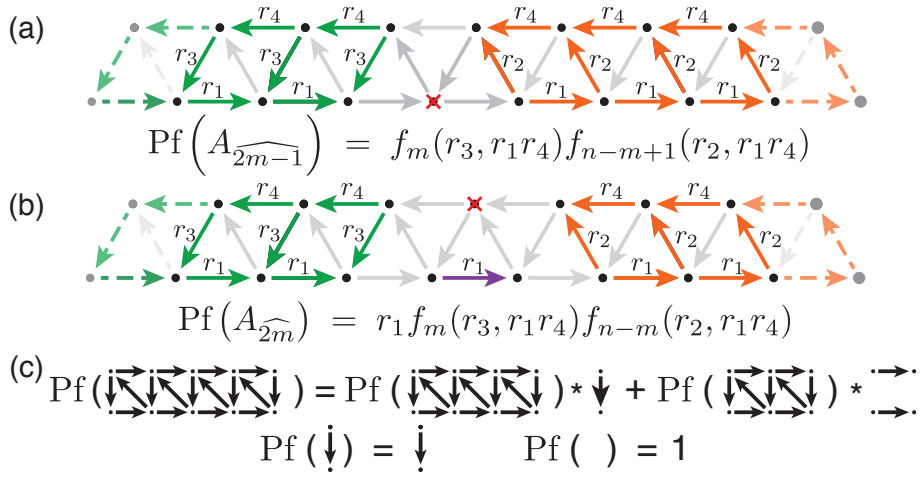

Figure 6.12: Calculation of the adjugate vector of the diamond chain. Odd components of the adjugate vector v_{2m-1} are determined by the Pfaffians of two unconnected subnetworks (green and orange) (a). For even components v_{2m}, in addition to the two subnetworks there is a contribution r_1 (purple) (b). The Pfaffians of the green and orange subnetworks both follow a linear recursion relation in their size, allowing for an analytic calculation of the Pfaffians using the results in Section 6.E.

Using the graph-theoretical definition of the Pfaffian introduced in Section 3.3.2, the adjugate vector of the diamond chain can be directly computed from its network topology.

When calculating the α-th component of the adjugate vector, v_α, we must find all perfect matchings of the subnetwork $A_{\hat{\alpha}}$, that is the subnetwork obtained by deleting vertex α.

Conveniently, when removing a vertex from the diamond chain, the remaining subnetwork separates into two networks of similar shape, so called ladder graphs, see also Figure 6.12 (a-b). As the two subnetworks are unconnected, we obtain the Pfaffian of the full subnetwork by multiplying the Pfaffians of the two ladder graphs for odd components, see Figure 6.12 (a). For even components, an additional factor of r_1 is added as one edge remains that is not part of the ladder graphs, see Figure 6.12 (b).

Since the diamond chain is a condensate vector, the ladder graphs are oriented in a Pfaffian orientation [57, 118, 55], such that all perfect matchings contribute additively: The sign in equation (3.2) is always positive.

As shown in Figure 6.12 (c), the Pfaffian of a subnetwork of size $n+1$ follows a recursion relation of second order. Applying also the boundary condition, we find that Pfaffian of the green network of size $2n$ follows the recursion relation $f_{n+1}(r_3, r_1r_4)$, while the orange network of size $2n$ has the Pfaffian $f_{n+1}(r_2, r_1r_4)$ (colors refer to the networks in Figure 6.12(a-b)). Here, $f_n(a,b)$ follows the definition in Section 6.E.

Taken together, the adjugate vector $\boldsymbol{c}$ of the diamond chain of size $S = 2n-1$ reads

$$\boldsymbol{v} = \begin{pmatrix} f_1(r_3,r_1r_4)f_n(r_2,r_1r_4) \\ r_1 f_1(r_3,r_1r_4)f_{n-1}(r_2,r_1r_4) \\ f_2(r_3,r_1r_4)f_{n-1}(r_2,r_1r_4) \\ r_1 f_2(r_3,r_1r_4)f_{n-2}(r_2,r_1r_4) \\ \vdots \\ f_m(r_3,r_1r_4)f_{n-m+1}(r_2,r_1r_4) \\ r_1 f_m(r_3,r_1r_4)f_{n-m}(r_2,r_1r_4) \\ \vdots \\ f_{n-1}(r_3,r_1r_4)f_2(r_2,r_1r_4) \\ r_1 f_{n-1}(r_3,r_1r_4)f_1(r_2,r_1r_4) \\ f_n(r_3,r_1r_4)f_1(r_2,r_1r_4) \end{pmatrix} \tag{6.34}$$

With a suitable normalization constant C, we recover the result presented in equation (6.7). Note that the adjugate vector consists of one increasing and one decreasing sequence.

The linear recursive sequences asymptotically approach $f_n(a,b) \sim \phi_+(a,b)^n$ is derived in Section 6.E. Using this result for the bulk of the condensate vector, that is far away from both boundaries, yields

$$\begin{pmatrix} c_{2m-1} \\ c_{2m} \end{pmatrix} \sim \begin{pmatrix} \phi_+(r_3,r_1r_4)^m \phi_+(r_2,r_1r_4)^{n-m+1} \\ r_1\phi_+(r_3,r_1r_4)^m \phi_+(r_2,r_1r_4)^{n-m} \end{pmatrix} = \left(\frac{\phi_+(r_2,r_1r_4)}{\phi_+(r_3,r_1r_4)}\right)^{-m} \begin{pmatrix} \phi_+(r_2,r_1r_4)^{n+1} \\ r_1\phi_+(r_2,r_1r_4)^n \end{pmatrix} . \tag{6.35}$$

From this form, we can read off the exponential decay $c_\alpha \sim e^{-\alpha/l_p} = e^{-2\alpha/\ln r'}$ with $r' = \frac{\phi_+(r_2,r_1r_4)}{\phi_+(r_3,r_1r_4)}$, as given in the main text.

6.B.2 Kernel vector of the K_4 chain

The adjugate vector of the K_4 can be decomposed into three classes of subnetworks for which we must find all perfect matchings, as indicated in Figure 6.13. Again, the polynomials arising from the subnetworks can be expressed as linear recursive sequences in the subnetworks size $2n$. The sequence in Figure 6.13 (c) is

$$X(n) = f_{n+1}(r_3, r_1r_4 - r_2r_5) ,$$

which is simply an extension of the sequence used for the original diamond chain. The sequence shown in Figure 6.13 (e), $Y(n)$, relies in the sequence defined in Figure 6.13 (e),

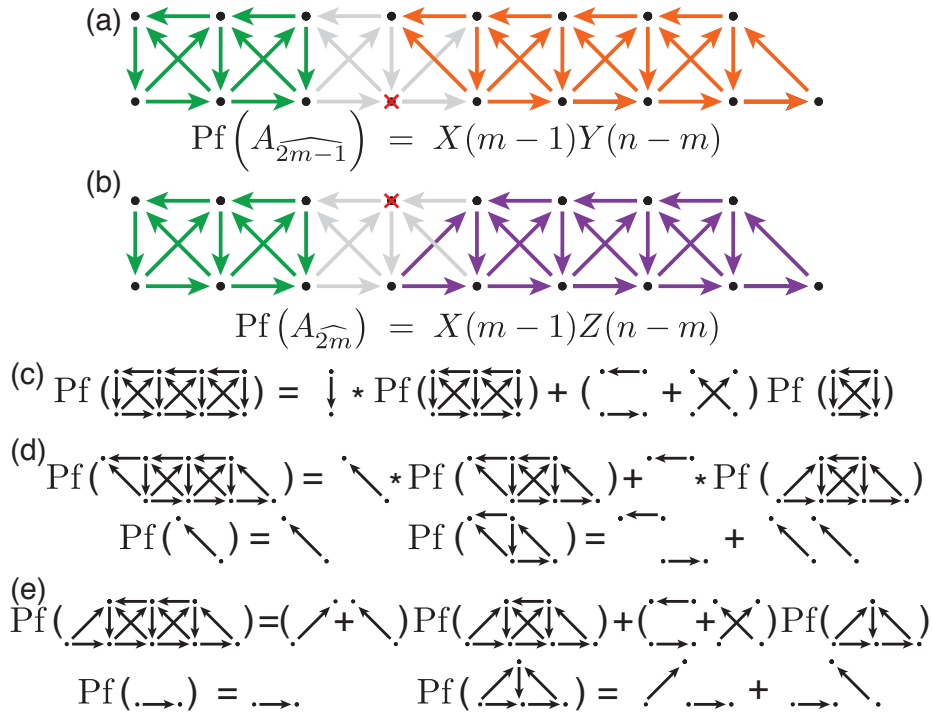

Figure 6.13: Calculation of the adjugate vector of the K_4 chain. For odd (a) and even (b) components of the adjugate vector, the Pfaffian of the corresponding subnetworks is calculated as the product of two sequences. The recursion relations and initial conditions necessary to identify the sequences are shown in (c) for the green, (d) for the orange and (e) for the purple network.

which is

$$Z(n) = r_1 f_{n+1}(r_2 + r_5, r_1 r_4 - r_2 r_5) \,.$$

As shown in Figure 6.13 (d), the final sequence, $Y(n)$, can be related to the sequence $Z(n)$ as $Y(n) = r_3 Y(n-1) + r_4 Z(n-1)$, consequently following the same recursion rules as $Z(n)$. Together with the initial conditions and the identities derived in Section 6.E, the full sequence reads

$$\begin{aligned} Y(n) &= r_2 g_n(r_2 + r_5, r_1 r_4 - r_2 r_5; 1/r_2) \\ &= r_2 f_n(r_2 + r_5, r_1 r_4 - r_2 r_5) + (r_1 r_4 - r_2 r_5) f_{n-1}(r_2 + r_5, r_1 r_4 - r_2 r_5) \\ &= f_{n+1}(r_2 + r_5, r_1 r_4 - r_2 r_5) - r_5 f_n(r_2 + r_5, r_1 r_4 - r_2 r_5) \,. \end{aligned}$$

Taken together, the adjugate vector of the K_4 chain of size $S = 2n-1$ has the form

$$\boldsymbol{v} = \begin{pmatrix} X(0)Y(n-1) \\ X(0)Z(n-1) \\ X(1)Y(n-2) \\ \vdots \\ X(m-1)Y(n-m) \\ X(m-1)Z(n-m) \\ \vdots \\ X(n-2)Y(1) \\ X(n-2)Z(1) \\ X(n-1)Y(0) \end{pmatrix} = \begin{pmatrix} f_1(r_3,r_1r_4-r_2r_5)[f_n(r_2+r_5,r_1r_4-r_2r_5)-r_5f_{n-1}(r_2+r_5,r_1r_4-r_2r_5)] \\ f_1(r_3,r_1r_4-r_2r_5)r_1f_{n-1}(r_2+r_5,r_1r_4-r_2r_5) \\ f_2(r_3,r_1r_4-r_2r_5)[f_{n-1}(r_2+r_5,r_1r_4-r_2r_5)-r_5f_{n-2}(r_2+r_5,r_1r_4-r_2r_5)] \\ \vdots \\ f_m(r_3,r_1r_4-r_2r_5)[f_{n-m+1}(r_2+r_5,r_1r_4-r_2r_5)-r_5f_{n-m}(r_2+r_5,r_1r_4-r_2r_5)] \\ f_m(r_3,r_1r_4-r_2r_5)r_1f_{n-m}(r_2+r_5,r_1r_4-r_2r_5) \\ \vdots \\ f_{n-1}(r_3,r_1r_4-r_2r_5)[f_2(r_2+r_5,r_1r_4-r_2r_5)-r_5f_1(r_2+r_5,r_1r_4-r_2r_5)] \\ f_{n-1}(r_3,r_1r_4-r_2r_5)r_1f_1(r_2+r_5,r_1r_4-r_2r_5) \\ f_n(r_3,r_1r_4-r_2r_5)[f_1(r_2+r_5,r_1r_4-r_2r_5)-r_5f_0(r_2+r_5,r_1r_4-r_2r_5)] \end{pmatrix} \tag{6.36}$$

Again, using the asymptotic behavior of $f_n(a,b)$ for values far away from both boundaries, we find the exponential decay $e^{-\alpha/l_p}$, with $e^{l_p/2} = r' = \frac{\phi_+(r_2+r_5,r_1r_4-r_2r_5)}{\phi_+(r_3,r_1r_4-r_2r_5)}$. Thus the topological transition depends on the control parameter $r = \frac{r_2+r_5}{r_3}$. Note that with $r_5 = 0$, the adjugate vector of the diamond chain is recovered.

6.C Extinction in the K_4 chain

In this section we show that when the adjugate vector (6.36) has negative entries, in the ALVE dynamics the augmented RPS chain dissects into disconnected chunks. First, we show that the K_4 chain is no coexistence network, such that coexistence of all states is dependent on the transition rates.

6.C.1 The K_4 chain is not a coexistence network

Here we show why the K_4 chain is not a coexistence network due to violation of the crossing condition (4.3).

The conditions which a hamiltonian network must fulfill in order to be a coexistence network are formulated in a labeling that is ascending along the hamiltonian cycle. Here, already the fragment formed by the first four vertices suffices to show that the K_4 chain is no coexistence network. An ascending labeling is achieved as follows (old vertex index comes first): $1 \to 3, 2 \to 2, 3 \to 4, 4 \to 1$. In this new labeling, this fragment has the following edges:

$$1 \xrightarrow{r_4} 2 \xrightarrow{r_3} 3 \xrightarrow{r_1} 4$$
$$3 \xrightarrow{r_5} 1 \xrightarrow{r_3} 4 \xrightarrow{r_2} 2$$

The two edges $4 \to 2$ and $3 \to 1$ cross, the difference between start-vertices (and between end-vertices) is one. Thus, the crossing condition is violated, the K_5 chain is not a coexistence network, and dependent on the rates, extinction can occur.

6.C.2 Conditions for extinction and the structure of the condensate vector

The adjugate vector is constructed from linear recursive sequences. In Section 6.E.2, we present conditions for when negative elements occur in a linear recursive sequence and at which positions these occurrences are. Ultimately, the presence of negative or zero elements in the adjugate vector, and with it extinction in the ALVE dynamics, is decided by the expression $a^2/4 + b$, where a and b are the coefficients of the recursion relation, see Section 6.E.

As introduced above, the adjugate vector of the K_4 chain consists of three sequences, X, Y and Z, all of which linear recursive of second order. For the sequence $X(m) = f_{m+1}(r_3, r_1r_4 - r_2r_5)$, depending on r_2r_5 negative values are possible. In contrast, the sequences Y and Z are based on $f_m(r_2 + r_5, r_1r_4 - r_2r_5)$. For this sequences, we find $a^2/4 + b = (r_2 + r_5)^2/4 + r_1r_4 - r_2r_5 = (r_2 - r_5)^2 + r_1r_4 > 0$. Thus, the sequences Y and Z never assume negative values in the network topology of the K_4 chain.

Coexistence of all states in the K_4 chain is thus decided by $X(m) = f_m(r_3, r_1r_4 - r_2r_5)$ or, more specifically, by $K = r_3^2/4 + r_1r_4 - r_2r_5$. As presented in Section 6.E.2, for $0 > K$ the position m of the first non-positive value, $X(m) \leq 0$, decreases with decreasing K. The first non-positive value decides the size of the surviving subnetworks:
When $0 > K$, so $r_2r_5 - r_1r_4 > r_3^2/4$, there is a finite value of $X(m)$ that is non-positive, there is extinction in the K_4 chain. When additionally $r_2r_5 - r_1r_4 > r_3^2$, only disconnected RPS cycles remain.

The dissection of the system can be easiest understood in the case that the surviving block size contains three states. As a subnetwork of three states is a RPS cycle, a coexistence network, this unit is sustainable for every choice of rates. This case is elaborated in the following, the logic translates to larger subsystems.

The smallest sustainable system has three states, and the kernel vector $\boldsymbol{v}_1 = \begin{pmatrix} r_4 & r_5 & r_3 \end{pmatrix}$ (e.g. for the states $1, 2$ and 4) or $\boldsymbol{v}_2 = \begin{pmatrix} r_2 & r_1 & r_3 \end{pmatrix}$ (for the states $S-2, S-1$ and S). From these vectors, we can construct a condensate vector of the K_4 chain:

$$\begin{pmatrix} 0 & r_3 & -r_1 & -r_5 & 0 & 0 & 0 & 0 & 0 \\ -r_3 & 0 & r_2 & r_4 & 0 & 0 & 0 & 0 & 0 \\ r_1 & -r_2 & 0 & r_3 & -r_1 & -r_5 & 0 & 0 & 0 \\ r_5 & -r_4 & -r_3 & 0 & r_2 & r_4 & 0 & 0 & 0 \\ 0 & 0 & r_1 & -r_2 & 0 & r_3 & -r_1 & 0 & 0 \\ 0 & 0 & r_5 & -r_4 & -r_3 & 0 & r_2 & r_4 & 0 \\ 0 & 0 & 0 & 0 & r_1 & -r_2 & 0 & r_3 & -r_1 \\ 0 & 0 & 0 & 0 & r_5 & -r_4 & -r_3 & 0 & r_2 \\ 0 & 0 & 0 & 0 & 0 & 0 & r_1 & -r_2 & 0 \end{pmatrix} \begin{pmatrix} r_4 \\ r_5 \\ 0 \\ r_3 \\ 0 \\ 0 \\ Kr_2 \\ Kr_1 \\ Kr_3 \end{pmatrix} = \begin{pmatrix} 0 \\ 0 \\ r_1r_4 - r_2r_5 + r_3^2 + Kr_4r_2 \\ 0 \\ -r_2r_3 - Kr_1r_2 \\ -r_3r_4 + K(r_2^2 + r_1r_4) \\ 0 \\ 0 \\ 0 \end{pmatrix} \tag{6.37}$$

As we assumed that $0 > r_3^2 + r_1r_4 - r_2r_5$, a fitting constant K can be found such that the vector fulfills the properties of the condensate vector, (2.2) and (2.3). Note that the condensate vector is not unique, indicating that, although the system will decay into RPS cycles, there is no way of knowing how the total mass is distributed among the disconnected subsystems.

Extinction in the diamond chain is only possible in the topologically non-trivial phase As shown above, extinction occurs only when $0 > r_3^2/4 + r_1 r_4 - r_2 r_5$. This requires that the K_4 chain is in the topologically nontrivial phase, as we will show in the following: The system is in the topologically trivial phase when $r' = \frac{r_2+r_5}{r_3} < 1$, or $r_2 + r_5 < r_3$. For K, this inequality implies

$$K = \frac{r_3^2}{4} + r_1 r_4 - r_2 r_5 > \frac{(r_2+r_5)^2}{4} + r_1 r_4 - r_2 r_5 = \frac{(r_2-r_5)^2}{4} + r_1 r_4 > 0\,. \tag{6.38}$$

With $r' < 1$ the value of K cannot be negative, so extinction only occurs in the topologically nontrivial phase.

6.D Calculation of the determinants and the Szegő-Widom theorem

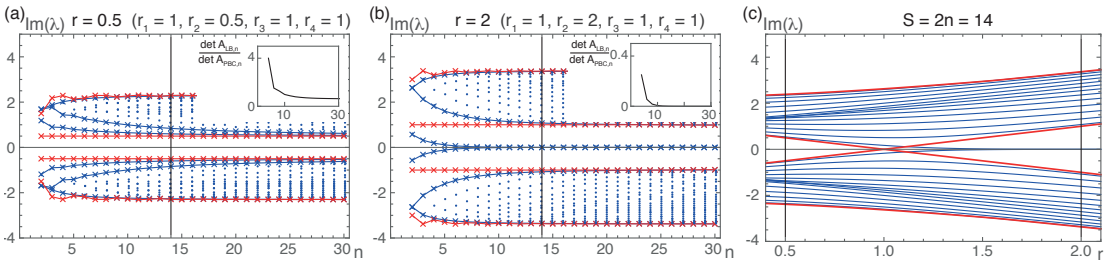

Figure 6.14: In the topologically nontrivial phase, A_{LB} becomes an asymptotic kernel vector. The largest and smallest eigenvalues by magnitude are shown for the closed (red) and the intermediate system (blue). In the topologically trivial phase (a), the spectra of both matrices behave similar, which is captured by the fraction of determinants of A_{PBC} and A_{LB}, which approaches one with increasing size (inset). In contrast, in the topologically nontrivial phase (b), A_{LB} has one pair of eigenvalues that approaches zero, such that the fraction of determinants converges to zero (inset). For fixed size, one observes that the spectrum of A_{LB} deviates from A_{PBC} above the transition point (c).

For the classification of the topological phase using the Szegő-Widom theorem, the exact form of the determinant of the closed system A_{PBC} and the intermediate system A_{LB} is necessary. As for the adjugate vectors, analytic expressions can be obtained from the Pfaffians of the networks, which are given by linear recursive polynomials.

6.D.1 Determinant of the closed diamond chain

For the diamond chain as defined in equation (6.1) and shown in Figure 6.1, we find the following expressions for the determinants of the open and closed system:

The case of the intermediate system, A_{LB}, the Pfaffian is obtained as the polynomial in Figure 6.12 (c):

$$\det(A_{PBC,n}) = [f_{n+1}(r_3, r_1r_4) + r_1r_4 f_{n-1}(r_3, r_1r_4)]^2 \tag{6.39}$$

In order to enumerate all perfect matchings of the closed system, A_{PBC}, we separate the set perfect matchings by which edge incident to the vertex 1 they contain. For example, the perfect matchings containing the edge $2 \to 1$ are obtained by removing this edge from the periodic system, finding for the resulting subnetwork all perfect matchings and adding the edge $2 \to 1$. This approach is convenient because by removing one edge, the system is dissected into a finite chain, for which the Pfaffian is easily calculated as a linear recursive polynomial, see Section 6.B.

Removing one edge breaks the periodicity of the system, and for the remaining network the Pfaffian is a linear recursive sequence.
We find

$$\begin{aligned}
\mathrm{Pf}(A_{LB,n}) = {} & r_3 \mathrm{sign}(id) f_n(r_3, r_1r_4) + r_2 \mathrm{sign}(2n, 1, id_{\hat{1},\hat{2n}}) f_n(r_2, r_1r_4) + \\
& r_1r_4 \underbrace{(\mathrm{sign}(2n-1, 1, 2, 2n, id_{\widehat{2n-1},\hat{1},\hat{2},\hat{2n}}) + \mathrm{sign}(3, 1, 2, 4, id_{\hat{3},\hat{1},\hat{4},\hat{2}}))}_{+2} f_{n-1}(r_3, r_1r_4) + \\
& r_1r_4 \underbrace{(\mathrm{sign}(2n-1, 1, 2n, 2n-2, id_{\widehat{2n-1},\hat{1},\hat{2n},\widehat{2n-2}}) + \mathrm{sign}(3, 1, 2, 2n, id_{\hat{3},\hat{1},\hat{2},\hat{2n}}))}_{-2} f_{n-1}(r_2, r_1r_4) \\
= {} & (r_3 f_n(r_3, r_1r_4) + 2r_1r_4 f_{n-1}(r_3, r_1r_4)) - (r_2 f_{n+1}(r_2, r_1r_4) + 2r_1r_4 f_{n-1}(r_2, r_1r_4))
\end{aligned} \tag{6.40}$$

$$\det(A_{LB,n}) = [(f_{n+1}(r_3, r_1r_4) + r_1r_4 f_{n-1}(r_3, r_1r_4)) - (f_{n+1}(r_2, r_1r_4) + r_1r_4 f_{n-1}(r_2, r_1r_4))]^2 \tag{6.41}$$

6.D.2 Determinant of the closed K_4 chain

The determinants of the open and closed K_4 chain are obtained in the same way as the ones discussed above.

The Pfaffian of the open system, A_{LB}, is given by the sequence $X(n)$ in Section 6.B.2, as can be seen from Figure 6.13 (c). The determinant of A_{LB} is

$$\det(A_{LB,n}) = [f_{n+1}(r_3, r_1r_4 - r_2r_5) + (r_1r_4 - r_2r_5) f_{n-1}(r_3, r_1r_4)]^2 \ . \tag{6.42}$$

For the periodic system, the Pfaffian is calculated in the same way as for the diamond chain, resulting in the following expression for the determinant:

$$\det(A_{PBC,n}) = \begin{bmatrix} (f_{n+1}(r_3, r_1r_4 - r_2r_5) + (r_1r_4 - r_2r_5) f_{n-1}(r_3, r_1r_4 - r_2r_5)) \\ -(f_{n+1}(r_2 + r_5, r_1r_4 - r_2r_5) + (r_1r_4 - r_2r_5) f_{n-1}(r_2 + r_5, r_1r_4 - r_2r_5)) \end{bmatrix}^2 \tag{6.43}$$

6.E Linear recursive polynomials of second order

The results in this Section are used for the analytic expressions for Pfaffians which appear when calculating determinants and adjugate vectors of one-dimensional chains.

A linear recursive polynomial of second order is defined by a recursion relation and an initial condition as follows:

$$\begin{aligned} f_{n+2}(a,b) &= a f_{n+1}(a,b) + b f_n(a,b) \ , \\ f_0(a,b) &= 0 \ , \\ f_1(a,b) &= 1 \ . \end{aligned} \tag{6.44}$$

Here, $f_1(a,b) = 1$ can always be achieved by dividing the full sequence as $f_n = \tilde{f}_n/\tilde{f}_1$. Note that we assume $a, b \neq 0$.

Analytic expression for f_n Analytic progress is possible using the characteristic function of f_n. which is given by $\phi^2 = a\phi + b$. The characteristic function has two solutions,

$$\phi_\pm = \frac{a}{2} \pm \sqrt{\frac{a^2}{4} + b} \ . \tag{6.45}$$

Every element of the sequence can be calculated (assuming $\phi_+ - \phi_- = 2\sqrt{\frac{a^2}{4} + b} \neq 0$) as

$$f_n(a,b) = \frac{\phi_+^n - \phi_-^n}{\phi_+ - \phi_-} \ , \tag{6.46}$$

$$f_0(a,b) = \frac{1-1}{\phi_+ - \phi_-} = 0 \ , \tag{6.47}$$

$$f_1(a,b) = \frac{\phi_+ - \phi_-}{\phi_+ - \phi_-} = 1 = b f_{n-1}(a,b) \ , \tag{6.48}$$

$$\begin{aligned} f_{n+1}(a,b) &= \frac{\phi_+^2 \phi_+^{n-1} - \phi_-^2 \phi_-^{n-1}}{\phi_+ - \phi_-} \ , \\ &= a\frac{\phi_+^n - \phi_-^n}{\phi_+ - \phi_-} + b\frac{\phi_+^{n-1} - \phi_-^{n-1}}{\phi_+ - \phi_-} = a f_n(a,b) + b f_{n-1}(a,b) \ . \end{aligned} \tag{6.49}$$

We can generalize this result to linear recursive sequences with differing initial conditions.

The elements of the sequence $g_n(a,b,g_0)$, which has the identical recursion relation as $f_n(a,b)$ but the initial condition $g_0(a,b,g_0) = g_0, g_1(a,bg_0) = 1$, can be calculated from $f_n(a,b)$ as

$$g_n(a,b,g_0) = f_n(a,b) + g_0 b f_{n-1}(a,b) \tag{6.50}$$

$$\begin{aligned} g_0(a,b,g_0) &= f_0(a,b) + g_0 b f_{-1}(a,b) = g_0 \frac{b}{b} = g_0 \\ g_1(a,b,g_0) &= f_1(a,b) + g_0 b f_0(a,b) = f_1(a,b) = 1 \ . \end{aligned} \tag{6.51}$$

6.E.1 Asymptotic behavior of f_n

When $|\phi_+| > |\phi_-|$, or equivalently $\sqrt{a^2/4+b} > 0$, the linear recursive sequence approaches exponential behavior for large values. The sequence is then approximated by

$$g_n(a,b) = \phi_+^{n-1}\frac{1-(\phi_-/\phi_+)^n}{1-(\phi_-/\phi_+)} + bg_0\phi_+^{(n-2)}\frac{1-(\phi_-/\phi_-)^{n-1}}{1-(\phi_-/\phi_+)} \approx \frac{\phi_+^{n-2}}{1-(\phi_-/\phi_+)}(\phi_+ + bg_0) \tag{6.52}$$

6.E.2 Negative values of f_n

In the K_4 chain, extinction occurs when the linear recursive sequences that make up the adjugate vector 6.B have non-positive entries. The size of the blocks of surviving strategies is then fixed by the first non-positive position of the linear recursive sequence.

As long as $\phi_\pm$ are real ($a^2/4+b>0$), the asymptotic law derived above applies and g_n is increasing, there are no negative entries. When $\sqrt{\frac{a^2}{4}+b}$ becomes imaginary, the polynomial begins to oscillate, such there will be negative values for g_m. With decreasing b, the position m for the first non-positive value decreases from $m=\infty$ to the smallest possible value, $m=3$.

Summarizing, we find three regions for the linear recursive polynomial:

- When $a^2/4 > -b$: f_n behaves asymptotically exponential as $g_n \sim \phi_+^n$
- For $a^2/4 > -b > a^2$: f_n fluctuates, for some $m>3$ there is a negative entry with $f_m < 0$. The value of m decreases with b and can thus far not be determined
- Finally, for $-a^2 \geq b$: The third element of the linear recursive sequence is nonpositive, $f_3 \leq 0$

6.E.3 Traveling wave solution

Here we verify that the solution (6.14) the differential equation (6.13).

As stated in Section 6.6, with $x_m = 0$, the differential equation for $y_m = u_m - v_m$ is

$$\partial_t y_m = y_m(y_{m-1} - y_m)\ . \tag{6.53}$$

Here we show that this equation is solved by

$$y_m = c_2\left(\frac{1}{\tanh(c_1)} - \tanh(c_1 m + c_2 t + \delta)\right). \tag{6.54}$$

Substituting $\zeta_m = c_1 m + c_2 t + \delta$, the time derivative of y_m is

$$\partial_t y_m = \partial_t c_2\left(\frac{1}{\tanh(c_1)} - \tanh(\zeta_m)\right) = -c_2^2(1-\tanh(\zeta_m)^2)\ . \tag{6.55}$$

On the other hand, with the identity for the hyperbolic tangent $\tanh(a+b) = \frac{\tanh a + \tanh b}{1+\tanh a \tanh b}$, we find

$$y_m(y)m - 1 - y_m) = c_2^2 \frac{1 - \tanh(c_1)\tanh(\zeta_m)}{\tanh(c_1)} \left(\frac{\tanh(\zeta_m) - \tanh(c_1)}{1 - \tanh(\zeta_m)\tanh(c_1)} - \tanh(\zeta_m) \right) \tag{6.56}$$

$$= \frac{c_2^2}{\tanh(c_1)} \left(-\tanh(c_1) + \tanh(\zeta_m)^2 \tanh(c_1) \right) \tag{6.57}$$

$$= -c_2^2 (1 - \tanh(\zeta_m)^2) \ . \tag{6.58}$$

Thus, y_m solves the differential difference equation (6.13).

Chapter 7

Conclusion, discussion and outlook

7.1 Summary

In this thesis we studied the role of network topology for the dynamics of the antisymmetric Lotka Volterra equation (2.1) (ALVE),

$$\frac{\mathrm{d}}{\mathrm{d}t}x_\alpha(t) = x_\alpha(t)\sum_{\beta=1}^{S} a_{\alpha\beta}x_\beta(t) \ .$$

The interaction between states α is defined through the antisymmetric interaction matrix $A = -A^T$. As the ALVE is mass conserving and antisymmetric matrices can be represented as directed networks, the ALVE dynamics can be interpreted as a mass flow on a network. This makes the ALVE a suitable model system for the study of the interplay between network topology and dynamics. Among other applications, this system of nonlinear differential equations is the replicator equation for zero sum games in the context of evolutionary game theory (see Section 1.3). For generic networks, one observes survival of some states and extinction of the remaining states. Interestingly, it can be shown that the set of surviving states depends only on the antisymmetric transition matrix and is independent of the initial conditions. More precisely, the set of survivors is defined by the so-called condensate vector of the matrix (see Section 2.2). In the special case that the condensate vector is a strictly positive kernel vector of the interaction matrix, *all* states survive, forming a network of interacting and competing species for all times. When additionally the kernel vector is unique, its entries characterize the long-time limit of the temporal average occupation, $\langle x_\alpha\rangle_T = 1/T\int_0^T \mathrm{d}t\ x_\alpha$. Kernel vectors of antisymmetric matrices A can be calculated analytically using the Pfaffian, a determinant-like function for antisymmetric matrices that is closely related to graph-theoretical properties of the network corresponding to A. This connection between the kernel vectors of antisymmetric matrices and survival, extinction and average mass distribution in the ALVE allows us to discuss the ALVE dynamics in terms of the network topology of the underlying network. The main findings of this thesis are:

Topologically robust coexistence and coexistence networks

In the first project, presented in Chapter 4, we introduced the notion of *coexistence networks*, that is, networks which show coexistence of all states in the ALVE as a consequence of the network topology alone. Exploiting the graph-theoretical interpretation of the Pfaffian, we characterized the kernel of A in terms of network topological properties, namely by all near-perfect matchings of the network defined by A. This interpretation enabled us to formulate conditions with which to identify coexistence networks. Algebraically speaking, coexistence networks correspond to antisymmetric matrices whose positions of positive, negative, and zero entries ensures a strictly positive kernel vector for each choice of entries magnitude. This project shows that in the ALVE, the qualitative dynamics, that is, survival of all states, can be a consequence of the network topology alone. Coexistence networks have relevance for population dynamics, as they are extraordinary robust network motifs. In the context of game theory, coexistence networks are of interest as they are zero sum games for which every strategy is necessary for every choice of payoff. Additional applications are discussed in Section 4.5.

Topological phase transition in coupled rock-paper-scissors cycles

In the second project, presented in Chapter 5, we analyzed the long-time behavior of a specific coexistence network, the RPS chain. The RPS chain is constructed by concatenation of identical RPS cycles. Numerical simulations of the ALVE on the RPS chain show that, depending on the skewness, a ratio of two rates in the RPS cycles, the temporal average mass polarizes to the boundaries. The system undergoes a transition from left to right polarization as the skewness parameter passes through a critical value, at the critical point, solitary waves are observed. Remarkably, this phase transition falls into symmetry class D within the "ten-fold way" classification scheme of gapped free-fermion systems, which also applies, for example, to 1D topological superconductors: The polarization can be understood from the unique strictly positive kernel vector of the system which arises from a topological phase transition of the chains interaction matrix through the bulk-boundary correspondence. Thus, we found that the polarization states are topological phases of the nonlinear ALVE dynamics. The discovery and characterization of topological phases in the ALVE are of interest as this is the first report of topological phases in the context of population dynamics. Additionally, for the ALVE the topological phases can discussed in full through the adjugate vector, and not only in a linearized region around the fixed point. As we present an algebraic characterization of the topological transition and discuss it in terms of properties of lattices with different boundary conditions, we hope that our work provides a relatively non-technical perspective on topological phases.

Topological phase transition beyond rock-paper-scissors

In the third project, presented in Chapter 6, we generalized the results on the RPS chain to other one dimensional chains. We found that the topological phase transition of the

temporal average mass found for the RPS chain is robust against augmentations of the network topology with additional edges. The topological phases can be understood on the basis of the strictly positive kernel vectors, which are obtained as combinations of linear recursive sequences. This knowledge allowed us to extend the discussion of topological phases beyond coexistence networks, where we showed that extinction occurs only in the topologically nontrivial phase. We close with a derivation of the differential difference equations for one dimensional chains at the transition point between the topological phases. As these equations have numerical solutions that resemble solitary waves, this may be a starting point for future research.

7.2 Outlook

The research presented in this thesis could be continued in different directions.

Population dynamics

As mentioned in the Introduction 1.3.1, the ALVE is a special case of both the replicator equation and the generalized Lotka Volterra equation. The results presented here are concerned with the exceptional stability of coexistence networks. If and how far this stability ranges when adding either a slight symmetric perturbance to the interaction matrix, or adding sources and sinks to the system is unknown so far. Mappings between the ALVE and other dynamical systems (for example interpret the ALVE as a replicator equation and map it onto a generalized Lotka Volterra equation or vice versa [25, 190]) one may transport our results to different contexts.

Evolution of interaction networks

In the context of the evolution and development of ecosystems and foodwebs, the role of coexistence networks is unknown. Assuming an evolutionary process in which network topologies evolve, for example by invasion of additional species (similar to [7]), appearance of new predation relations, and other mechanisms, the network topology would be continuously augmented and changed. In such a dynamics, a network could be extended by mutation, followed by a reduction through extinction due to new interactions. As extinction reduces the dynamics to subnetworks in which all states survive, coexistence networks, the most robust networks of survivors, could take the role of attractors of this evolutionary process.

Topological phase transitions beyond one dimensional chains

The investigation of topological phase transitions in the context of population dynamics could be continued in various ways:
As a continuation of our work, recently topological phase transition and chiral edge states in

Kagome lattices constructed from RPS cycles were reported [191]. So far the analysis only covers a linearization if the ALVE. For the Kagome lattice, the kernel is high-dimensional such that a detailed connection between the condensate vector and the long-time behavior of the system as for the RPS chain is not possible. The fact that the consequences of the topological phases, namely chiral edge states, are nonetheless strikingly visible may give new insights into the non-linear dynamics of the ALVE.

Interplay of topological phase transitions depending on density

In the context of microscopic reactions as introduced in Section 1.3.2, naturally a sub-leading term in the population size can be included by allowing mutations. Through the polarization of mass, the population density is reduced in parts of the system (due to exponential decay from the boundary), such that an interplay between the leading order dynamics and sub-leading effects may arise. Recently it was shown that diffusive dynamics on one dimensional lattices can lead to topological phase transitions [167]. Coupling these effects with the ALVE dynamics might lead to interesting interplay of two topological phases in distinct density regions of the system.

Constructing topological systems by combination of directed multi-state oscillators

The topological phase transitions on one-dimensional chains can be interpreted as a consequence of the coupling topology. Potentially, using coupling topologies that are known to give rise to topological phase transitions with local oscillators such as [30, 26, 192] instead of the RPS cycle may lead to the discovery of robust dynamical modes.

Integrability of one dimensional chains at the topological transition point

Finally, exact solutions for the ALVE dynamics at the topological transition point remain unknown so far. As the structure of the differential difference equations derived in Section 6.6 is closely related to several integrable systems that show solitary waves [41], the existence of a closed solution seems reasonable. Additionally, as in the presented models solitary waves can move into both directions, and are transformed into each other at the edges of finite systems, new phenomena such as reflection of solitary waves at the systems boundary may be investigated.

Bibliography

[1] J. Knebel, T. Krüger, M. F. Weber, and E. Frey. Coexistence and survival in conservative Lotka-Volterra networks. *Phys. Rev. Lett.*, 110(16):168106, 2013. URL: 10.1103/PhysRevLett.110.168106, doi:10.1103/PhysRevLett.110.168106.

[2] J. Knebel, M. F. Weber, T. Krüger, and E. Frey. Evolutionary games of condensates in coupled birth-death processes. *Nature Communications*, 6:6977, Apr 2015. URL: 10.1038/ncomms7977, doi:10.1038/ncomms7977.

[3] Ernesto Estrada and Philip A. Knight. *A First Course in Network Theory*. Oxford University Press, Oxford, UNITED KINGDOM, 2015. URL: http://ebookcentral.proquest.com/lib/ub-lmu/detail.action?docID=1992297.

[4] S. H. Strogatz. *Nonlinear dynamics and chaos : with applications to physics, biology, chemistry, and engineering*. Westview Press, 2015.

[5] Eli Ben-Naim, Hans Frauenfelder, and Zoltan Toroczkai. *Complex networks*, volume 650 of *Lecture notes in physics*. Springer Science & Business Media, 2004.

[6] J. O. Haerter, N. Mitarai, and K. Sneppen. Food web assembly rules for generalized lotka-volterra equations. *PLOS Computational Biology*, 12(2):1–17, 02 2016. URL: 10.1371/journal.pcbi.1004727, doi:10.1371/journal.pcbi.1004727.

[7] J. O. Haerter, N. Mitarai, and K. Sneppen. Theory of invasion extinction dynamics in minimal food webs. *Phys. Rev. E*, 97:022404, Feb 2018. URL: 10.1103/PhysRevE.97.022404, doi:10.1103/PhysRevE.97.022404.

[8] Brad K. Hulse, Hannah Haberkern, Romain Franconville, Daniel B. Turner-Evans, Shinya Takemura, Tanya Wolff, Marcella Noorman, Marisa Dreher, Chuntao Dan, Ruchi Parekh, Ann M. Hermundstad, Gerald M. Rubin, and Vivek Jayaraman. A connectome of the drosophila central complex reveals network motifs suitable for flexible navigation and context-dependent action selection. *bioRxiv*, 2020. URL: https://www.biorxiv.org/content/early/2020/12/22/2020.12.08.413955, arXiv:https://www.biorxiv.org/content/early/2020/12/22/2020.12.08.413955.full.pdf, doi:10.1101/2020.12.08.413955.

[9] Rekin's Janky, Annelien Verfaillie, Hana Imrichová, Bram Van de Sande, Laura Standaert, Valerie Christiaens, Gert Hulselmans, Koen Herten, Marina Naval Sanchez, Delphine Potier, Dmitry Svetlichnyy, Zeynep Kalender Atak, Mark Fiers, Jean-Christophe Marine, and Stein Aerts. iregulon: From a gene list to a gene regulatory network using large motif and track collections. *PLOS Computational Biology*, 10(7):1–19, 07 2014. URL: https://doi.org/10.1371/journal.pcbi.1003731, doi:10.1371/journal.pcbi.1003731.

[10] Daniele Mercatelli, Laura Scalambra, Luca Triboli, Forest Ray, and Federico M. Giorgi. Gene regulatory network inference resources: A practical overview. *Biochimica et Biophysica Acta (BBA) - Gene Regulatory Mechanisms*, 1863(6):194430, 2020. Transcriptional Profiles and Regulatory Gene Networks. URL: http://www.sciencedirect.com/science/article/pii/S1874939919300410, doi:https://doi.org/10.1016/j.bbagrm.2019.194430.

[11] Daniel J. Knight, G. Shinar, and M. Feinberg. Sharper graph-theoretical conditions for the stabilization of complex reaction networks. *Mathematical biosciences*, 262:10–27, 2015.

[12] Peter Krawitz and Ilya Shmulevich. *Boolean Modeling of Biological Networks*, pages 599–608. Springer New York, New York, NY, 2009. URL: https://doi.org/10.1007/978-0-387-30440-3_40, doi:10.1007/978-0-387-30440-3_40.

[13] R. Milo, S. Shen-Orr, S. Itzkovitz, N. Kashtan, D. Chklovskii, and U. Alon. Network motifs: simple building blocks of complex networks. *Science*, 298(5594):824–827, 2002. URL: 10.1126/science.298.5594.824, doi:10.1126/science.298.5594.824.

[14] Uri Alon. Network motifs: theory and experimental approaches. *Nature Reviews Genetics*, 8(6):450–461, 2007. URL: https://doi.org/10.1038/nrg2102, doi:10.1038/nrg2102.

[15] Erik van Nimwegen, James P. Crutchfield, and Martijn Huynen. Neutral evolution of mutational robustness. *Proceedings of the National Academy of Sciences*, 96(17):9716, 08 1999. URL: http://www.pnas.org/content/96/17/9716.abstract, doi:10.1073/pnas.96.17.9716.

[16] J. Gao, B. Barzel, and A.-L. Barabási. Universal resilience patterns in complex networks. *Nature*, 530:307 EP –, 02 2016. URL: 10.1038/nature16948, doi:10.1038/nature16948.

[17] Jeremy Gunawardena. Chemical reaction network theory for in-silico biologists. *Notes available for download at http://vcp. med. harvard. edu/papers/crnt. pdf*, 2003.

[18] Amir Bashan, Ronny P. Bartsch, Jan. W. Kantelhardt, Shlomo Havlin, and Plamen Ch. Ivanov. Network physiology reveals relations between network topology and physiological function. *Nature Communications*, 3(1):702, 2012. URL: https://doi.org/10.1038/ncomms1705, doi:10.1038/ncomms1705.

[19] V. Volterra. *Leçons sur la Théorie Mathématique de la Lutte pour la Vie*. Gauthier-Villars, Paris, 1931.

[20] E. Frey. Evolutionary game theory: Theoretical concepts and applications to microbial communities. *Physica A*, 389(20):4265–4298, 2010. URL: 10.1016/j.physa.2010.02.047, doi:10.1016/j.physa.2010.02.047.

[21] [online]URL: https://en.wikipedia.org/wiki/Rock_paper_scissors [cited 03.01.2021].

[22] J. v. Neumann. Zur theorie der gesellschaftsspiele. *Mathematische Annalen*, 100(1):295–320, 1928. URL: https://doi.org/10.1007/BF01448847, doi:10.1007/BF01448847.

[23] M. F. Weber, G. Poxleitner, E. Hebisch, E. Frey, and M. Opitz. Chemical warfare and survival strategies in bacterial range expansions. *J. R. Soc. Interface*, 11(96):20140172, 2014. URL: 10.1098/rsif.2014.0172, doi:10.1098/rsif.2014.0172.

[24] B. Sinervo and C. M. Lively. The rock-paper-scissors game and the evolution of alternative male strategies. *Nature*, 380(6571):240–243, 1996. URL: 10.1038/380240a0, doi:10.1038/380240a0.

[25] J. Hofbauer and K. Sigmund. *Evolutionary Games and Population Dynamics*. Cambridge University Press, Cambridge, 1998.

[26] M. A. Nowak and R. M. May. Evolutionary games and spatial chaos. *Nature*, 359:826–829, 1992. URL: 10.1038/359826a0, doi:10.1038/359826a0.

[27] E. Akin and V. Losert. Evolutionary dynamics of zero-sum games. *J. Math. Biol.*, 20(3):231–258, 1984. URL: 10.1007/BF00275987, doi:10.1007/BF00275987.

[28] T. Chawanya and K. Tokita. Large-dimensional replicator equations with antisymmetric random interactions. *J. Phys. Soc. Jpn.*, 71(2):429–431, 2002. URL: 10.1143/JPSJ.71.429, doi:10.1143/JPSJ.71.429.

[29] Junpyo Park. Nonlinear dynamics with hopf bifurcations by targeted mutation in the system of rock-paper-scissors metaphor. *Chaos: An Interdisciplinary Journal of Nonlinear Science*, 29(3):033102, 2021/01/04 2019. URL: https://doi.org/10.1063/1.5081966, doi:10.1063/1.5081966.

[30] R. M. May. *Stability and Complexity in Model Ecosystems*. Princeton University Press, Princeton, NJ, 1973.

[31] Y. Itoh. Boltzmann equation on some algebraic structure concerning struggle for existence. *Proc. Japan Acad.*, 47:854–858, 1971. URL: 10.3792/pja/1195526389, doi:10.3792/pja/1195526389.

[32] E. Di Cera, P. E. Phillipson, and J. Wyman. Chemical oscillations in closed macromolecular systems. *Proc. Natl. Acad. Sci. USA*, 85(16):5923–5926, 1988. URL: 10.1073/pnas.85.16.5923, doi:10.1073/pnas.85.16.5923.

[33] E. Di Cera, P. E. Phillipson, and J. Wyman. Limit-cycle oscillations and chaos in reaction networks subject to conservation of mass. *Proc. Natl. Acad. Sci. USA*, 86(1):142–146, 1989. URL: 10.1073/pnas.86.1.142, doi:10.1073/pnas.86.1.142.

[34] C. Gardiner. *Stochastic Methods: A Handbook for the Natural and Social Sciences*. Springer, Berlin, 2009.

[35] T. Reichenbach, M. Mobilia, and E. Frey. Mobility promotes and jeopardizes biodiversity in rock-paper-scissors games. *Nature*, 448(7157):1046–1049, 2007. URL: 10.1038/nature06095, doi:10.1038/nature06095.

[36] A. Szolnoki, M. Mobilia, L.-L. Jiang, B. Szczesny, A. M. Rucklidge, and M. Perc. Cyclic dominance in evolutionary games: a review. *J. R. Soc. Interface*, 11(100):20140735, 2014. URL: 10.1098/rsif.2014.0735, doi:10.1098/rsif.2014.0735.

[37] D. Vorberg, W. Wustmann, R. Ketzmerick, and A. Eckardt. Generalized Bose-Einstein condensation into multiple states in driven-dissipative systems. *Phys. Rev. Lett.*, 111(24):240405, Dec 2013. URL: 10.1103/PhysRevLett.111.240405, doi:10.1103/PhysRevLett.111.240405.

[38] D. Vorberg, W. Wustmann, H. Schomerus, R. Ketzmerick, and A. Eckardt. Nonequilibrium steady states of ideal bosonic and fermionic quantum gases. *Phys. Rev. E*, 92:062119, Dec 2015. URL: 10.1103/PhysRevE.92.062119, doi:10.1103/PhysRevE.92.062119.

[39] C. W. Gardiner and P. Zoller. *Quantum Noise*. Springer, Berlin Heidelberg, 2004.

[40] A. Schnell, R. Ketzmerick, and A. Eckardt. On the number of bose-selected modes in driven-dissipative ideal bose gases. *Phys. Rev. E*, 97:032136, Mar 2018. URL: 10.1103/PhysRevE.97.032136, doi:10.1103/PhysRevE.97.032136.

[41] Y. B. Suris. *The Problem of Integrable Discretization: Hamiltonian Approach*. Progress in Mathematics. Birkhäuser, 2003.

[42] S. V. Manakov. Complete integrability and stochastization of discrete dynamical systems. *Sov. Phys.-JETP*, 40(2):269–274, 1975. URL: http://jetp.ac.ru/cgi-bin/dn/e_040_02_0269.pdf.

[43] M Kac and Pierre van Moerbeke. On an explicitly soluble system of nonlinear differential equations related to certain toda lattices. *Advances in Mathematics*, 16(2):160–169, 1975. URL: http://www.sciencedirect.com/science/article/pii/0001870875901486, doi:https://doi.org/10.1016/0001-8708(75)90148-6.

[44] Joana M. Nunes da Costa and Pantelis A. Damianou. The negative relativistic toda hierarchy and rational poisson brackets. *Qualitative Theory of Dynamical Systems*, 5(1):121–134, 2004. URL: https://doi.org/10.1007/BF02968133, doi:10.1007/BF02968133.

[45] J Moser. Three integrable hamiltonian systems connected with isospectral deformations. *Advances in Mathematics*, 16(2):197–220, 1975. URL: http://www.sciencedirect.com/science/article/pii/0001870875901516, doi:https://doi.org/10.1016/0001-8708(75)90151-6.

[46] Robert M. Miura. Korteweg-de vries equation and generalizations. i. a remarkable explicit nonlinear transformation. *Journal of Mathematical Physics*, 9(8):1202–1204, 1968. URL: https://doi.org/10.1063/1.1664700, arXiv:https://doi.org/10.1063/1.1664700, doi:10.1063/1.1664700.

[47] V. E. Zakharov, S. L. Musher, and A. M. Rubenchik. Nonlinear stage of parametric wave excitation in a plasma. *Sov. Phys.-JETP*, 19:151, March 1974. URL: http://adsabs.harvard.edu/abs/1974JETPL..19..151Z.

[48] S. N. M. Ruijsenaars. Relativistic toda systems. *Comm. Math. Phys.*, 133(2):217–247, 1990. URL: https://projecteuclid.org:443/euclid.cmp/1104201396.

[49] Philipp M. Geiger, Johannes Knebel, and Erwin Frey. Topologically robust zero-sum games and pfaffian orientation: How network topology determines the long-time dynamics of the antisymmetric lotka-volterra equation. *Physical Review E*, 98(6):062316–, 12 2018. URL: https://link.aps.org/doi/10.1103/PhysRevE.98.062316, doi:10.1103/PhysRevE.98.062316.

[50] Johannes Knebel, Philipp M. Geiger, and Erwin Frey. Topological phase transition in coupled rock-paper-scissors cycles. *Phys. Rev. Lett.*, 125:258301, Dec 2020. URL: https://link.aps.org/doi/10.1103/PhysRevLett.125.258301, doi:10.1103/PhysRevLett.125.258301.

[51] H.W. Kuhn and A.W. Tucker. *Linear Inequalities and Related Systems*. Princeton University Press, Princeton, NJ, 1956.

[52] Edwin T Jaynes. *Probability theory: The logic of science*. Cambridge university press, 2003.

[53] D. B. West. *Introduction to Graph Theory*, volume 2 of *Math Classics*. Prentice Hall, 2001.

[54] T. Muir and W. H. Metzler. *A treatise on the theory of determinants*. Dover Publications, 1960.

[55] P. W. Kasteleyn. *Graph Theory and Theoretical Physics*, chapter Graph theory and Crystal physics, pages 43–110. Academic Press, 1967.

[56] M. Wimmer. Efficient numerical computation of the pfaffian for dense and banded skew-symmetric matrices. 2011. arXiv:arXiv:1102.3440, doi:10.1145/2331130.2331138.

[57] P. W. Kasteleyn. The statistics of dimers on a lattice: I. the number of dimer arrangements on a quadratic lattice. *Physica*, 27(12):1209 – 1225, 1961. URL: 10.1016/0031-8914(61)90063-5, doi:10.1016/0031-8914(61)90063-5.

[58] H. N. V. Temperley and M. E. Fisher. Dimer problem in statistical mechanics-an exact result. *The Philosophical Magazine: A Journal of Theoretical Experimental and Applied Physics*, 6(68):1061–1063, 1961. URL: 10.1080/14786436108243366, doi:10.1080/14786436108243366.

[59] M. E. Fisher. Statistical mechanics of dimers on a plane lattice. *Phys. Rev.*, 124:1664–1672, Dec 1961. URL: 10.1103/PhysRev.124.1664, doi:10.1103/PhysRev.124.1664.

[60] F. Y. Wu. Dimers on two-dimensional lattices. *International Journal of Modern Physics B*, 20(32):5357–5371, 2006. URL: 10.1142/S0217979206036478, doi:10.1142/S0217979206036478.

[61] R. Thomas. A survey of pfaffian orientations of graphs. *Proceedings of the International Congress of Mathematicians Madrid*, pages 963–984, 2006. URL: 10.4171/022-3/47, doi:10.4171/022-3/47.

[62] C. E. Cullis. *Matrices and Determinoids*, volume I and II. Cambridge University Press, Cambridge, 1913.

[63] L. Mirsky. *An Introduction to Linear Algebra*. Dover Books on Mathematics. Dover, 1990.

[64] P. G. Drazin. *Nonlinear Systems*. Cambridge Texts in Applied Mathematics. Cambridge University Press, 1992. URL: 10.1017/CBO9781139172455, doi:10.1017/CBO9781139172455.

[65] M. W. Hirsch, S. Smale, and R. L. Devaney. *Differential Equations, Dynamical Systems, and an Introduction to Chaos*. Academic Press. Academic Press, 2013. URL: https://books.google.de/books?id=csYhsrOEh_MC.

[66] A. Mellor, M. Mobilia, and R. K. P. Zia. Characterization of the nonequilibrium steady state of a heterogeneous nonlinear q-voter model with zealotry. *EPL (Europhysics Letters)*, 113(4):48001, 2016. URL: 10.1209/0295-5075/113/48001, doi:10.1209/0295-5075/113/48001.

[67] L. Dai, D. Vorselen, K. S. Korolev, and J. Gore. Generic indicators for loss of resilience before a tipping point leading to population collapse. *Science*, 336(6085):1175–1177, 2012. URL: 10.1126/science.1219805, doi:10.1126/science.1219805.

[68] L. Dai, K. S. Korolev, and J. Gore. Relation between stability and resilience determines the performance of early warning signals under different environmental drivers. *Proc. Natl. Acad. Sci. USA*, 112(32):10056–10061, 2015. URL: 10.1073/pnas.1418415112, doi:10.1073/pnas.1418415112.

[69] R. P. Rohr, S. Saavedra, and J. Bascompte. On the structural stability of mutualistic systems. *Science*, 345(6195), 2014. URL: 10.1126/science.1253497, doi:10.1126/science.1253497.

[70] S. Allesina and S. Tang. Stability criteria for complex ecosystems. *Nature*, 483:205 EP –, 02 2012. URL: 10.1038/nature10832, doi:10.1038/nature10832.

[71] A. Szolnoki, M. Perc, and G. Szabó. Topology-independent impact of noise on cooperation in spatial public goods games. *Phys. Rev. E*, 80:056109, Nov 2009. URL: 10.1103/PhysRevE.80.056109, doi:10.1103/PhysRevE.80.056109.

[72] B. Intoy and M. Pleimling. Synchronization and extinction in cyclic games with mixed strategies. *Phys. Rev. E*, 91:052135, May 2015. URL: 10.1103/PhysRevE.91.052135, doi:10.1103/PhysRevE.91.052135.

[73] C. Tu, J. Grilli, F. Schuessler, and S. Suweis. Collapse of resilience patterns in generalized lotka-volterra dynamics and beyond. *Phys. Rev. E*, 95:062307, Jun 2017. URL: 10.1103/PhysRevE.95.062307, doi:10.1103/PhysRevE.95.062307.

[74] S. Allesina and M. Pascual. Network structure, predator–prey modules, and stability in large food webs. *Theoretical Ecology*, 1(1):55–64, Mar 2008. URL: 10.1007/s12080-007-0007-8, doi:10.1007/s12080-007-0007-8.

[75] J. Vukov, A. Szolnoki, and G. Szabó. Diverging fluctuations in a spatial five-species cyclic dominance game. *Phys. Rev. E*, 88:022123, Aug 2013. URL: 10.1103/PhysRevE.88.022123, doi:10.1103/PhysRevE.88.022123.

[76] K. A. Hawick. Cycles, diversity and competition in rock-paper-scissors-lizard-spock spatial game agent simulations. Technical report, Massey University, 2011. URL: http://www.massey.ac.nz/~kahawick/cstn/129/cstn-129.pdf.

[77] Y. Kang, Q. Pan, X. Wang, and M. He. A golden point rule in rock–paper–scissors–lizard–spock game. *Physica A: Statistical Mechanics and its Applications*, 392(11):2652 – 2659, 2013. URL: 10.1016/j.physa.2012.10.011, doi:10.1016/j.physa.2012.10.011.

[78] H. Cheng, N. Yao, ZG. Huang, J. Park, Y. Do, and YG. Lai. Mesoscopic interactions and species coexistence in evolutionary game dynamics of cyclic competitions. *Scientific Reports*, 4:7486, 12 2014. URL: 10.1038/srep07486, doi:10.1038/srep07486.

[79] J. Park, Y. Do, B. Jang, and Y.-C. Lai. Emergence of unusual coexistence states in cyclic game systems. *Scientific Reports*, 7(1):7465, 2017. URL: 10.1038/s41598-017-07911-4, doi:10.1038/s41598-017-07911-4.

[80] R. K. P. Zia. General properties of a system of S species competing pairwise. *pre-print arXiv:1101.0018*, 2010. URL: arxiv.org/abs/1101.0018.

[81] C. H. Durney, S. O. Case, M. Pleimling, and R. K. P. Zia. Saddles, arrows, and spirals: deterministic trajectories in cyclic competition of four species. *Phys. Rev. E*, 83(5):051108, 2011. URL: 10.1103/PhysRevE.83.051108, doi:10.1103/PhysRevE.83.051108.

[82] H.E. Robbins. A theorem on graphs, with an application to a problem of traffic control. *The American Mathematical Monthly*, 46(5):281–283, 1939. URL: 10.2307/2303897, doi:10.2307/2303897.

[83] L. Lovász and M.D. Plummer. *Matching Theory*. Number Nr. 121 in Annals of discrete mathematics. North-Holland, 1986. URL: https://books.google.de/books?id=SGz6lAEACAAJ.

[84] R.P. Grimaldi. *Fibonacci and Catalan Numbers: An Introduction*. John Wiley and Sons, Inc., 2012. URL: 10.1002/9781118159743, doi:10.1002/9781118159743.

[85] P. Chandra and E. W. Weisstein. Fibonacci number – from wolfram mathworld, 2003. URL: http://mathworld.wolfram.com/FibonacciNumber.html [cited 06.02.2018].

[86] R. M. May. Will a large complex system be stable? *Nature*, 238(5364):413–414, 1972. URL: 10.1038/238413a0, doi:10.1038/238413a0.

[87] T. Reichenbach, M. Mobilia, and E. Frey. Coexistence versus extinction in the stochastic cyclic Lotka-Volterra model. *Phys. Rev. E*, 74(5):51907, 2006. URL: 10.1103/PhysRevE.74.051907, doi:10.1103/PhysRevE.74.051907.

[88] N. S. Goel, S. C. Maitra, and E. W. Montroll. On the Volterra and other nonlinear models of interacting populations. *Rev. Mod. Phys.*, 43(2):231–276, 1971. URL: 10.1103/RevModPhys.43.231, doi:10.1103/RevModPhys.43.231.

[89] S. Sadeghi and A. Engel. Random matrices and condensation into multiple states. *Phys. Rev. E*, 97:032133, Mar 2018. URL: 10.1103/PhysRevE.97.032133, doi:10.1103/PhysRevE.97.032133.

[90] B. Intoy and M. Pleimling. Extinction in four species cyclic competition. *Journal of Statistical Mechanics: Theory and Experiment*, 2013(08):P08011, 2013. URL: 10.1088/1742-5468/2013/08/P08011, doi:10.1088/1742-5468/2013/08/P08011.

[91] Cilie W. Feldager, Namiko Mitarai, and Hiroki Ohta. Deterministic extinction by mixing in cyclically competing species. *Phys. Rev. E*, 95:032318, Mar 2017. URL: 10.1103/PhysRevE.95.032318, doi:10.1103/PhysRevE.95.032318.

[92] A. Dobrinevski and E. Frey. Extinction in neutrally stable stochastic Lotka-Volterra models. *Phys. Rev. E*, 85(5):051903, 2012. URL: 10.1103/PhysRevE.85.051903, doi:10.1103/PhysRevE.85.051903.

[93] M. Berr, T. Reichenbach, M. Schottenloher, and E. Frey. Zero-one survival behavior of cyclically competing species. *Phys. Rev. Lett.*, 102:048102, Jan 2009. URL: 10.1103/PhysRevLett.102.048102, doi:10.1103/PhysRevLett.102.048102.

[94] G. Szabó and F. Gábor. Evolutionary games on graphs. *Physics Reports*, 446(4):97 – 216, 2007. URL: 10.1016/j.physrep.2007.04.004, doi:10.1016/j.physrep.2007.04.004.

[95] L. Frachebourg, P. L. Krapivsky, and E. Ben-Naim. Segregation in a one-dimensional model of interacting species. *Phys. Rev. Lett.*, 77:2125–2128, Sep 1996. URL: 10.1103/PhysRevLett.77.2125, doi:10.1103/PhysRevLett.77.2125.

[96] R. Blümel, A. Buchleitner, R. Graham, L. Sirko, U. Smilansky, and H. Walther. Dynamical localization in the microwave interaction of Rydberg atoms: the influence of noise. *Phys. Rev. A*, 44:4521–4540, Oct 1991. URL: 10.1103/PhysRevA.44.4521, doi:10.1103/PhysRevA.44.4521.

[97] S. Kohler, T. Dittrich, and P. Hänggi. Floquet-Markovian description of the parametrically driven, dissipative harmonic quantum oscillator. *Phys. Rev. E*, 55:300–313, Jan 1997. URL: 10.1103/PhysRevE.55.300, doi:10.1103/PhysRevE.55.300.

[98] HP. Breuer, W. Huber, and F. Petruccione. Quasistationary distributions of dissipative nonlinear quantum oscillators in strong periodic driving fields. *Phys. Rev. E*, 61(5):4883–4889, May 2000. URL: 10.1103/PhysRevE.61.4883, doi:10.1103/PhysRevE.61.4883.

[99] S. Choudhury and E. J. Mueller. Stability of a bose-einstein condensate in a driven optical lattice: Crossover between weak and tight transverse confinement. *Phys. Rev. A*, 92:063639, Dec 2015. URL: 10.1103/PhysRevA.92.063639, doi:10.1103/PhysRevA.92.063639.

[100] H. A. M. Leymann, D. Vorberg, T. Lettau, C. Hopfmann, C. Schneider, M. Kamp, S. Höfling, R. Ketzmerick, J. Wiersig, S. Reitzenstein, and A. Eckardt. Pump-power-driven mode switching in a microcavity device and its relation to bose-einstein condensation. *Phys. Rev. X*, 7:021045, Jun 2017. URL: 10.1103/PhysRevX.7.021045, doi:10.1103/PhysRevX.7.021045.

[101] S. Klembt, P. Stepanov, T. Klein, A. Minguzzi, and M. Richard. Thermal decoherence of a nonequilibrium polariton fluid. *Phys. Rev. Lett.*, 120:035301, Jan 2018. URL: 10.1103/PhysRevLett.120.035301, doi:10.1103/PhysRevLett.120.035301.

[102] L. Vidmar, J. P. Ronzheimer, M. Schreiber, S. Braun, S. S. Hodgman, S. Langer, F. Heidrich-Meisner, I. Bloch, and U. Schneider. Dynamical quasicondensation of hard-core bosons at finite momenta. *Phys. Rev. Lett.*, 115:175301, Oct 2015. URL: 10.1103/PhysRevLett.115.175301, doi:10.1103/PhysRevLett.115.175301.

[103] D. C. Fisher and J. Ryan. Optimal strategies for a generalized "scissors, paper, and stone" game. *The American Mathematical Monthly*, 99(10):935–942, 1992. URL: 10.2307/2324486, doi:10.2307/2324486.

[104] F. Brandl. The distribution of optimal strategies in symmetric zero-sum games. *Games and Economic Behavior*, 104:674 – 680, 2017. URL: http://www.sciencedirect.com/science/article/pii/S089982561730115X, doi:https://doi.org/10.1016/j.geb.2017.06.017.

[105] F. Brandt. Tournament solutions: Extensions of maximality and their applications to decision-making, 2009. URL: http://dss.in.tum.de/files/brandt-research/habil.pdf.

[106] R. B. Bapat. *Matrix Games Based on Graphs*, pages 165–177. Springer London, London, 2014. URL: 10.1007/978-1-4471-6569-9_13, doi:10.1007/978-1-4471-6569-9_13.

[107] P. De Donder, M. Le Breton, and M. Truchon. Choosing from a weighted tournament. *Mathematical Social Sciences*, 40(1):85 – 109, 2000. URL: 10.1016/S0165-4896(99)00042-6, doi:10.1016/S0165-4896(99)00042-6.

[108] M. Brill, R> Freeman, and V. Conitzer. Aaai conference on artificial intelligence, 2016. URL: https://www.aaai.org/ocs/index.php/AAAI/AAAI16/paper/view/12480 [cited 2016-02-21].

[109] H. Aziz, M. Brill, F. Fischer, P. Harrenstein, J. Lang, and H. G. Seedig. Possible and necessary winners of partial tournaments. *Journal of Artificial Intelligence Research*, 54:493–534, 2015. URL: 10.1613/jair.4856, doi:10.1613/jair.4856.

[110] E. N. Barron. *Game theory: an introduction*, volume 2. John Wiley and Sons, Inc., 2013.

[111] J. González-Díaz, I. García-Jurado, and M.G. Fiestras-Janeiro. *An introductory course on mathematical game theory*, volume 115. American Mathematical Society Providence, 2010.

[112] G. Laffond, J.-F. Laslier, and M. Le Breton. The bipartisan set of a tournament game. *Games and Economic Behavior*, 5(1):182 – 201, 1993. URL: http://www.sciencedirect.com/science/article/pii/S0899825683710109, doi:https://doi.org/10.1006/game.1993.1010.

[113] T. S. Michael and T. Quint. Optimal strategies for node selection games on oriented graphs: Skew matrices and symmetric games. *Linear Algebra and its Applications*, 412(2):77 – 92, 2006. URL: http://www.sciencedirect.com/science/article/pii/S002437950500234X, doi:https://doi.org/10.1016/j.laa.2005.04.009.

[114] I. Kaplansky. A contribution to von neumann's theory of games. ii. *Linear Algebra and its Applications*, 226-228:371 – 373, 1995. URL: 10.1016/0024-3795(95)00167-P, doi:10.1016/0024-3795(95)00167-P.

[115] M. Le Breton. On the uniqueness of equilibrium in symmetric two-player zero-sum games with integer payoffs. *Économie publique/Public economics*, (17), 2007. URL: economiepublique.revues.org/pdf/2655.

[116] D. P. Roberts. Nash equilibria of cauchy-random zero-sum and coordination matrix games. *International Journal of Game Theory*, 34(2):167–184, Aug 2006. URL: 10.1007/s00182-006-0016-7, doi:10.1007/s00182-006-0016-7.

[117] H. Arsham. Stability of essential strategy in two-person zero-sum games. 110:167–180, 07 1995.

[118] P. W. Kasteleyn. Dimer statistics and phase transitions. *Journal of Mathematical Physics*, 4(2):287–293, 1963. URL: 10.1063/1.1703953, doi:10.1063/1.1703953.

[119] M. E. Fisher. On the dimer solution of planar ising models. *Journal of Mathematical Physics*, 7(10):1776–1781, 1966. URL: 10.1063/1.1704825, doi:10.1063/1.1704825.

[120] D. S. Rokhsar and S. A. Kivelson. Superconductivity and the quantum hard-core dimer gas. *Phys. Rev. Lett.*, 61:2376–2379, Nov 1988. URL: 10.1103/PhysRevLett.61.2376, doi:10.1103/PhysRevLett.61.2376.

[121] P. Fendley, R. Moessner, and S. L. Sondhi. Classical dimers on the triangular lattice. *Phys. Rev. B*, 66:214513, Dec 2002. URL: 10.1103/PhysRevB.66.214513, doi:10.1103/PhysRevB.66.214513.

[122] C. H. C. Little. An extension of kasteleyn's method of enumerating the 1-factors of planar graphs. In D. A. Holton, editor, *Combinatorial Mathematics*, pages 63–72, Berlin, Heidelberg, 1974. Springer Berlin Heidelberg.

[123] V. V. Vazirani and M. Yannakakis. Pfaffian orientations, 0–1 permanents, and even cycles in directed graphs. *Discrete Applied Mathematics*, 25(1):179 – 190, 1989. URL: 10.1016/0166-218X(89)90053-X, doi:10.1016/0166-218X(89)90053-X.

[124] G. Tesler. Matchings in graphs on non-orientable surfaces. *Journal of Combinatorial Theory, Series B*, 78(2):198 – 231, 2000. URL: 10.1006/jctb.1999.1941, doi:10.1006/jctb.1999.1941.

[125] S. Norine. Pfaffian graphs, t-joins and crossing numbers. *Combinatorica*, 28(1):89–98, Jan 2008. URL: 10.1007/s00493-008-2150-2, doi:10.1007/s00493-008-2150-2.

[126] F. Y. Wu. Remarks on the modified potassium dihydrogen phosphate model of a ferroelectric. *Phys. Rev.*, 168:539–543, Apr 1968. URL: 10.1103/PhysRev.168.539, doi:10.1103/PhysRev.168.539.

[127] F. Lu, L. Zhang, and F. Lin. Enumeration of perfect matchings of a type of quadratic lattice on the torus. *The Electronic Journal of Combinatorics*, 17(1):Research Paper R36, 14 p.–Research Paper R36, 14 p., 2010. URL: http://eudml.org/doc/222565.

[128] Y. L. Loh, Dao-Xin Yao, and E. W. Carlson. Dimers on the triangular kagome lattice. *Phys. Rev. B*, 78:224410, Dec 2008. URL: 10.1103/PhysRevB.78.224410, doi:10.1103/PhysRevB.78.224410.

[129] F. Y. Wu and F. Wang. Dimers on the kagome lattice i: Finite lattices. *Physica A: Statistical Mechanics and its Applications*, 387(16):4148 – 4156, 2008. URL: 10.1016/j.physa.2008.02.054, doi:10.1016/j.physa.2008.02.054.

[130] F. Wang and F. Y. Wu. Exact solution of close-packed dimers on the kagomé lattice. *Phys. Rev. E*, 75:040105, Apr 2007. URL: 10.1103/PhysRevE.75.040105, doi:10.1103/PhysRevE.75.040105.

[131] R. Kenyon. The planar dimer model with boundary: a survey. In *CRM Proceedings and Lecture Notes*, 13, pages 307–328, 2000. URL: http://www.math.brown.edu/~rkenyon/papers/dimers.pdf.

[132] S. Li and W. Yan. Dimers on the 33.42 lattice. *Physica A: Statistical Mechanics and its Applications*, 452:251 – 257, 2016. URL: 10.1016/j.physa.2016.02.033, doi:10.1016/j.physa.2016.02.033.

[133] S. Li, W. Yan, and T. Tian. Some physical and chemical indices of the union jack lattice. *Journal of Statistical Mechanics: Theory and Experiment*, 2015(2):P02014, 2015. URL: 10.1088/1742-5468/2015/02/P02014, doi:10.1088/1742-5468/2015/02/P02014.

[134] F. Dong, W. Yan, and F. Zhang. On the number of perfect matchings of line graphs. *Discrete Applied Mathematics*, 161(6):794 – 801, 2013. URL: 10.1016/j.dam.2012.10.032, doi:10.1016/j.dam.2012.10.032.

[135] W. Yan, Y.-N. Yeh, and F. Zhang. Dimer problem on the cylinder and torus. *Physica A: Statistical Mechanics and its Applications*, 387(24):6069 – 6078, 2008. URL: 10.1016/j.physa.2008.06.042, doi:10.1016/j.physa.2008.06.042.

[136] F. Lu, L. Zhang, and F. Lin. Dimer statistics on the klein bottle. *Physica A: Statistical Mechanics and its Applications*, 390(12):2315 – 2324, 2011. URL: 10.1016/j.physa.2011.02.038, doi:10.1016/j.physa.2011.02.038.

[137] Z. Zhang and B. Wu. Pfaffian orientations and perfect matchings of scale-free networks. *Theoretical Computer Science*, 570:55 – 69, 2015. URL: 10.1016/j.tcs.2014.12.024, doi:10.1016/j.tcs.2014.12.024.

[138] H. Li and Z. Zhang. Maximum matchings in scale-free networks with identical degree distribution. *Theoretical Computer Science*, 675:64 – 81, 2017. URL: 10.1016/j.tcs.2017.02.027, doi:10.1016/j.tcs.2017.02.027.

[139] C. Tu, S. Suweis, J. Grillib, M. Formentin, and A. Maritan. Reconciling cooperation, biodiversity and stability in complex ecological communities, 2018. URL: https://arxiv.org/abs/1805.03527v2, arXiv:arXiv:1805.03527.

[140] F. Botta and N. Mitarai. Disturbance accelerates the transition from low- to high-diversity state in a model ecosystem. *Phys. Rev. E*, 89:022704, Feb 2014. URL: 10.1103/PhysRevE.89.022704, doi:10.1103/PhysRevE.89.022704.

[141] R. West, M. Mobilia, and A. M. Rucklidge. Survival behavior in the cyclic lotka-volterra model with a randomly switching reaction rate. *Phys. Rev. E*, 97:022406, Feb 2018. URL: 10.1103/PhysRevE.97.022406, doi:10.1103/PhysRevE.97.022406.

[142] D. M. Busiello, S. Suweis, J. Hidalgo, and A. Maritan. Explorability and the origin of network sparsity in living systems. *Scientific Reports*, 7(1):12323, 2017. URL: 10.1038/s41598-017-12521-1, doi:10.1038/s41598-017-12521-1.

[143] R. A. Brualdi and H. J. Ryser. *Combinatorial Matrix Theory*. Encyclopedia of Mathematics and its Applications. Cambridge University Press, 1991. URL: 10.1017/CBO9781107325708, doi:10.1017/CBO9781107325708.

[144] B. McKay. Graphs, 2017. URL: http://users.cecs.anu.edu.au/~bdm/data/graphs.html [cited 27.11.2017].

[145] K. v. Klitzing, G. Dorda, and M. Pepper. New method for high-accuracy determination of the fine-structure constant based on quantized hall resistance. *Phys. Rev. Lett.*, 45:494–497, Aug 1980. URL: https://link.aps.org/doi/10.1103/PhysRevLett.45.494, doi:10.1103/PhysRevLett.45.494.

[146] D. J. Thouless, M. Kohmoto, M. P. Nightingale, and M. den Nijs. Quantized hall conductance in a two-dimensional periodic potential. *Phys. Rev. Lett.*, 49:405–408, Aug 1982. URL: https://link.aps.org/doi/10.1103/PhysRevLett.49.405, doi:10.1103/PhysRevLett.49.405.

[147] F. D. M. Haldane. Model for a quantum hall effect without landau levels: Condensed-matter realization of the "parity anomaly". *Phys. Rev. Lett.*, 61:2015–2018, Oct 1988. URL: https://link.aps.org/doi/10.1103/PhysRevLett.61.2015, doi:10.1103/PhysRevLett.61.2015.

[148] M. Z. Hasan and C. L. Kane. Colloquium: Topological insulators. *Rev. Mod. Phys.*, 82:3045–3067, Nov 2010. URL: https://link.aps.org/doi/10.1103/RevModPhys.82.3045, doi:10.1103/RevModPhys.82.3045.

[149] Ching-Kai Chiu, Jeffrey C. Y. Teo, Andreas P. Schnyder, and Shinsei Ryu. Classification of topological quantum matter with symmetries. *Reviews of Modern Physics*, 88(3):035005–, 08 2016. URL: https://link.aps.org/doi/10.1103/RevModPhys.88.035005, doi:10.1103/RevModPhys.88.035005.

[150] C. L. Kane and T. C. Lubensky. Topological boundary modes in isostatic lattices. *Nature Physics*, 10(1):39–45, 2014. URL: https://doi.org/10.1038/nphys2835, doi:10.1038/nphys2835.

[151] J. Paulose, B. G. Chen, and V. Vitelli. Topological modes bound to dislocations in mechanical metamaterials. *Nature Physics*, 11(2):153–156, 2015. URL: https://doi.org/10.1038/nphys3185, doi:10.1038/nphys3185.

[152] Lisa M. Nash, Dustin Kleckner, Alismari Read, Vincenzo Vitelli, Ari M. Turner, and William T. M. Irvine. Topological mechanics of gyroscopic metamaterials. *Proceedings of the National Academy of Sciences*, 112(47):14495–14500, 2015. URL: https://www.pnas.org/content/112/47/14495, doi:10.1073/pnas.1507413112.

[153] Roman Süsstrunk and Sebastian D. Huber. Classification of topological phonons in linear mechanical metamaterials. *Proceedings of the National Academy of Sciences*, 113(33):E4767, 08 2016. URL: http://www.pnas.org/content/113/33/E4767.abstract, doi:10.1073/pnas.1605462113.

[154] H. Kedia, A. Souslov, and D. Z. Rocklin. Soft topological modes protected by symmetry in rigid mechanical metamaterials. *pre-print arXiv:2008.01914v3*, 2020. URL: https://arxiv.org/pdf/2008.01914.pdf.

[155] Pierre Delplace, J. B. Marston, and Antoine Venaille. Topological origin of equatorial waves. *Science*, 358(6366):1075–1077, 2017. URL: https://science.sciencemag.org/content/358/6366/1075, arXiv:https://science.sciencemag.org/content/358/6366/1075.full.pdf, doi:10.1126/science.aan8819.

[156] Di Zhou, Leyou Zhang, and Xiaoming Mao. Topological edge floppy modes in disordered fiber networks. *Phys. Rev. Lett.*, 120:068003, Feb 2018. URL: https://link.aps.org/doi/10.1103/PhysRevLett.120.068003, doi:10.1103/PhysRevLett.120.068003.

[157] Ricardo Pablo Pedro, Jayson Paulose, Anton Souslov, Mildred Dresselhaus, and Vincenzo Vitelli. Topological protection can arise from thermal fluctuations and interactions. *Phys. Rev. Lett.*, 122:118001, Mar 2019. URL: https://link.aps.org/doi/10.1103/PhysRevLett.122.118001, doi:10.1103/PhysRevLett.122.118001.

[158] Colin Scheibner, William T. M. Irvine, and Vincenzo Vitelli. Non-hermitian band topology and skin modes in active elastic media. *Phys. Rev. Lett.*, 125:118001, Sep 2020. URL: https://link.aps.org/doi/10.1103/PhysRevLett.125.118001, doi:10.1103/PhysRevLett.125.118001.

[159] Emil Prodan and Camelia Prodan. Topological phonon modes and their role in dynamic instability of microtubules. *Phys. Rev. Lett.*, 103:248101, Dec 2009. URL: https://link.aps.org/doi/10.1103/PhysRevLett.103.248101, doi:10.1103/PhysRevLett.103.248101.

[160] Lisa Yamauchi, Tomoya Hayata, Masahito Uwamichi, Tomoki Ozawa, and Kyogo Kawaguchi. Chirality-driven edge flow and non-hermitian topology in active nematic cells, 2020. arXiv:2008.10852.

[161] A. Souslov, B. C. van Zuiden, D. Bartolo, and V. Vitelli. Topological sound in active-liquid metamaterials. *Nature Physics*, 13:1091–1094, 2017. URL: https://doi.org/10.1038/nphys4193, doi:10.1038/nphys4193.

[162] Suraj Shankar, Mark J. Bowick, and M. Cristina Marchetti. Topological sound and flocking on curved surfaces. *Phys. Rev. X*, 7:031039, Sep 2017. URL: https://link.aps.org/doi/10.1103/PhysRevX.7.031039, doi:10.1103/PhysRevX.7.031039.

[163] Anton Souslov, Kinjal Dasbiswas, Michel Fruchart, Suriyanarayanan Vaikuntanathan, and Vincenzo Vitelli. Topological waves in fluids with odd viscosity. *Phys. Rev. Lett.*, 122:128001, Mar 2019. URL: https://link.aps.org/doi/10.1103/PhysRevLett.122.128001, doi:10.1103/PhysRevLett.122.128001.

[164] Kazuki Sone and Yuto Ashida. Anomalous topological active matter. *Phys. Rev. Lett.*, 123:205502, Nov 2019. URL: https://link.aps.org/doi/10.1103/PhysRevLett.123.205502, doi:10.1103/PhysRevLett.123.205502.

[165] Arvind Murugan and Suriyanarayanan Vaikuntanathan. Topologically protected modes in non-equilibrium stochastic systems. *Nature Communications*, 8(1):13881, 2017. URL: https://doi.org/10.1038/ncomms13881, doi:10.1038/ncomms13881.

[166] Kinjal Dasbiswas, Kranthi K. Mandadapu, and Suriyanarayanan Vaikuntanathan. Topological localization in out-of-equilibrium dissipative systems. *Proceedings of the National Academy of Sciences*, 115(39):E9031–E9040, 2018. URL: https://www.pnas.org/content/115/39/E9031, doi:10.1073/pnas.1721096115.

[167] Tsuneya Yoshida and Yasuhiro Hatsugai. Bulk-edge correspondence of classical diffusion phenomena, 2020. arXiv:2007.08730.

[168] Evelyn Tang, Jaime Agudo-Canalejo, and Ramin Golestanian. Topology protects chiral edge currents in stochastic systems, 2020. arXiv:2010.02845.

[169] J. C. Claussen and A. Traulsen. Cyclic dominance and biodiversity in well-mixed populations. *Phys. Rev. Lett.*, 100:058104, Feb 2008. URL: https://link.aps.org/doi/10.1103/PhysRevLett.100.058104, doi:10.1103/PhysRevLett.100.058104.

[170] M. Remoissenet. *Waves Called Solitons*, volume 3. Springer, 1999.

[171] M. A. Ablowitz and P. A. Clarkson. *Solitons, Nonlinear Evolution Equations and Inverse Scattering*. London Mathematical Society Lecture Note Series. Cambridge University Press, 1991. doi:10.1017/CBO9780511623998.

[172] Zhenya Yan. Discrete exact solutions of modified volterra and volterra lattice equations via the new discrete sine-gordon expansion algorithm. *Nonlinear Analysis: Theory, Methods & Applications*, 64(8):1798 – 1811, 2006. URL: http://www.sciencedirect.com/science/article/pii/S0362546X05007194, doi:https://doi.org/10.1016/j.na.2005.07.018.

[173] B. G. Chen, N. Upadhyaya, and V. Vitelli. Nonlinear conduction via solitons in a topological mechanical insulator. *Proceedings of the National Academy of Sciences*, 111(36):13004–13009, 2014. URL: https://www.pnas.org/content/111/36/13004, doi:10.1073/pnas.1405969111.

[174] R. Chaunsali and G. Theocharis. Self-induced topological transition in phononic crystals by nonlinearity management. *Phys. Rev. B*, 100:014302, Jul 2019. URL: https://link.aps.org/doi/10.1103/PhysRevB.100.014302, doi:10.1103/PhysRevB.100.014302.

[175] P. J. Davis. *Circulant Matrices*. Chelsea Publishing Series. Chelsea, 1994.

[176] R. M. Gray. Toeplitz and circulant matrices: A review. *Foundations and Trends in Communications and Information Theory*, 2(3):155–239, 2006. URL: http://dx.doi.org/10.1561/0100000006, doi:10.1561/0100000006.

[177] C. L. Kane. *Topological Insulators*, chapter 1 - Topological Band Theory and the $\mathbb{Z}_2$ Invariant, pages 3–34. Elsevier, 2013.

[178] G. Arfken. *Mathematical Methods for Physicists*, volume 3. Academic Press, 1985.

[179] A Yu Kitaev. Unpaired majorana fermions in quantum wires. 44(10S):131–136, 2001. URL: http://dx.doi.org/10.1070/1063-7869/44/10S/S29, doi:10.1070/1063-7869/44/10s/s29.

[180] S. Ryu and Y. Hatsugai. Topological origin of zero-energy edge states in particle-hole symmetric systems. *Phys. Rev. Lett.*, 89:077002, Jul 2002. URL: https://link.aps.org/doi/10.1103/PhysRevLett.89.077002, doi:10.1103/PhysRevLett.89.077002.

[181] Jan Carl Budich and Eddy Ardonne. Equivalent topological invariants for one-dimensional majorana wires in symmetry class d. *Physical Review B*, 88(7):075419–, 08 2013. URL: https://link.aps.org/doi/10.1103/PhysRevB.88.075419, doi:10.1103/PhysRevB.88.075419.

[182] E. Basor, J. Dubail, T. Emig, and R. Santachiara. Modified szegö–widom asymptotics for block toeplitz matrices with zero modes. *Journal of Statistical Physics*, 174(1):28–39, 2019. URL: https://doi.org/10.1007/s10955-018-2177-8, doi:10.1007/s10955-018-2177-8.

[183] J Dubail, R Santachiara, and T Emig. Conformal field theory of critical casimir forces between surfaces with alternating boundary conditions in two dimensions. *Journal of Statistical Mechanics: Theory and Experiment*, 2017(3):033201, 2017. URL: http://dx.doi.org/10.1088/1742-5468/aa5a68, doi:10.1088/1742-5468/aa5a68.

[184] Percy Deift, Alexander Its, and Igor Krasovsky. Toeplitz matrices and toeplitz determinants under the impetus of the ising model: Some history and some recent results. *Communications on Pure and Applied Mathematics*, 66(9):1360–1438, 2013. URL: https://onlinelibrary.wiley.com/doi/abs/10.1002/cpa.21467, doi:10.1002/cpa.21467.

[185] B. Novák and J. J. Tyson. Design principles of biochemical oscillators. *Nature Reviews Molecular Cell Biology*, 9:981–991, 2008. URL: https://doi.org/10.1038/nrm2530, doi:10.1038/nrm2530.

[186] S. P. Hubbell. *The Unified Neutral Theory of Biodiversity and Biogeography*. Princeton University Press, 2001.

[187] V. E. Zakharov, S. L. Musher, and A. M. Rubenchik. Weak langmuir turbulence of an isothermal plasma. *Zhurnal Eksperimentalnoi i Teoreticheskoi Fiziki*, 69:155–168, 07 1975. URL: https://ui.adsabs.harvard.edu/abs/1975ZhETF..69..155Z.

[188] Zheng-Yi Ma, Jia-Min Zhu, and Chun-Long Zheng. Solitary Wave and Periodic Wave Solutions for the Relativistic Toda Lattices. *Communications in Theoretical Physics*, 43(1):27–30, January 2005. doi:10.1088/0253-6102/43/1/006.

[189] William F. Trench. On the eigenvalue problem for toeplitz band matrices. *Linear Algebra and its Applications*, 64:199 – 214, 1985. URL: http://www.sciencedirect.com/science/article/pii/0024379585902770, doi:https://doi.org/10.1016/0024-3795(85)90277-0.

[190] Nobuya Watanabe, Yoshio Togawa, and Ken Sawada. Hamiltonians which are induced from anti-symmetric replicator equations. *Nonlinear Analysis: Theory, Methods & Applications*, 36(5):655 – 660, 1999. URL: http://www.sciencedirect.com/science/article/pii/S0362546X98001643, doi:https://doi.org/10.1016/S0362-546X(98)00164-3.

[191] Tsuneya Yoshida, Tomonari Mizoguchi, and Yasuhiro Hatsugai. Chiral edge modes in game theory: a kagome network of rock-paper-scissors, 2020. arXiv:2012.05562.

[192] Sundarapandian Vaidyanathan. Dynamics and control of brusselator chemical reaction. *Int J ChemTech Res*, 8(6):740–749, 2015.

Danksagung

Zuerst einmal danke ich dem aufmerksamen Leser dieser Dissertation für bemerkenswertes Durchhaltevermögen.

Vielen Dank an Erwin für die letzten sechs Jahre am Lehrstuhl, für wissenschaftliche Diskussionen, unterhaltsame Abende in Antholz und bei Konferenzen. Die verschiedenen Reisen, Konferenzen, Diskussionsrunden und Begegnungen die du mir ermöglicht hast waren und sind eine große Bereicherung für mich.

Vielen Dank an Hannes für die gute Zusammenarbeit, ich habe viel von dir gelernt.

Vielen Dank an den ganzen Lehrstuhl, ob an der Kaffee-Maschine, in Antholz oder bei Weihnachtsfeiern, es gab immer wieder schöne, alberne, interessante und absurde Situationen. Insbesondere bedanke ich mich bei den Self-Assemblers für großartige Zusammenarbeit und Unterhaltung trotz diverser Absagen von Magazinen, bei Felix, einen besseren Büromitbewohner hab ich nicht verdient, bei Moritz, Emanuel und dem ganzen Rest.

Vielen Dank an Isarstan, Fortschritt durch Elektrifizierung!

Vielen Dank an meine Eltern und meine Geschwister für ihre Unterstützung und interessierte Nachfragen trotz meiner Unfähigkeit meine Forschung verständlich zu erklären.

Danke an Mechtild und Uli für das Allgäu-Asyl während des aufschreibens.

Und schlussendlich vielen Dank an Hannah, danke dass du mich während diverser Krisen aushältst, immer wieder versuchst mich vom Arbeiten abzulenken und zu wichtigeren und lustigeren Dingen überredest.